

UC San Diego

UC San Diego Electronic Theses and Dissertations

Title

Ultrasound based NDE/SHM techniques for critical components in aerospace and transportation structures

Permalink

<https://escholarship.org/uc/item/6fk3j3sh>

Author

Cui, Ranting

Publication Date

2021

Peer reviewed|Thesis/dissertation

UNIVERSITY OF CALIFORNIA SAN DIEGO

**Ultrasound based NDE/SHM techniques for critical components
in aerospace and transportation structures**

A dissertation submitted in partial satisfaction of the requirements for the degree

Doctor of Philosophy

in

Structural Engineering

by

Ranting Cui

Committee in Charge:

Professor Francesco Lanza di Scalea, Chair
Professor William S. Hodgkiss
Professor Hyonny Kim
Professor William A. Kuperman
Professor Kenneth J. Loh

2021

Copyright

Ranting Cui, 2021

All rights reserved.

The dissertation of Ranting Cui is approved, and it is acceptable in quality and form for publication on microfilm and electronically.

University of California San Diego

2021

DEDICATION

To my parents, Wenzuo Cui and Ye Li

To my husband, Chaojun Wei

EPIGRAPH

*Even though I walk
Through the valley of the shadow of death,
I do not fear evil,
For You are with me;
Your rod and Your staff,
They comfort me.*

Psalm 23:4

TABLE OF CONTENTS

| | |
|---|------|
| Dissertation approval page..... | iii |
| Dedication..... | iv |
| Epigraph..... | v |
| Table of contents..... | vi |
| List of figures..... | x |
| List of tables..... | xvi |
| Acknowledgements..... | xvii |
| Vita..... | xx |
| Abstract of the dissertation..... | xxii |
| Chapter 1. Introduction..... | 1 |
| Chapter 2. On the identification of the elastic properties of composites by guided waves and optimization algorithm..... | 6 |
| 2.1. Abstract..... | 6 |
| 2.2. Introduction..... | 7 |
| 2.3. Methodology for the inversion process..... | 11 |
| 2.3.1. Semi-Analytical Finite Element (SAFE) method for predicting ultrasonic guided wave propagation in laminated composites..... | 11 |
| 2.3.2. Effective engineering properties..... | 14 |
| 2.3.3. Property identification algorithm by dispersion curve matching and Simulated Annealing optimization..... | 17 |
| 2.4. Property identification case studies..... | 21 |
| 2.4.1. Unidirectional laminate..... | 21 |
| 2.4.2. Quasi-isotropic laminate..... | 28 |
| 2.4.3. Anisotropic laminate..... | 34 |
| 2.5. Discussion and conclusions..... | 39 |

| | |
|---|-----------|
| 2.6. Acknowledgments..... | 42 |
| 2.7. References..... | 43 |
| Chapter 3. Identification of elastic properties of composites by inversion of ultrasonic guided wave data | 46 |
| 3.1. Abstract | 46 |
| 3.2. Introduction..... | 47 |
| 3.3. Experimental procedure for measuring phase velocity dispersion curves..... | 51 |
| 3.4. Property identification algorithm..... | 53 |
| 3.4.1. SAFE wave propagation model | 53 |
| 3.4.2. Identification of global “engineering” laminate properties | 55 |
| 3.4.3. Simulated Annealing optimization | 55 |
| 3.5. Experimental property identification: case studies | 58 |
| 3.5.1. Aluminum plate | 58 |
| 3.5.2. Quasi-Isotropic laminate..... | 61 |
| 3.5.3. Anisotropic laminate..... | 65 |
| 3.6. Discussion and conclusions | 70 |
| 3.7. Acknowledgments..... | 72 |
| 3.8. References..... | 72 |
| Chapter 4. Damage imaging in skin-stringer composite aircraft panel by ultrasonic guided waves using deep learning with convolutional neural network | 76 |
| 4.1. Abstract | 76 |
| 4.2. Introduction..... | 77 |
| 4.3. Experimental setup and procedure..... | 79 |
| 4.4. Details of the Convolutional Neural Network (CNN) Algorithm | 85 |
| 4.5. Results..... | 89 |
| 4.5.1. Simulated damage positions co-located with training positions..... | 89 |

| | |
|--|------------|
| 4.5.2. Results: simulated damage positions offset from training positions. | 95 |
| 4.5.3. Results: saw-cut damage in stringer cap. | 99 |
| 4.6. Results: classification performance evaluation. | 100 |
| 4.7. Discussion and conclusions | 103 |
| 4.8. Acknowledgments. | 104 |
| 4.9. References. | 105 |
| Chapter 5. Non-destructive inspection of skin-stringer composite flat panel by data driven method and ultrasonic guided-wave transfer function method. | 109 |
| 5.1. Introduction. | 109 |
| 5.2. The cross-sectional damage characterization of the composite panel with skin-stringer geometry | 110 |
| 5.2.1. Data-driven matched field processing (DDMFP) | 110 |
| 5.2.2. Results: defect localization on the skin-stringer cross-section | 111 |
| 5.3. The excitation localization by Convolutional Neural Network (CNN) | 114 |
| 5.3.1. Simulated data preparation from ABAQUS | 114 |
| 5.3.2. Training scheme by using MATALB Deep Learning Toolbox | 115 |
| 5.3.3. Results of impact location prediction. | 118 |
| 5.4. Ultrasonic guided-wave transfer function extraction on inspecting composite aerospace structures | 119 |
| 5.4.1. Experimental setup. | 121 |
| 5.4.2. Damage detection of the simple zone of curved composite (skin-stringer structure) | 122 |
| 5.4.3. Damage detection of curved composite skin-stringer-shear_tie structure | 129 |
| 5.5. Conclusions. | 139 |
| 5.6. Acknowledgements | 140 |
| 5.7. References. | 140 |
| Chapter 6. Ultrasonic beamforming imaging for damage characterization in solids | 143 |

| | |
|---|------------|
| 6.1. Introduction..... | 143 |
| 6.2. Time delay estimation with the wedge | 144 |
| 6.3. Experimental setup..... | 146 |
| 6.4. Frequency domain beamforming (FDB) algorithm and results..... | 148 |
| 6.4.1. FDB Algorithm | 148 |
| 6.4.2. Results: the aluminum block with two drilling hole defects..... | 150 |
| 6.4.3. Results: the railhead with one drilling hole defect..... | 151 |
| 6.5. Time domain beamforming (TDB) algorithm and results | 152 |
| 6.5.1. TDB Algorithm..... | 152 |
| 6.5.2. Averaging and the prob-wedge coupling impact | 153 |
| 6.5.3. 3D defect reconstruction in real-time with encoder..... | 156 |
| 6.5.4. Results: Experimentation in Transportation Technology Center, Inc (TTCI) defect library. | 157 |
| 6.6. Conclusions..... | 163 |
| 6.7. Fatigue history prediction of the railway track (future work /preliminary study) ... | 164 |
| 6.7.1. Data preparation and training schedule..... | 165 |
| 6.7.2. Results..... | 168 |
| 6.8. Acknowledgments..... | 171 |
| 6.9. References | 172 |
| Chapter 7. Conclusions..... | 174 |

LIST OF FIGURES

| | |
|---|----|
| Figure 2.1. (a) SAFE model. (b) Local (lamina) and global (laminate) coordinate systems. (c) Laminate load convention..... | 12 |
| Figure 2.2. Overall workflow of composite property identification by using guided-wave phase velocity matching and Simulated Annealing optimization. | 20 |
| Figure 2.3. Unidirectional laminate: SAFE results of phase velocity dispersion curves along with displacement, strain and stress cross-sectional profiles at 160 kHz. | 23 |
| Figure 2.4. 1D identification of lamina elastic constants in unidirectional laminate | 25 |
| Figure 2.5. 5D identification of lamina elastic constants and laminate engineering properties in unidirectional laminate..... | 27 |
| Figure 2.6. Quasi-isotropic laminate: SAFE results of phase velocity dispersion curves along with displacement, strain and stress cross-sectional profiles at 160 kHz. | 28 |
| Figure 2.7. 1D identification of lamina elastic constants in quasi-isotropic laminate..... | 30 |
| Figure 2.8. 5D identification of lamina elastic constants in quasi-isotropic laminate..... | 31 |
| Figure 2.9. 5D identification of axial and shear laminate engineering properties in quasi-isotropic laminate..... | 32 |
| Figure 2.10. 5D identification of flexural and torsional laminate engineering properties in quasi-isotropic laminate..... | 33 |
| Figure 2.11. Anisotropic laminate: SAFE results of phase velocity dispersion curves along with displacement, strain and stress cross-sectional profiles at 160 kHz. | 35 |
| Figure 2.12. 1D identification of lamina elastic constants in anisotropic laminate..... | 35 |
| Figure 2.13. 5D identification of lamina elastic constants in anisotropic laminate..... | 36 |
| Figure 2.14. 5D identification of axial and shear laminate engineering properties in anisotropic laminate..... | 38 |
| Figure 2.15. 5D identification of flexural and torsional laminate engineering properties in anisotropic laminate. | 39 |
| Figure 3.1. Experimental setup for extraction of phase velocity dispersion curves from the test plates. | 52 |
| Figure 3.2. (a) SAFE representation of guided wave propagation. (b) Local (lamina) and global (laminate) coordinate system arrangements. (c) Classical Lamination Theory (CLT) load convention..... | 54 |

| | |
|--|----|
| Figure 3.3. The property identification workflow using SAFE as the forward model and Simulated Annealing optimization..... | 57 |
| Figure 3.4. Aluminum plate: a typical experimental waveform, along with SAFE results of displacement, strain, and stress cross-sectional profiles for S_0 and A_0 guided modes at 500 kHz. | 59 |
| Figure 3.5. 2D identification of Young’s modulus and Poisson’s ratio of the isotropic plate, along with a comparison of phase velocity dispersion curves between experiment and optimum SAFE prediction | 61 |
| Figure 3.6. Quasi-isotropic laminate: (a) the lay-up arrangement; (b) a typical experimental waveform; (c) SAFE results of displacement, strain and stress cross-sectional profiles for the SH_0 guided mode at 400kHz. | 63 |
| Figure 3.7. 5D identification of engineering constants of the quasi-isotropic laminate by the SH_0 mode..... | 65 |
| Figure 3.8. Anisotropic laminate: the lay-up arrangement; typical signal in the experiment; SAFE results of displacement, strain and stress cross-sectional profiles of the S_0 mode at 400 kHz and the A_0 mode at 200 kHz. | 66 |
| Figure 3.9. 5D identification of engineering properties of the anisotropic laminate by the A_0 mode. | 67 |
| Figure 3.10. 5D identification of engineering properties of the anisotropic laminate by the S_0 mode. | 68 |
| Figure 3.11. 5D identification of engineering properties of the anisotropic laminate by both A_0 and S_0 modes..... | 69 |
| Figure 4.1. (a) Test panel with CNN training section and CNN testing sections; (b) The putty clay next to a quarter, and schematic of PZT transducers, training locations and simulated damage locations; (c) schematic for real saw-cut damage section..... | 80 |
| Figure 4.2. The test panel with (a) the wireless device unit for routing the transducers’ signals and (b) the host computer laptop. | 81 |
| Figure 4.3. Example of the toneburst excitation signal to the PZT transmitters. | 82 |
| Figure 4.4. Main steps of the CNN decision model..... | 84 |
| Figure 4.5. Structure of the CNN architecture utilized in the present study..... | 86 |
| Figure 4.6. CNN prediction of damage locations co-located with training locations for excitation toneburst with 10 V amplitude, 250 kHz central frequency, and 6.5 cycles. | 90 |

| | |
|--|-----|
| Figure 4.7. CNN prediction of damage locations co-located with training locations for excitation toneburst with 10 V amplitude, 250 kHz central frequency, and 15.5 cycles. | 92 |
| Figure 4.8. CNN prediction of damage locations co-located with training locations when summing all excitation toneburst cases. | 93 |
| Figure 4.9 RAPID prediction of damage locations co-located with training locations | 95 |
| Figure 4.10. CNN prediction of damage locations offset from training locations for excitation toneburst with 10 V amplitude, 250 kHz central frequency, and 6.5 cycles | 96 |
| Figure 4.11. CNN prediction of damage locations offset from training locations for excitation toneburst with 10 V amplitude, 250 kHz central frequency, and 15.5 cycles. | 97 |
| Figure 4.12. CNN prediction of damage locations offset from training locations when summing all excitation toneburst cases. | 98 |
| Figure 4.13. CNN prediction of location of real saw-cut damage in stringer’s cap when summing all excitation toneburst cases. | 99 |
| Figure 4.14. Training accuracy and validation accuracy versus training iterations for (a) the Pristine-Skin-Stringer_Flange model and (b) the Stringer_Cap model..... | 100 |
| Figure 5.1. Experimental setup, (a). Top view of the composite panel; (b). bottom view of the composite panel; (c). sensor placement | 112 |
| Figure 5.2. Damage on the skin. (a) the damage location identified by algorithm; (b) real damage location..... | 112 |
| Figure 5.3. Damage on the stringer. (a) the damage location identified by the algorithm. (b) bottom view of real damage. (c) front view of real damage | 113 |
| Figure 5.4. Sensor locations in Abaqus simulation..... | 114 |
| Figure 5.5. The pulse excitation applied in the simulation. | 115 |
| Figure 5.6. The assembled receiving signal with 20 excitations | 116 |
| Figure 5.7. CNN training schedule | 117 |
| Figure 5.8. The result compared with simulated ground truth: (a) The predicated location of the excitation; (b) The simulated location of the excitation | 118 |
| Figure 5.9. The structural transfer function extraction by a dual-output scheme | 120 |
| Figure 5.10. The zone definition of curved composite panel 4_1. | 121 |
| Figure 5.11. The devices used in the experiment..... | 122 |

| | |
|--|-----|
| Figure 5.12. Stringer 2: Signal and frequency spectra of receiver 1 and receiver 2..... | 123 |
| Figure 5.13. Damage localization on stringer 2: (a) Mahalanobis distance; (b) transfer function comparison on clean stringer and stringer with hot glue. | 124 |
| Figure 5.14. Stringer 3: Signal and frequency spectra of receiver 1 and receiver 2..... | 125 |
| Figure 5.15. Damage localization on stringer 3: (a) Mahalanobis distance; (b) transfer function comparison on clean stringer and stringer with hot glue. | 126 |
| Figure 5.16. Stringer 4: Signal and frequency spectra of receiver 1 and receiver 2..... | 127 |
| Figure 5.17. Damage localization on stringer 4: (a) Mahalanobis distance; (b) transfer function comparison on clean stringer and stringer with the hot glue. | 128 |
| Figure 5.18. Investigation of the ultrasonic waves propagating through the shear-tie. | 130 |
| Figure 5.19. Signal for tracing waves in shear-tie triggered by impactor..... | 131 |
| Figure 5.20. Frequency spectra for pico-sensors on the shear-tie region triggered by the impactor. | 131 |
| Figure 5.21. The shear-tie region investigation with contact transmitter and three pico-sensors: (a) the illustration of the experiment; (b) the transmitter; (c) real experiment on the surface of the panel | 133 |
| Figure 5.22. Investigation of transfer function between receiver 1 and receiver 2 on the surface | 133 |
| Figure 5.23. Investigation of transfer function between middle bottom pico-receiver and pico-receiver 2 through shear-tie | 134 |
| Figure 5.24. Shear tie region inspection using the impactor and air-couple receivers | 135 |
| Figure 5.25. Investigation of transfer function between AC-receiver 1 and AC-receiver 2 with 500 test samples on the surface..... | 136 |
| Figure 5.26. Investigation of transfer function between AC-receiver 1 and AC-receiver 2 with 1000 test samples on the surface..... | 137 |
| Figure 5.27. Receiver operating characteristic of detectability of air-couple receivers in shear-tie region | 138 |
| Figure 6.1. Time delay calculation with wedge [11] | 145 |
| Figure 6.2. Experimental Setup: (a) Wedge; (b) Probe; (c) Encoder..... | 146 |
| Figure 6.3. A full-matrix capture (FMC) controller | 147 |

| | |
|--|-----|
| Figure 6.4. Frequency domain beamforming algorithm workflow. [12] | 148 |
| Figure 6.5. Two holes imaging in aluminum block: (a) the real experiment; (b) the result with uniform window; (c) the result with hamming window; (d) the result with Chebyshev window | 150 |
| Figure 6.6. Drilling hole imaging in railhead: (a) real experiments; (b) results with uniform window; (c) results with hamming window; (d) results with Chebyshev window | 151 |
| Figure 6.7. Time domain beamforming algorithm workflow [12] | 152 |
| Figure 6.8. Auto configuration file adjustment..... | 153 |
| Figure 6.9. The comparison of the imaging on averaging and no-averaging | 154 |
| Figure 6.10. The coupling impact between probe and wedge: (a) comparisons among three different scenarios; (b) 32 array with SA11-N55S wedge; (c) 64 array with SA12 - N55S wedge | 155 |
| Figure 6.11. The real-time 3D image reconstruction with encoder control..... | 157 |
| Figure 6.12. The scheme of 3D defect reconstruction of railhead..... | 158 |
| Figure 6.13. The comparison between TDB and FDB on the sample B6 115RE | 159 |
| Figure 6.14. Comparison of 3D imaging reconstructions..... | 159 |
| Figure 6.15. The geometry calibration and reconstruction on the sample N3 136RE..... | 160 |
| Figure 6.16. The defect reconstruction of sample B8 (136RE): (a). Real experimental setup and 2D real-time defect imaging; (b) 3D-point clouds and surface reconstruction | 161 |
| Figure 6.17. The defect reconstruction of sample TD-in-the-weld (136RE): (a). Real experimental setup and 2D real-time defect imaging; (b) 3D-point clouds and surface reconstruction. | 162 |
| Figure 6.18. Data preparation: (a) The theoretical curve; (b) The theoretical curve with gaussian noise. | 166 |
| Figure 6.19. Data preparation: (a) The theoretical curve with gaussian noise; (b) Zoom-in window. | 166 |
| Figure 6.20. Data preparation: (a) whole signal; (b) validation set; (c) training set..... | 167 |
| Figure 6.21. The comparison of the validation set and the prediction set | 168 |
| Figure 6.22. The training convergence analysis | 169 |
| Figure 6.23. The training efficiency analysis of the loss and the learning rate | 169 |

Figure 6.24. The efficient learning rate discussion with the largest learning step..... 170

LIST OF TABLES

| | |
|--|-----|
| Table 2.1. Single lamina elastic constants (from Ref. [37]) | 21 |
| Table 3.1 Single lamina elastic constants (T800/3900-2) for the quasi-isotropic laminate (from Ref. [38])..... | 62 |
| Table 3.2. Single lamina elastic constants (T300/5208) for the anisotropic laminate (from Ref. [39])..... | 65 |
| Table 4.1. Test panel material, thickness and lay-up..... | 79 |
| Table 4.2. CNN classification performance for the eight simulated damage cases using all excitation tonebursts. | 102 |
| Table 6.1 Comparison between A-scan and ultrasonic imaging..... | 163 |

ACKNOWLEDGEMENTS

I want to express my true gratitude to all the people who helped me during my PhD experience. Especially, I would like to thank my advisor Prof. Francesco Lanza di Scalea who gave me this life-changing opportunity to experience the beauty and the charm of research at UC San Diego. His passion encourages me to persist in academia. He has always been an excellent mentor and a shining lighthouse constantly supporting and guiding me throughout these years.

A special acknowledgement goes to my family, who always believe in and encourage me during my academic career. Their constant supporting makes me feel close to home even if we are half a world apart. Specially, I want to thank to my husband, whose love drives and helps me go forward even in the most desperate time.

I would like to give thanks to all the colleagues present and past in the NDE/ExpMech laboratory. Their presence makes this journey amazing and unforgettable. The special mention goes to Diptojit Datta, Ali Zare Hosseinzadeh, Izabela Batista, Chengyang Huang, Dr. Simone Sternini, Dr. Margherita Capriotti, Dr. Albert Liang, Dr. Xuan “Peter” Zhu for their technical inputs and friendship. A big acknowledgement also goes to Guillermo Azuara De Pablo for nearly one year collaboration and nice friendship. I would also like to thank Prof. Kim, Chaiane Wiggers de Souza and Eyung Kim for the wonderful collaboration and providing me with insights into problems in research.

Special thanks go to all my friends who showed a fundamental and profound part of my life during these years. They have introduced special meaning of life to me. Their love and care will be always in my heart. In particular, I would like to thank Jingxue Lu, Xiaowen Zhan, Zheng Fu, Dan Wang, Nancy Lo, Tomoko Miyake, Grace Hsiung, Iris Chen, Michael Teng, Priscilla

Teng and many others! You all have been my family and this journey has become the best because of you all.

This dissertation is a collection of papers (that have been accepted or submitted) and some ongoing work.

Chapter 2 is, in full, a reprint of material published in Cui, Ranting, and Francesco Lanza di Scalea. "On the identification of the elastic properties of composites by ultrasonic guided waves and optimization algorithm." *Composite Structures* 223 (2019): 110969. The dissertation author was the primary investigator and author of this paper.

Chapter 3 is, in full, a reprint of material published in Cui, Ranting, and Francesco Lanza di Scalea. "Identification of Elastic Properties of Composites by Inversion of Ultrasonic Guided Wave Data." *Experimental Mechanics*(2021): 1-14. The dissertation author was the primary investigator and author of this paper.

Chapter 4 is, in full, a reprint of material published in Cui, Ranting, Guillermo Azuara, Francesco Lanza di Scalea, Eduardo Barrera. "Damage Imaging in Skin-Stringer Composite Aircraft Panel by Ultrasonic Guided Waves Using Deep Learning with Convolutional Neural Network." *Structural Health Monitoring*, June (2021). The dissertation author was the primary investigator and author of this paper.

Chapter 5 is, in part, has been published in Ranting Cui, Guillermo Azuara, and Francesco Lanza di Scalea. "Composite elastic property identification through guided wave inversion and damage detection by data-driven process." *In Health Monitoring of Structural and Biological Systems XIV*, vol. 11381, p. 113810I. International Society for Optics and Photonics, 2020. The dissertation author was the primary investigator and author of this paper.

Chapter 6 is, in part, has been published in Chengyang Huang, Ranting Cui, and Francesco Lanza di Scalea "Deliverable 1.1: Chapter on Task 1 - SAFT Imaging Algorithm Finalization and 3D Image Generation based on Laboratory Tests at TTCI and UCSD", U.S Department of Transportation, Federal Railroad Administration, February, 2021. The dissertation author was the primary investigator and author of this technical report.

Chapter 7 is the final conclusions.

VITA

- 2015 Bachelor of Engineering in Civil Engineering, Central South University, Changsha, China.
- 2016-2017 Teaching Assistant, University of California San Diego, La Jolla, USA
- 2017 Master of Science in Structural Engineering, University of California San Diego, La Jolla, USA
- 2018-2021 Research Assistant, University of California San Diego, La Jolla, USA
- 2021 Doctor of Philosophy in Structural Engineering, University of California San Diego, La Jolla, USA.

Publications

JOURNAL ARTICLES:

1. **Ranting Cui**, and Francesco Lanza di Scalea. "On the identification of the elastic properties of composites by ultrasonic guided waves and optimization algorithm." *Composite Structures*, 223 (2019): 110969.
2. **Ranting Cui**, and Francesco Lanza di Scalea. "Identification of Elastic Properties of Composites by Inversion of Ultrasonic Guided Wave Data." *Experimental Mechanics*, (2021): 1-14.
3. **Ranting Cui**, Guillermo Azuara and Francesco Lanza di Scalea, Eduardo Barrera. "Damage Imaging in Skin-Stringer Composite Aircraft Panel by Ultrasonic Guided Waves Using Deep Learning with Convolutional Neural Network. " *Structural Health Monitoring*, June (2021)
4. **Ranting Cui**, Chaiane Wiggers de Souza, Hyonny Kim, Benjamin J. Katko, Francesco Lanza di Scalea. "Non-Destructive damage localization of composite aerospace structures by ultrasonic guided-wave transfer function and statistical processing in multi-output mobile systems." *In preparation*

CONFERENCE PROCEEDINGS:

1. **Ranting Cui** and Francesco Lanza di Scalea. "Composite Property Identification from Inversion of Guided Wave Dispersion Curves and Simulated Annealing Optimization." *IWSHM*, 2019.
2. Margherita Capriotti, **Ranting Cui**, and Francesco Lanza di Scalea. "Guided wave techniques for damage detection and property characterization in composite aerospace structures." *Health Monitoring of Structural and Biological Systems XIII*. Vol. 10972. International Society for Optics and Photonics, 2019.
3. Antonino Spada, Margherita Capriotti, **Ranting Cui**, and Francesco Lanza di Scalea. "Improved global-local model to predict guided-wave scattering patterns from discontinuities in complex parts." In *Health Monitoring of Structural and Biological Systems XIII*, vol. 10972, p. 109720M. International Society for Optics and Photonics, 2019.
4. Margherita Capriotti, **Ranting Cui**, and Francesco Lanza di Scalea. "Damage Detection and Visco-Elastic Property Characterization of Composite Aerospace Panels Using Ultrasonic Guided Waves." In *Mechanics of Composite, Hybrid and Multifunctional Materials, Volume 5*, pp. 205-208. Springer, Cham, 2019.
5. **Ranting Cui**, Guillermo Azuara, and Francesco Lanza di Scalea. "Composite elastic property identification through guided wave inversion and damage detection by data-driven process." In *Health Monitoring of Structural and Biological Systems XIV*, vol. 11381, p. 113810I. International Society for Optics and Photonics, 2020.
6. Datta, Diptojit, Albert Liang, **Ranting Cui**, and Francesco Lanza di Scalea. "Defect detection performance of a high-speed rail inspection system from passive acoustic identification." In *Sensors and Smart Structures Technologies for Civil, Mechanical, and Aerospace Systems 2020*, vol. 11379, p. 113791G. International Society for Optics and Photonics, 2020.
7. Datta, Diptojit, **Ranting Cui**, Francesco Lanza di Scalea, and Robert Wilson. "High-speed Rail Inspection by a Non-contact Passive Ultrasonic Technique." *No. TRBAM-21-01881*. 2021.

ABSTRACT OF THE DISSERTATION

Ultrasound based NDE/SHM techniques for critical components in aerospace and transportation structures

by

Ranting Cui

Doctor of Philosophy in Structural Engineering

University of California San Diego, 2021

Professor Francesco Lanza di Scalea, Chair

Nondestructive Evaluation (NDE) and Structural Health Monitoring (SHM) using ultrasonic waves have become compelling techniques for identifying various defects in structural components. Ultrasonic guided-wave testing has the potential to identify the elastic properties of the fiber-reinforced composite laminates. A nondestructive tool for characterization of the composite properties is particularly advantageous when components involve manufacturing variances and service quality degradation. The first part of this dissertation examines the potential for composite property characterization by a single wave propagation direction to enable the accurate identification of several elastic properties away from the wave propagation direction

because of the anisotropy of the composite providing the “coupling” effect. A property inversion scheme was proposed based on matching phase velocity dispersion curves of relevant guided modes by means of a Simulated Annealing optimization algorithm and a Semi-Analytical Finite Element method to solve the forward problem.

The second part of the dissertation is focused on defect detection and localization in a stiffened skin-to-stringer composite panel. A data-driven Deep Learning approach based on Convolutional Neural Network is exploited to detect the damages even generalized to non-training scenarios. Moreover, a matched-field-data-driven method and the structural transfer function method (the deconvolution of the “dual-output” scheme) are also discussed to explore a wide field for the damage detection of the skin-to-stringer assembly.

The third part of this dissertation targets the defect imaging on homogeneous solids using ultrasonic bulk waves to reconstruct 2D and 3D images of defects. Sensor arrays and a frequency-domain-based beamforming algorithm are employed to improve the defect characterization process. The experimental applications are performed on both a simulated defect on an aluminum block in the lab and natural transverse defects on the railroad tracks at the Transportation Technology Center Inc (TTCI) in Pueblo, CO. Moreover, a preliminary study of the fatigue history prediction of the railway track is also discussed for future investigation.

Chapter 1. Introduction

Non-destructive evaluation (NDE) and structure health monitoring (SHM) are dependent on the benefit of reliable and robust indicators that provide the detection, localization, quantification, and even prediction of damages in mechanical structures. Composite materials have become popular candidates for fabrication due to their outstanding advantages, such as high strength, high stiffness to mass ratio, and high capacity to resist fatigue and corrosion [1,2]. However, the failure mechanisms of composite structures also come into service, for instance, delamination, fiber rupture, and matrix damage. Those damages can easily spread throughout the laminate structure leading to catastrophic failure [3]. Therefore, composite structural monitoring and evaluation technologies aim to provide security and cost efficiency regarding maintenance.

In recent decades, the methods of detecting damage at an early stage gain special attention to avoid sudden structural-component failure. Specifically, structural vibration measurements predicting structural integrity have been the focus of many researchers, acceptance function together with a proper theoretical model to illustrate the location and magnitude of the defect [4]. At the same time, the realization of damages causing stiffness reduction leads to shifts in the natural frequencies of the structure in question. The impact of delamination on the natural frequencies of laminated composite beams has been studied by [5]. Furthermore, the transversal cracks in composite structures are investigated by [6] to reveal their appearance resulting in the changes of stiffness as well as natural frequencies.

Optimization techniques help monitor and evaluate structural integrity to find the best estimation among vast possible scenarios. Genetic algorithm (GA) provides a robust solution to complex problems due to the efficacy of exploiting the region of interest and avoiding local

minimum traps [7]. Artificial intelligence (AI) is a significant improvement in exaggerating the functionality of the optimization techniques, which is even able to predict the unknown results of future inputs by learning a set of given data samples [8, 9]. An ideal assessment methodology should be capable of recognizing individual damage patterns from historically structural responses to determine the extent of current damage, which is fulfilled by the AI techniques. The motivation to apply AI (especially Neural Networks) in damage detection procedures is the possibility of various kinds of damages occurring in several locations making damage detection an extremely complex process [10]. The neural network models of delamination size prediction in composite beams have been investigated [11], which showed promising results of correct identification and localization.

Besides, physics-based methods keep the attention of the researchers in the NDE and SHM fields. The impulse response function (Green's function) is one of the compelling ways to represent structural conditions by reconstructing the direct signal between two air-coupled transducers to eliminate ambient noise fields [12, 13]. Lanza et al. [14] estimated the impulse response function of a piece of rail track in the moving train when the ambient noise had a significant portion of the final acquired signal. The different occasions, such as joints and bolts, were classified by passive-only reconstruction of the structural coherence.

The first part of this dissertation included chapters 2 and 3, showing the large-field damage detection using elastic material properties as indicators. A new framework of identifying composite material elastic properties was proposed by matching the phase velocity dispersion curves with the Semi-Analytical Finite Element (SAFE) model [15] as a forward solver and Simulated Annealing [16] as optimization. The framework inversely achieved the five independent lamina constants and seven global engineering constants of three composite plates in simulation,

proving itself the efficacy of identifying the properties even if they were off-wave-propagation direction. Three guided wave modes, SH_0 (Shear-horizontal mode), S_0 (Axial mode), A_0 , were investigated. Later, in chapter 3, the experimental implementations were applied on three plates to inversely obtain engineering constants with a discussion of single-mode identification and multi-mode identification.

The second part of this dissertation showed the various techniques of defect classification and localization of the complex composite skin-stringer panel covering chapters 4 and 5. In particular, a Convolutional Neural Network (CNN) [17] was applied to identify the defect in typical positions of the complex composite panel (skin, stringer_flange, stringer_cap_top, and stringer_cap_side), with a sparse sensor array. The well-trained model predicted the positions of the non-trained simulated points even the real cut damage besides the trained points with about three millisecond time consumption. The generalization capability and fast prediction speed shine the light on real-time health monitoring based on given in-service data or even simulated data. The drawback of the CNN application was that the contact piezoelectrical sensors were employed to collect the data, which reduced the mobility and flexibility of the experimental setup. As a complement, chapter 5 discussed the methodology of using air-coupled transducers to identify the defect in the composite panel by structural transfer function extraction. The structural transfer function of two target points did not change unless the anomaly showed between two target points, which led to itself an excellent indicator for defect detection.

The third part moved to the homogeneous material, such as aluminum block and railhead, to construct damage images by ultrasonic imaging techniques [18]. Two algorithms, frequency-domain beamforming (FDB) and time-domain beamforming (TDB), were compared. The results were obtained from an aluminum block with two simulated damages (drilling holes) and real

natural transverse defects on the railhead. Finally, in chapter 7, the preliminary study of rail track fatigue estimation was performed based on synthetic data with considerable noise. The deep neural network was implemented to predict the failure state with the discussion in terms of accuracy and computation efficiency.

References

- [1] Jones RM. *Mechanics of Composite Materials*. 2nd ed. CRC press; 2014.
- [2] Gomes GF, Mendéz YAD, Alexandrino P da SL, da Cunha Jr SS, Ancelotti Jr AC. The use of intelligent computational tools for damage detection and identification with an emphasis on composites—A review. *Compos Struct* 2018;196:44–54.
- [3] Chakraborty D. Artificial neural network based delamination prediction in laminated composites. *Mater Des* 2005;26:1–7.
- [4] Adams RD, Cawley P, Pye CJ, Stone BJ. A vibration technique for non-destructively assessing the integrity of structures. *J Mech Eng Sci* 1978;20:93–100.
- [5] Valdes SHD, Soutis C. Delamination detection in composite laminates from variations of their modal characteristics. *J Sound Vib* 1999;228:1–9.
- [6] Negru I, Gillich GR, Praisach ZI, Tufoi M, Gillich N. Natural frequency changes due to damage in composite beams. *J. Phys. Conf. Ser.*, vol. 628, IOP Publishing; 2015, p. 12091.
- [7] Worden K, Staszewski W, Manson G, Ruotulo A, Surace C. Optimization techniques for damage detection. *Encycl Struct Heal Monit* 2009.
- [8] Gomes GF, Ancelotti Jr AC, da Cunha Jr SS. Residual stress prediction in porous cfrp using artificial neural networks. *Compos Mech Comput Appl An Int J* 2018;9.
- [9] Gomes GF, Diniz CA, da Cunha SS, Ancelotti AC. Design optimization of composite prosthetic tubes using ga-ann algorithm considering tsai-wu failure criteria. *J Fail Anal Prev* 2017;17:740–9.
- [10] Montalvao D, Maia NMM, Ribeiro AMR. A review of vibration-based structural health monitoring with special emphasis on composite materials. *Shock Vib Dig* 2006;38:295–324.
- [11] Okafor AC, Chandrashekhara K, Jiang YP. Delamination prediction in composite beams with built-in piezoelectric devices using modal analysis and neural network. *Smart Mater Struct* 1996;5:338.
- [12] Weaver RL, Lobkis OI. Diffuse fields in open systems and the emergence of the Green's function (L). *J Acoust Soc Am* 2004;116:2731–4. <https://doi.org/10.1121/1.1810232>.

- [13] Roux P, Sabra KG, Kuperman WA, Roux A. Ambient noise cross correlation in free space: Theoretical approach. *J Acoust Soc Am* 2005;117:79–84.
- [14] di Scalea FL, Zhu X, Capriotti M, Liang A, Mariani S, Sternini S, et al. High-speed non-contact ultrasound system for rail track integrity evaluation. *Heal. Monit. Struct. Biol. Syst.* XII, vol. 10600, International Society for Optics and Photonics; 2018, p. 106000J.
- [15] Bartoli I, Marzani A, Lanza di Scalea F, Viola E. Modeling wave propagation in damped waveguides of arbitrary cross-section. *J Sound Vib* 2006;295:685–707. <https://doi.org/10.1016/j.jsv.2006.01.021>.
- [16] Ryden N, Park CB. Fast simulated annealing inversion pavement using phase-velocity spectra 2006;71.
- [17] Goodfellow I, Bengio Y, Courville A, Bengio Y. *Deep learning*. vol. 1. MIT press Cambridge; 2016.
- [18] Jensen JA, Nikolov SI, Gammelmark KL, Pedersen MH. Synthetic aperture ultrasound imaging. *Ultrasonics* 2006;44. <https://doi.org/10.1016/j.ultras.2006.07.017>.

Chapter 2. On the identification of the elastic properties of composites by guided waves and optimization algorithm

2.1. Abstract

This paper examines the potential of ultrasonic guided waves to identify the elastic properties of fiber-reinforced composite laminates widely used in light-weight structures. Due to variability in manufacturing processes, complexities involved in the constituent materials, or degradation in service, a non-destructive tool for the characterization of the composite's properties can be extremely useful. A common assumption is the necessity for multiple wave propagation directions to fully characterize the properties. This paper examines the potential for property characterization by a single wave propagation direction. It proposes a property inversion scheme based on matching phase velocity dispersion curves of relevant guided modes by means of a Simulated Annealing optimization algorithm and a Semi-Analytical Finite Element method to solve the forward problem. Proof-of-principle numerical studies are presented to demonstrate the potential of each selected wave mode to provide identification of several properties, including the lamina elastic constants and the laminate effective constants. It is shown that the complex stress and strain profiles generated by the waves, aided by the anisotropy of the composite, create interesting "coupling" effects that ultimately enable accurate identification of several elastic properties away from the wave propagation direction.

2.2. Introduction

The characterization of the elastic properties of composite parts is of great interest in many structural and industrial applications of these materials. This is especially the case because of the inherent heterogeneity of the components, coupled with the large variabilities expected in the manufacturing process, which make it extremely difficult to accurately predict the properties of the final part from those of the individual constituents (e.g. fibers and matrix). Property identification is also relevant to the condition monitoring of composite structures in service to detect any possible degradation caused by aging or damage. Desirable requisites of an ideal identification technique are its non-destructive nature and the possibility to implement in-situ on actual structures in service.

Consequently, several studies have been conducted by using vibrational techniques (mostly based on modal analysis) to non-destructively identify the elastic constants of composite plates, as recently reviewed by Tam et al [1]. Vibrational techniques, by their very nature, are sensitive to the “effective” or “engineering” constants of the part. The majority of vibrational techniques have been applied to thin anisotropic plates, where the independent unknowns are the four in-plane elastic properties (longitudinal and transverse in-plane Young’s moduli, in-plane shear modulus and in-plane Poisson’s ratio) [2-7]. Additional investigations have expanded the identification to five independent constants including the out-of-plane shear modulus (or out-of-plane Poisson’s ratio), by studying thick plates in order to sufficiently activate the out-of-plane effects [8-13]. Most of these studies are based on matching the “true” modal behavior of the plate (e.g. from experimental tests) with the “predicted” vibrational behavior corresponding to a given set of elastic constants. The identification algorithm involves some kind of minimization operation that can be either a simple least-square method or more sophisticated optimization schemes [13-14]. Although

nondestructive, the vibrational techniques of property identification are naturally “global” identification approaches using low frequency modal behavior that is quite sensitive to the boundary conditions of the part. Hence many tests involve freely suspended plates where modal predictions are more robust. It is much more difficult to utilize vibrational techniques in-situ on an existing composite structure because of the difficulty to properly model boundary conditions.

An identification method that is alternative to the vibrational testing technique, although somewhat related to it because it also involves dynamics, is the use of propagating elastic waves in the kHz or MHz range (ultrasonic range). These waves are typically not sensitive to boundary conditions of the test plate, lending themselves to non-destructive property identification in independent plate coupons as well as in-situ on actual structures [15-16]. The ultrasonic range of wave dynamics is very sensitive to the elastic constants and can provide high sensitivity to the lamina-by-lamina properties, in addition to the laminate effective (engineering) properties. Several studies of composite property identification with optimization algorithms have involved the use of bulk waves (e.g. quasi longitudinal and quasi shear) and wave velocity predictions such as the Christoffel equation for orthotropic plates [17-18]. Bulk wave testing, however, can only identify properties in a very localized region of the composite.

By exploiting the waveguide geometry typical of most composite parts (e.g. plate-like geometry), ultrasonic guided waves in the 100’s of kHz range are increasingly considered as an excellent means for probing composite parts in the Non-Destructive Evaluation (NDE) and Structural Health Monitoring fields [19-21]. Guided waves offer the unique combined capability of large monitoring ranges (~ a few centimeters to ~ a few meters) and high sensitivity to the test part owing to relatively large frequencies/small wavelengths employed. Complexities of guided waves include their multimode character (several modes propagating simultaneously) and their

dispersive character (propagation velocity dependent on frequency), particularly challenging in laminated composites. Because of these complexities, the majority of guided wave testing on composite plates has been focused on defect detection, with much fewer studies dealing with the task of property identification. Balasubramanian [22] first identified the properties of composite plates based on the phase velocity dispersion curves of the fundamental axial and flexural wave modes and Genetic Algorithm optimization. He used the transfer matrix method as the forward wave propagation model. Vishnuvardhan et al. [23] also used optimization routines associated to guided wave velocities in various propagation directions (one transmitter and multiple receivers) to identify all nine elastic constants of orthotropic plates and using the Christoffel equation at a single frequency value as the forward model. Vepakomma et al. [24] estimated elastic constants in composites using a similar approach. Glushkov et al. [25] identified the engineering constants of unidirectional and cross-ply laminates using group velocity dispersion curve matching and optimization algorithms. In this study the forward model was computed using general elastodynamic theory involving integral Green's functions for layered media. Other investigations have explored the use of non-contact wave transduction for the identification of composite properties by guided waves [26].

The wave prediction models utilized in these studies involve transcendental equations or close-form solutions that become quite complicated in the case of multilayered laminates and whose solutions often involve a root searching routine that can slow down an identification problem based on multiple iterations.

In alternative to purely theoretical modes, the Semi-Analytical Finite Element (SAFE) method has gained increasing interest for modeling the multimode and dispersive behavior of ultrasonic guided waves in waveguides that are complex in either geometry (e.g. arbitrary cross-

sections) or material properties (e.g. multilayered composites) [27-29]. The SAFE technique efficiently discretizes by finite elements solely the cross-section of the waveguide and, instead, utilizes theoretical harmonic solutions in the wave propagation direction of the waveguide. SAFE offers a direct means to predict complicated wave dispersion behavior in a multilayered laminate as a function of the elastic constants of the individual laminae. These advantages were recently exploited by Marzani and De Marchi [16] to identify lamina constants in a unidirectional laminate and a cross-ply laminate. That study matched the group velocity dispersion curves between the pseudo-experimental case (a SAFE forced solution obtained for a set a “true” constants) and trial cases obtained by SAFE with varying constants. The SAFE solution directly outputs phase velocity curves. A mode tracking algorithm [30] becomes necessary to move from the phase velocity solutions to the group velocity solutions. The work by Marzani and Demarchi [16] utilized axial and flexural modes, with multiple propagation directions (two directions for the unidirectional laminate and four directions for the cross-ply laminate) to provide sensitivity to the lamina’s full stiffness matrix.

The present paper utilizes the phase velocity dispersion curves of ultrasonic guided waves propagating in a single direction to identify both the elastic constants of the individual laminae and the effective (engineering) constants of the laminate. The forward wave propagation solution is here obtained by the SAFE method, that is coupled with a Simulated Annealing (SA) optimization algorithm to match pseudo-experimental phase velocity curves to trial velocity curves obtained with varying constants. A similar SA optimization scheme was previously shown to be effective for property inversion in Rayleigh wave data applied to pavement characterization by Ryden and Park [31]. The common difficulties of the SA inversion processes with multiple local minima of the objective function and fixed iteration intervals [32] are here relieved by using the Metropolis

Rule [33] and Cauchy distributions for the iterated variables [31]. Particular care in the present study is devoted to the individual role of the fundamental axial wave mode (S_0), flexural mode (A_0) and shear-horizontal mode (SH_0), that are considered in a broad frequency range (20 kHz – 200 kHz). Three different laminate layups are studied, namely: a unidirectional laminate, a quasi-isotropic laminate, and a fully anisotropic laminate. The study shows that the majority of the properties in these laminates can be properly identified by these three wave modes, despite propagating in only a single direction. This performance is the result of the interesting coupling of stress/strain components that occurs among different planes in the high-frequency guided-wave range, as well as the natural anisotropy of the laminate.

2.3. Methodology for the inversion process

2.3.1. Semi-Analytical Finite Element (SAFE) method for predicting ultrasonic guided wave propagation in laminated composites

The SAFE method is an efficient tool to calculate ultrasonic guided wave propagation solutions in prismatic waveguides [27-29]. As schematized in Fig. 1(a), SAFE uses analytical wave propagation solutions in the wave propagation direction, x , and limits the FE discretization to the waveguide's cross-sectional plane, (y, z) . This technique lends itself to study multilayered waveguides such as laminated composites in a broad frequency range where analytical solutions are either non-existent or generally difficult to obtain. In addition, the 2D FE discretization greatly relaxes the computational requirements and improves the solution accuracy at the high frequencies compared to a full 3D FE discretization.

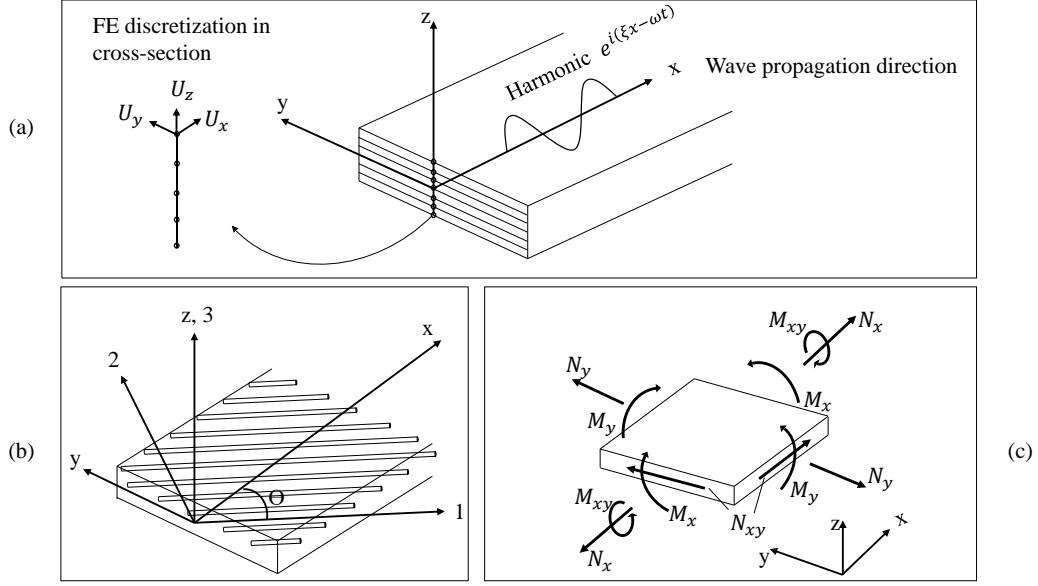


Figure 2.1. (a) SAFE model. (b) Local (lamina) and global (laminated) coordinate systems. (c) Laminated load convention.

Without considering external forces and traction, the governing equation of the problem is represented by the virtual work's principle in the volume V of the waveguide:

$$\int_V \delta \mathbf{u}^T (\rho \ddot{\mathbf{u}}) dV + \int_V \delta \boldsymbol{\varepsilon}^T \boldsymbol{\sigma} dV = 0 \quad (2.1)$$

where \mathbf{u} is the displacement vector, $\boldsymbol{\varepsilon}$ is the strain vector, $\boldsymbol{\sigma}$ is the stress vector, T means the transpose operation, and $\ddot{\mathbf{u}}$ represents the second derivative with respect to time. The displacement field is approximated in SAFE by the following discretization in the (y, z) cross-sectional plane and analytical harmonic behavior in the wave propagation direction x :

$$\mathbf{u}^e(x, y, z, t) = \mathbf{N}(y, z) \mathbf{q}^e e^{i(\xi x - \omega t)} \quad (2.2)$$

where t is time, $\mathbf{N}(y, z)$ is the 3×6 matrix of FE shape functions, \mathbf{q}^e is the vector of nodal

displacements for the e -th finite element, i is the imaginary unit, and ξ is the wavenumber associated with frequency ω .

For the subject applications to composite laminates, a transversely isotropic thin layer is considered as the individual unidirectional lamina. Considering 1 the fiber direction, 2 the in-plane direction perpendicular to the fibers, and 3 the out-of-plane direction perpendicular to the fibers, Figure 2.1 (b), the following 3D constitutive relation in the lamina principal directions of material symmetry (local coordinates) applies:

$$\begin{bmatrix} \varepsilon_1 \\ \varepsilon_2 \\ \varepsilon_3 \\ \varepsilon_4 \\ \varepsilon_5 \\ \varepsilon_6 \end{bmatrix} = \begin{bmatrix} \frac{1}{E_{11}} & -\frac{\nu_{12}}{E_{11}} & -\frac{\nu_{13}}{E_{11}} & 0 & 0 & 0 \\ -\frac{\nu_{12}}{E_{11}} & \frac{1}{E_{22}} & -\frac{\nu_{23}}{E_{22}} & 0 & 0 & 0 \\ -\frac{\nu_{13}}{E_{11}} & -\frac{\nu_{23}}{E_{22}} & \frac{1}{E_{33}} & 0 & 0 & 0 \\ 0 & 0 & 0 & \frac{1}{G_{23}} & 0 & 0 \\ 0 & 0 & 0 & 0 & \frac{1}{G_{13}} & 0 \\ 0 & 0 & 0 & 0 & 0 & \frac{1}{G_{12}} \end{bmatrix} \begin{bmatrix} \sigma_1 \\ \sigma_2 \\ \sigma_3 \\ \sigma_4 \\ \sigma_5 \\ \sigma_6 \end{bmatrix} \quad (2.3)$$

where $E_{33}=E_{22}$, $\nu_{13}=\nu_{12}$, $G_{13} = G_{12}$, $G_{23} = E_{22}/(2(1+\nu_{23}))$. The 6×6 matrix in the above equation is the inverse of the lamina's stiffness matrix in the local coordinate, i.e. \mathbf{Q}^{-1} . In the case of a multilayered composite laminate, the local stiffness matrix of each lamina \mathbf{Q} is rotated into the global (x, y, z) reference system of the laminate using the following transformation relation [28]:

$$\bar{\mathbf{Q}} = \mathbf{R}_1 \mathbf{Q} \mathbf{R}_2^{-1} \quad (2.4)$$

The stiffness matrixes $\bar{\mathbf{Q}}$ in the global laminate coordinates are then assembled in the cross-sectional FE discretization to describe the entire laminate. Substituting Eqs. (2.2) and (2.3) into Eq. (2.1) leads to the following eigenvalue problem:

$$[\mathbf{H} - \xi \mathbf{L}]_{2M} \mathbf{U} = \mathbf{0} \quad (2.5)$$

where the subscript M is the number of degrees of freedom of the FE mesh, $\mathbf{U} = [\mathbf{q} \ \xi \mathbf{q}]^T$ is a nodal displacement vector of double size, and the real symmetric matrices \mathbf{H} and \mathbf{L} contain stiffness terms, mass terms and the frequency ω [27]. The eigensystem is solved by finding the $2M$ wavenumbers ξ 's for each frequency ω , and the corresponding eigenvectors \mathbf{U} . The solutions represent the M forward-propagating guided wave modes and the M backward-propagating guided wave modes. The phase velocity for these modes is calculated at each frequency by $c_{ph} = \omega / \xi_{real}$ (phase velocity dispersion curves), and the eigenvectors represent the cross-sectional displacement mode shapes for each (ξ, ω) combination, i.e. at each point of the dispersion curves. For each composite laminate, these solutions are therefore calculated directly as a function of the five elastic constants in the principal directions of material symmetry of each (transversely isotropic) lamina, i.e. E_{11} , E_{22} , ν_{12} , G_{12} and ν_{23} .

2.3.2. Effective engineering properties

In many practical engineering uses of composites, it is of interest to know the “engineering” or “effective” elastic properties of the laminate as a whole. In this paper both in-plane properties (extensional and shear) and out-of-plane properties (flexural and torsional) are being sought. The laminate’s engineering properties can be calculated from the lamina’s elastic constants using

Classical Lamination Theory (CLT). Assuming a symmetrical laminate lay-up, that is often utilized to eliminate the coupling between extensional-shear behavior and flexural-torsional behavior (\mathbf{B} matrix of CLT equal to 0), the laminate's constitutive relation in the global coordinate system (x, y, z) can be written as:

$$\begin{bmatrix} \boldsymbol{\varepsilon}^0 \\ \boldsymbol{\kappa} \end{bmatrix} = \begin{bmatrix} \mathbf{A}^{-1} & 0 \\ 0 & \mathbf{D}^{-1} \end{bmatrix} \begin{bmatrix} \mathbf{N} \\ \mathbf{M} \end{bmatrix} \quad (2.6)$$

where $\boldsymbol{\varepsilon}^0 = [\varepsilon_x^0 \quad \varepsilon_y^0 \quad \gamma_{xy}^0]^T$ is the vector containing in-plane normal strains and shear strain, $\boldsymbol{\kappa} = [\kappa_x \quad \kappa_y \quad \kappa_{xy}]^T$ is the vector containing out-of-plane curvatures and twist, $\mathbf{N} = [N_x \quad N_y \quad N_{xy}]^T$ is the vector containing in-plane axial loads and shear load, $\mathbf{M} = [M_x \quad M_y \quad M_{xy}]^T$ is the vector containing flexural moments and torque, and the matrices \mathbf{A} and \mathbf{D} are calculated from the individual lamina's stiffness coefficients in the global coordinate system \bar{Q}_{ij} as:

$$\begin{cases} A_{ij} = \sum_{k=1}^n (\bar{Q}_{ij})_k (h_k - h_{k-1}) \\ D_{ij} = \frac{1}{3} \sum_{k=1}^n (\bar{Q}_{ij})_k (h_k^3 - h_{k-1}^3) \end{cases} \quad (2.7)$$

The laminate's engineering properties can therefore be calculated from the lamina's stiffness coefficients \bar{Q}_{ij} from the following relations:

$$E_x = \frac{N_x}{\varepsilon_x^0 h} \Big|_{N_y=N_{xy}=0} = \frac{1}{A_{11}^{-1} h} = \frac{\det(\mathbf{A})}{(A_{22}A_{66} - A_{26}^2) h} \quad \text{axial stiffness along } x \quad (2.8)$$

$$E_y = \left. \frac{N_y}{\varepsilon_y^0 h} \right|_{N_x=N_{xy}=0} = \frac{1}{A_{22}^{-1} h} = \frac{\det(\mathbf{A})}{(A_{11}A_{66} - A_{16}^2) h} \quad \text{axial stiffness along } y \quad (2.9)$$

$$\nu_{xy} = - \left. \frac{\varepsilon_y^0}{\varepsilon_x^0} \right|_{N_y=N_{xy}=0} = - \frac{A_{12}^{-1}}{A_{11}^{-1}} = \frac{A_{12}}{A_{22}} \quad \text{in-plane Poisson's ratio} \quad (2.10)$$

$$G_{xy} = \left. \frac{N_{xy}}{\gamma_{xy}^0 h} \right|_{N_x=N_y=0} = \frac{1}{A_{66}^{-1} h} = \frac{\det(\mathbf{A})}{(A_{11}A_{22} - A_{12}^2) h} \quad \text{in-plane shear stiffness} \quad (2.11)$$

$$K_x = \left. \frac{M_x}{\kappa_x} \right|_{M_y=M_{xy}=0} = \frac{1}{D_{11}^{-1}} = \frac{\det(\mathbf{D})}{(D_{22}D_{66} - D_{26}^2)} \quad \text{flexural rigidity around } x \quad (2.12)$$

$$K_y = \left. \frac{M_y}{\kappa_y} \right|_{M_x=M_{xy}=0} = \frac{1}{D_{22}^{-1}} = \frac{\det(\mathbf{D})}{(D_{11}D_{66} - D_{16}^2)} \quad \text{flexural rigidity around } y \quad (2.13)$$

$$K_{xy} = \left. \frac{M_{xy}}{\kappa_{xy}} \right|_{M_x=M_y=0} = \frac{1}{D_{66}^{-1}} = \frac{\det(\mathbf{D})}{(D_{11}D_{22} - D_{12}^2)} \quad \text{torsional rigidity} \quad (2.14)$$

The above expressions further simplify in the case of special lay-up symmetries. For example, for balanced laminates (pairs of laminae at $\pm\theta$), the extensional-shear coupling vanishes and $A_{16} = A_{26} = 0$. Similarly, for unidirectional (0 deg) or cross-ply (0 and 90 deg) laminates, as well as for antisymmetric laminates (for a $+\theta$ lamina there is a $-\theta$ lamina at a symmetric position), the flexural-torsional coupling vanishes and $D_{16} = D_{26} = 0$.

2.3.3. Property identification algorithm by dispersion curve matching and Simulated Annealing optimization

The overall flowchart of the composite property identification is presented in Figure 2.2. The identification is based on matching the “ideal” phase velocity dispersion curves for guided waves propagating in one direction for the given laminate to “tentative” versions of the phase velocity dispersion curves calculated by SAFE models for varying elastic constants. The set of elastic constants that best matches the dispersion curves therefore identifies the given composite. In this study, the lay-up of the composite is assumed to be known (although this could also become an optimization variable if needed). The guided modes that are used in the analysis are the three fundamental modes of S_0 (axial), A_0 (flexural) and SH_0 (shear horizontal) [20] considered in a broad frequency range (20 kHz – 200kHz). Up to five independent optimization variables are considered, i.e. the five elastic constants of the individual laminae [E_{11} , E_{22} , G_{12} , ν_{12} , ν_{23}]. From the lamina’s constants, the laminate engineering properties [E_x , E_y , ν_{xy} , G_{xy} , K_x , K_y , K_{xy}] are then calculated from Eqs. (2.8)-(2.14).

The dispersion curve matching process is performed through an optimization that utilizes the Simulated Annealing (SA) algorithm that originates from a physical process involving the cooling of crystals from high-energy state to low-energy state, eventually reaching an energy-stable state [34]. The objective function that needs to be minimized is defined as the following discrepancy metric:

$$d = \sqrt{\frac{1}{N} \sum_{i=1}^N \frac{(c_{\text{ph,pred}}(\omega_i) - c_{\text{ph,true}}(\omega_i))^2}{c_{\text{ph,true}}(\omega_i)}} \quad \text{for } S_0, A_0 \text{ or } SH_0 \quad (2.15)$$

where $c_{\text{ph,true}}$ is the phase velocity for the given mode (S_0 , A_0 or SH_0) at the frequency ω_1 calculated from the SAFE model of the composite with the correct elastic constants, $c_{\text{ph,pred}}$ is the corresponding phase velocity calculated from the SAFE model for the trial elastic constants, and N is the number of frequency values. For the results shown in this study, a frequency range of 20 kHz – 200 kHz was considered because this is typically used to probe structural composites in ultrasonic guided-wave testing. By considering each guided mode separately, the analysis determines the mode-specific suitability and sensitivity to certain properties (e.g. the axial and flexural modes are expected to be more sensitive to in-plane longitudinal stiffnesses and Poisson’s ratios, whereas the shear horizontal mode is expected to be more sensitive to the in-plane shear modulus). Clearly, the general framework can be applied to combinations of multiple guided modes if so desired in future applications.

Referring again to Figure 2.2, in the initial iteration variables (\mathbf{M}_0) and iteration interval ($\Delta\mathbf{M}_0$) are selected and set as the first accepted transition to pass through the SAFE model for the calculation of the phase velocity curves. The first trial is completed with the second iteration of $\mathbf{M}_0 + \Delta\mathbf{M}_0$. After comparing the two discrepancy values through the Metropolis Rule (MR) [33], the decision is made of either accepting the current iteration as a new transition perturbing the interval size, or returning to the previous step for another test with the same interval. The MR increases the chance to find the global minimum of the objective function by only searching the most probable variables. It also provides the second opportunity for the current test to be accepted if its mismatch value is larger than the previously-accepted transition. The comparison is performed between r , a uniformly-distributed random number in $[0,1]$, and $e^{(-\Delta d/T)}$, where Δd is the difference of mismatch values between two models and T is the present value. To further increase the speed of reaching the global minimum, a Cauchy-distribution perturbation is

performed to associate the annealing value with the variable-interval adjustments [35]. The SA algorithm is used to minimize the objective function by utilizing the “temperature” (T) and the “cooling schedule coefficient” (α) as two control factors to perform perturbations of the variables. The variable-perturbation equation utilized in this study is based on the work of Ref. [31]:

$$\begin{cases} \mathbf{M}_j = \mathbf{M}_i + \Delta\mathbf{M}_i \\ \Delta\mathbf{M}_i = \Delta\mathbf{M}_0 \left(\frac{T}{T_0} \right) \left(\eta_1 \tan \left(\frac{\eta_2 \pi}{2} \right) \right) \\ T = T_0 \alpha^{i+1} \end{cases} \quad (2.16)$$

where \mathbf{M}_j is the vector of the new iterations for the variables, \mathbf{M}_i are the last accepted transitions, $\Delta\mathbf{M}_i$ are the corresponding perturbation intervals, $\Delta\mathbf{M}_0$ is the initial increment of the variables, T_0 and T are the “initial” and the “current” temperatures, and η_1 and η_2 are random numbers uniformly distributed in $[-1,1]$. All variables can be perturbed simultaneously if they are all assumed unknown. In the results that follow, T_0 was set to 30° and α was set to 0.99. These two values were considered a suitable pair for good accuracy and computational efficiency [31]. In this study the SA algorithm is run three times [36]. For each SA run, 1000 iterations are set as the stop condition because after that the substantial exploration is greatly reduced based on the characteristics of the Cauchy distribution [32].

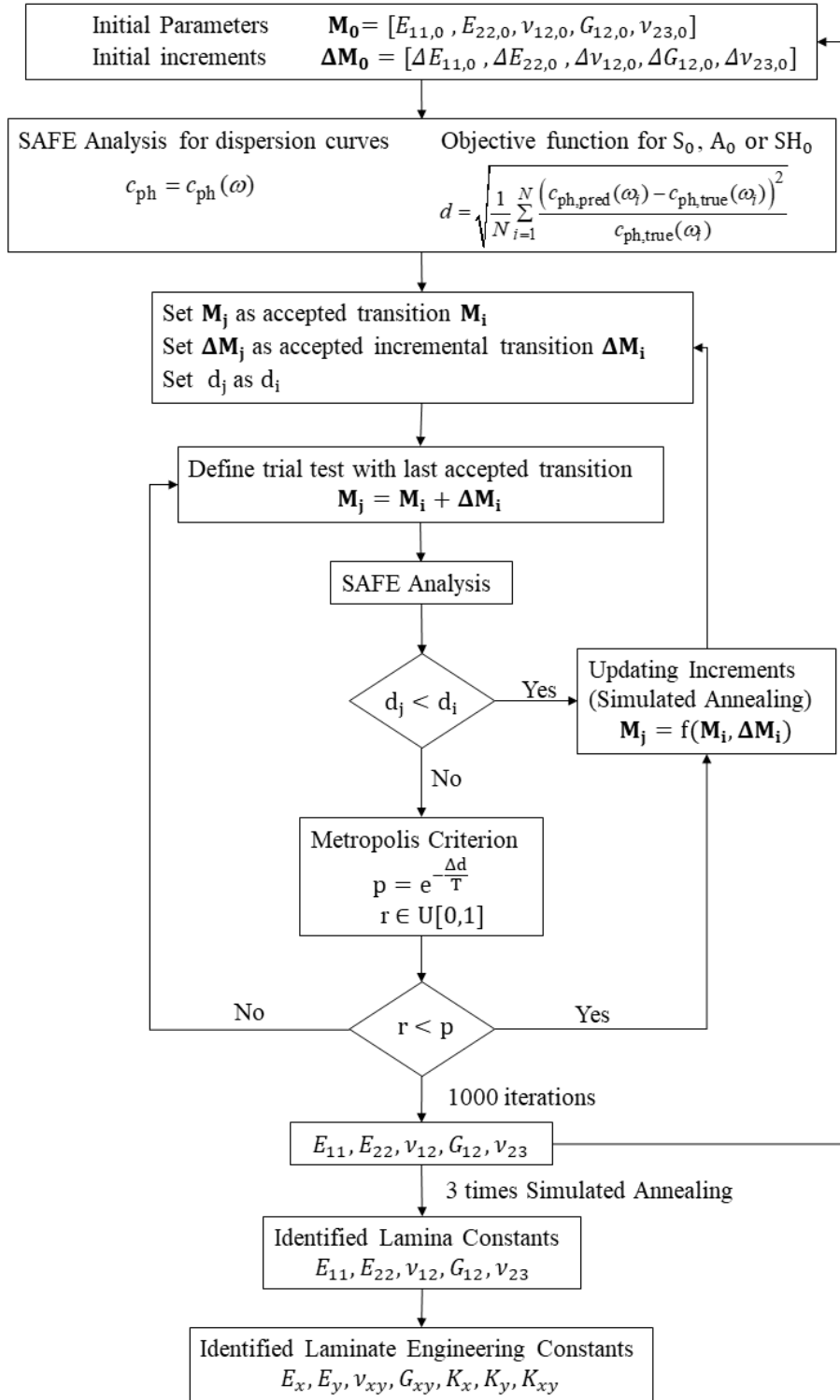


Figure 2.2. Overall workflow of composite property identification by using guided-wave phase velocity matching and Simulated Annealing optimization.

2.4. Property identification case studies

2.4.1. Unidirectional laminate

The first case study consisted of an 8-ply unidirectional laminate with a thickness of 1.3 mm with “true” individual lamina properties listed in Table 1 and density of 1550 kg/m³. The properties were typical values for a T800/3900-2-graphite-epoxy lamina from [37]. This case is shown in Figure 2.3. In this case, the local lamina coordinate system ($1, 2, 3$) is aligned with the global laminate coordinate system (x, y, z). Wave propagation was considered along direction x (1). The objective of this analysis was to identify the elastic constants of the individual laminae ($E_{11}, E_{22}, \nu_{12}, G_{12}, \nu_{23}$) from the optimization algorithm, as well as the engineering constants of the entire laminate ($E_x, E_y, \nu_{xy}, G_{xy}, K_x, K_y, K_{xy}$).

Table 2.1. Single lamina elastic constants (from Ref. [37])

| Constant | E_{11} | E_{22} | E_{33} | ν_{12} | ν_{13} | ν_{23} | G_{12} | G_{13} | G_{23} |
|-------------|----------|----------|----------|------------|------------|------------|----------|----------|----------|
| Value (GPa) | 160.08 | 8.97 | 8.97 | 0.28 | 0.28 | 0.36 | 6.21 | 6.21 | 3.30 |

Figure 2.3 shows the SAFE calculated phase velocity dispersion curves for this laminate, using the “true” elastic constants, showing the three fundamental modes of S_0 , A_0 and SH_0 . As expected, S_0 and SH_0 show little dispersion throughout this frequency range, whereas A_0 is highly dispersive at the low frequencies. These characteristics are very similar in nature to those of Rayleigh-Lamb guided modes propagating in isotropic plates (key differences in composites being the obvious dependence on the propagation direction due to anisotropy and the general mode coupling in wave propagation directions away from principal directions of material symmetry).

The displacement cross-sectional mode shapes (profiles) for these modes at a frequency of 160 kHz are also shown in Figure 2.3, along with the corresponding cross-sectional strain and stress profiles. The displacement profiles are the eigenvector of the SAFE eigenproblem in Eq. (2.5). The strain profiles were obtained from spatial differentiation of the displacement profiles [38]. The stress profiles were then calculated from the strains using the constitutive equations with the layer-specific elastic constants. The displacement profiles clearly indicate the axial nature of the S_0 mode (symmetric horizontal displacement u_x), the flexural nature of the A_0 mode (antisymmetric horizontal displacement u_x), and the shear nature of the SH_0 mode (pure transverse displacement u_y). The strain and stress profiles shed light on the sensitivity that may be expected by a certain wave mode to specific elastic properties to be identified. For example, the S_0 mode shows predominant σ_{xx} and ε_{xx} behavior, suggesting particular sensitivity to axial-type constants such as Young's moduli and Poisson's ratios. The A_0 mode, in addition, shows significant shear τ_{xz} and γ_{xz} in the transverse plane (associated to cross-sectional "warping" at the high frequency, well beyond the Bernoulli-Euler low-frequency approximation) which suggests an added sensitivity to shear moduli in the transverse (x, z) plane. The SH_0 mode, as expected, shows predominant horizontal shear τ_{xy} and γ_{xy} , suggesting sensitivity to shear modulus in the horizontal (x, y) plane.

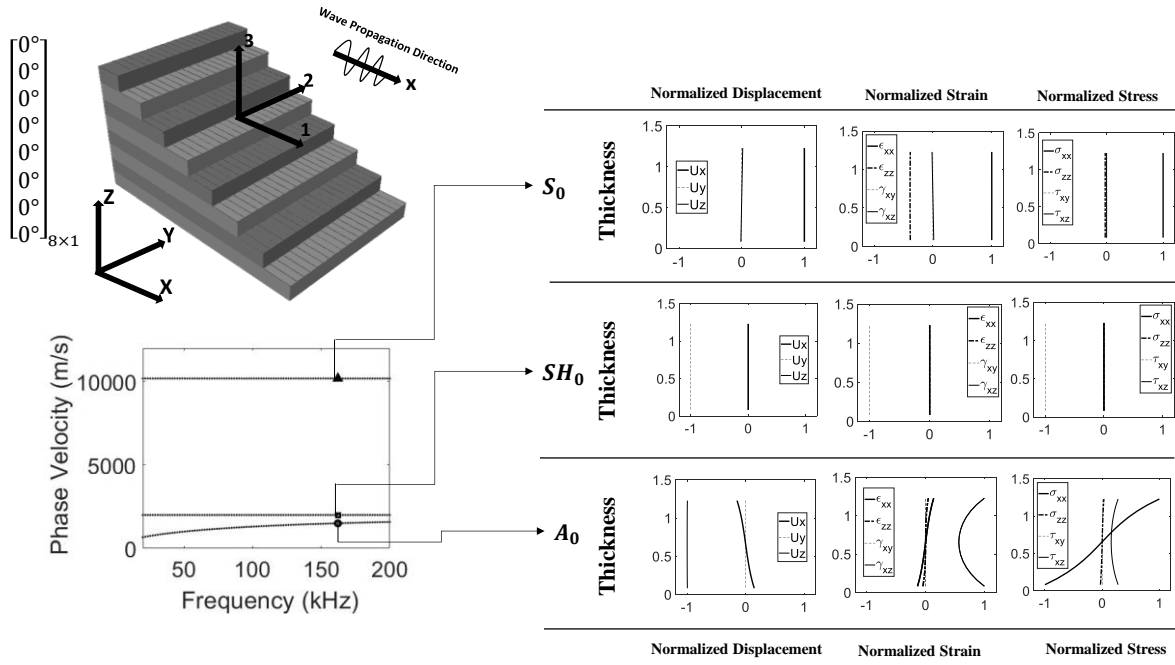


Figure 2.3. Unidirectional laminate: SAFE results of phase velocity dispersion curves along with displacement, strain and stress cross-sectional profiles at 160 kHz.

The first identification analysis was conducted in 1D, whereby only one of the five elastic constants of the lamina was considered at a time as the optimization variable, and the other four constants were fixed to their known “true” values. The results of the 1D identification are shown in Figure 2.4, where the individual sensitivity of each of the guided modes to the various elastic constants can be examined independently of the others. The figure plots the discrepancy metric d from Eq. (2.15), representing the mismatch between the “trial” and the “true” phase velocity dispersion curves, versus the % error between the “trial” variable values and the “true” (known) values. The slope (or sharpness) of the curves represents the rate of convergence (sensitivity) of the mode to the specific constant. In the subject analysis, the unknown variable trials were uniformly distributed between $\pm 50\%$ of the true values. Figure 2.4(a) for E_{11} shows that the highest

sensitivity is achieved by the S_0 mode (largest slope), as expected by the predominant σ_{xx} and ε_{xx} behavior discussed above in Figure 2.3. A good second candidate for E_{11} identification is also shown to be A_0 , since this mode also features significant σ_{xx} and ε_{xx} components from Figure 2.3. As far as the transverse moduli $E_{22}=E_{33}$, Figure 2.4(b) also shows an appreciable sensitivity by mode S_0 followed by mode A_0 , although the slopes are much smaller than those for the E_{11} identification. This lower sensitivity to constants in the transverse plane is quite expected because of the chosen wave propagation direction in the longitudinal direction [16]. However, the results interestingly show that such “transverse sensitivity” is not zero as too often assumed, because of the appreciable (although small) vertical components σ_{zz} and ε_{zz} that are present in both S_0 and A_0 . A similar observation can be drawn for the identification of the Poisson’s ratios $\nu_{12}=\nu_{13}$ (Figure 2.4(c)). These results thus suggest that it is theoretically possible to launch the wave in one direction and identify the constants in orthogonal directions, provided that the frequency range considered is broad enough to activate the cross terms in the mode’s cross-sectional profiles. Regarding the in-plane shear moduli $G_{12}=G_{13}$ (Figure 2.4(d)), as expected the shear horizontal mode SH_0 offers the highest sensitivity (through the predominant in-plane shear components τ_{xy} and γ_{xy} seen in Figure 2.3). Interestingly and less expectedly, Figure 2.4(d) also reveals that the A_0 mode can be quite successful in identifying $G_{12}=G_{13}$ through the significant transverse shear components τ_{xz} and γ_{xz} (cross-sectional “warping”) as discussed above. The most difficult constant to identify by the single wave propagation direction is the Poisson’s ratio in the transverse plane, ν_{23} (Figure 2.4(e)), where the curve slopes are at least two orders of magnitude smaller than for the other constants. A similar conclusion on this specific constant was made by Marzani and de Marchi (2012) [16].

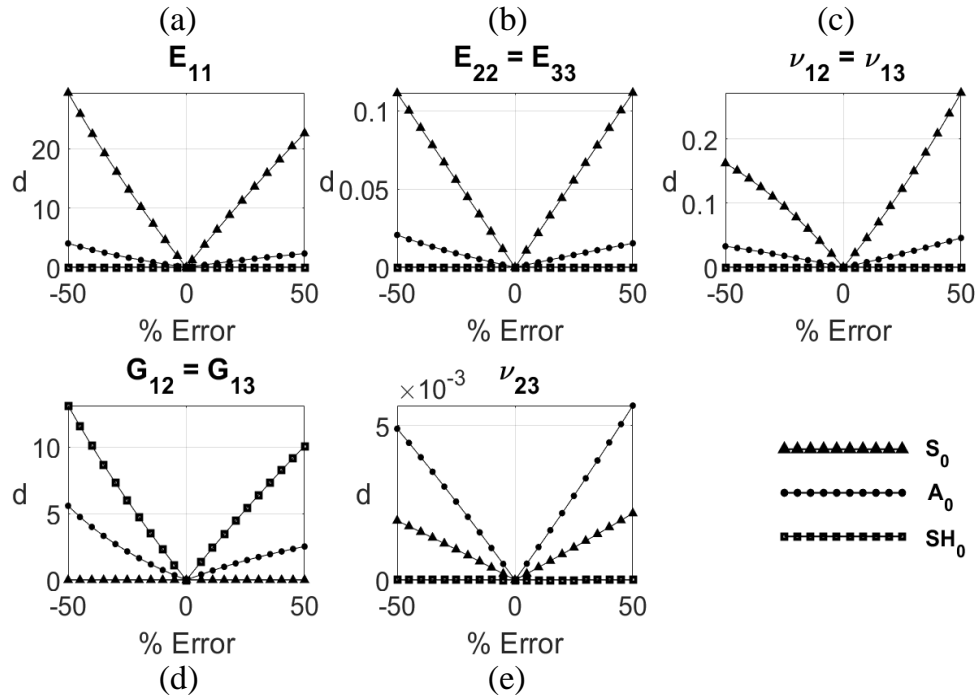


Figure 2.4. 1D identification of lamina elastic constants in unidirectional laminate.

The next analysis was the multidimensional identification where all of the five lamina constants were simultaneously iterated as unknown optimization variables. Since this is a case of unidirectional laminate, the local reference system $(1, 2, 3)$ for each lamina is aligned with the global reference system (x, y, z) . Hence the seven engineering properties of Eqs. (2.8)-(2.14) for this laminate reduce to five independent terms corresponding to the five lamina's constants through the following relations: $E_x = K_x/I_y = E_{11}$; $E_y = K_y/I_x = E_{22}$; $\nu_{xy} = \nu_{12}$; $G_{xy} = K_{xy}/I_{xy} = G_{12}$; and $\nu_{yz} = \nu_{23}$. In these relations, I_x and I_y are moments of inertia of the laminate's cross-section with respect to x and y , respectively, and I_{xy} is the polar moment of inertia of the cross-section. The 5D property identification results are shown in Figure 2.5, again in terms of velocity curve discrepancy d versus variable % error. The final optimization result (smallest d value) is marked with a *Star* symbol (*)

and an arrow in each of the plots. The closer the *Star* symbol is to the 0 value on the x -axis, the more accurate the answer (perfect accuracy would be % Error=0). Similarly, the closer the *Star* symbol is to the 0 value on the y -axis, the more correlation exists between the dispersion curve of a particular guided wave mode and a particular property. Also, these plots show ranges for d that are below 0.2 (i.e. a zoom-in around the minimum of the objective function) so as to better evaluate the relative identification performance of the various guided modes.

The general results of the multidimensional identification of Figure 2.5 essentially confirm those of the 1D identification of Figure 2.4, with expectedly less perfect performance due to the multiple simultaneous unknowns. Hence Figure 2.5 confirms that the identification of the axial stiffness E_x (and flexural rigidity K_x) (first column) is best achieved by the S_0 , with the *Star* symbol (final optimization result) at a near perfect position and all final iterations along the 0% Error line. This behavior is expected due to the predominance of σ_{xx} and ε_{xx} components in S_0 . The A_0 mode (that also features large σ_{xx} and ε_{xx} components) also proves effective for E_x (K_x) with slightly larger discrepancy values as a result of the low frequency dispersion. The SH_0 mode instead is quite ineffective for E_x (K_x) showing very scattered iteration points with a final *Star* value close to 50% error. The multidimensional identification of the transverse stiffness E_y (and the flexural rigidity K_y) – second column in Figure 2.5 - becomes more challenging, with increased scattering of the results for all the modes. Nevertheless, a final accuracy of $\sim 10\%$ can be achieved with the A_0 mode and an even better accuracy is seen with the SH_0 mode, although the scatter of the transitions indicates a poor stability of the solution. This is the result of the single guided wave propagation direction (x) that is only indirectly related to the stiffness in the transverse direction. In regards to the in-plane Poisson's ratio ν_{xy} (third column of Figure 2.5), mode S_0 remains the best candidate with close to a (numerical) 0% error, although this identification is less stable than

for the E_x stiffness given, again, the indirect sensitivity to transverse properties. As also expected, the best identification of the in-plane shear stiffness G_{xy} (and torsional rigidity K_{xy}) -fourth column in Figure 2.5- is achieved by the SH_0 mode with an ideal $(0,0)$ Star value and stability of the iterations due to the predominant τ_{xy} and γ_{xy} components for this mode. As also noted in the 1D optimization study, the A_0 mode shows satisfactory identification performance for G_{xy} ($=G_{xz}$ in this case) due to the cross-sectional “warping” shear components τ_{xz} and γ_{xz} . Finally, as found in the 1D optimization, the Poisson’s ratio in the transverse plane ν_{yz} (fifth column in Figure 2.5) is the only parameter whose identification becomes very unstable for any of the modes propagating along x .

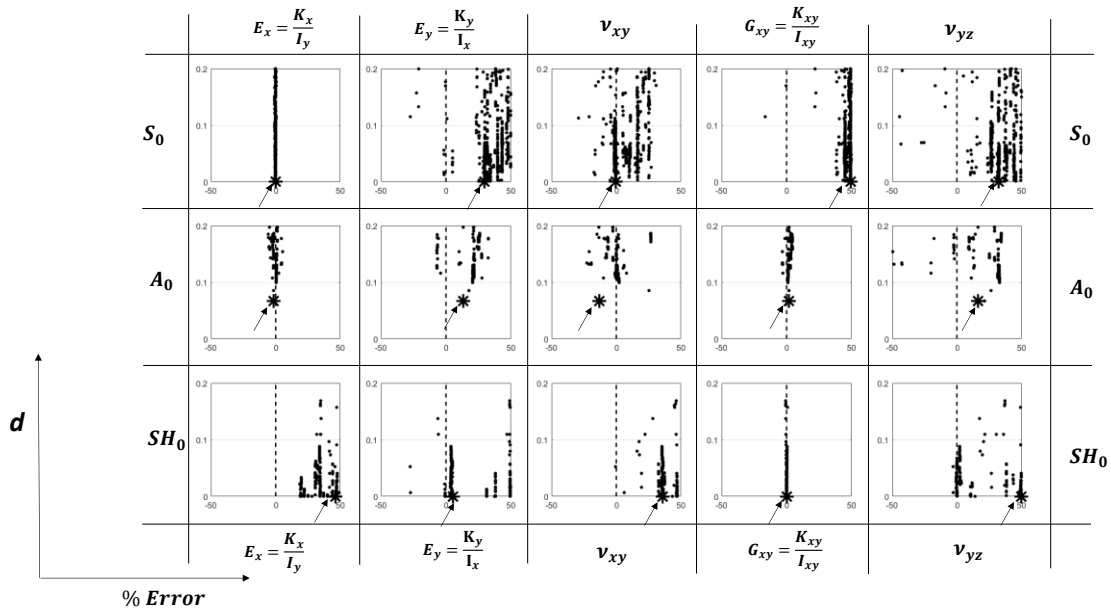


Figure 2.5. 5D identification of lamina elastic constants and laminate engineering properties in unidirectional laminate.

2.4.2. Quasi-isotropic laminate

The second case study is a quasi-isotropic 16-layer laminate with a lay-up of $[+45^\circ/-45^\circ/0^\circ/+45^\circ/90^\circ/-45^\circ/0^\circ/90^\circ]_S$ with the lamina properties of Table 2.1. The guided waves are still considered propagating along the x global direction.

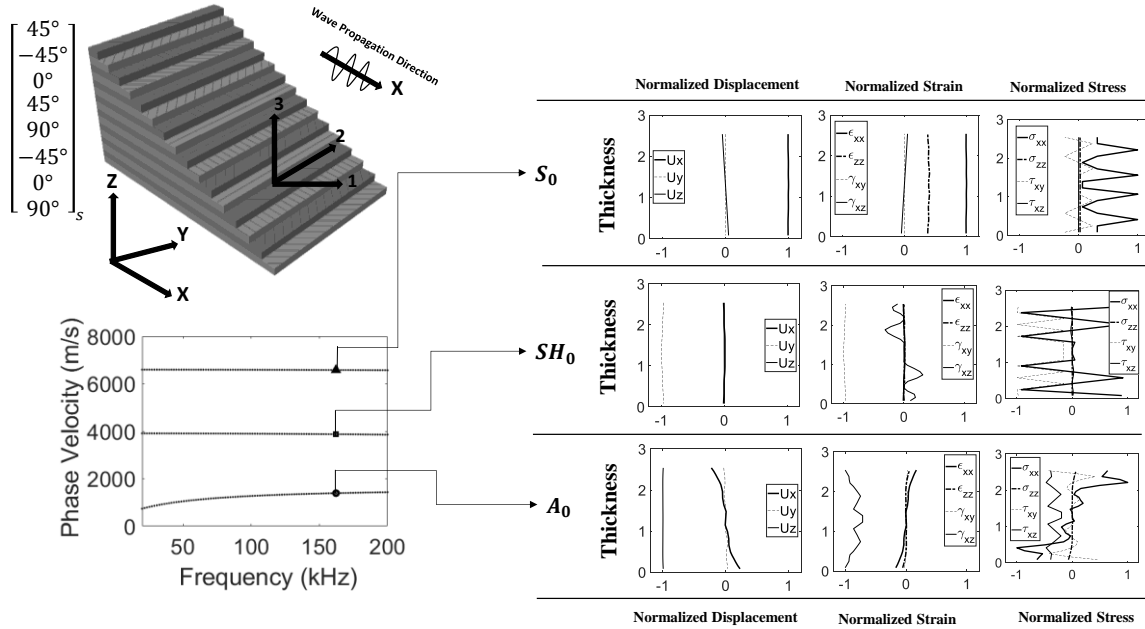


Figure 2.6. Quasi-isotropic laminate: SAFE results of phase velocity dispersion curves along with displacement, strain and stress cross-sectional profiles at 160 kHz.

Figure 2.6 shows the SAFE solutions for this laminate in terms of phase velocity dispersion curves in the 20kHz – 200 kHz range for S_0 , A_0 and SH_0 , along with displacement, strain and stress cross-sectional profiles at 160 kHz. The first observation from these profiles, compared to the profiles of the unidirectional laminate of Figure 2.3 in the previous section, is the “jumpy” behavior of the stress components in the global reference system, due to the different orientations of the various laminae. Also, in addition to the expected dominant components for the various modes

(normal stress σ_{xx} for S_0 and A_0 , and in-plane shear stress τ_{xy} for SH_0), clear coupling between normal stress and shear stress components is seen, such as significant τ_{xy} for S_0 and A_0 , and significant σ_{xx} for SH_0 .

Figure 2.7 shows the results of the 1D identification of the local lamina elastic constants (one constant at a time being inverted with the other constants assumed known). As expected, mode S_0 offers the largest sensitivity to the longitudinal axial modulus E_{11} (Figure 2.7(a)) through the predominant σ_{xx} component operating on the 0-deg laminae. Most interestingly, the shear horizontal mode SH_0 also offers large sensitivity to E_{11} as a result of the $\pm 45^\circ$ lamina orientations. This was not seen in the unidirectional laminate for E_{11} in Figure 2.4(a). For the same reasons, modes S_0 and SH_0 are both found very sensitive to the Poisson's ratios $\nu_{12} = \nu_{13}$ in Figure 2.7(c). As for the transverse moduli $E_{22} = E_{33}$ (Figure 2.7(b)), mode A_0 is the most sensitive due to the non-negligible vertical stresses σ_{zz} , followed by mode S_0 . The sensitivity of these modes to $E_{22} = E_{33}$ in the quasi-isotropic laminate is much larger (by about one order of magnitude) than that for the same constants in the unidirectional laminate (Figure 2.4(b)) as a result of the $\pm 45^\circ$ and 90° lamina orientations. Hence the off-axis fiber orientations provide guided modes propagating in one direction with added sensitivity to constants in other directions. Regarding the shear moduli $G_{12} = G_{13}$ in Figure 2.7(d), mode SH_0 offers the expected large sensitivity to G_{12} through the in-plane shear component τ_{xy} , and mode A_0 does the same for G_{13} through the vertical shear component τ_{xz} (cross-sectional warping). Lastly, regarding the Poisson's ratio in the transverse plane, ν_{23} (Figure 2.7(e)), mode A_0 shows the best sensitivity that is, again, much larger than that shown for the same constant in the unidirectional composite case (Figure 2.4(e)). This is another result of the off-axis

lamina orientations that improve the sensitivity of the guided modes propagating in one direction to constants in various other directions.

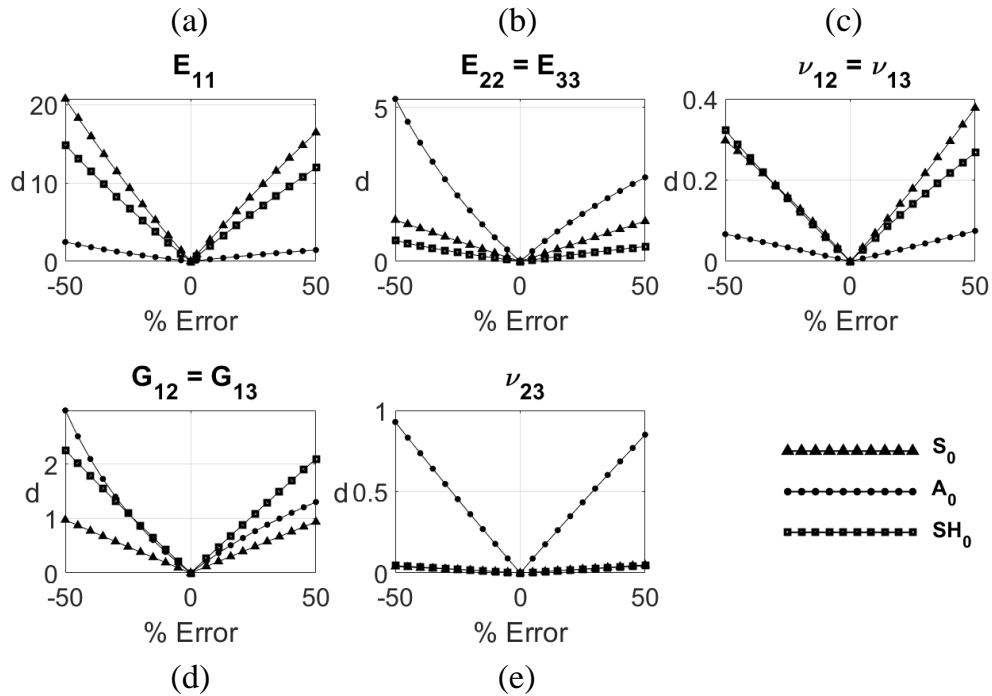


Figure 2.7. 1D identification of lamina elastic constants in quasi-isotropic laminate.

The results of the 5D inversion of the lamina constants are shown in Figure 2.8 in terms of phase velocity curve discrepancy d versus variable % error in the identified constant. In this case all five constants are optimization variables in the SA algorithm. The final optimization result (smallest d value) is marked with a *Star* symbol (*) and an arrow in each of the plots. The 5D results confirm several of the conclusions from the 1D results of Figure 2.7, with differences due the multiple unknowns. Hence mode S_0 proves the best candidate for identifying E_{11} , followed by mode SH_0 (first column in Figure 2.8). Modes S_0 and A_0 are good candidates to identify $E_{22} = E_{33}$, with accuracies on the order of 5% and much better performance compared to the same case for

the unidirectional laminate case (second column in Figure 2.5). This is one more confirmation that the off-axis lamina orientations are beneficial to the comprehensive property identification by a single wave propagation direction. The identification of the Poisson's ratios $\nu_{12} = \nu_{13}$ (third column in Figure 2.8) is best performed by modes S_0 and A_0 , with an accuracy of $\sim 5\%$ and much better stability compared to the same constant for the unidirectional laminate case (third column in Figure 2.5). The shear moduli $G_{12} = G_{13}$ are best identified by modes SH_0 and A_0 as seen in the 1D optimization. The Poisson's ratio in the transverse plane, ν_{23} (fifth column in Figure 2.8) remains very difficult to identify accurately with any of the modes in the multidimensional optimization, with large errors of the final solution. The same difficulty was found for this constant in the unidirectional laminate case in Figure 2.5.

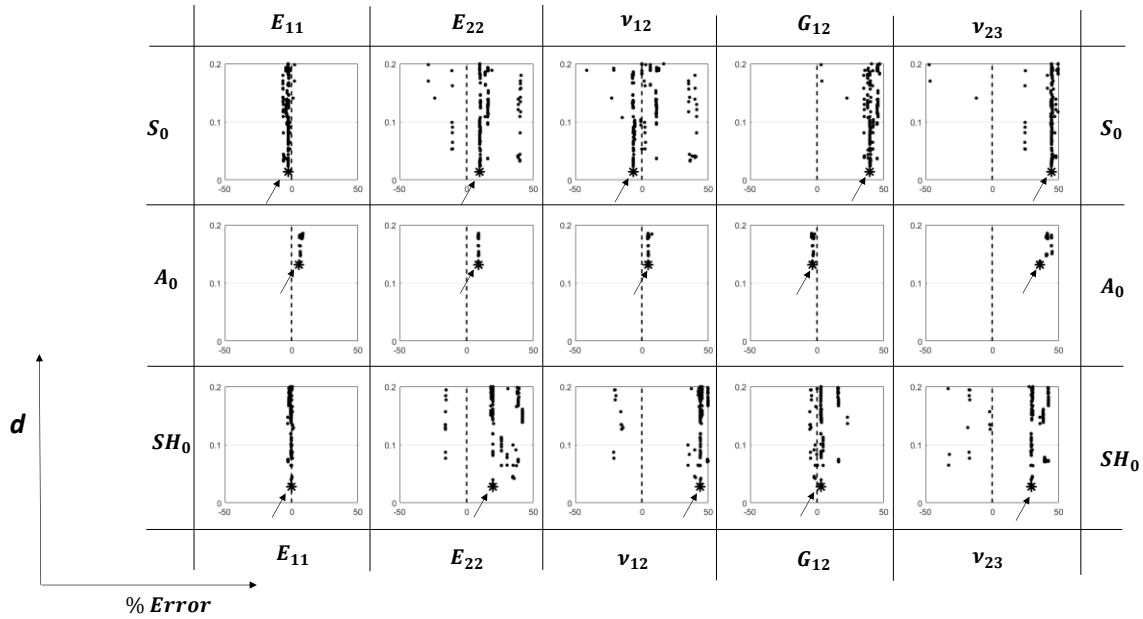


Figure 2.8. 5D identification of lamina elastic constants in quasi-isotropic laminate.

The next results are the laminate in-plane engineering properties in Figure 2.9. These

properties were calculated from the lamina constants following the 5D optimization procedure. This figure shows very good identification of all properties with many of the modes, and with an overall better stability compared to the same properties for the unidirectional laminate case of Figure 2.5. In fact, the figure shows that each of the modes considered is a good candidate for identifying any of the properties due to the cross-coupling provided by the off-axis lamina orientations. The most accurate result for the axial stiffness E_x (and E_y since it is equal to E_x for the quasi-isotropic layout) is obtained by S_0 and SH_0 (first two columns Figure 2.9); the most accurate result for the Poisson's ratio ν_{xy} is obtained by A_0 (third column of Figure 2.9); and the most accurate result for the shear stiffness G_{xy} is obtained by SH_0 (fourth column of Figure 2.9).

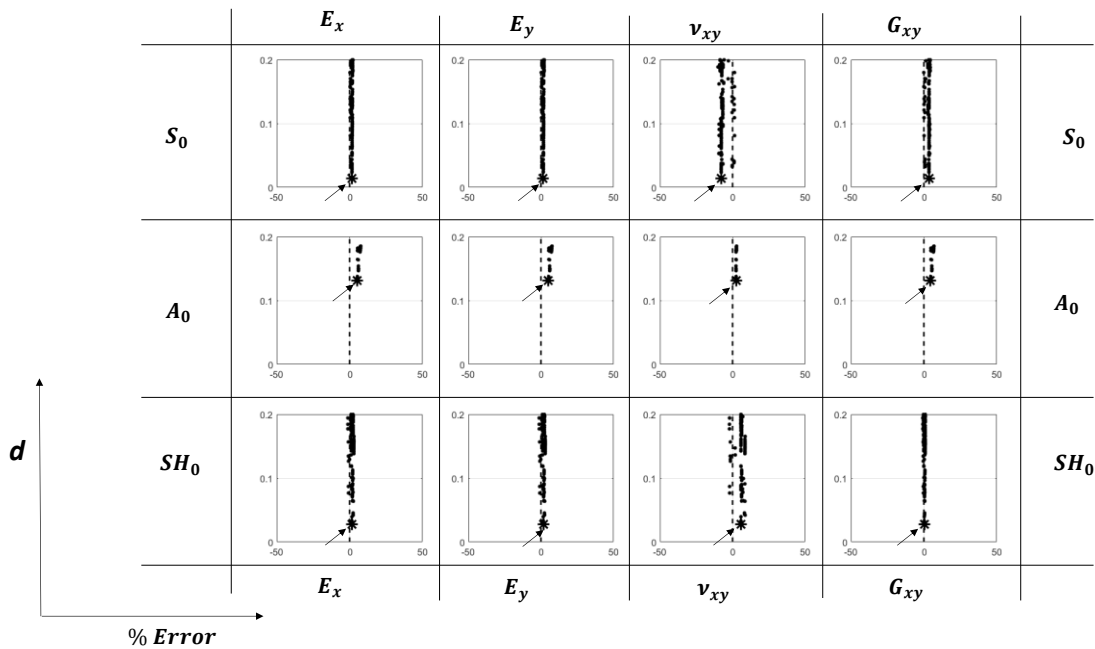


Figure 2.9. 5D identification of axial and shear laminate engineering properties in quasi-isotropic laminate.

The final set of results is the identification of the flexural and torsional engineering

properties of the laminate, shown in Figure 2.10. Again, all of the modes seem to be able to identify all of these properties with sufficient accuracy and stability of the solution. The most accurate result for the flexural rigidity K_x is obtained by SH_0 (first column in Figure 2.10), The sensitivity of SH_0 to the flexural rigidity is the results of the longitudinal-shear coupling that is, for example, seen in the stress profile of this mode in Fig.6 where significant σ_{xx} stress components are present. Both S_0 and SH_0 give the most accurate identification of the torsional rigidity K_{xy} (third column in Figure 2.10). This is likely the result of the large τ_{xy} stresses naturally present in SH_0 and also seen in S_0 through the same type of longitudinal-shear coupling in Figure 2.6.

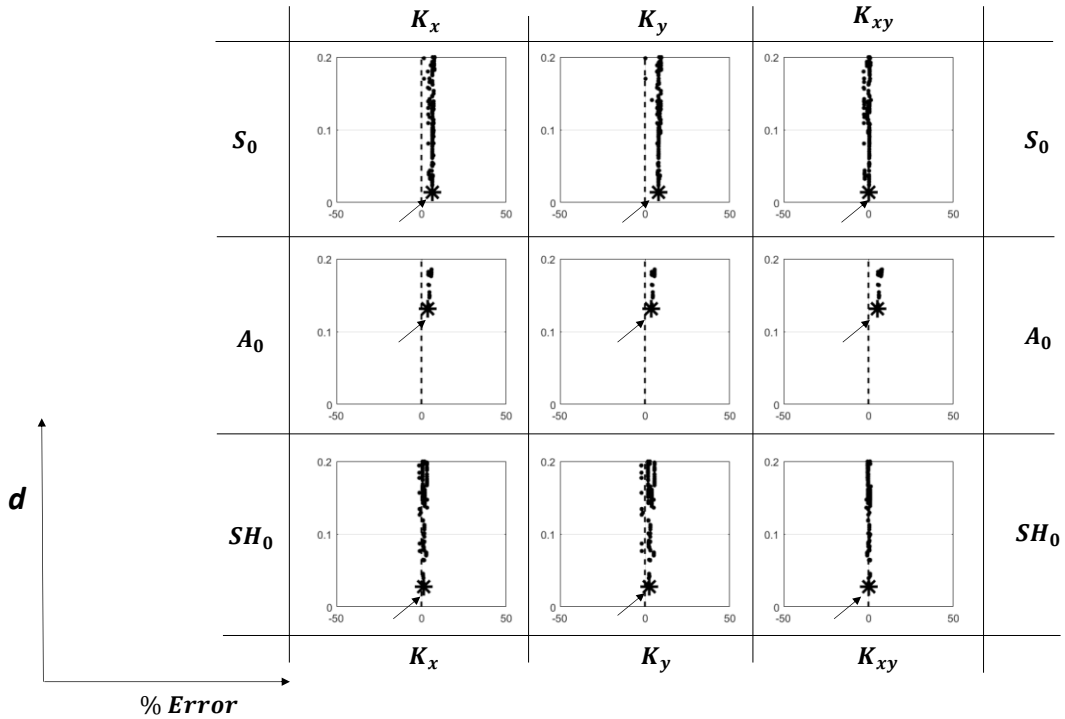


Figure 2.10. 5D identification of flexural and torsional laminate engineering properties in quasi-isotropic laminate.

2.4.3. Anisotropic laminate

The final case study was conducted on a 16-layer laminate with a lay-up of $[+45^\circ/-45^\circ/0^\circ/+45^\circ/0^\circ/-45^\circ/0^\circ/0^\circ]_s$, where the four 90° laminae of the previous quasi-isotropic laminate were replaced by 0° laminae to create full anisotropy in the global reference system. The same lamina properties of Table 2.1 were used. The dispersion curves and cross-sectional mode shapes for this anisotropic laminate are shown in Figure 2.11. The profiles are generally similar to those for the quasi-isotropic laminate in Figure 2.6, with some differences particularly at the location of the four rotated laminae. Therefore, significant coupling between in-plane longitudinal and in-plane shear behavior (e.g. co-existence of σ_{xx} and τ_{xy} components in each of the modes S_0 , A_0 and SH_0) is again seen due to the $\pm 45^\circ$ off-axis laminae.

The results of the 1D identification of the lamina elastic constants for this laminate are shown in Figure 2.12. The general conclusions are similar to those discussed for Figure 2.7 for the quasi-isotropic laminate, and particularly so in the specific modes that are most sensitive to specific constants. The most noticeable difference is the \sim twofold decrease in sensitivity for the identification of the transverse moduli $E_{22}=E_{33}$ (Figure 2.12(b)) due to the absence of 90° laminae. Hence it is harder to identify the transverse modulus in a highly anisotropic laminate using waves propagating in the longitudinal direction. At the same time, the increased anisotropy improves the sensitivity to the longitudinal modulus E_{11} by mode S_0 (Figure 2.12(a)) as well as the sensitivity to the shear moduli $G_{12}=G_{13}$ by mode A_0 (Figure 2.12(d)) when compared to the quasi-isotropic case (Figure 2.7(a) and (d)). The identification of the Poisson's ratios $\nu_{12}=\nu_{13}$ (Figure 2.12(c)) is basically equivalent to the quasi-isotropic case (Figure 2.7(c)). The sensitivity to the Poisson's ratio in the transverse plane ν_{23} (Figure 2.7(e)) remains the lowest, although it remains much improved compared to the unidirectional laminate (Figure 2.4(e)).

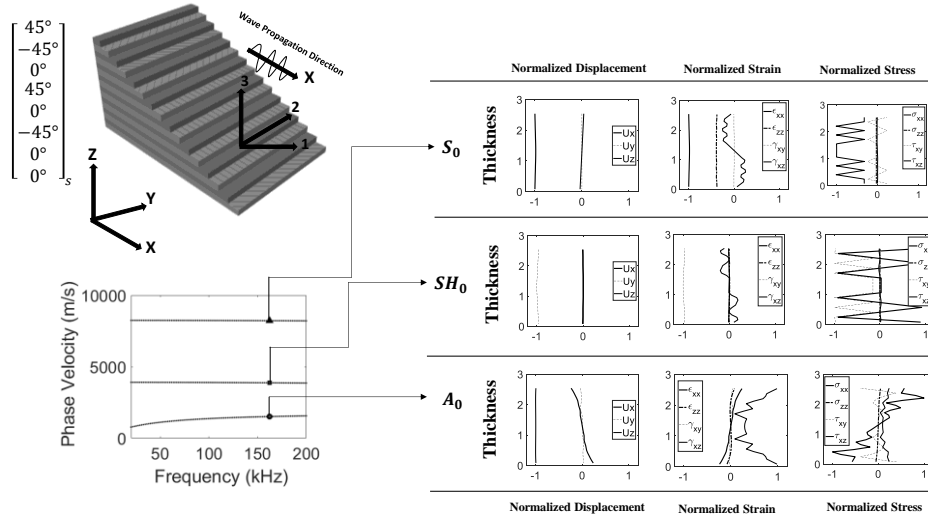


Figure 2.11. Anisotropic laminate: SAFE results of phase velocity dispersion curves along with displacement, strain and stress cross-sectional profiles at 160 kHz.

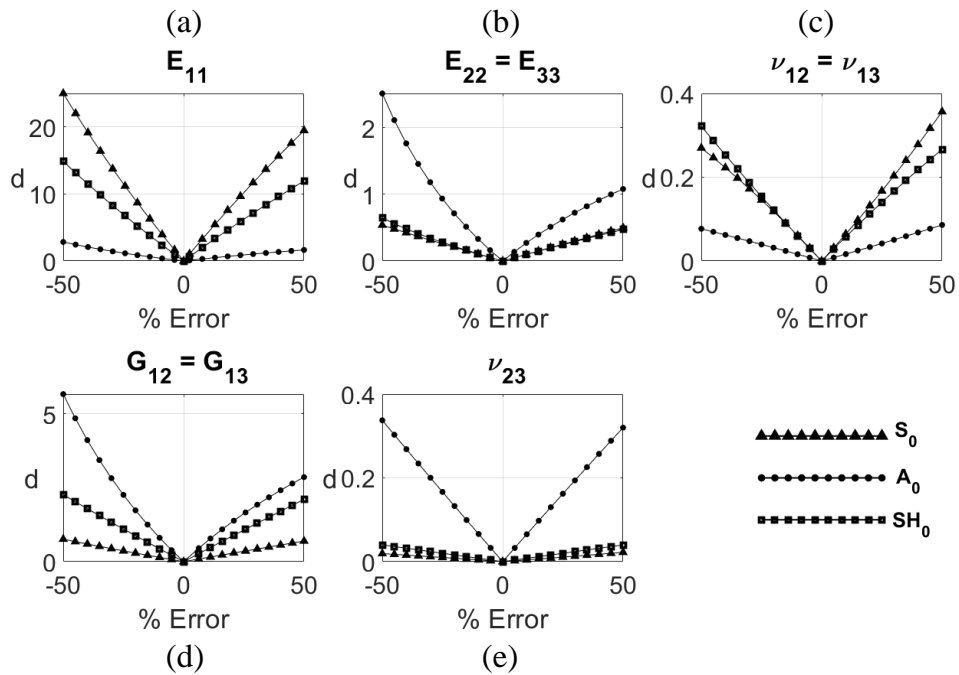


Figure 2.12. 1D identification of lamina elastic constants in anisotropic laminate.

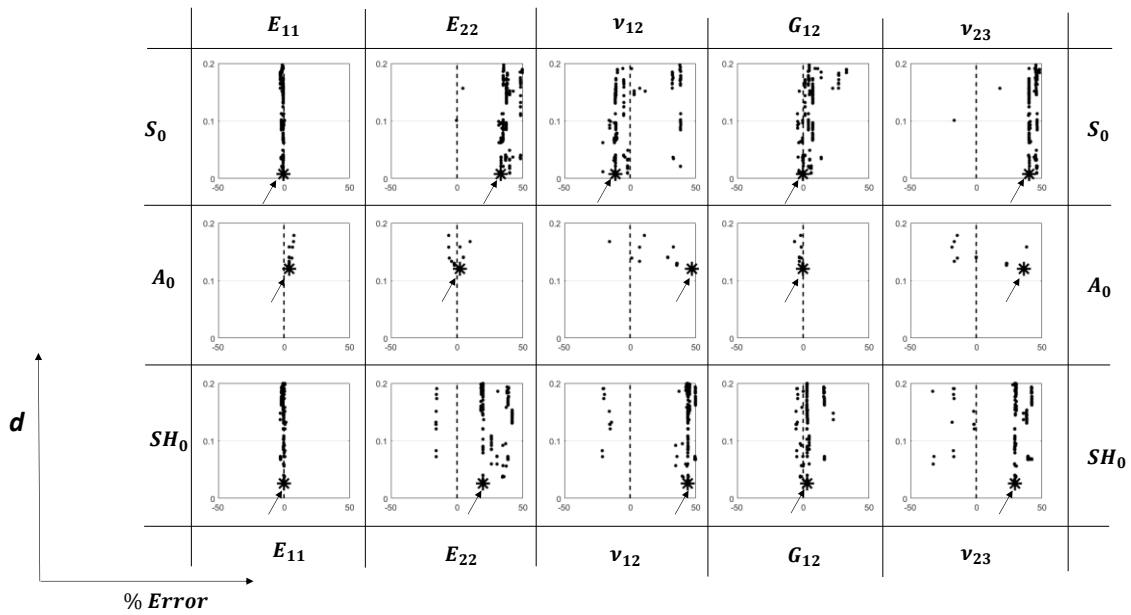


Figure 2.13. 5D identification of lamina elastic constants in anisotropic laminate.

The identification of the lamina constants in the 5D optimization analysis are shown in Figure 2.13. As seen in the quasi-isotropic laminate in Figure 2.8, modes S_0 and SH_0 confirm the most suitable for the identification of E_{11} (first column of Figure 2.13), with additional stability of the solution for S_0 compared to the quasi-isotropic case due to the increased anisotropy. The identification of the transverse modulus E_{22} (second column in Figure 2.13), instead, worsens compared to the quasi-isotropic case with S_0 providing accuracies of only $\sim 40\%$ and A_0 providing a very accurate optimization minimum (to within less than 5%) but with less stability of the solution (more scatter). This confirms the challenge in identifying the transverse modulus with longitudinal wave propagation in a highly anisotropic laminate with only few off-axis lamina orientations. The identification of the Poisson's ratios $\nu_{12} = \nu_{13}$ (third column in Figure 2.13) also degrades compared to the quasi-isotropic case, with mode S_0 providing the best performance and

mode A_0 leading instead to a very inaccurate solution. Interestingly, a better overall performance compared to the quasi-isotropic case is seen for the identification of the shear moduli $G_{12} = G_{13}$ (fourth column in Figure 2.13), the SH_0 and the A_0 modes are confirmed quite effective (with an even improved accuracy for the A_0 solution compared to the quasi-isotropic case), and the addition of mode S_0 as another suitable candidate for these constants. Finally, the identification of the ν_{13} Poisson's ratio remains unfeasible with any of the guided modes considered, as also seen in the other two laminates.

The identification of the engineering properties for the anisotropic laminate from the 5D optimization is shown in Figure 2.14 and Figure 2.15. As found in the quasi-isotropic laminate, it is shown that the coupling provided by the off-axis laminae allow many of the modes to properly identify the engineering constants with an excellent level of accuracy. The main difference in the anisotropic laminate case is that now $E_x \neq E_y$. As in the quasi-isotropic case, identification of the axial stiffness E_x (first column in Figure 2.14) is best done with S_0 or SH_0 (accuracy less than $\sim 1\%$) although A_0 still provides an accuracy to within $\sim 5\%$. The transverse stiffness E_y (second column in Figure 2.14) can also be identified by S_0 or SH_0 due to the ± 45 laminae, although the accuracy is slightly worse compared to the quasi-isotropic case because of the fewer off-axis laminae. The identification of the in-plane Poisson's ratio ν_{xy} (third column in Figure 2.14) improves compared to the quasi-isotropic case, with very small accuracy ($\sim 1\%$) obtained by S_0 and SH_0 and good accuracy ($< 5\%$) obtained by A_0 . As for the in-plane shear stiffness G_{xy} (fourth column in Figure 2.14), mode SH_0 confirms a nearly "perfect" result, with S_0 and A_0 also providing very good solutions, and even slightly more accurate than those seen in the quasi-isotropic laminate for these two modes. Improvements over the quasi-isotropic case are also seen in the identification of the flexural rigidities K_x and K_y . In the case of K_x , first column in Figure 2.15, SH_0 is confirmed

as a quite suitable candidate with great accuracy (less than $\sim 1\%$) and stability of the solution. In addition, modes S_0 and A_0 also yields excellent results that are more accurate than what found for these modes in the quasi-isotropic case of Figure 2.10. Accuracy improvements (less than 1%) are also seen for the identification of K_y , second column in Figure 2.15, by either mode S_0 or A_0 when compared to the quasi-isotropic case. As for the torsional rigidity K_{xy} , third column in Figure 2.15, modes S_0 and SH_0 confirm their suitability as found for the quasi-isotropic case. In addition, the accuracy performance of A_0 for this property improves compared to the quasi-isotropic case.

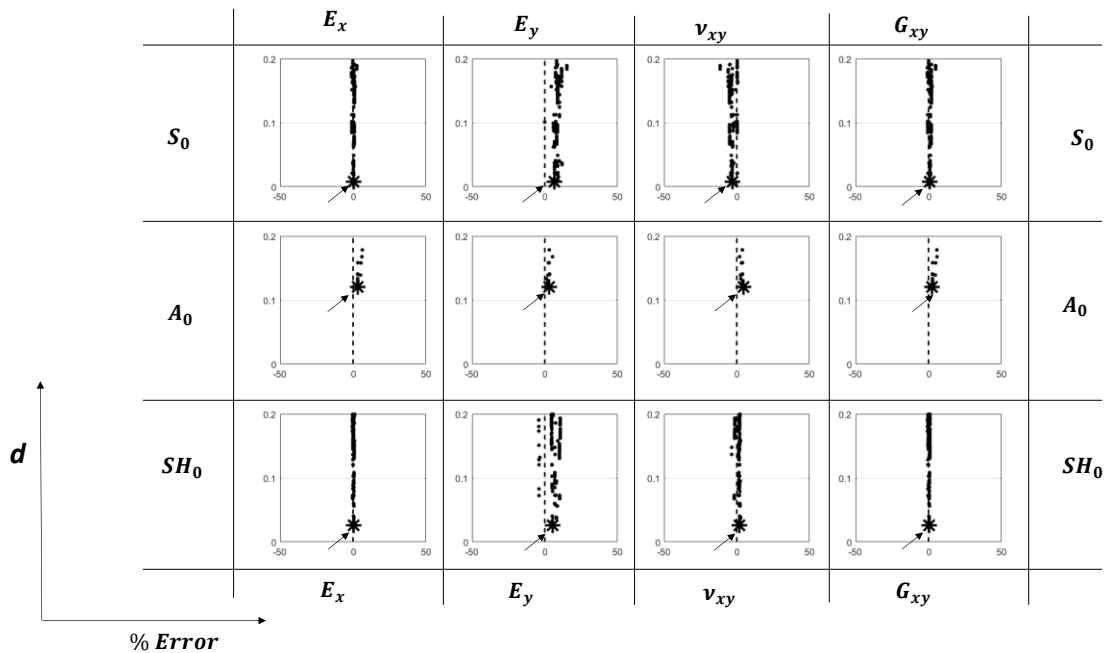


Figure 2.14. 5D identification of axial and shear laminate engineering properties in anisotropic laminate.

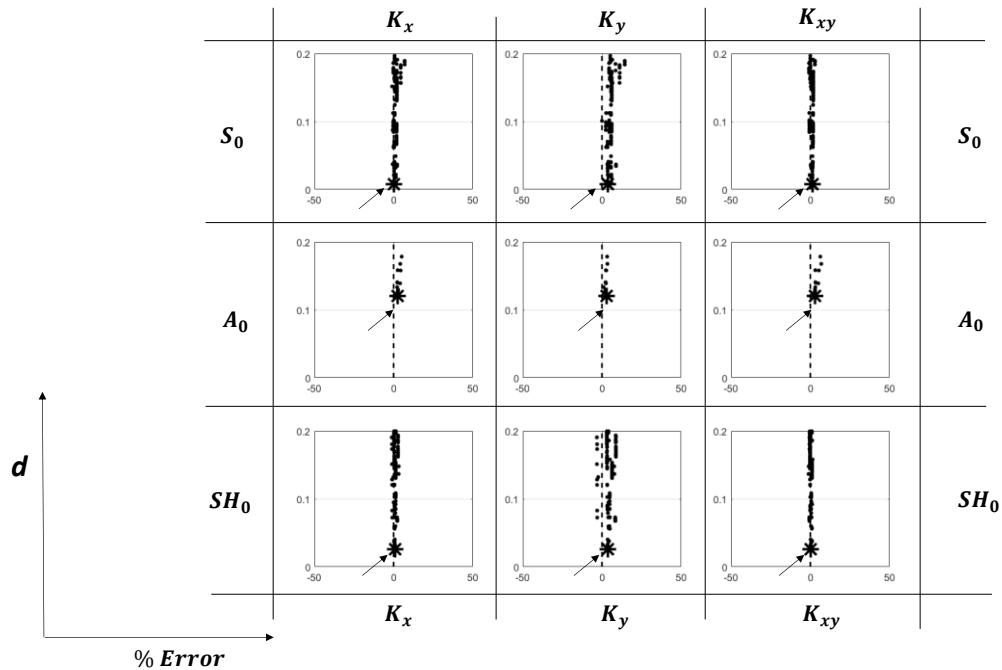


Figure 2.15. 5D identification of flexural and torsional laminate engineering properties in anisotropic laminate.

2.5. Discussion and Conclusions

This paper has explored the potential for ultrasonic guided waves in the ~ 100 s of kHz range to identify elastic properties of composite laminates commonly used in light-weight structures. Guided waves exploit the plate-like geometry of most composite structural components to provide unique advantages in terms of large ranges (\sim centimeters to \sim meters) and high sensitivity to both lamina-by-lamina properties and laminate engineering properties owing to the complex stress and strain cross-sectional distributions. Since guided waves are largely unaffected by boundary conditions of the test part (as possible boundary reflections, for example, are easily eliminated by appropriate time gating), they lend themselves to property identification in situ on an actual structure. The inverse identification procedure is based on matching “true” phase velocity

dispersion curves to “trial” phase velocity dispersion curves obtained for a given set of elastic constants. The match is here done by using a Simulated Annealing optimization algorithm.

This study pushes the limit of composite property identification by considering waves propagating in a single direction of the laminate. The three fundamental guided modes of axial (S_0), flexural (A_0) and shear-horizontal (SH_0) are considered, as these are typically used in various NDE and SHM applications. Each of these modes offers particular features that are attractive to an NDE/SHM practitioner. For example, the SH_0 mode is notoriously attractive because nondispersive, although its transduction can be more challenging. On the other hand, the transduction of S_0 and A_0 is typically easier although the analysis is more complicated by dispersion. Three different laminates are considered (unidirectional, quasi-isotropic, and fully anisotropic).

Contrary to what commonly assumed, guided waves propagating in one direction offer appreciable sensitivity to constants in the orthogonal directions. This interesting “coupling” effect is due to the co-existence of normal and shear stresses/strains in multiple planes, as indicated by the cross-sectional profiles of the guided modes, caused by the nature of the modes and the anisotropy of the laminate. Not surprisingly, this coupling increases with increasing numbers of off-axis laminae (e.g. $\pm 45^\circ$ and 90° laminae for a 0° wave propagation direction). The most obvious result is that the identification of the longitudinal lamina modulus E_{11} and of the laminate axial stiffness E_x are best achieved by modes S_0 and A_0 propagating along x (due to the predominant σ_{xx} and ε_{xx} components) for all of the laminates examined. However, for the quasi-isotropic and the anisotropic laminates, E_{11} and E_x can be also identified effectively by mode SH_0 propagating along x , due to the shear-normal coupling $\tau_{xy} - \sigma_{xx}$ for this mode resulting from the off-axis laminae ($\pm 45^\circ$ and 90°). Similar conclusions can be drawn for the in-plane Poisson’s

ratios for the lamina $\nu_{12}=\nu_{13}$ and for the laminate ν_{xy} , since these properties depend on the same axial stress as the E_{11} and E_x moduli. Most interestingly, modes S_0 and A_0 propagating along x also show sufficient sensitivity to identify the lamina transverse modulus $E_{22} = E_{33}$ and the laminate transverse axial stiffness E_y , due partly to the longitudinal-transverse coupling $\sigma_{xx}-\sigma_{zz}$ for these modes. This “transverse” sensitivity improves in the quasi-isotropic and anisotropic laminates due to the off-axis laminae. In these two laminates, E_y can be also well identified by the SH_0 mode due to shear-normal coupling.

It is not surprising that the in-plane shear modulus of the lamina $G_{12} = G_{13}$ and the in-plane shear stiffness of the laminate G_{xy} are identified well by mode SH_0 , due to its predominant τ_{xy} components. It is less obvious that, for all laminates considered, these in-plane shear moduli can be also identified effectively by the flexural mode A_0 propagating along x due to the transverse shear components τ_{xz} and γ_{xz} (cross-sectional warping) at these high frequencies that are well beyond the Bernoulli-Euler beam approximation. The lamina’s transverse Poisson’s ratio ν_{23} remains challenging to identify with any of the modes propagating in the x direction. Finally, in analogy with the longitudinal and transverse stiffnesses E_x and E_y , the laminate axial and transverse flexural rigidities K_x and K_y can be effectively identified by modes S_0 and A_0 propagating along x in all laminate cases, in addition to mode SH_0 in the quasi-isotropic and anisotropic laminates due to the normal-shear coupling resulting from the off-axis laminae. Finally, the laminate torsional rigidity K_{xy} can be identified by either S_0 , A_0 or SH_0 for these laminates.

This study has assumed that the same elastic constants apply to each lamina comprising the laminate, resulting in a 5D optimization problem. Since SAFE considers each lamina independently, the laminae could be easily decoupled to extend the investigation to an inhomogeneous case (e.g. damage or other structural degradation affecting only some of the

laminae of the part). This generalization would of course also increase the dimension of the optimization problem.

This study has been limited to elastic properties of the composite. It is theoretically possible to extend the results to the visco-elastic property identification by considering the appropriate complex stiffness coefficients in the SAFE formulation [28].

Finally, similarly to the work by Marzani and De Marchi [16], the present study has considered “pseudo-experimental” data as the “true” dispersion curves to which the trial curves were matched. Hence the results represent quite ideal testing conditions. In practice, the “true” dispersion curves would be extracted experimentally on a given part, with unavoidable experimental noise and errors that were not considered here. Additional work is needed for an experimental validation of the numerical results.

2.6. Acknowledgments

This work was funded in part by the Federal Aviation Administration Joint Center of Excellence for Advanced Materials (FAA Cooperative Agreement 12-C-AM-UCSD) and by the Federal Railroad Administration (contract # 693JJ618C000002).

Chapter 2 is, in full, a reprint of material published in Cui, Ranting, and Francesco Lanza di Scalea. "On the identification of the elastic properties of composites by ultrasonic guided waves and optimization algorithm." *Composite Structures* 223 (2019): 110969. The dissertation author was the primary investigator and author of this paper.

2.7. References

- [1] Tam JH, Ong ZC, Ismail Z, Ang BC, Khoo SY. Identification of material properties of composite materials using nondestructive vibrational evaluation approaches: A review. *Mech Adv Mater Struct* 2016;24:971–86.
- [2] Gibson RF. Modal vibration response measurements for characterization of composite materials and structures. *Compos Sci Technol* 2000;60:2769–80.
- [3] Deobald LR, Gibson RF. Determination of elastic constants of orthotropic plates by a modal analysis/Rayleigh-Ritz technique. *J Sound Vib* 1988;124:269–83.
- [4] Ayorinde EO, Gibson RF. Elastic constants of orthotropic composite materials using plate resonance frequencies, classical lamination theory and an optimized three-mode Rayleigh formulation. *Compos Eng* 1993;3:395–407.
- [5] McIntyre ME, Woodhouse J. On measuring the elastic and damping constants of orthotropic sheet materials. *Acta Metall* 1988;36:1397–416.
- [6] De Visscher J, Sol H, De Wilde WP, Vantomme J. Identification of the damping properties of orthotropic composite materials using a mixed numerical experimental method. *Appl Compos Mater* 1997;4:13–33.
- [7] Lauwagie T, Lambrinou K, Patsias S, Heylen W, Vleugels J. Resonant-based identification of the elastic properties of layered materials: application to air-plasma sprayed thermal barrier coatings. *Ndt e Int* 2008;41:88–97.
- [8] Frederiksen PS. Single-layer plate theories applied to the flexural vibration of completely free thick laminates. *J Sound Vib* 1995;186:743–59.
- [9] Frederiksen PS. Experimental Procedure and Results for the Identification of Elastic Constants of Thick Orthotropic Plates. *J Compos Mater* 1997;31:360–82.
- [10] Ayorinde EO. Elastic Constants of Thick Orthotropic Composite Plates. *J Compos Mater* 1995;29:1025–39.
- [11] Daghia F, de Miranda S, Ubertini F, Viola E. Estimation of elastic constants of thick laminated plates within a Bayesian framework. *Compos Struct* 2007;80:461–73.
- [12] Cugnoni J, Gmu T, Schorderet A. Inverse method based on modal analysis for characterizing the constitutive properties of thick composite plates. *Comput Struct* 2007;85:1310–20.
- [13] Hwang S, Wu J, He R. Identification of effective elastic constants of composite plates based on a hybrid genetic algorithm. *Compos Struct* 2009;90:217–24.
- [14] Cunha J, Cogan S, Berthod C. Application of genetic algorithms for the identification of

- elastic constants of composite materials from dynamic tests. *Int J Numer Methods Eng* 1999;45:891–900.
- [15] Vary A. Ultrasonic characterization of material properties. In: Moore P, Workma G, Kishoni D, editors. *Nondestruct. Test. Handb. Ultrason. Test.*, The American Society for Nondestructive Testing; 2007, p. 305–56.
- [16] Marzani A, De Marchi L. Characterization of the elastic moduli in composite plates via dispersive guided waves data and genetic algorithms. *J Intell Mater Syst Struct* 2012;24:2135–47.
- [17] Balasubramaniam K, Rao NS. Inversion of composite material elastic constants from ultrasonic bulk wave phase velocity data using genetic algorithms. *Compos Part B Eng* 1998;29:171–80.
- [18] Vishnuvardhan J, Krishnamurthy C V, Balasubramaniam K. Genetic algorithm reconstruction of orthotropic composite plate elastic constants from a single non-symmetric plane ultrasonic velocity data. *Compos Part B Eng* 2007;38:216–27.
- [19] Staszewski W, Boller C, Tomlinson GR. *Health monitoring of aerospace structures: smart sensor technologies and signal processing*. John Wiley & Sons; 2004.
- [20] Rose JL. *Ultrasonic guided waves in solid media*. Cambridge university press; 2014.
- [21] Giurgiutiu V. *Structural health monitoring (SHM) of aerospace composites*. Polym. Compos. Aerosp. Ind., Elsevier; 2015, p. 449–507.
- [22] Balasubramaniam K. Inversion of the ply lay-up sequence for multi-layered fiber reinforced composite plates using genetic algorithm. *Nondestruct Test Eval* 1998;15:311–31.
- [23] Vishnuvardhan J, Krishnamurthy C V, Balasubramaniam K. Genetic algorithm based reconstruction of the elastic moduli of orthotropic plates using an ultrasonic guided wave single-transmitter-multiple-receiver SHM array. *Smart Mater Struct* 2007;16:1639–50.
- [24] Vepakomma R, Janapati V, Balasubramaniam K. Global material characterization of composite structures using Lamb wave STMR array technique. *AIP Conf. Proc.*, 2010, p. 1812–9.
- [25] Glushkov E, Glushkova N, Eremin A. Elastic guided wave based assessment of laminate composite material constants. 11th Eur Conf Non-Destructive Test (ECNDT 2014) Prague, Crech Repub 2014.
- [26] Hosten B, Castaings M, Tretout H, Voillaume H. Identification of composite materials elastic moduli from Lamb wave velocities measured with single sided, contactless ultrasonic method. *AIP Conf Proc* 2001;557:1023–30.
- [27] Hayashi T, Song WJ, Rose JL. Guided wave dispersion curves for a bar with an arbitrary

- cross-section, a rod and rail example. *Ultrasonics* 2003;41:175–83.
- [28] Bartoli I, Marzani A, Lanza di Scalea F, Viola E. Modeling wave propagation in damped waveguides of arbitrary cross-section. *J Sound Vib* 2006;295:685–707.
- [29] Marzani A. Time-transient response for ultrasonic guided waves propagating in damped cylinders. *Int J Solids Struct* 2008;45:6347–68.
- [30] Loveday PW. Simulation of piezoelectric excitation of guided waves using waveguide finite elements. *IEEE Trans Ultrason Ferroelectr Freq Control* 2008;55:2038–45.
- [31] Ryden N, Park CB. Fast simulated annealing inversion pavement using phase-velocity spectra. *Geophysics* 2006;71:R49–58.
- [32] Szu H, Hartley R. Fast simulated annealing. *Phys Lett A* 1987;122:157–62.
- [33] Mosegaard K, Sambridge M. Monte Carlo analysis of inverse problems. *Inverse Probl* 2002;18:R29–54.
- [34] Laarhoven P, Aarts E. *Simulated Annealing: Theory and Applications*. Springer Science+Business Media; 1989.
- [35] Tsallis C, Stariolo DA. Generalized simulated annealing. *Phys A Stat Mech Its Appl* 1996;233:395–406.
- [36] Ingber L. Very Fast Simulated Re-annealing. *Math Comput Model* 1989;12:967–73.
- [37] Tong L, Soutis C. *Recent Advances in Structural Joints and Repairs for Composite Materials*. Springer Science & Business Media; 2013.
- [38] Matt H, Bartoli I, Lanza di Scalea F. Ultrasonic guided wave monitoring of composite wing skin-to-spar bonded joints in aerospace structures. *J Acoust Soc Am* 2005;118:2240–52.

Chapter 3. Identification of elastic properties of composites by inversion of ultrasonic guided wave data

3.1. Abstract

Background: Given the inherent manufacturing variabilities and potential for in-service damage of composite parts, the identification of the elastic properties of composites is important to ensuring the safety and the proper performance of the part. **Objective:** The primary objective of this manuscript is to determine, nondestructively, the elastic properties of composite parts, whether as in-situ components that are part of a larger system, or as laboratory coupons. **Methods:** The proposed technique is based on multimode and dispersive ultrasonic guided waves propagating along a single direction, and the inversion of their phase velocity dispersion curves. The inversion procedure utilizes an efficient Semi-Analytical Finite Element method to solve the forward problem, and a Simulated Annealing algorithm as the optimization tool. The method is particularly well-suited for the characterization of composite laminates. In particular, the manuscript presents experimental evidence of the effectiveness of this technique, that was suggested earlier in a solely numerical work previously conducted by the authors. **Results:** The test results show that reasonable accuracy can be obtained in the identification of four in-plane and three out-of-plane engineering constants of a quasi-isotropic laminate and a highly anisotropic laminate utilizing the single wave propagation direction. Non-obvious sensitivities of certain wave modes to particular constants are explained on the basis of stress coupling phenomena that are

revealed by the SAFE wave propagation models. **Conclusions:** The study gives experimental evidence of the suitability of ultrasonic guided wave inversion schemes to identify the engineering constants of laminated composites, with the potential to properly characterize parts in-situ, because of the insensitivity of guided waves to boundary conditions located outside of the transmitter-receiver path.

3.2. Introduction

Fiber-reinforced composite materials are widely used in high performance and light weight structures, such as modern aircraft. However, manufacturing variabilities and changing in-service conditions make it challenging to reliably know the elastic properties of a composite part in service. Hence many techniques have been historically devoted to the identification of the elastic properties of composites. This kind of material characterization can also be useful to detect the presence of potential structural damage in these components. Of particular interest to this paper are non-destructive techniques that can be applied *in-situ* on an actual structure in-service, i.e. without requiring disassembly or sectioning for off-line material characterization tests.

The most common strategies for property identification, as reviewed by Tam et al. [1], consist of matching experimental data with theoretical or numerical predictions, usually by means of optimization techniques. One method that is often used for this purpose is the vibration test that is quite sensitive to the “effective” or “engineering” elastic constants of composite laminates. Vibration tests have been employed to identify four in-plane elastic constants (E_x , E_y , G_{xy} , and ν_{xy}) on thin laminates [2-8]. Further investigations including the through-thickness shear behavior have been conducted to extend the identification to the out-of-plane shear moduli [9-13]. Since they

typically operate on the “global” dynamic behavior of the part (i.e. in a relatively low frequency range, e.g. < 10 kHz), the vibration behavior is highly dependent on the boundary conditions of the test part, with the free-hanging condition usually utilized in the laboratory [14]. Hence the vibration techniques may be challenging to apply to components that are part of a larger structures, i.e. *in-situ*, where the boundary conditions may be difficult to accurately replicate in the accompanying theoretical or numerical models.

A related, but significantly different property identification approach utilizes elastic waves propagating in the ultrasonic range (> 20 kHz). These waves are only sensitive to the material properties of the part between the wave transmitter and the wave receiver, and hence insensitive to the boundary conditions outside of the wave propagation path (i.e. suitable for *in-situ* property characterization). Ultrasonic guided waves (that are multimode and dispersive) are particularly suited to probing plate-like composite parts where the geometry can effectively “guide” the wave through long distances, that range typically from a few centimeters to a few meters [15-17]. Previous studies have explored ultrasonic guided waves for composite property identification in both laboratory coupons and *in-situ* structures [18,19]. The ability of ultrasonic guided waves to propagate long distances at high frequencies ensures a potentially high sensitivity to both “global” (effective or engineering) elastic constants of the laminated plate, and “local” elastic constants of the individual laminae (lamina-by-lamina properties), as recently shown by the authors of the present paper in an exclusively numerical work [20].

A review article on the use of guided waves for composite materials characterization appears as early as in 1997 [21]. This review covers several aspects pertaining to guided wave generation and detection, dispersion curve calculation and experimental demonstrations. Balasubramaniam [22] first inverted the properties of a cross-ply composite plate by minimizing

the difference between experimentally extracted wave dispersion curves and numerical predictions from a Thomson-Haskell model. He used a Genetic Algorithm to speed up the inversion process. Later, Castaings et al. [23,24] applied the wave dispersion curve optimization to a unidirectional composite plate, further identifying multiple properties. Vishnuvardhan et al. [25] proposed an array of transducers, with one transmitter encircled by multiple receivers, to identify nine elastic constants of an orthotropic plates using the Christoffel equation as the forward model. Vepakomma et al. [26] estimated elastic constants in composites using a similar approach. Glushkov et al. [27] used elasto-dynamic theories for layered media (Green's functions) as the forward model of group velocity dispersion curves to identify the engineering constants of unidirectional and cross-ply laminates. Sale et al. [28] also identified the elastic constants of isotropic plates utilizing group velocity dispersion curves of guided waves as well as applying an upgraded Simplex optimization method. Gsell and Dual [29] estimated the elastic constants of anisotropic cylindrical shells by matching experimental phase velocities of non-axis-symmetric guided waves to theoretical velocities computed using Hamilton's principle. The forward theoretical models employed by the studies above contain either transcendental functions or closed-form solutions whose calculation is time-consuming, especially when the problems involve complicated geometries, such as multilayer composite materials. Since the inverse property identification procedure requires multiple iterations of these models, computational efficiency (and accuracy) are quite relevant.

The Semi-Analytical Finite Element (SAFE) method is a particularly efficient tool to calculate phase or group velocity dispersion curves of multilayered composite laminates [30-32]. The SAFE method only requires the FE discretization of the cross-section of the waveguide and exploits theoretical harmonic functions along the waveguide's lengthwise direction. Compared with the traditional 3D FE technique, SAFE requires only a 2D or 1D discretization, leading to

less stringent computational requirements for accurate solutions at high frequencies or small wavelengths. Moreover, SAFE establishes a direct relation between the lamina-to-lamina elastic constants and the complex guided wave dispersive behavior at the level of the global laminate. Marzani and De Marchi [19] exploited these features to identify the elastic constants of an isotropic plate, a unidirectional laminate, and a cross-ply laminate using SAFE as the forward model. They utilized trial group velocity curves from SAFE to match “pseudo-experimental” results (solutions from SAFE with the “true” elastic constants) by using a Genetic Algorithm to accelerate convergence. Their study utilized axial and flexural guided waves propagating in multiple directions to extract the different terms of the stiffness matrix. In a recent study [20], the authors of the present paper utilized SAFE, coupled with a Simulated Annealing (SA) optimization algorithm, to identify elastic constants of various composite laminates by matching phase velocity dispersion curves extracted in a single wave propagation direction. That work was purely numerical (i.e. experimental curves were simulated numerically by using “true” constants in the model). That study highlighted interesting coupling mechanisms in the stress/strain distributions associated to the fundamental axial (S_0), flexural (A_0) and shear-horizontal (SH_0) guided modes, that can actually enable the identification of most of the elastic constants (both at the lamina level and the laminate level) using the single wave propagation direction.

The present study extends the numerical work by Cui and Lanza di Scalea [20] to actual parts tested experimentally. In particular, guided wave dispersion data were measured using the known 2D Fast-Fourier Transform (2D FFT) method [33] for an isotropic (aluminum) plate, a quasi-isotropic composite laminate, and an anisotropic composite laminate. The property inversion process was conducted by iterating SAFE dispersion solutions corroborated by a SA optimization algorithm of the type previously used to identify properties of pavements from inversion of

Rayleigh wave data [34]. The first test case utilized the flexural mode (A_0) and the axial mode (S_0), respectively, to identify the Young's modulus and Poisson's ratio of the aluminum plate. The second test case verified the sensitivity found in the previous paper [20] of the shear-horizontal mode (SH_0) in a quasi-isotropic laminate. In particular, the tests confirmed that the engineering (effective) laminate constants can be identified by only launching guided waves along a single direction. The third test case looked at a fully anisotropic laminate probed by both the A_0 mode and the S_0 mode, and identified best practices of using the multiple modes propagating along the single direction for accurate property identification.

3.3. Experimental procedure for measuring phase velocity dispersion curves

The procedure to extract the phase velocity dispersion curves of guided waves in the test plates involved a contact piezoelectric transducer as the wave transmitter and a non-contact air-coupled transducer as the wave receiver (Figure 3.1). The non-contact receiver allowed easy scanning along a linear direction, as well as consistency of receiver response, as required by the 2D FFT method. The transmitter was an Olympus longitudinal narrowband crystal, 0.5 in diameter, centered at 1 MHz and with a 1MHz -6 dB bandwidth. It was coupled to the specimens using conventional ultrasonic couplant. The signal excitation was provided by a square-wave ultrasonic pulser (Panametrics) generating a -200 V negative pulse. The air-coupled receiver was a broadband micro-machined capacitive device (Micro-Acoustics Corporation) with a 10 mm element size, and a rather flat frequency response between DC and 2 MHz. The receiver was placed at a lift-off distance of about 5 mm from the test plates.

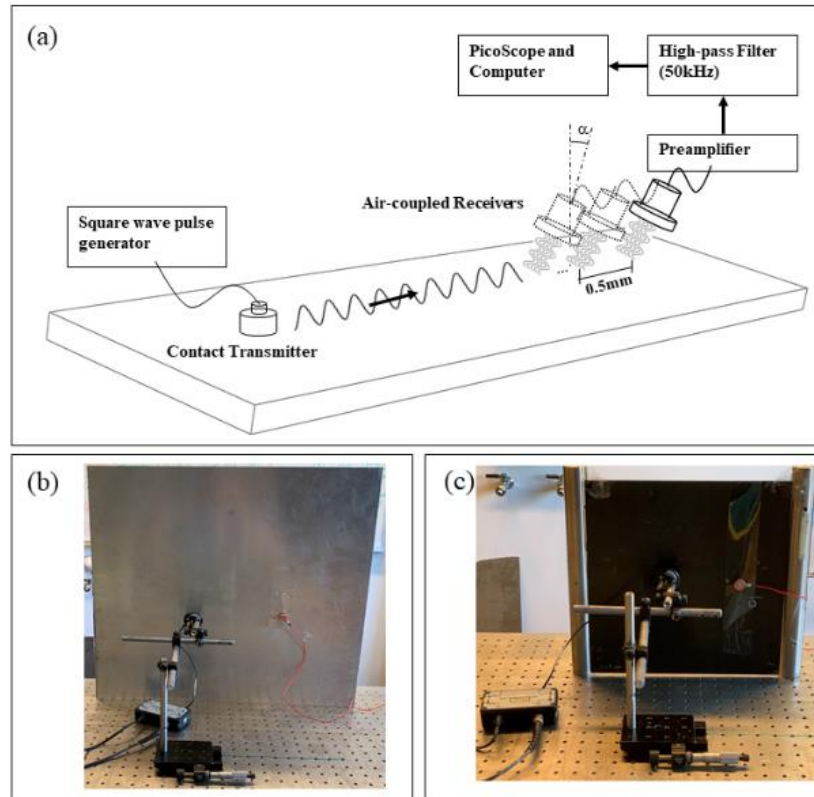


Figure 3.1. Experimental setup for extraction of phase velocity dispersion curves from the test plates.

The receiver was scanned by a micrometer-controlled platform across 50 different positions with a 0.5 mm spacing, starting from a distance from the transmitter of 100 mm. An ultrasonic preamplifier and a 50 kHz high-pass filter were used prior to collecting the signals in an oscilloscope. The signals at each receiver position were averaged 200 times to eliminate incoherent noise. Figure 3.1(b) shows the transducers on the aluminum plate; Figure 3.1c shows them on one of the composite laminate plates. The effective frequency content that was measured in the experiments depended on various parameters, including the wave damping of each of the test materials. The specific bandwidths successfully measured can be seen in the dispersion curve plots

shown later for each of the specimens. The receiver angle was fixed to ~ 6 deg in all cases. It was found that this fixed angle allowed for wave detection with sufficient Signal-to-Noise ratios in a rather broad frequency range.

3.4. Property identification algorithm

3.4.1. SAFE wave propagation model

As shown in Figure 3.2(a) and discussed in the Introduction section, SAFE requires that the plate is only discretized by finite elements in the cross-section (the y - z plane), and harmonic functions are employed in the wave propagation direction, x . For the case considered, the discretization is actually only required on a line (1D). Based on the principle of virtual work, the governing equation is represented in the volume V of the waveguide as [30]:

$$\int_V \delta \mathbf{u}^T (\rho \ddot{\mathbf{u}}) dV + \int_V \delta \boldsymbol{\varepsilon}^T \boldsymbol{\sigma} dV = 0 \quad (3.1)$$

$$\boldsymbol{\sigma} = \mathbf{Q} \boldsymbol{\varepsilon} \quad (3.2)$$

where \mathbf{u} is the displacement vector, $\boldsymbol{\varepsilon}$ is the strain vector, $\boldsymbol{\sigma}$ is the stress vector, T is the transpose operation, $\ddot{\mathbf{u}}$ serves as the second derivative w.r.t. time, and \mathbf{Q} is the stiffness matrix. A multilayered composite laminate of arbitrary lay-up can be easily studied in its global reference system by utilizing the rotation matrices \mathbf{R}_1 and \mathbf{R}_2 for the “local” stiffness matrix of each constituent lamina [31] (Figure 3.2(b)):

$$\bar{\mathbf{Q}} = \mathbf{R}_1 \mathbf{Q} \mathbf{R}_2^{-1} \quad (3.3)$$

where $\bar{\mathbf{Q}}$ is the stiffness matrix of the entire laminate in the global reference system.

Substituting Eqs. (3.2) and (3.3) into Eq. (3.1) yields to the following eigenvalue problem:

$$[\mathbf{H} - \xi \mathbf{L}]_{2M} \mathbf{U} = \mathbf{0} \quad (3.4)$$

where \mathbf{H} and \mathbf{L} are the complex matrices containing stiffness terms, mass terms, and frequency ω ; M is the total degrees of freedom of the FE mesh; ξ is the eigenvalue (the wavenumber); and \mathbf{U} is the corresponding eigenvector [30]. By looping over each frequency ω , the eigensolver offers $2M$ wavenumbers ξ 's and eigenvectors \mathbf{U} . The phase velocity is calculated by $c_{ph} = \omega / \xi_{real}$, for each combination (ξ, ω) , where ξ_{real} is the real part of the wavenumber.

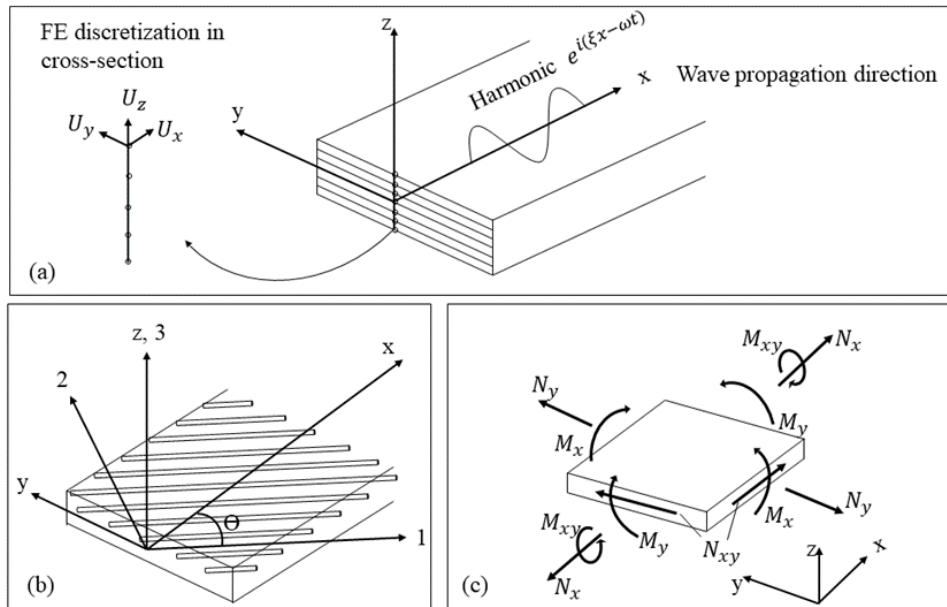


Figure 3.2. (a) SAFE representation of guided wave propagation. (b) Local (lamina) and global (laminate) coordinate system arrangements. (c) Classical Lamination Theory (CLT) load convention.

3.4.2. Identification of global “engineering” laminate properties

The SAFE model requires, as inputs, the elastic constants of each lamina comprising the laminate (along with each lamina direction). Hence the property identification algorithm directly estimates the lamina constants. Classical Lamination Theory (CLT) [35] can be used to calculate the laminate’s engineering properties, including four in-plane properties (axial stiffness along x , E_x ; axial stiffness along y , E_y ; in-plane Poisson’s ratio, ν_{xy} ; and in-plane shear stiffness, G_{xy}) and three out-of-plane properties (flexural rigidity around x , K_x ; flexural rigidity around y , K_y ; and torsional rigidity, K_{xy}):

$$\begin{bmatrix} \boldsymbol{\varepsilon}^0 \\ \boldsymbol{\kappa} \end{bmatrix} = \begin{bmatrix} \mathbf{A}^{-1} & 0 \\ 0 & \mathbf{D}^{-1} \end{bmatrix} \begin{bmatrix} \mathbf{N} \\ \mathbf{M} \end{bmatrix} \quad (3.5)$$

In the above relation, $\boldsymbol{\varepsilon}^0$ is the strain vector, including in-plane strain and shear strain, $\boldsymbol{\kappa}$ contains out-of-plane curvature and twist, \mathbf{N} and \mathbf{M} are vectors containing the external loads, and \mathbf{A} and \mathbf{D} are matrices calculated from lamina stiffness terms in the global reference system. Proper inversion of the above equation allows to calculate each engineering laminate constant from the lamina stiffness terms (see, e.g. Ref. [20]).

3.4.3. Simulated Annealing optimization

The general workflow of the property identification is schematized in Figure 3.3. The identification is achieved by matching the experimental phase velocity dispersion curves for the unknown material ($c_{ph,exp}$) to simulated curves predicted by the SAFE forward model by iterating the lamina elastic constants ($c_{ph,pred}$). The objective function to minimize is a discrepancy metric defined as:

$$d = \sqrt{\frac{1}{N} \sum_{i=1}^N \frac{(c_{\text{ph,pred}}(\omega_i) - c_{\text{ph,exp}}(\omega_i))^2}{c_{\text{ph,exp}}(\omega_i)}} \quad (3.6)$$

where N is the number of points used to discretize the dispersion curves.

The SA algorithm is employed to accelerate the determination of the optimum state as given by:

$$\begin{cases} \mathbf{Z}_j = \mathbf{Z}_i + \Delta\mathbf{Z}_i \\ \Delta\mathbf{Z}_i = \Delta\mathbf{Z}_0 \left(\frac{T}{T_0} \right) \left(\eta_1 \tan \left(\frac{\eta_2 \pi}{2} \right) \right) \\ T = T_0 \alpha^{i+1} \end{cases} \quad (3.7)$$

where T is the current temperature, and η_1 and η_2 are two uniformly random numbers in $[-1, 1]$.

Revisiting Figure 3.3, the initiated variables (\mathbf{Z}_0) and corresponding intervals ($\Delta\mathbf{Z}_0$) are chosen as the first accepted transition passing through SAFE for the calculation of the dispersion curves. The second iteration is $\mathbf{Z}_0 + \Delta\mathbf{Z}_0$. Thus, the first two discrepancies (d 's) are calculated to make the decision of either accepting the current iteration or returning to the previous transition for another attempt with the same intervals. The Metropolis Rule (MR) [36] is used to extend the searching range to all the most probable variables, even if the mismatch value is higher than the latest accepted transition. In turn, this enhances the ability to locate the global minimum of the objective function. In addition, a Cauchy distribution is used in the perturbation scheme to help circumvent risks of local minima. The two control parameters of the SA algorithm, the “temperature” (T_0) and the “cooling coefficient” (α), are set at 30°C and 0.99, respectively. These two values were chosen as a good compromise between accuracy and computational efficiency

[34]. The SA algorithm is run three times with 1000 iterations per run, which is expected to cover the meaningful and necessary possibilities based on the characteristics of the Cauchy distribution [37].

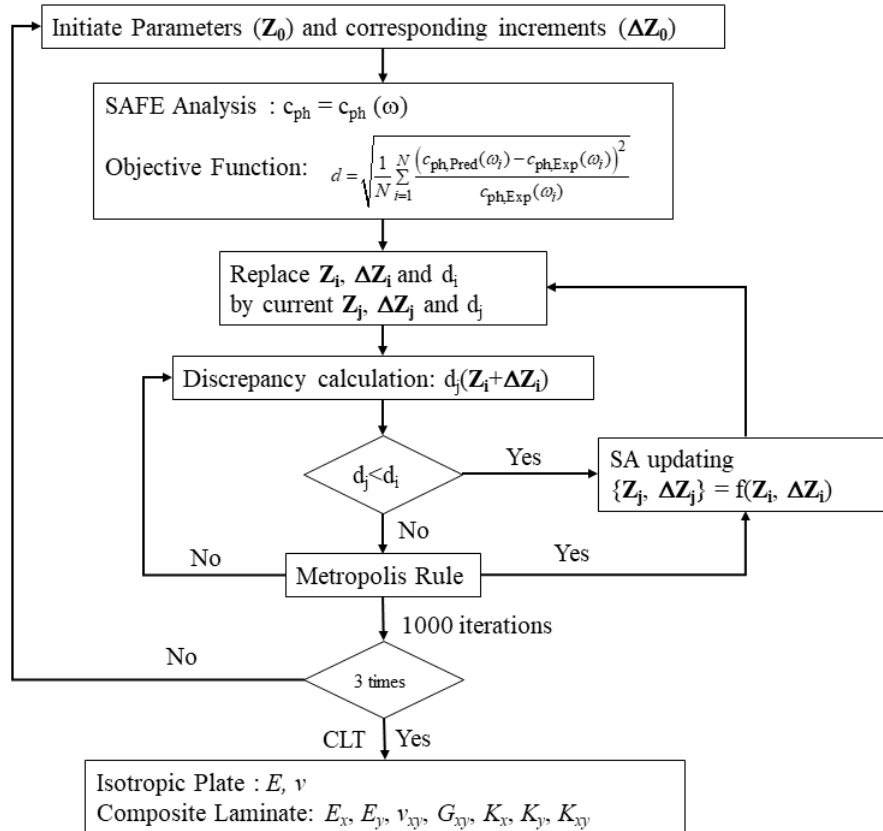


Figure 3.3. The property identification workflow using SAFE as the forward model and Simulated Annealing optimization.

3.5. Experimental property identification: case studies

3.5.1. Aluminum plate

The first test case consisted of an aluminum plate with a thickness of 1.5 mm, manufacturer's Young's modulus $E = 68.9$ GPa, Poisson's ratio $\nu = 0.33$ and density $\rho = 2700$ kg/m³. The objective was to identify the two independent isotropic elastic constants (E and ν) from the guided wave dispersion inversion strategy described above. As shown in Figure 3.4, the guided waves are propagating along direction x , and (y, z) is the plate's cross-sectional plane.

The waves were excited by the contact PZT transmitter and received by the non-contact air-coupled receiver that was scanned along the various positions according to the procedure in Section 2. Since both axial (S_0) and flexural (A_0) Lamb modes generally contain out-of-plane displacement components at the plate's surface [16], both modes are excited by the transmitter. The air-coupled receiver was oriented at an angle of about 4° from the normal to the plate, which gave sensitivity to both S_0 and A_0 modes according to phase-matching Snell's law [16]. A typical recorded waveform is shown in Figure 3.4, clearly indicating successful recording of the faster S_0 mode and the slower A_0 mode. Figure 3.4. also shows the SAFE calculated displacement, strain, and stress cross-sectional profiles at a frequency of 500 kHz, for the two fundamental Lamb modes A_0 and S_0 in that plate. The displacement profiles are the first M elements of eigenvector (\mathbf{U}) in Eq. (3.4). The strain profiles were obtained through spatial differentiation of the displacements. The stresses were obtained from the material constitutive law. The profiles follow known behavior of these Rayleigh-Lamb waves, with symmetric horizontal displacement u_x , strain ε_{xx} , and stress σ_{xx} for S_0 (indicating its axial nature), and antisymmetric u_x , ε_{xx} , and σ_{xx} for A_0 (indicating its flexural nature).

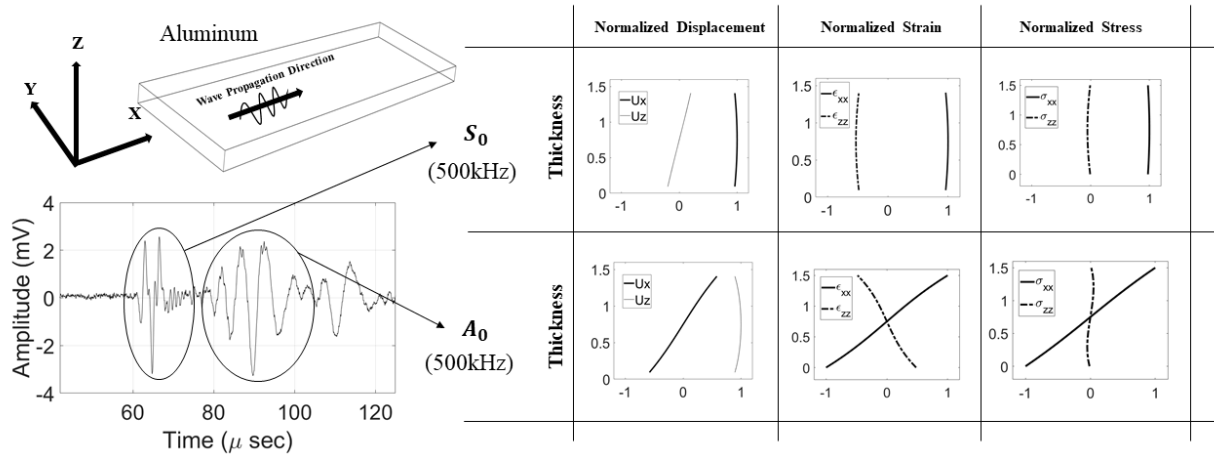


Figure 3.4. Aluminum plate: a typical experimental waveform, along with SAFE results of displacement, strain, and stress cross-sectional profiles for S_0 and A_0 guided modes at 500 kHz.

The property identification analysis was conducted using the A_0 and S_0 modes separately. Phase velocity dispersion curves were extracted experimentally using the 2D-FFT technique. Time gating was used to separate the two modes. The predicted dispersion curves were calculated by SAFE using the set of “trial” properties according to Section 3. Young’s modulus (E) and Poisson’s Ratio (ν) were considered as two unknown independent variables optimized simultaneously (2D inversion).

The 2D property identification results are shown in the first two columns of Figure 3.5, in terms of the phase velocity discrepancy metric d of Eq. (6) versus the variable % error (identified constants relative to true constants). The final outcome of the SA optimization (smallest d value) is marked by a *Star* symbol (*) and an arrow in each plot. The closer the *Star* symbol is to the 0 value on the x -axis, the more accurate the answer is (perfect accuracy would be % error = 0). Similarly, the closer the *Star* symbol is to the 0 value on the y -axis, the more correlation exists

between the dispersion curves of a particular guided mode and a specific property. Also, these plots show ranges for d that are between 1 and 5 (corresponding to a zoom-in around the minimum of the objective function) to better evaluate the relative identification performance of the various modes. In the first column of Figure 3.5, the S_0 mode demonstrates a good identification of Young's modulus with an accuracy error less than 5%. This is expected owing to the dominant ε_{xx} and σ_{xx} components of the S_0 mode shown in the cross-sectional profiles of Figure 3.4. The A_0 mode (that also features significant ε_{xx} and σ_{xx} components in Fig. 4) is also effective in identifying E , although it exhibits a smaller sensitivity to this property (slope of the optimization curves) compared to S_0 . The identification of the Poisson's ratio - second column in Figure 3.5 - becomes more challenging, with an increasing scatter of the optimization results for both modes. It therefore appears that the sensitivity of the dispersion curves to the material Poisson's ratio is less than that to the material Young's modulus. Nevertheless, S_0 mode achieves the final answer for ν with a $\sim 15\%$ error, although the sensitivity is smaller than that for E . The final column of Figure 3.5 compares the experimental phase velocity dispersion curves to the SAFE predicted curves for the final optimization step. It is seen that both modes can achieve a satisfactory match in a quite broad frequency range, confirming the sufficiency of the inversion process. The better match exhibited by the S_0 mode curves compared to the A_0 mode curves is consistent with the improved identification performance for both E and ν .

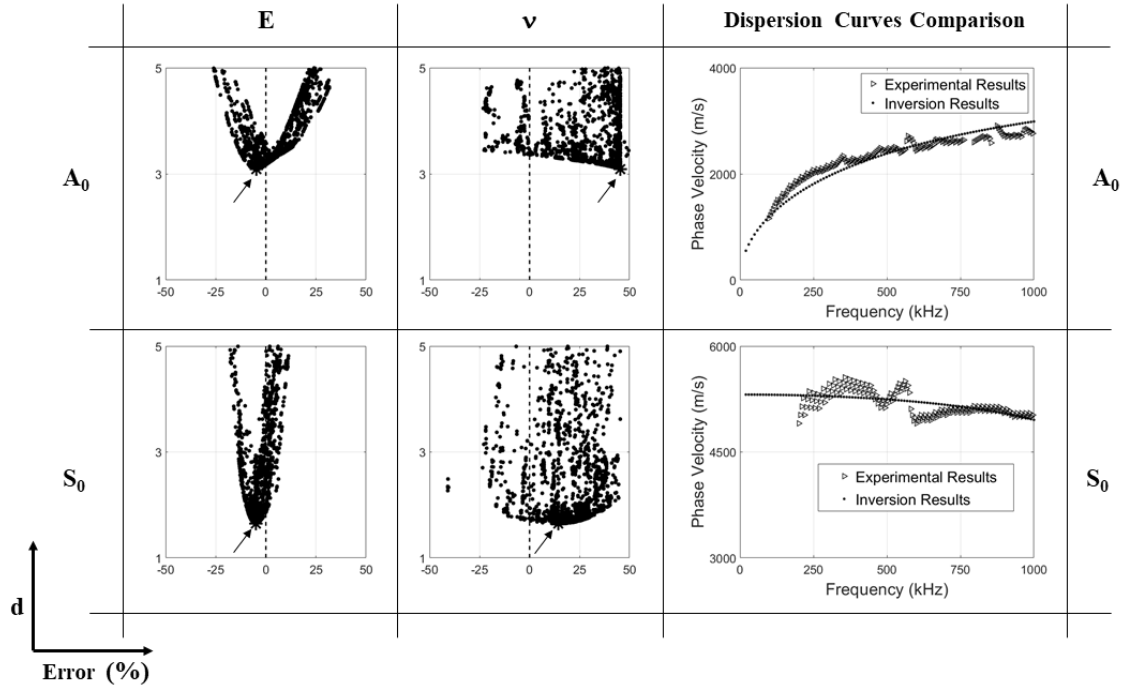


Figure 3.5. 2D identification of Young’s modulus and Poisson’s ratio of the isotropic plate, along with a comparison of phase velocity dispersion curves between experiment and optimum SAFE prediction.

3.5.2. Quasi-Isotropic laminate

The second test case considered a quasi-isotropic, 16-layer T800/3900-2 graphite-epoxy laminate with a lay-up of $[+45^\circ/-45^\circ/0^\circ/+45^\circ/90^\circ/-45^\circ/0^\circ/90^\circ]_S$. The “true” individual lamina properties were taken from Tong and Soutis [38] for this material, and are shown in Table 1. There are only five independent lamina constants given the transversely isotropic behavior. Material density was 1550 kg/m^3 and the total laminate thickness was 2.6 mm. From CLT using the explicit expressions in Ref. [20], the “true” laminate engineering constants were calculated as: axial stiffness along x , $E_x = 62.11 \text{ GPa}$; axial stiffness along y , $E_y = 62.11 \text{ GPa}$; in-plane Poisson’s ratio,

$\nu_{xy}=0.30$; in-plane shear stiffness, $G_{xy}= 23.9$ GPa ; flexural rigidity around x , $K_x = 78.82$ N·m²; flexural rigidity around y , $K_y = 57.85$ N·m²; and torsional rigidity, $K_{xy}= 47.00$ N·m².

Table 3.1 Single lamina elastic constants (T800/3900-2) for the quasi-isotropic laminate (from Ref. [38]).

| Constant | E_{11} | E_{22} | E_{33} | ν_{12} | ν_{13} | ν_{23} | G_{12} | G_{13} | G_{23} |
|-------------|----------|----------|----------|------------|------------|------------|----------|----------|----------|
| Value (GPa) | 160.08 | 8.97 | 8.97 | 0.28 | 0.28 | 0.36 | 6.21 | 6.21 | 3.30 |

This case is shown in Figure 3.6(a), indicating the local lamina coordinate system ($1, 2, 3$) and the global laminate coordinate system (x, y, z). The guided waves are propagating along the x global direction. The objective was to identify the laminate engineering constants from the optimization algorithm. The experimental setup and procedure were the same as adopted for the previous aluminum plate case. A typical waveform recorded from the quasi-isotropic composite plate is shown in Figure 3.6(b). Comparing this waveform to the recording from the aluminum plate (Figure 3.4), it can be seen that only a single wave mode, rather than two separate modes, is detected in the composite. Time of flight extraction reveals this mode to be the shear-horizontal SH_0 , that for composites is a hybrid mode with concurrent normal and shear stresses [16]. Figure 3.6(c) shows the SAFE-predicted cross-sectional mode shapes for this mode in terms of displacement, strain, and stress profiles at 400 kHz. Comparing again with the profiles of the isotropic plate, the composite laminate exhibits significant “jumps”, more evident in the strain and stress profiles, as a result of the different lamina orientations. In addition, besides the expected dominant transverse shear stress τ_{xy} for the SH_0 mode, a strong shear-normal coupling exists with the appearance of significant normal stresses σ_{xx} and σ_{zz} . This coupling is absent in isotropic plates

where the SH_0 mode contains solely shear stresses (pure shear case). The presence of the out-of-plane components ε_{zz} and σ_{zz} at the laminate's surface explains why this mode is efficiently transmitted and received by the experimental setup adopted [24]. It is also possible that the relatively large thickness of the laminate (2.6 mm) is partly responsible for the activation of the SH_0 mode. The previous Ref. [24] also found this mode activated by air-coupled transducers in a laminate of comparable thickness (3.2 mm).

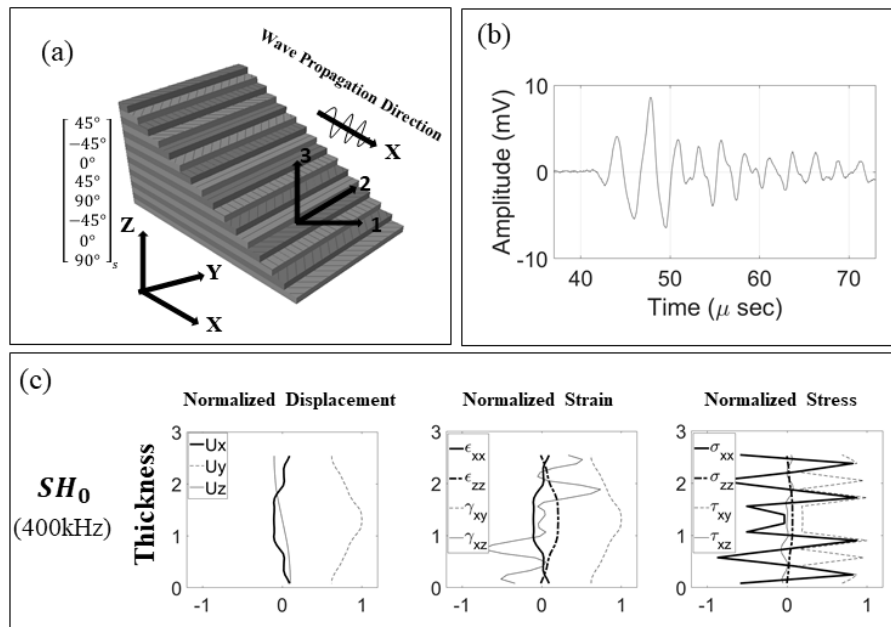


Figure 3.6. Quasi-isotropic laminate: (a) the lay-up arrangement; (b) a typical experimental waveform; (c) SAFE results of displacement, strain and stress cross-sectional profiles for the SH_0 guided mode at 400kHz.

As discussed above, the optimization algorithm first identifies the five independent lamina constants given as inputs to the SAFE model, i.e. E_{11} , $E_{22} = E_{33}$, $\nu_{12} = \nu_{13}$, $G_{12} = G_{13}$, and $G_{23} = E_{33}/(2*(1+\nu_{23}))$. The optimization was conducted for all five constants simultaneously (5D inversion). For each set of five lamina constants, CLT was then used to calculate the seven laminate

engineering constants (in plane properties E_x , E_y , ν_{xy} and G_{xy} ; and out-of-plane properties K_x , K_y and K_{xy}) as discussed in Section 3.2.

The results of the 5D inversion are shown in Figure 3.7 in terms of the phase velocity discrepancy d versus the variable % error in the identified constants. The search range was set to +/- 50% w.r.t the true values. The final optimization result (smallest d value) is also marked with a *Star* symbol (*) and the arrow in the plots. It should be remembered that these results used a single guided wave mode (SH_0) propagating along a single direction (x). The plots show that all of the seven constants can be identified with a reasonable degree of accuracy. A very good result is obtained, as expected, for properties directly along the wave propagation direction (i.e. E_x and K_x in Figure 3.7(a)(e)), where the final identification brings only a 5% error. The sensitivity of SH_0 to these properties is due to the coupling with the normal stress components (ε_{xx} and σ_{xx}) as discussed in Figure 3.6(c). As for the constant in the other direction, K_y in Figure 3.7(f) (E_y is numerically equal to E_x for this quasi-isotropic layup), the final optimum is slightly worse but still within a reasonable ~10% error. This is quite remarkable considering that this property is in a direction orthogonal to the wave propagation direction. This sensitivity is due to the strain stress couplings previously predicted in the numerical work of Ref. [20]. The identification of the shear stiffness G_{xy} (Figure 3.7(d)) presents a nearly perfect result with only ~1% error, owing to the naturally dominant transverse shear component τ_{xy} of SH_0 as shown in Figure 3.6(c). The final comparison between the experimental dispersion curve and that of SAFE with the optimized constants is shown in Figure 3.7(h). The good match confirms the suitability of this mode for the inversion process.

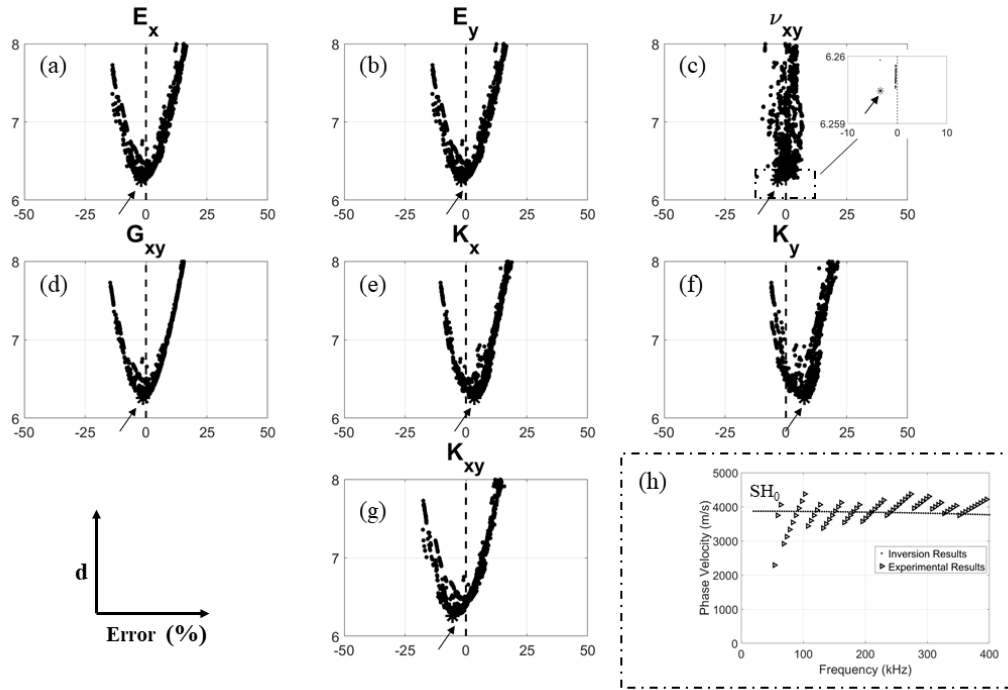


Figure 3.7. 5D identification of engineering constants of the quasi-isotropic laminate by the SH_0 mode.

3.5.3. Anisotropic laminate

The final test case considered an 8-layer, T300/5208 graphite-epoxy laminate with a lay-up of $[0^\circ/-45^\circ/+45^\circ/0^\circ]_s$, which is of course fully anisotropic. This laminate had a 1 mm thickness and a density of 1530 kg/m^3 . The same laminate was the subject of an earlier work by the present research group [39]. The “true” lamina constants taken from that work are shown in Table 2.

Table 3.2. Single lamina elastic constants (T300/5208) for the anisotropic laminate (from Ref. [39]).

| Constant | E_{11} | E_{22} | E_{33} | ν_{12} | ν_{13} | ν_{23} | G_{12} | G_{13} | G_{23} |
|-------------|----------|----------|----------|------------|------------|------------|----------|----------|----------|
| Value (GPa) | 132.14 | 9.06 | 9.06 | 0.25 | 0.25 | 0.59 | 4.55 | 4.55 | 2.86 |

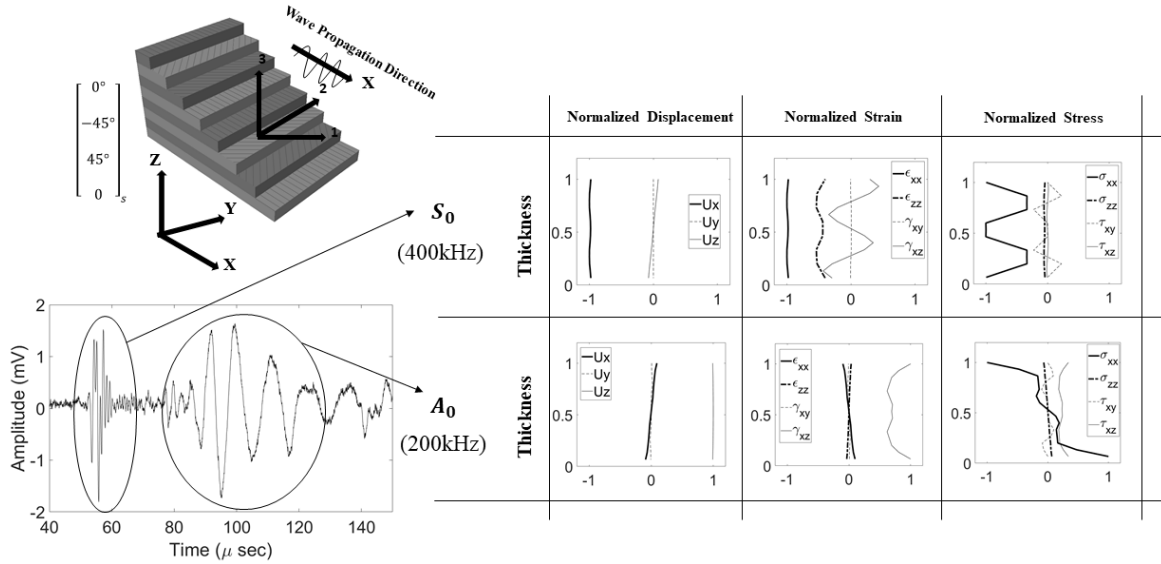


Figure 3.8. Anisotropic laminate: the lay-up arrangement; typical signal in the experiment; SAFE results of displacement, strain and stress cross-sectional profiles of the S_0 mode at 400 kHz and the A_0 mode at 200 kHz.

A typical waveform measured from this plate is shown in Figure 3.8. Interestingly, the signal shows an excellent detection of the two modes, the faster axial (S_0) and the slower flexural (A_0), similarly to the measurements on the isotropic aluminum plate (Figure 3.4). The SAFE displacement, strain, and stress cross-sectional profiles of these two modes at certain frequencies are also shown in Figure 3.8. These profiles suggest the more complex coupling phenomena between normal and shear variables compared to the isotropic plate in Figure 3.4. In particular, significant coupling between in-plane longitudinal and in-plane shear behavior is observed (i.e. co-existence of σ_{xx} and τ_{xy} for both A_0 and S_0 modes). This is a result of the $\pm 45^\circ$ off-axis laminae as observed for a similar laminate in the earlier numerical work by the authors [20]. As for the previous quasi-isotropic laminate, the inversion algorithm identifies first the five independent

lamina properties in a 5D inversion scheme. The laminate engineering properties are then calculated from CLT. In this case (anisotropic laminate), however, $E_x \neq E_y$.

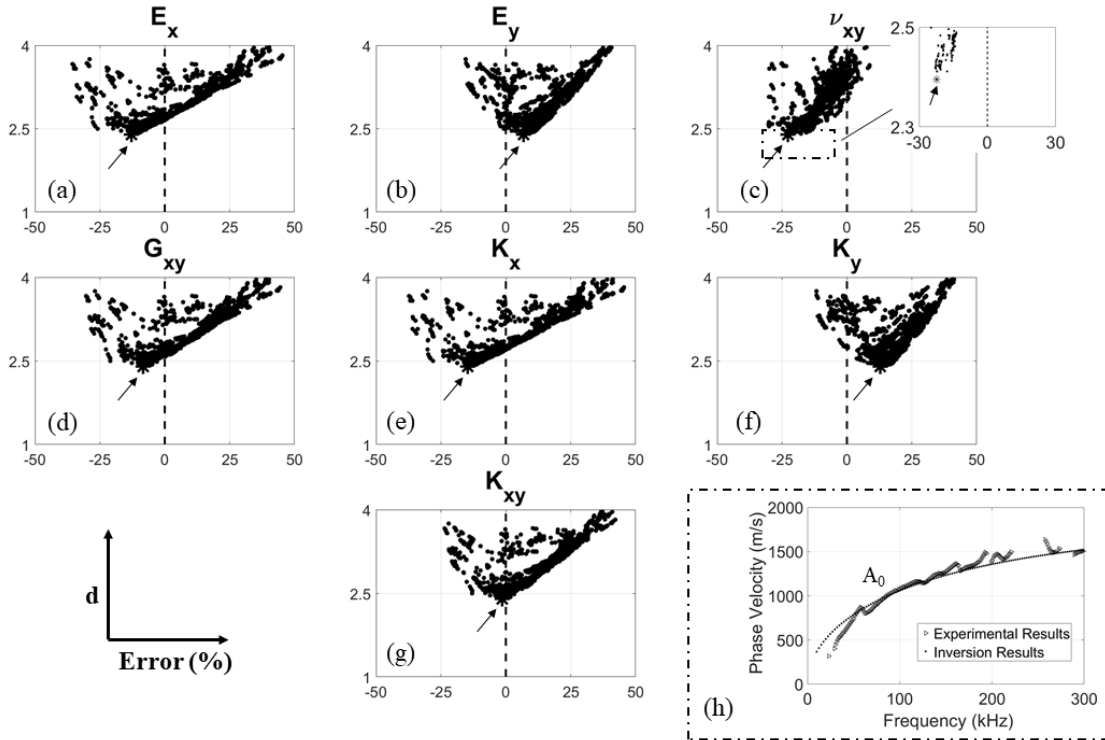


Figure 3.9. 5D identification of engineering properties of the anisotropic laminate by the A_0 mode.

Figure 3.9 shows the 5D identification result utilizing solely the A_0 mode propagating along direction x . Similarly to what found in the quasi-isotropic laminate, the coupling provided by the off-axis laminae ($\pm 45^\circ$) helps the single wave propagation direction to identify all of the engineering constants with a reasonable level of accuracy. However, the identification results for the anisotropic laminate with A_0 is slightly worse than that for the quasi-isotropic laminate with SH_0 . Nevertheless, the constants E_x and K_x are reasonably identified with a $\sim 10\%$ error of the optimum solution. K_y is also identified with the same level of error. The torsional rigidity (K_{xy}) is

actually better identified than in the quasi-isotropic laminate, with only a 2% error. The Poisson's ratio ν_{xy} presents some challenges in identification, consistently with some of the earlier results. The sensitivities of the other constants (slopes of the curves) is quite similar.

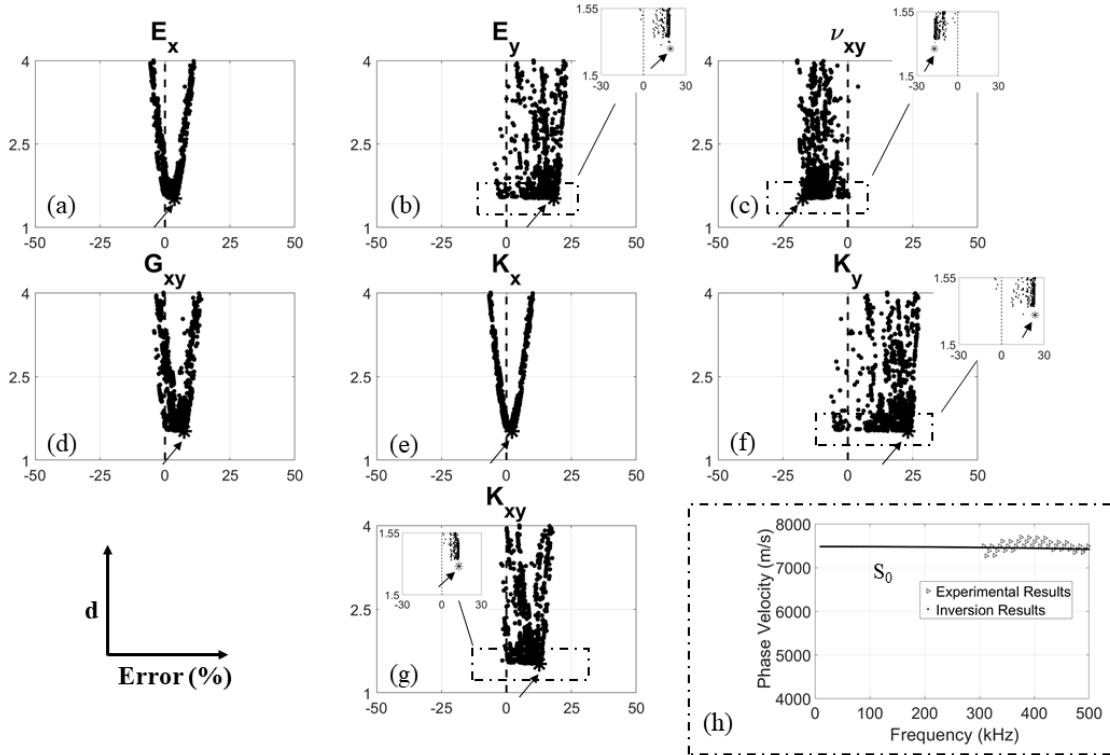


Figure 3.10. 5D identification of engineering properties of the anisotropic laminate by the S_0 mode.

The next analysis was conducted to study the sensitivity of the S_0 mode to the laminate constants. The results are shown in Figure 3.10. Compared to the performance by the A_0 mode, one of the most noticeable differences for S_0 is the excellent identification of E_x and K_x ($< 5\%$ error), as a result of the dominant normal stress σ_{xx} in the axial mode. Interestingly, the transverse constants E_y and K_y show a worse result compared to A_0 . The identification of the Poisson's ratio ν_{xy} remains the most challenging, with an error as high as $\sim 25\%$.

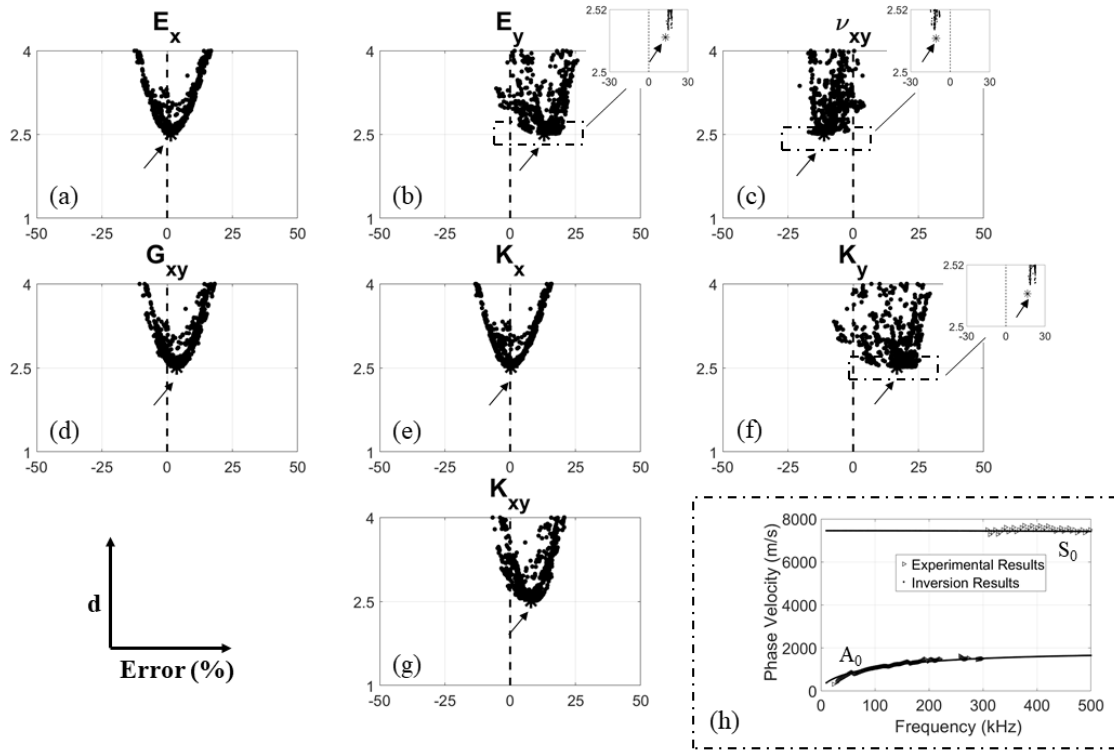


Figure 3.11. 5D identification of engineering properties of the anisotropic laminate by both A_0 and S_0 modes.

The final analysis combined the dispersion results of A_0 and S_0 modes to investigate whether the simultaneous match of the two modes can be beneficial to the laminate property identification. The results of this combination are shown in Figure 3.11. In this case, E_x and K_x are identified perfectly with a $\sim 0\%$ error (Figure 3.11(a) and (e)), since both A_0 and S_0 have a significant component of σ_{xx} . The in-plane shear stiffness G_{xy} (Figure 3.11(d)) is also identified more accurately than with any one of the modes considered separately, owing to the $\sigma_{xx} - \tau_{xy}$ coupling existing in both A_0 and S_0 modes. The Poisson's ratio ν_{xy} (Figure 3.11(c)) is also identified more accurately by the two-mode combination, with a $\sim 10\%$ error. The transverse constants, E_y (Figure 3.11(b)) and K_y (Figure 3.11(f)), achieve better identification than the

individual S_0 mode. The concluding comparison between the experimental and the numerical dispersion curves of Figure 3.11(h), where both modes show a good match, further confirms the opportunity to combine the modes for a comprehensive laminate property identification.

3.6. Discussion and Conclusions

This paper presents an experimental validation of using guided wave dispersion curves to identify the elastic properties of composite laminates. The property identification method involves measuring phase velocity dispersion curves via a 2D-FFT method and matching these curves to SAFE-predicted curves through a Simulated Annealing optimization algorithm. Of interest here is to determine, experimentally, the effectiveness of a single guided wave propagation direction to identify global “engineering” constants of the laminate, both in the wave propagation direction and in the transverse direction.

Results were obtained for an isotropic plate, a quasi-isotropic composite laminate, and an anisotropic composite laminate. It was shown that typical guided modes used to inspect these components, i.e. the S_0 , A_0 and the SH_0 modes, are indeed quite sensitive to the elastic constants. In particular, interesting normal-shear coupling phenomena occurring in the composites due to the off-axis laminae impart sensitivity of the single wave propagation to various properties, including shear moduli and stiffnesses along orthogonal directions. In particular, the SH_0 mode is shown to effectively identify all of the seven engineering constants of the quasi-isotropic laminate (in plane properties E_x , E_y , ν_{xy} and G_{xy} ; and out-of-plane properties K_x , K_y and K_{xy}) with reasonable accuracies below $\sim 10\%$ errors. The S_0 and A_0 modes were also effective in identifying the constants of the anisotropic laminate, although ν_{xy} and K_y present the least accuracy. A better

overall identification for the anisotropic laminate was obtained when combining the dispersion curves of S_0 and A_0 in a “joint” optimization scheme.

Overall, the experimental results from this paper corroborate the conclusions from the earlier numerical work of Cui and Lanza di Scalea [20], indicating that guided waves in a single wave propagation direction can indeed be a reasonable tool for property identification of multilayered composite laminates. This method can be applied to structural components *in-situ*, with little or no regard for the boundary conditions (as long as these boundary conditions do not affect the wave propagation path between the transmitting and the receiving transducers).

The SAFE analysis utilized as the forward problem assumed that all the laminae comprising the laminate had the same properties. This assumption can be reasonably adopted in the case of undamaged laminates. On the other hand, the SAFE discretization could of course allow to treat each individual lamina separately (i.e. with different elastic constants). While this approach would clearly increase the computational burden of the inversion algorithm (by increasing the number of optimization variables), it would allow, for example, to identify damage or material degradation that affects only a certain thickness of the laminate.

By their very nature, guided wave measurements “average” the material behavior along the wave propagation path. Therefore, localized changes in properties, if their spatial extent is substantially smaller than the transmitter-receiver distance, might be difficult to resolve.

Other suitable wave receivers could have been selected for this application. This includes the use of a laser vibrometer, whose broadband characteristics and pointwise probing would make it an attractive option. An interesting aspect that could be addressed in a future paper is the role of measurement uncertainties, for example measurement repeatability. This analysis could be carried

out by repeating the measurements at different points of the same panel or on different panels with similar properties.

3.7. Acknowledgments

This work was funded in part by the US Federal Aviation Administration Joint Center of Excellence for Advanced Materials (FAA Cooperative Agreement 12-C-AM-UCSD) and by the US Federal Railroad Administration (contract # 693JJ619C000008).

Chapter 3 is, in full, a reprint of material published in Cui, Ranting, and Francesco Lanza di Scalea. "Identification of Elastic Properties of Composites by Inversion of Ultrasonic Guided Wave Data." *Experimental Mechanics* (2021): 1-14. The dissertation author was the primary investigator and author of this paper.

3.8. References

- [1] Tam JH, Ong ZC, Ismail Z, Ang BC, Khoo SY. Identification of material properties of composite materials using nondestructive vibrational evaluation approaches: A review. *Mech Adv Mater Struct* 2017;24:971–86. <https://doi.org/10.1080/15376494.2016.1196798>.
- [2] Gibson RF. Modal vibration response measurements for characterization of composite materials and structures. *Compos Sci Technol* 2000;60:2769–80. [https://doi.org/10.1016/S0266-3538\(00\)00092-0](https://doi.org/10.1016/S0266-3538(00)00092-0).
- [3] McIntyre ME, Woodhouse J. On measuring the elastic and damping constants of orthotropic sheet materials. *Acta Metall* 1988;36:1397–416.
- [4] Hwang S, Wu J, He R. Identification of effective elastic constants of composite plates based on a hybrid genetic algorithm. *Compos Struct* 2009;90:217–24. <https://doi.org/10.1016/j.compstruct.2009.03.021>.
- [5] Matter M, Gmür T, Cugnoni J, Schorderet A. Numerical-experimental identification of the

- elastic and damping properties in composite plates. *Compos Struct* 2009;90:180–7. <https://doi.org/10.1016/j.compstruct.2009.03.001>.
- [6] Genovese K, Lamberti L, Pappalettere C. A new hybrid technique for in-plane characterization of orthotropic materials. *Exp Mech* 2004;44:584–92.
- [7] Lauwagie T, Lambrinou K, Sol H, Heylen W. Resonant-based identification of the Poisson's ratio of orthotropic materials. *Exp Mech* 2010;50:437–47.
- [8] Du X, Yan J, Laflamme S, Leifsson L, Tesfahunegn Y, Koziel S. Model-assisted probability of detection for structural health monitoring of flat plates. *Int. Conf. Comput. Sci.*, Springer; 2018, p. 618–28.
- [9] Frederiksen PS. Experimental Procedure and Results for the Identification of Elastic Constants of Thick Orthotropic Plates. *J Compos Mater* 1997;31:360–82. <https://doi.org/10.1177/002199839703100403>.
- [10] Ayorinde EO. Elastic Constants of Thick Orthotropic Composite Plates. *J Compos Mater* 1995;29:1025–39. <https://doi.org/10.1177/002199839502900802>.
- [11] Daghia F, de Miranda S, Ubertini F, Viola E. Estimation of elastic constants of thick laminated plates within a Bayesian framework. *Compos Struct* 2007;80:461–73.
- [12] Cugnoni J, Gmür T, Schorderet A. Inverse method based on modal analysis for characterizing the constitutive properties of thick composite plates. *Comput Struct* 2007;85:1310–20.
- [13] Mishra AK, Chakraborty S. Determination of material parameters of FRP plates with rotational flexibility at boundaries using experimental modal testing and model updating. *Exp Mech* 2015;55:803–15.
- [14] Cunha J, Piranda J. Identification of stiffness properties of composite tubes from dynamic tests. *Exp Mech* 2000;40:211–8.
- [15] Staszewski W, Boller C, Tomlinson GR. Health monitoring of aerospace structures: smart sensor technologies and signal processing. John Wiley & Sons; 2004.
- [16] Rose JL. Ultrasonic guided waves in solid media. Cambridge university press; 2014.
- [17] Giurgiutiu V. Structural health monitoring (SHM) of aerospace composites. *Polym. Compos. Aerosp. Ind.*, Elsevier; 2015, p. 449–507.
- [18] Vary A. Ultrasonic characterization of material properties. In: Moore P, Workma G, Kishoni D, editors. *Nondestruct. Test. Handb. Ultrason. Test.*, The American Society for Nondestructive Testing; 2007, p. 305–56.
- [19] Marzani A, De Marchi L. Characterization of the elastic moduli in composite plates via dispersive guided waves data and genetic algorithms. *J Intell Mater Syst Struct*

- 2013;24:2135–47. <https://doi.org/10.1177/1045389X12462645>.
- [20] Cui R, Lanza di Scalea F. On the identification of the elastic properties of composites by ultrasonic guided waves and optimization algorithm. *Compos Struct* 2019;223:110969.
- [21] Chimenti DE. Guided waves in plates and their use in materials characterization. *Appl Mech Rev* 1997;50:247–84.
- [22] Balasubramaniam K. Inversion of the ply lay-up sequence for multi-layered fiber reinforced composite plates using genetic algorithm. *Nondestruct Test Eval* 1998;15:311–31.
- [23] Castaings M, Hosten B, Kundu T. Inversion of ultrasonic , plane-wave transmission data in composite plates to infer viscoelastic material properties. *NDT E Int* 2000;33:377–92.
- [24] Castaings M, Hosten B. Lamb and SH waves generated and detected by air-coupled ultrasonic transducers in composite material plates. *Ndt E Int* 2001;34:249–58.
- [25] Vishnuvardhan J, Krishnamurthy C V, Balasubramaniam K. Genetic algorithm based reconstruction of the elastic moduli of orthotropic plates using an ultrasonic guided wave single-transmitter-multiple-receiver SHM array. *Smart Mater Struct* 2007;16:1639–50.
- [26] Vepakomma R, Janapati VV, Balasubramaniam K, Krishnamurthy C V. Global material characterization of composite structures using Lamb wave STMR array technique. *AIP Conf. Proc.*, vol. 1211, American Institute of Physics; 2010, p. 1812–9.
- [27] Glushkov E, Glushkova N, Eremin A. Elastic guided wave based assessment of laminate composite material constants. 11th Eur Conf Non-Destructive Test (ECNDT 2014), Prague, Czech Repub 2014.
- [28] Sale M, Rizzo P, Marzani A. Guided waves based approach for the reconstruction of the elastic moduli of plates. 2009 IEEE Int. Ultrason. Symp., IEEE; 2009, p. 1499–502.
- [29] Gsell D, Dual J. Non-destructive evaluation of elastic material properties in anisotropic circular cylindrical structures. *Ultrasonics* 2004;43:123–32.
- [30] Hayashi T, Song WJ, Rose JL. Guided wave dispersion curves for a bar with an arbitrary cross-section, a rod and rail example. *Ultrasonics* 2003;41:175–83. [https://doi.org/10.1016/S0041-624X\(03\)00097-0](https://doi.org/10.1016/S0041-624X(03)00097-0).
- [31] Bartoli I, Marzani A, Lanza di Scalea F, Viola E. Modeling wave propagation in damped waveguides of arbitrary cross-section. *J Sound Vib* 2006;295:685–707. <https://doi.org/10.1016/j.jsv.2006.01.021>.
- [32] Marzani A. Time-transient response for ultrasonic guided waves propagating in damped cylinders. *Int J Solids Struct* 2008;45:6347–68. <https://doi.org/10.1016/j.ijsolstr.2008.07.028>.
- [33] Alleyne D, Cawley P. A two-dimensional Fourier transform method for the measurement

- of propagating multimode signals. *J Acoust Soc Am* 1991;89:1159–68.
- [34] Ryden N, Park CB. Fast simulated annealing inversion of surface waves on pavement using phase-velocity spectra. *Geophysics* 2006;71:R49–58.
- [35] Jones RM. *Mechanics of composite materials*. CRC press; 1998.
- [36] Mosegaard K, Sambridge M. Monte Carlo analysis of inverse problems. *Inverse Probl* 2002;18:29–54.
- [37] Ingber L. Very Fast Simulated Re-annealing. *Math Comput Model* 1989;V 12:967–73.
- [38] Tong L, Soutis C. *Recent Advances in Structural Joints and Repairs for Composite Materials*. Kluwer Academic Publishers; 2003.
- [39] Matt H, Bartoli I, Lanza di Scalea F. Ultrasonic guided wave monitoring of composite wing skin-to-spar bonded joints in aerospace structures. *J Acoust Soc Am* 2005;118:2240–52. <https://doi.org/10.1121/1.2033574>.

Chapter 4. Damage imaging in skin-stringer composite aircraft panel by ultrasonic guided waves using deep learning with convolutional neural network

4.1. Abstract

The detection and localization of structural damage in a stiffened skin-to-stringer composite panel typical of modern aircraft construction can be addressed by ultrasonic guided wave transducer arrays. However, the geometrical and material complexities of this part make it quite difficult to utilize physics-based concepts of wave scattering. A data-driven Deep Learning (DL) approach based on Convolutional Neural Network (CNN) is used instead for this application. The DL technique automatically selects the most sensitive wave features based on the learned training data. In addition, the generalization abilities of the network allow to detect damage that can be different from the training scenarios. The paper describes a specific 1D-CNN algorithm that has been designed for this application, and it demonstrates its ability to image damage in key regions of the stiffened composite test panel, particularly the skin region, the stringer's flange region and the stringer's cap region. Covering the stringer's regions from guided wave transducers located solely on the skin is a particularly attractive feature of the proposed SHM approach for this kind of complex structures.

4.2. Introduction

Detection and localization of damage in structural components is one of the main objectives of Structural Health Monitoring (SHM) systems. In the case of modern aircraft construction, largely employing fiber-reinforced composite materials, SHM damage detection techniques based on Ultrasonic Guided Waves (UGWs) with attached wafer-like PZT transducers are very popular [1-7]. Of particular interest are damage detection techniques that can be deployed with sparse UGW transducer arrays, operated either in an active mode or in a passive mode, both requiring careful decisions on signal feature extraction [8-13] and/or damage imaging algorithms [14-18].

Traditional UGW SHM damage imaging techniques rely on knowledge of the material properties of the test part and/or extraction of physics-based predetermined signal features considered sensitive to damage (e.g. wave amplitude, time of flight, etc..). In fiber-reinforced composite parts, and particularly built-up components such as stiffened composite panels, such physics-based knowledge is difficult to obtain. For these complex wave propagation patterns, data-driven approaches may be more effective.

Deep Learning (DL) is increasingly used in various data-driven measurements, including computer vision, speech recognition and natural language processing [19]. Since DL focuses on high-level data abstractions to define high-level meanings, it can efficiently and automatically compress large number of signal features [20]. The central branches of DL include deduction, reasoning, and learning [21]. One attractive capability of DL is to extract hierarchical expressions of inputs automatically, as the later stacked layers learn more complex features from the former layers. In addition, DL automatically learns sensitive features from every input data, in contrast to a priori feature extraction. For these reasons DL strategies have been recently examined in vibration-based structural condition monitoring ranging from machine fault detection [22] to wind

turbine fault detection [23]. In SHM systems using UGWs, recent DL applications have included acoustic emission source location [24], damage location in metal plates [25-27], sub-wavelength damage detection in metal plates [28], and characterization of cortical bones via inversion of guided wave data [29].

A DL technique that has gained much attention for high-dimensional data compression is the Convolutional Neural Network (CNN). CNN combines feature extraction and weights determination via the training process, which automatically emphasizes compelling features while mitigating redundant features [30]. Specific advantages of CNN compared to fully-connected Neural Networks (NN) include Parameters Sharing and Connection Sparsity [19]. Parameter Sharing simplifies the training from a large amount of parameters to a much smaller one by allowing feature detectors to go through all regions of each training example and shared by regions with similar features. Connection Sparsity further reduces the number of trained parameters hence keeping a low number of necessary inputs. CNN are also known to capture translation invariances, meaning that the target's main features are still captured under limited shifts [31]. Although the CNN training phase can be lengthy, the testing time is usually fast, especially on GPUs, leading to the possibility of real-time detection [32]. 1-D CNN was recently applied to raw vibration data to detect loosen joints on a steel frame [33] and for bearing fault diagnosis [34]. The aforementioned works [42-45] used some form of CNN in their DL architecture applied to damage detection in SHM UGW systems.

The present study applies a specially designed 1D-CNN algorithm to detect and locate structural damage in a stiffened composite panel (skin-to-stringer assembly) representative of modern commercial aircraft construction (e.g., B787 and A380). Section 2 describes the experimental setup and the localization workflow. Section 3 presents the details of core functions

of the CNN architecture. Section 4 includes the imaging results, including simulated damage positions co-located with the training positions, offset from the training positions, and a case of a saw-cut damage in the stringer cap. This section also includes a comparison with a “traditional” imaging method, the RAPID algorithm. Finally, Section 5 shows the damage classification performance evaluation. The discussion and conclusions are provided in Section 6.

4.3. Experimental setup and procedure

The test part considered in this study was a composite stiffened panel with a co-cured stringer made of T800/3900-2 Carbon-Fiber Reinforced Polymer (CFRP), with overall dimensions of 1000×265 mm– Figure 4.1(a). Thickness and layup of the panel skin, stringer flange and stringer cap are given in Table 1.

Table 4.1. Test panel material, thickness and lay-up.

| Component | Material | Number of layers | Thickness (mm) | Lay-up |
|--------------------|-------------------------------|------------------|----------------|---|
| Skin | T800/3900-2 Graphite/Epoxy | 16 | 2.62 | [45/-45/0/45/90/-45/0/90] _s |
| Stringer Flange | | 32 | 5.41 | [45/-45/0/45/90/-45/0/90] _{2s} |
| Stringer Cap | | 16 | 2.62 | [45/-45/0/45/90/-45/0/90] _s |

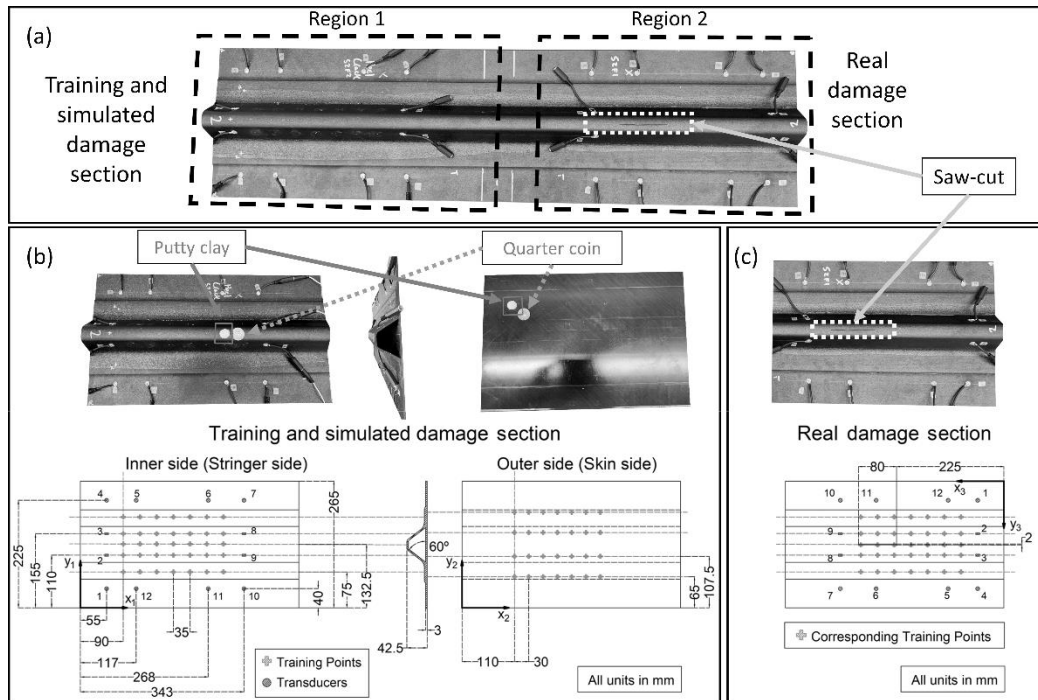


Figure 4.1. (a) Test panel with CNN training section and CNN testing sections; (b) The putty clay next to a quarter, and schematic of PZT transducers, training locations and simulated damage locations; (c) schematic for real saw-cut damage section.

Of interest was to detect and locate damage at the following locations: in the skin, in the stringer's flange, and in the stringer's cap (cap-side and cap-top). Because of the necessity to train and test the results at various locations, these damage scenarios were simulated by hand placing a spot of putty clay smaller than the size of a quarter at the various points (Figure 4.1(b)). The putty clay created a weak scattering of the waves and is often used to simulate damage in UGW tests. In addition to these simulated damage scenarios, the tests included a real damage case of a saw-cut of 80 mm in length at the top of the stringer's cap (Figure 4.1(a) and (c)).

The test panel was divided into two regions. Region 1 (left half in Figure 4.1(a)) was used for the CNN training as well as for the testing with the simulated putty clay defects. Region 2 (right half in Figure 4.1(a)) was used to test the real saw-cut damage in the stringer's cap. In each of the

two regions, a set of twelve PZT transducers (Ceramtec - Sonox P502, 10 mm diameter) were bonded to the inner side of the panel using ambient-cure epoxy adhesive (Loctite from Henkel Corporation, Rocky Hill, CT). The transducers were placed in a sparse array configuration encircling the skin-to stringer region of interest. The transducer configurations in Region 1 and Region 2 were meant to mirror one another, so that the training data from Region 1 could be used in the CNN algorithm with the testing data of Region 2 for the saw-cut damage. The transducer numbering and origin of the geometrical reference system were chosen for each of the two regions to guarantee this equivalency (Figure 4.1(b) and (c)). The transducer array was operated in a full-matrix capture mode that considered all pitch-catch pairs and excluded the pulse-echo signals, hence resulting in a 12×11 matrix of UGW signals captured for each matrix sweep.

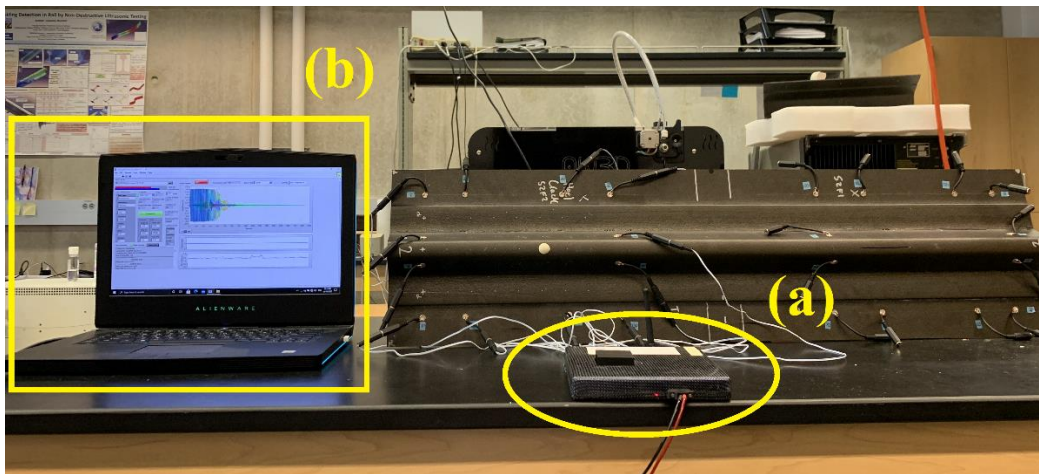


Figure 4.2. The test panel with (a) the wireless device unit for routing the transducers' signals and (b) the host computer laptop.

Shown in Figure 4.2, the signal excitation and acquisition were carried out using a data acquisition system (DAQ) based on an FPGA interface capable of handling 12 independent channels with a sampling rate of 12.5 MHz at 12 bit resolution [50]. This device was connected

wirelessly to a host computer laptop with a LabVIEW interface for further data processing in Matlab®.

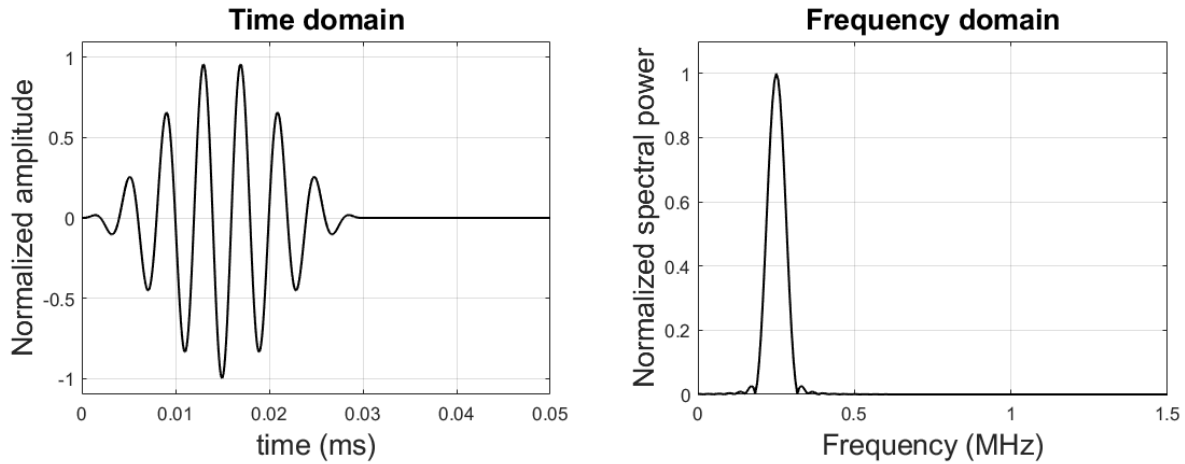


Figure 4.3. Example of the toneburst excitation signal to the PZT transmitters.

The PZT excitation signals were Hanning-windowed sinusoidal tonebursts (Figure 3). In order to provide the CNN analysis with a sufficiently comprehensive dataset, the training signal generations involved sweeping among excitation amplitude, central frequency, and number of toneburst cycles. In particular, the excitation parameters were varied as follows: frequency sweeping in the range of 240 - 280 kHz with 10 kHz intervals (covering the useful frequency range of the PZT transducers), voltage amplitudes of 10 V and 20 V, and number of toneburst cycles ranging from 6.5 to 15.5 (for a total of 100 excitations), and from 6.5 to 30.5 (for a total of 250 excitations) with 1 cycle intervals. In addition to these variables, each pitch-catch waveform was down-sampled by a factor of three, for a three-fold increase in the total available number of data samples.

The CNN was trained by acquiring the 12×11 full-matrix pitch-catch waveforms from the twelve PZT transducers in Region 1 of the panel (left half in Figure 1(a)) by hand placing the

simulated damage (putty clay) on a grid of several points. As shown in Fig. 1b, a training grid of $7 \times 5 = 35$ locations was used on the inner side of the panel to test for stringer-type damage, and a training grid of $7 \times 4 = 28$ locations was used on the outer side of the panel to test for skin-type damage. In both cases, the CNN validation was performed by extracting around one third of the total training data (i.e. 30% validation data sets and 70% training data sets).

Another data group was used to create three kinds of testing sets: (1) testing damage positions that were co-located with the training positions; (2) testing damage positions that were offset from the training positions, and (3) testing the real saw-cut damage. Accordingly, the co-located testing positions for damage in the stringer were some of the training positions in the inner side of Region 1 (Figure 4.1(b)); and the co-located testing positions for the damage in the skin were some of the training positions in the outer side of Region 1 (Figure 4.1(b)). The testing data for the real saw-cut damage were acquired from Region 2 (Figure 4.1(c)) using the training data from Region 1 with the equivalent geometry.

The key steps of the CNN decision model are summarized in Figure 4.4. All three CNN models are data-driven. The data collection step for each of damage positions involves capturing the full-matrix waveforms from the twelve PZT transducers, with sweeping of excitation toneburst amplitude, frequency, and # of cycles. This step is followed by a first pre-processing step where pulse-echo signals are eliminated and only the 12×11 pitch-catch combinations are retained. The waveforms are then concatenated into a single vector to be used as the CNN data input, the dimension is (1, 11088, 1), where the signal dimension is # of points $\times 12 \times 11 = 11088$, and the other two dimensions are set to one. This input vector is fed to a cap decision model to determine whether the data should be associated to damage in the stringer's cap region, or to any of the other cases (pristine, damage in the skin, or damage in the stringer's flange). If the data set is determined

to be associated to damage in the stringer’s cap, the signals are further simplified by eliminating the pitch-catch wave paths that do not cross the stringer, the dimension becoming (1, 70056, 1), where the signal dimension is # of points \times cross-channels = 70056, the other two dimensions are one. After that, the stringer’s cap data is fed through the “Stringer_Cap” model that determines more precisely the damage location (in the cap-side or in the cap-top). On the other hand, data sets not associated to the stringer’s cap are fed to another model that determines the predictions of pristine case, skin damage or stringer’s flange damage (“Pristine-Skin-Stringer_Flange” model).

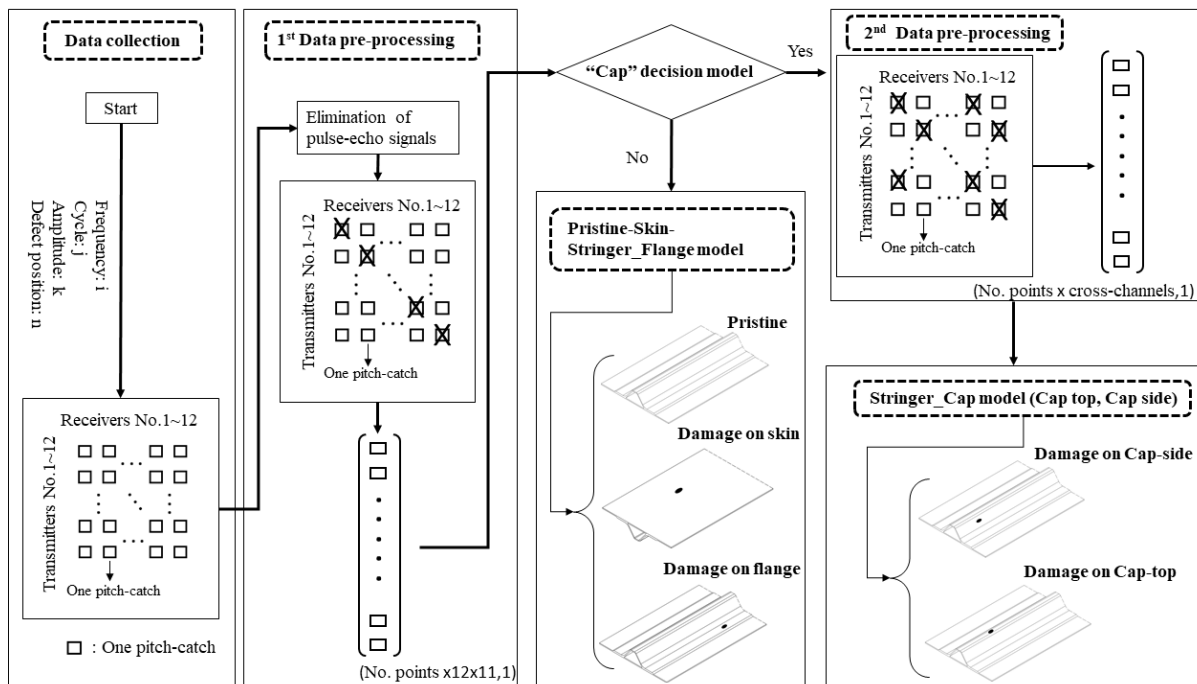


Figure 4.4. Main steps of the CNN decision model.

4.4. Details of the Convolutional Neural Network (CNN) Algorithm

One issue that was considered is the use of a 2D-CNN algorithm versus a 1D-CNN algorithm. In general, concatenating time-history signals in a 1D architecture may cause edge effects. However, in the problem at hand it was more important to track amplitude or phase changes between healthy wave paths and damaged paths. With the 12 PZT transducers used, there were up to $12 \times 11 = 132$ paths (in full-matrix capture). It was expected that each of the paths could provide spatial characteristics to the monitored area, so all paths were concatenated into one vector. An additional concern with 2D-CNNs was that the putty clay used to simulate damage was small, and the resulting signal changes might be comparable to noise levels. Some preliminary analyses were conducted with a 2D-CNN architecture, and obtained imaging results significantly worse than those shown later in the paper with the 1D-CNN. Hence it was ultimately decided to employ a 1D architecture for the results presented in this study.

The structure of the specific CNN algorithm employed in the present study is schematized in Figure 4.5. The fully connected layer has the same size as the softmax-layer and the final categories: 1) the “Cap” decision model yields two categories, 2) the Pristine-Skin-Stringer_Flange model covers 42 damage positions plus one pristine position, 3) the Stringer_Cap model covers 21 damage positions on the Cap region. All three CNN models are trained by the architecture shown in Figure 5. It involves multiple steps aimed at increasing the computational efficiency and accuracy of the damage location predictions. The training fulfillment was done by the Deep Learning Toolbox in Matlab®.

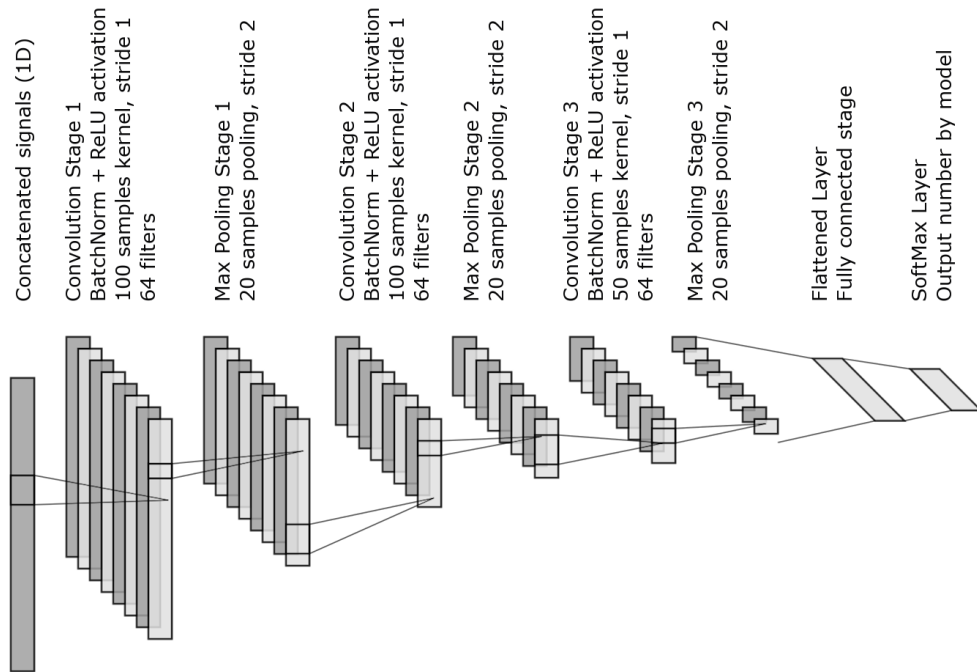


Figure 4.5 Structure of the CNN architecture utilized in the present study.

The specific steps programmed in the algorithm are: (1) Batch Normalization, (2) Nonlinear Activation Function, (3) Minibatches, (4) L2-Norm Regularization, and (5) Adaptive Moment Estimation (ADAM).

Batch Normalization forces the weights in the deeper layers of the CNN to be more robust to changes in the earlier layers. When the input data change, even if the ground truth or the true solutions of the objective function stay the same, the network will change accordingly (covariate shift). Batch normalization will reduce the effects of the covariate shift. It also weakens the coupling between the functionalities of earlier layers and those of the deeper layers, allowing each layer of the network to relatively learn by itself, effectively speeding up learning through the whole

network. In this study, batch normalization was applied before the activation functions [36] to help learning by the central hidden layers.

The Nonlinear Activation Function assists the training algorithm to learn sophisticated nonlinear features from the input beyond the linear region. This study used a Rectified Linear Unit (ReLU) activation function which helps gradients to be either 1 (if input is positive) or 0 (if input is negative or zero), further speeding up the learning algorithm [37]. In addition, the softmax activation function was utilized to perform the multi-class classification needed for the different damage scenarios. The length of the softmax layer was equal to the number of classes to be identified. Accordingly, the outputs of the softmax layer showed each class's probability based on the given training set.

$$a_i^{[l]} = \frac{e^{(z_i^{[l]})}}{\sum_i^N e^{(z_i^{[l]})}} \quad (4.1)$$

where $a_i^{[l]}$ is the probability of the i -th class for the given training set, N is the total number of classes, and $Z_i^{[l]}$ is the prediction from the l -th layer and the i -th unit.

The use of Minibatches is commonly implemented in DL algorithms. Since traditional batch learning must consider all training examples for every cost (forward) and gradient (backward) calculation, resulting in high computational cost, the application of minibatches (i.e. small sections of the whole training data) allows to monitor the progress of the trained model in considerably less time. This study utilized the Minibatch Gradient-Descent (MGD) algorithm that outperforms the Stochastic Gradient Descent (SGD), that is known to produce large oscillation when the process is approaching the optima. The oscillation effects of the MGD were minimized using an optimization algorithm discussed next. The study used 16 and 32 minibatch sizes to keep the power of 2 benefits within the computation limits of the GPU memory utilized (8 GB) [38].

L2-Norm Regularization was another step employed to reduce the variance issue, the so-called overfitting problem. This step prevents data overfitting by adding additional terms to penalize the weight matrices from being too large. However, if the regularization factor is too large, it will force the weight matrices close to zero, basically penalizing the hidden units and potentially leading to a high bias issue (underfitting). This study used an L2 regularization factor of 0.001.

The last step adopted is the Adaptive Moment Estimation (ADAM) optimization. This method minimizes the oscillations resulting in short training time [39]. It combines the advantages of the adaptive SGD algorithm [54] and the RMSProp algorithm [41,42] to push the boundary of the Gradient Descent method with less memory requirement and faster speed when approaching the optima. The fundamental update rules of the ADAM algorithm used here were:

$$V_{d\theta,t} \leftarrow \beta_1 V_{d\theta,(t-1)} + (1 - \beta_1) d\theta_t \quad (4.2)$$

$$S_{d\theta,t} \leftarrow \beta_2 S_{d\theta,(t-1)} + (1 - \beta_2) d\theta_t^2 \quad (4.3)$$

In the above relations: V is the first-moment vector (initialized at 0); S is the second-moment vector (also initialized at 0); β_1 is the hyperparameter that smooths out the gradient descent path toward the optima (0.9 chosen in the present study [39]); β_2 is the hyperparameter that applies the weighted averages to smooth out the second moments (0.99 chosen in the present study corresponding to ~ 100 averages applied per update[43,44]); t is the iteration step; θ is the optimizing parameter; and $d\theta_t$ is the gradient of parameter θ for iteration step t . Averaging from the first and the second moments avoids large oscillations during the training process. However, averages also cause an issue of initial bias in the model. To avoid the initial bias issue, the following corrected update versions were utilized [39]:

$$V_{d\theta}^{corrected} \leftarrow \frac{V_{d\theta}}{1 - \beta_1^t}, \quad S_{d\theta}^{corrected} \leftarrow \frac{S_{d\theta}}{1 - \beta_2^t} \quad (4.4)$$

Finally, the following numerical stabilization was employed in the final ADAM version:

$$\theta_t \leftarrow \theta_{t-1} - \alpha \frac{V_{d\theta,t}^{corrected}}{\sqrt{S_{d\theta,t}^{corrected} + \varepsilon}} \quad (4.5)$$

where $\varepsilon = 10^{-8}$ and α is the learning rate.

4.5. Results

4.5.1. Simulated damage positions co-located with training positions

4.5.1.1. Using the CNN decision model

As shown in the schematic of Figure 4.6, four different cases of simulated damage co-located with the training positions were tested, namely: damage in the skin – test point (a); damage in the stringer’s flange – test point (b); damage in the stringer’s cap top – test point (c); and damage in the stringer’s cap side – test point (d). As many as 100 different tests were performed for each location, resulting in 300 different testing samples after the 1:3 downsampling.

Plots (a)-(d) in Figure 4.6 show the damage location results predicted by the CNN classification using the toneburst excitation of 10 V in amplitude, 250 kHz in central frequency, and 6.5 cycles in duration. The red squares correspond to the “ground truth” - true location of the damage (simulated by the putty). The gray scale values correspond to the likelihood of the damage as predicted by the algorithm, with the white value corresponding to 0% confidence and the black value corresponding to 100% confidence. The damage in the skin (test point (a) in Figure 4.6(a)) is predicted with a 91.7% confidence at the true damage location. The damage in the stringer’s flange (test point (b) in Figure 4.6(b)) is predicted with a 69.7% confidence at the true damage location. It can be seen in Figure 4.6(b) that an adjacent point is also predicted with a confidence of 21.1%, and a couple of other locations on the other side of the stringer are also slightly appearing.

Although these spurious points are predicted with substantially lower confidence than the correct location, they reflect the challenges associated with locating damage in the stringer with transducers located solely on the skin.

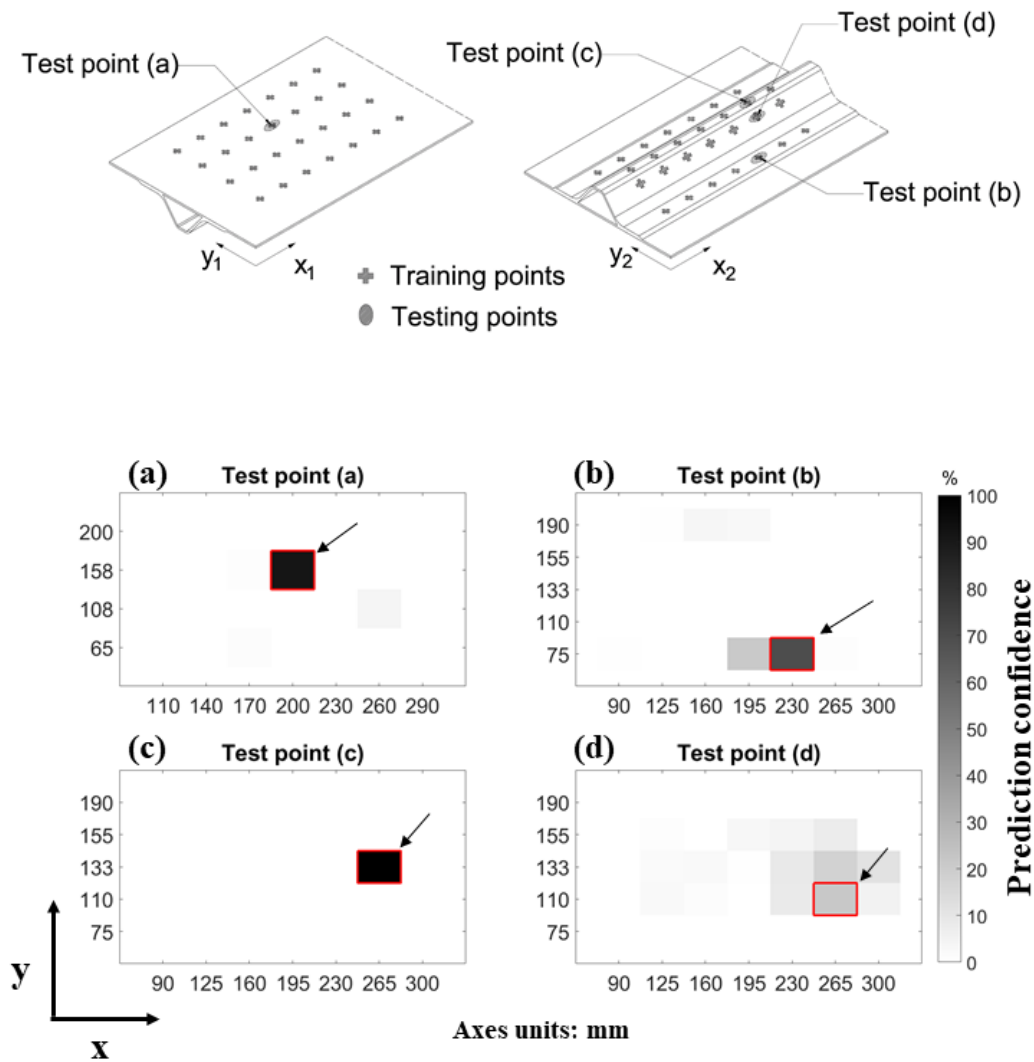


Figure 4.6. CNN prediction of damage locations co-located with training locations for excitation toneburst with 10 V amplitude, 250 kHz central frequency, and 6.5 cycles.

Remarkably, the damage in the stringer's cap (test point (c) in Figure 4.6(c)) is correctly predicted at the true damage location with a 99.9% confidence, with no spurious predictions being generated in this case. The excellent detection of this stringer defect in a location quite remote from the skin is one of the most encouraging results of the data-driven CNN algorithm. As for the damage in the stringer's cap side (test point (d) in Figure 4.6(d)), the prediction yields a correct location (along with some less remarkable spurious locations), but only with 21.8% confidence due to the challenging position of this defect.

Plots (a)-(d) in Figure 4.7 show the damage location results predicted using a toneburst excitation that is nearly twice in energy as the previous one, specifically 10 V in amplitude, 250 kHz in central frequency, and 15.5 cycles in duration. It can be seen that the increased excitation energy generally improves the accuracy of the damage prediction locations, as a larger amount of wave energy penetrates into the stringer. In particular, this case confirms the excellent location accuracy for the skin damage (test point (a) in Figure 4.7(a)) and the stringer's cap damage (test point (c) in Figure 4.7(c)). The high energy excitation also improves the location accuracy for the stringer's flange damage (test point (b) in Figure 4.7(b), located correctly with a 99.8% confidence vs. the previous 69.7% confidence), and the stringer's cap side damage (test point (d) in Figure 4.7(d), located correctly with an 84.6% confidence vs. the previous 21.8% confidence). The spurious location predictions that were present with the lower energy excitation are also greatly reduced with the higher energy excitation.

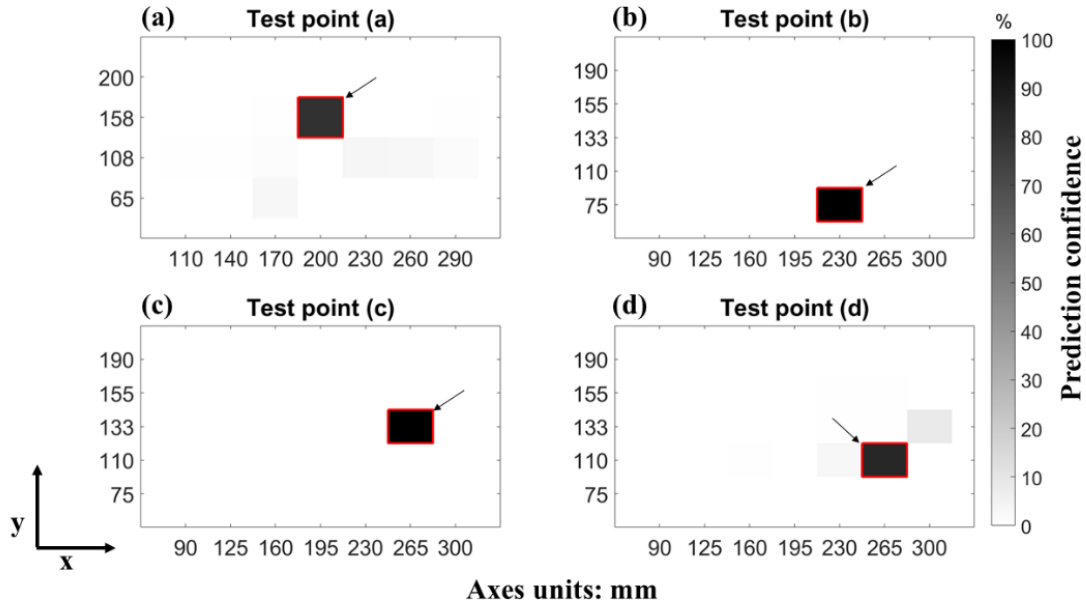


Figure 4.7. CNN prediction of damage locations co-located with training locations for excitation toneburst with 10 V amplitude, 250 kHz central frequency, and 15.5 cycles.

The last results shown in Figure 4.8 were obtained by combining all of the excitation cases that were used in the training phase. This combination was made by incoherently summing the prediction confidence plots obtained from each excitation. Figure 4.8 indicates that an excellent location prediction is obtained with the combined excitations for all of the damage cases. For the first three cases (Figure 4.8(a) through (c)), the damage is almost exclusively identified at the true location. For the stringer's cap side damage (Figure 4.8(d)), some less likely locations appear next to the true damage location that is nevertheless correctly identified with the highest prediction confidence. Moreover, the surrounding less likely locations indicate that the closer the distance, the deeper the connection.

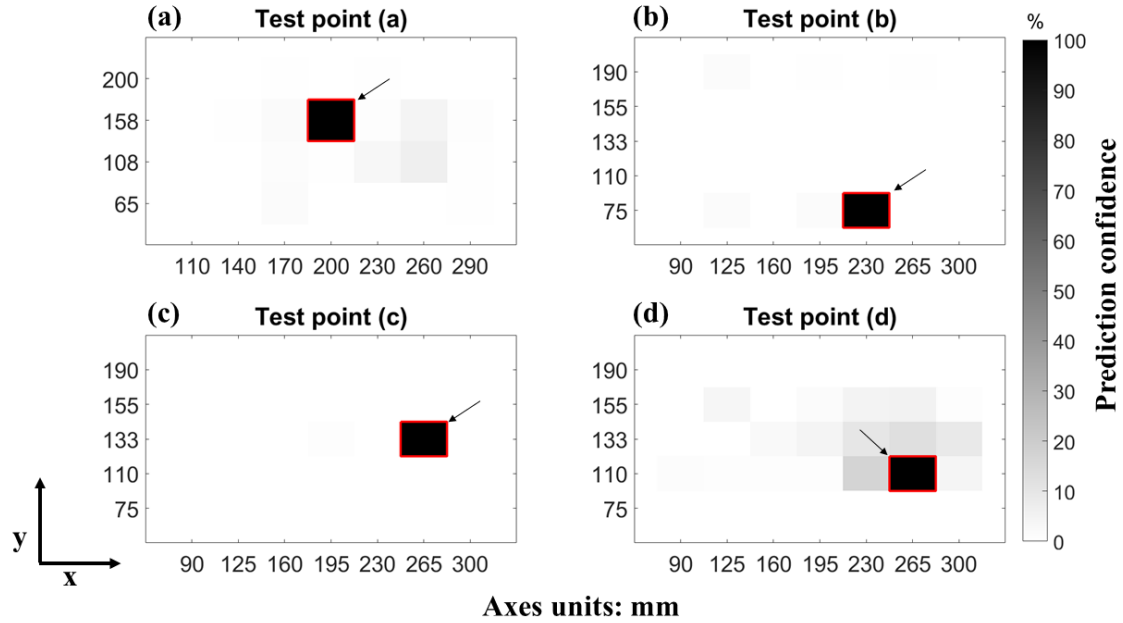


Figure 4.8. CNN prediction of damage locations co-located with training locations when summing all excitation toneburst cases.

4.5.1.2. Comparison with traditional imaging algorithm (RAPID)

In this section we present comparative results using the Reconstruction Algorithm for Probabilistic Inspection of Damage (RAPID) [14] method. The advantages of the RAPID method over time-of-flight based imaging is the elimination of the need for wave speed values, which should be a considerable advantage when probing the complex test piece at hand. RAPID is a tomography algorithm based on the following factors:

1. A sparse distribution of the transducers, resulting in a pitch-catch configuration which allows recording the propagated wave through the structure and its variation when it interferes with a defect present in the propagation path, or its influence zone.
2. A damage index (DI_{ij}) obtained from the feature-extraction analysis of the signals coming from two different damage states of the plate.

3. An elliptical distribution (E_{ij}), whose size is controlled by a β parameter, that weights the damage index from the signals depending on the distance from the calculated pixel of the image (x_p, y_p) to the direct path of propagation.

In this case, the DI will be calculated using the signals from pristine state ($\mathbf{s}_{baseline}$) and the signals from damage state ($\mathbf{s}_{damaged}$), through the SSM indicator (6):

$$DI_{ij} = \frac{1}{nT} \int_0^{nT} (\mathbf{s}_{damaged}(t) - \mathbf{s}_{baseline}(t))_{ij}^2 dt \quad (4.6)$$

The effectiveness of this indicator relies on variations both in amplitude and in phase, causing area shifting when the integration is performed. Once the DI is calculated for every transmitter-receiver pair of transducers, a final summation $P(x_p, y_p)$ is performed through (7)(8)(9)(10), where RD_{ij} and R_{ij} are the geometrical factors which regulate the size of the ellipse and, consequently, the influence of each transmitter-receiver path:

$$RD_{ij}(x_p, y_p) = \frac{\sqrt{(x_p - x_i)^2 + (y_p - y_i)^2} + \sqrt{(x_p - x_j)^2 + (y_p - y_j)^2}}{\sqrt{(x_j - x_i)^2 + (y_j - y_i)^2}} \quad (4.7)$$

$$R_{ij}(x_p, y_p) = \begin{cases} RD_{ij}(x_p, y_p) & \text{if } RD_{ij}(x_p, y_p) < \beta \\ \beta & \text{if } RD_{ij}(x_p, y_p) \geq \beta \end{cases} \quad (4.8)$$

$$E_{ij}(x_p, y_p) = \left[\frac{\beta - R_{ij}(x_p, y_p)}{\beta - 1} \right] \quad (4.9)$$

$$P(x_p, y_p) = \sum_{i=1}^N \sum_{j=1, j \neq i}^N DI_{ij} E_{ij}(x_p, y_p) \quad (4.10)$$

Figure 4.9 shows the results for the same co-located points (a)(b)(c) and (d). Compared to the results from the CNN architecture in Figures 4.6-4.8, the RAPID images clearly offer a worse performance. The true damage locations are not properly identified, and several false positives also appear. This comparison reaffirms the superior performance of the proposed deep learning architecture to handle the material and geometrical complexities of the test piece at hand.

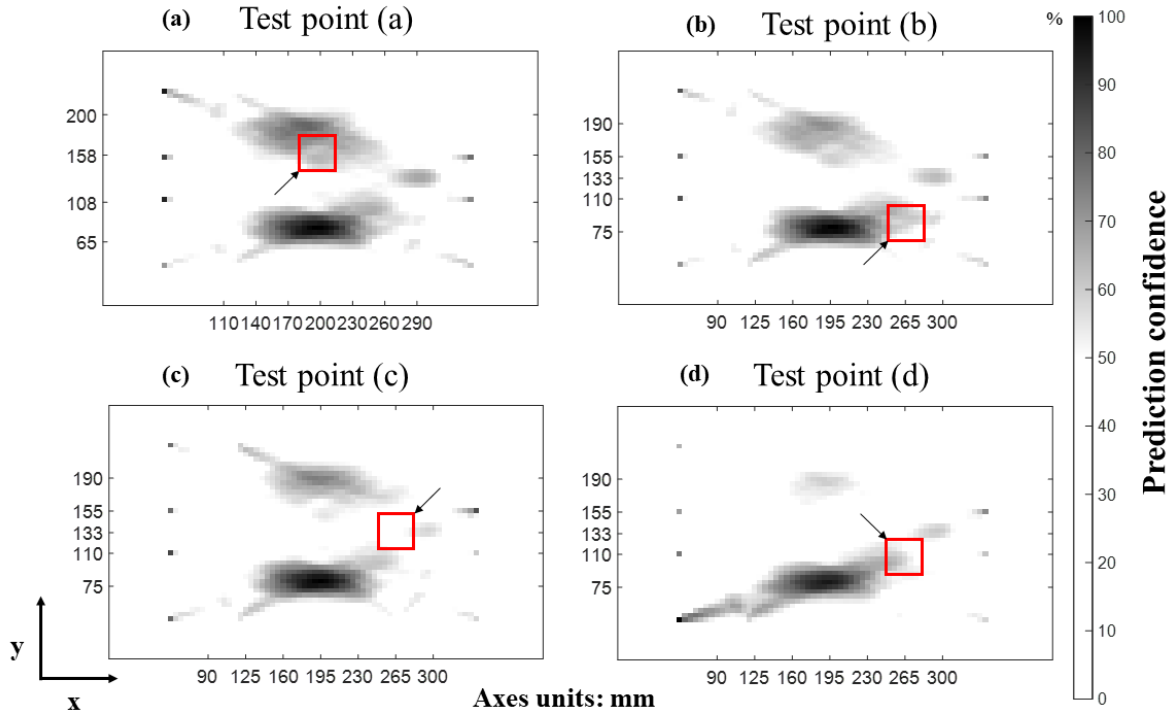


Figure 4.9 RAPID prediction of damage locations co-located with training locations.

4.5.2. Results: simulated damage positions offset from training positions

By exploiting generalization abilities of the CNN algorithm, tests were carried out to predict damage locations that were slightly offset from the training locations (not co-located). The expected outcome was an increased location prediction confidence for test positions that were closer to the training positions, and a lower location confidence for test positions that were further away from the training positions.

As shown in the schematic of Figure 4.10, the offset damage was placed in the same general locations discussed in Sections 4.3 and 4.5, and specifically: damage in the skin – test point (e); damage in the stringer’s flange – test point (f); damage in the stringer’s cap top – test point (g); and damage in the stringer’s cap side – test point (h).

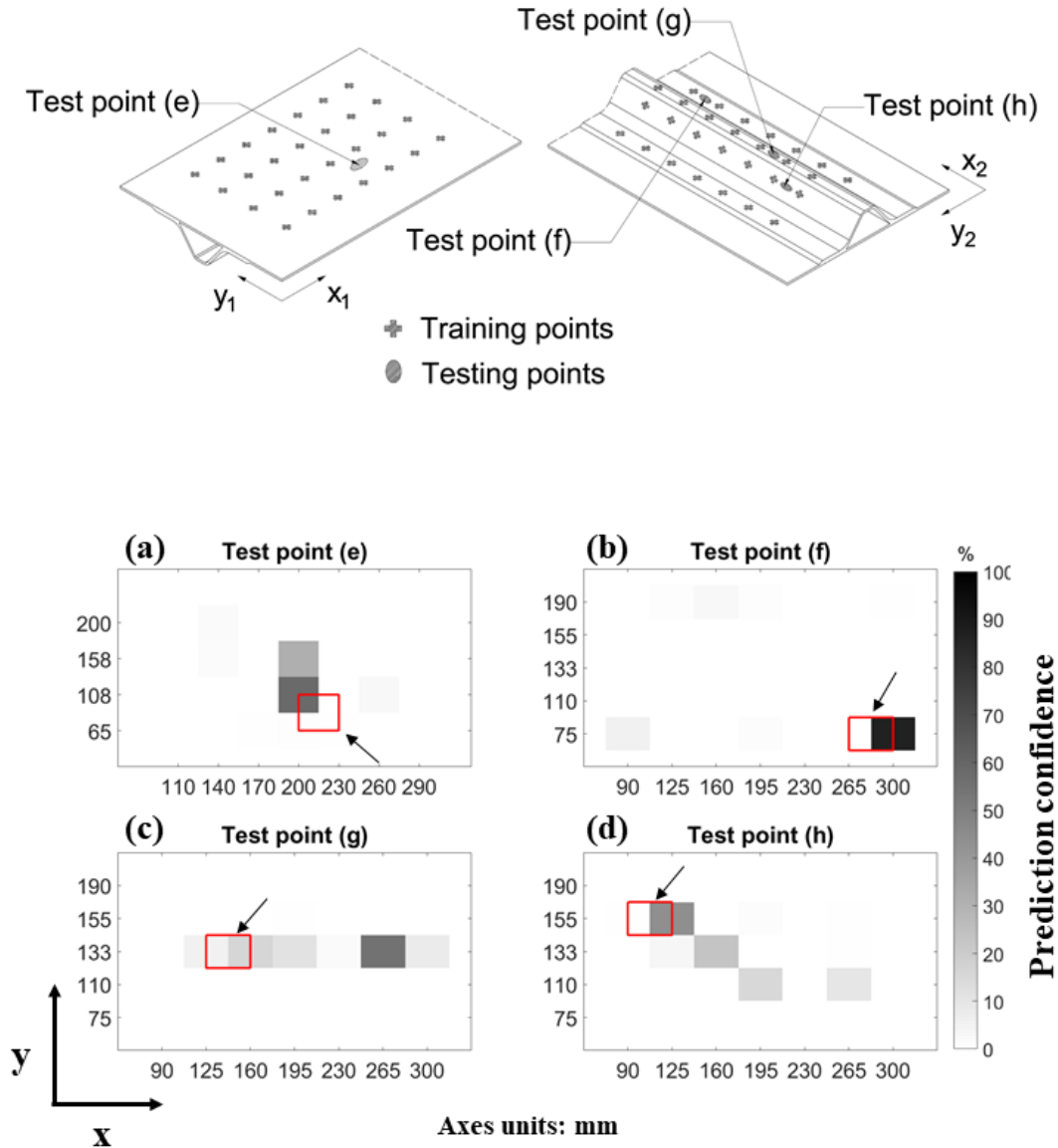


Figure 4.10. CNN prediction of damage locations offset from training locations for excitation toneburst with 10 V amplitude, 250 kHz central frequency, and 6.5 cycles.

Plots (a)-(d) in Figure 4.10 show the CNN location predictions for the four offset damage cases when using the excitation toneburst of 10V in amplitude, 250 kHz in central frequency, and 6.5 cycles in duration. In some cases, the offset damage gives similar or even improved results compared to the corresponding co-located damage from Figure 4.6. For example, the location

prediction confidence for the offset stinger's flange damage (test point (f) in Figure 4.10(b)) is 86.93% compared to 69.7% for the co-located stinger's flange damage (Figure 4.6(b)). Similarly, the prediction confidence for the offset stinger's cap side (test point (h) in Figure 4.10(d)) is 44% compared to 21% of the co-located damage (Figure 4.6(d)). In the other two cases, the offset performance degrades: the prediction confidence for the offset skin damage (test point (e) in Figure 4.10(a)) is 58.42% compared to 91.7% of the co-located skin damage (Figure 4.6(a)); and the offset stinger's cap damage (test point (g) in Figure 4.10(c)) is predicted at an erroneous location (although still identified in the general stinger's cap area). It will be shown in the next figure that these results can be further improved by using a higher energy excitation signal.

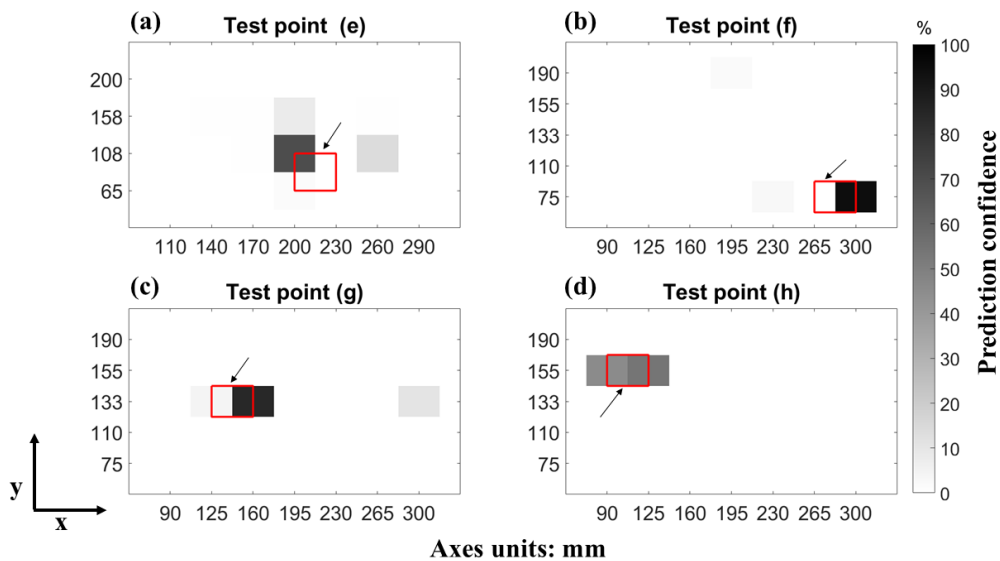


Figure 4.11. CNN prediction of damage locations offset from training locations for excitation toneburst with 10 V amplitude, 250 kHz central frequency, and 15.5 cycles.

This improvement is clearly seen in Figure 4.11 obtained using the high energy excitation toneburst with 10 V in amplitude, 250 kHz in central frequency, and 15.5 cycles in duration. Correct locations are predicted with high confidence in all of the offset damage cases considered, with few or no spurious predictions. This confirms the generalization ability of the CNN algorithm

that does not necessarily require testing cases exactly matching the training cases. The results in Figure 4.11 actually resemble the corresponding predictions made for the damage co-located with the training grid in Figure 4.7. For example, the offset skin damage (test point (e) in Figure 4.11(a)) is correctly located with 70% confidence. The offset damage in the stringer's flange (test point (f) in Figure 4.11(b)) is also correctly located with a 94.7% confidence. And the offset damage in the stringer's cap top (test point (g) in Figure 4.11(c)), that was located incorrectly with the lower energy excitation, is now located correctly. The higher energy excitation helps the wave penetration into the stringer, and hence the improved performance in this region.

The prediction results for the offset damage obtained by combining the multiple excitations are shown in Figure 4.12. As found in the case of the co-located damage (Figure 4.8), the combined results generally improve the confidence in the correct damage location predictions, and decrease the likelihood of spurious locations away from the true damage locations.

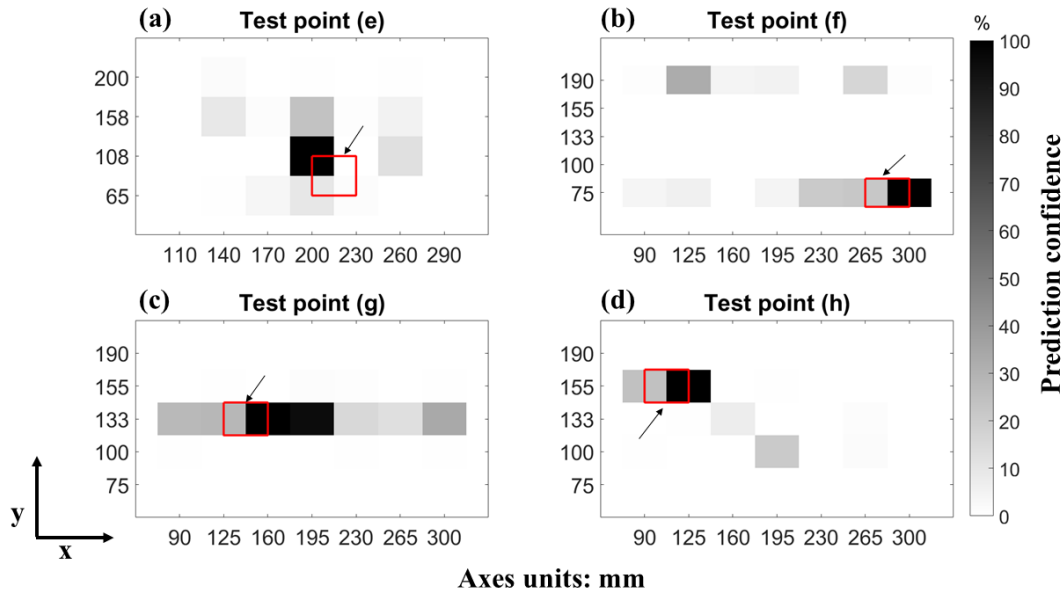


Figure 4.12. CNN prediction of damage locations offset from training locations when summing all excitation toneburst cases.

4.5.3. Results: saw-cut damage in stringer cap

Damage predictions for the case of the real saw-cut in the stringer cap are shown in Figure 4.13. In this case, as shown previously in Figure 4.1(a) and Figure 4.1(c), the testing signals were acquired from Region 2 of the test panel and the training signals were acquired from Region 1 of the panel.

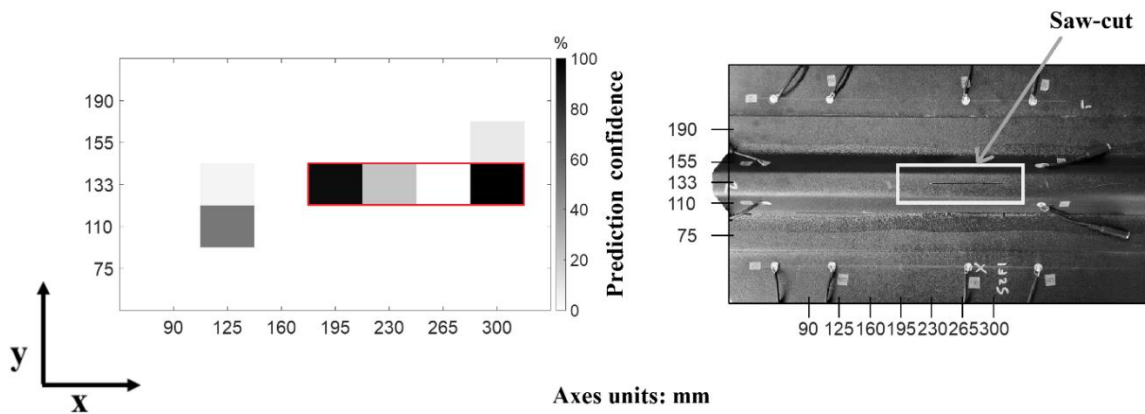


Figure 4.13. CNN prediction of location of real saw-cut damage in stringer's cap when summing all excitation toneburst cases.

The prediction results in Figure 4.13, obtained by using the full set of excitation signals, show that the ends of the saw-cut are correctly located with very high confidence (94.72% for the left end and 100% for the right end). The correct location of the cut ends underscores the importance of wave scattering phenomena, that are the basic defect detection mechanisms exploited by the sparse UGW transducer array. The less scattering inner portion of the saw-cut is less visible in the predictions. Accurately locating the saw-cut ends provides a reliable estimate of the size of the cut. These encouraging results suggest the potential for the proposed DL CNN architecture to accurately locate structural damage that is of a very different nature as that utilized to train the system (putty clay). Hence the suggestion is that the given training data can be generalized to a larger variety of damage in this kind of structures. Finally, it is quite encouraging

to confirm the ability to detect and locate damage deep into the stringer by using PZT transducers located solely on the skin.

4.6. Results: classification performance evaluation

This section provides a quantitative evaluation of the fitness of the proposed CNN algorithm for damage localization. This analysis was performed for the eight cases of putty-clay simulated damage discussed in the previous Section 4.5.1 (damage co-located with the training positions) and Section 4.5.2 (damage offset from training positions).

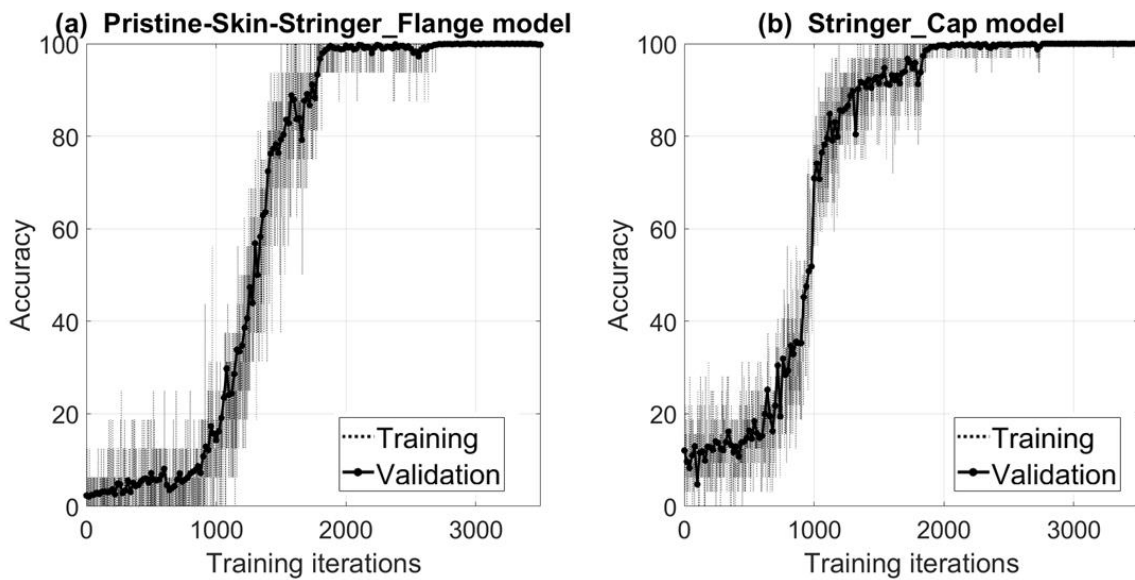


Figure 4.14. Training accuracy and validation accuracy versus training iterations for (a) the Pristine-Skin-Stringer_Flange model and (b) the Stringer_Cap model.

Figure 4.14 plots the training accuracy and the validation accuracy of the Pristine-Skin-Stringer_Flange model (Figure 4.14(a)) and that of the Stringer_Cap model (Figure 4.14(b)) as a

function of training iterations. As a reminder, the ratio between the number of validation data and that of training data was approximately 1:2. The ratios of training data for pristine, skin and stringer flange were 1:1:1. The ratio of training data between the cap top region and the cap side region was 10:1. It can be seen that in both plots of Figure 4.14 the training accuracy follows well the validation accuracy, which confirms the goodness of the proposed models with little or no overfitting issues. The final accuracy results are also quite encouraging, with 100% final training accuracy for both models, and 99.86% and 99.97% final validation accuracies for the Pristine-Skin-Stringer_Flange model and the Stringer_Cap model, respectively.

The next metrics considered were the percentages of Precision, Recall and F1-score. These are defined in the following relations according to known ML considerations. Essentially, the Precision tracks the false positives, the Recall tracks the false negatives, and the F1-score combines the prior two metrics. A perfect prediction would have Precision, Recall and F1-score all equal to 100%.

$$\left\{ \begin{array}{l} \text{Precision (\%)} = \frac{\sum(\text{true positives})}{\sum(\text{true positives}) + \sum(\text{false positives})} \times 100 \\ \text{Recall (\%)} = \frac{\sum(\text{true positives})}{\sum(\text{true positives}) + \sum(\text{false negatives})} \times 100 \\ \text{F1-score (\%)} = \frac{1}{\frac{1}{2} \times \left(\frac{100}{\text{Precision(\%)}} + \frac{100}{\text{Recall(\%)}} \right)} \end{array} \right. \quad (4.11)$$

These metrics were computed for each of the eight simulated damage cases discussed in Sections 4.5.1 and 4.5.2, and considering the entire set of toneburst excitations. For each case, the panel location with the largest confidence from the CNN model was considered the final prediction. These results were then compared to the true damage locations to calculate true positives, false positives and false negatives.

Table.4.2 shows Precision, Recall, and F1-score for the eight damage cases. It can be seen that the Precision score is quite high for all of the damage locations, whether the damage is co-located with or offset from the training locations, with all cases resulting in a Precision score higher than 90% and many yielding a score of 100%. The Recall score is also higher than 80% in most of the damage cases, and close to 100% for some. The lowest Recall score of 43% is found for the stringer’s cap top damage in the offset location. This is not unexpected due to the aforementioned challenge for the skin-generated waves to penetrate deep into the stringer. The comprehensive F1-score metric in the last column of Table 4.2 summarizes the system’s performance. The overall result is quite encouraging. The marginal performance for the offset damage in the stringer’s cap top (F1 of 59.3%) is substantially improved for the co-located damage in the same location (F1 of 99.7%). The second lowest performance is for the co-located stringer’s cap side damage (F1 of 72%). All of the other damage cases have an F1-score above 84%, with many above 95%.

Table 4.2. CNN classification performance for the eight simulated damage cases using all excitation tonebursts.

| | Damage location | Precision (%) | Recall (%) | F1-score (%) |
|---|---------------------------|---------------|------------|--------------|
| Damage co-located with training positions | Test point (a) (skin) | 100.00 | 98.00 | 98.99 |
| | Test point (b) (flange) | 91.84 | 99.00 | 95.28 |
| | Test point (c) (cap top) | 100.00 | 99.47 | 99.73 |
| | Test point (d) (cap side) | 100.00 | 83.72 | 72.00 |
| Damage offset from training positions | Test point (e) (skin) | 100.00 | 82.00 | 90.11 |
| | Test point (f) (flange) | 100.00 | 73.00 | 84.39 |
| | Test point (g) (cap top) | 93.54 | 43.46 | 59.35 |
| | Test point (h) (cap side) | 99.85 | 98.70 | 99.27 |

4.7. Discussion and Conclusions

This paper has addressed the detection and localization of damage in a realistic skin-to-stringer composite panel typical of modern aircraft construction. For this kind of complex part, physics-based methods of damage imaging via ultrasonic guided waves can be very challenging. This work utilizes a data-driven technique based on the latest developments in Deep Learning (DL) and Convolutional Neural Networks (CNNs). A specific CNN has been designed for this application. The classification algorithm includes Batch Normalization, Minibatches, L2-Norm Regularization and ADAM optimization to enhance the performance of both training phases and testing phases.

The algorithm is tested on various damage scenarios that are relevant to this structure, including some damage locations that are co-located with the training locations and some damage locations that are offset from the training locations. The generalization abilities of the CNN algorithm are exploited to detect the damage scenarios that are different from the training scenarios, including a real saw-cut in the stringer's cap. Damage regions of interest were the panel's skin region, the stringer's flange region and the stringer's cap region. To increase accuracy, the algorithm utilizes two different classification models to separate the skin and stringer's flange damage from the stringer's cap damage. Several results are presented showing a promising damage prediction performance. The stringer's region, that is notoriously very hard to access by ultrasonic wave transducers located solely on the skin, can also be probed with reasonable accuracy. The saw-cut in the stringer's cap, for example, is imaged very accurately. Good results are also shown for damage that is offset from the training locations, further highlighting the generalization abilities of the classification algorithm.

The results indicate that the damage imaging performance depends on the type of signal excitation utilized for the PZT transmitters. As expected, higher-energy excitations generally improve the damage imaging performance, especially for the stringer's region that benefits from the stronger wave penetration from the skin. Damage classification performance metrics are given for a selected combination of excitation signals. These metrics will likely change for a different part or different damage scenarios. Currently, the study only considers "fixed" laboratory conditions without involving temperature changes, structural changes and sensor network changes. Future research should consider the effects of these factors and possibly examine an appropriate transfer learning scheme able to compensate for these changes.

4.8. Acknowledgments

This work was funded in part by the US Federal Aviation Administration Joint Center of Excellence for Advanced Materials (FAA Cooperative Agreement 12-C-AM-UCSD) and by the US Federal Railroad Administration (contract # 693JJ619C000008). Guillermo Azuara also acknowledges the Ph.D. Study Abroad Program of the Universidad Politécnica de Madrid that funded his stay at UCSD for the conduction of this research.

Chapter 4 is, in full, a reprint of material accepted for publication in Cui, Ranting, Guillermo Azuara, Francesco Lanza di Scalea, Eduardo Barrera. "Damage Imaging in Skin-Stringer Composite Aircraft Panel by Ultrasonic Guided Waves Using Deep Learning with Convolutional Neural Network." *Structural Health Monitoring*, June 2021. The dissertation author was the primary investigator and author of this paper.

4.9. References

- [1] Staszewski W, Boller C, Tomlinson GR. Health monitoring of aerospace structures: smart sensor technologies and signal processing. John Wiley & Sons; 2004.
- [2] Giurgiutiu V. Structural health monitoring: with piezoelectric wafer active sensors. Elsevier; 2007.
- [3] Ihn JB, Chang FK. Pitch-catch active sensing methods in structural health monitoring for aircraft structures. *Struct Heal Monit* 2008;7:5–19. <https://doi.org/10.1177/1475921707081979>.
- [4] Ostachowicz W, Kudela P, Krawczuk M, Zak A. Guided waves in structures for SHM: the time-domain spectral element method. John Wiley & Sons; 2011.
- [5] Mal A, Ricci F, Samajder H, Baid H. NDE of composite structures using ultrasonic guided waves. *Heal. Monit. Struct. Biol. Syst.* 2013, vol. 8695, International Society for Optics and Photonics; 2013, p. 86950E.
- [6] Yuan F-G. Structural health monitoring (SHM) in aerospace structures. Woodhead Publishing; 2016.
- [7] Mitra M, Gopalakrishnan S. Guided wave based structural health monitoring: A review. *Smart Mater Struct* 2016;25:53001.
- [8] Matt H, Bartoli I, Lanza di Scalea F. Ultrasonic guided wave monitoring of composite wing skin-to-spar bonded joints in aerospace structures. *J Acoust Soc Am* 2005;118:2240–52. <https://doi.org/10.1121/1.2033574>.
- [9] Yan J, Downey A, Chen A, Laflamme S, Hassan S. Capacitance-based sensor with layered carbon-fiber reinforced polymer and titania-filled epoxy. *Compos Struct* 2019;227:111247.
- [10] Harley JB, Moura JMF. Data-driven matched field processing for Lamb wave structural health monitoring. *J Acoust Soc Am* 2014;135:1231–44. <https://doi.org/10.1121/1.4863651>.
- [11] Flynn EB, Todd MD. Optimal placement of piezoelectric actuators and sensors for detecting damage in plate structures. *J Intell Mater Syst Struct* 2010;21:265–74.
- [12] Ebrahimkhanlou A, Dubuc B, Salamone S. Damage localization in metallic plate structures using edge-reflected lamb waves. *Smart Mater Struct* 2016;25:85035.
- [13] Flynn EB, Todd MD, Wilcox PD, Drinkwater BW, Croxford AJ. Maximum-likelihood estimation of damage location in guided-wave structural health monitoring. *Proc R Soc A Math Phys Eng Sci* 2011;467:2575–96.
- [14] Zhao X, Gao H, Zhang G, Ayhan B, Yan F, Kwan C, Rose J. Active health monitoring of an aircraft wing with embedded piezoelectric sensor/actuator network: I. Defect detection,

- localization and growth monitoring. *Smart Mater Struct* 2007;16:1208–17. <https://doi.org/10.1088/0964-1726/16/4/032>.
- [15] Azuara G, Barrera E, Ruiz M, Bekas D. Damage Detection and Characterization in Composites Using a Geometric Modification of the RAPID Algorithm. *IEEE Sens J* 2019;20:2084–93.
- [16] Azuara G, Barrera E. Influence and compensation of temperature effects for damage detection and localization in aerospace composites. *Sensors (Switzerland)* 2020;20:1–18. <https://doi.org/10.3390/s20154153>.
- [17] Wang CH, Rose JT, Chang F-K. A synthetic time-reversal imaging method for structural health monitoring. *Smart Mater Struct* 2004;13:415.
- [18] Sternini S, Pau A, Di Scalea FL. Minimum-Variance Imaging in Plates Using Guided-Wave-Mode Beamforming. *IEEE Trans Ultrason Ferroelectr Freq Control* 2019;66:1906–19.
- [19] Goodfellow I, Bengio Y, Courville A, Bengio Y. *Deep learning*. vol. 1. MIT press Cambridge; 2016.
- [20] Khan S, Yairi T. A review on the application of deep learning in system health management. *Mech Syst Signal Process* 2018;107:241–65. <https://doi.org/10.1016/j.ymssp.2017.11.024>.
- [21] Abbas N, Nasser Y, El Ahmad K. Recent advances on artificial intelligence and learning techniques in cognitive radio networks. *EURASIP J Wirel Commun Netw* 2015;2015:174.
- [22] Ince T, Kiranyaz S, Eren L, Askar M, Gabbouj M. Real-Time Motor Fault Detection by 1-D Convolutional Neural Networks. *IEEE Trans Ind Electron* 2016;63:7067–75. <https://doi.org/10.1109/TIE.2016.2582729>.
- [23] Helbing G, Ritter M. Deep Learning for fault detection in wind turbines. *Renew Sustain Energy Rev* 2018;98:189–98. <https://doi.org/10.1016/j.rser.2018.09.012>.
- [24] Ebrahimkhanlou A, Salamone S. Single-sensor acoustic emission source localization in plate-like structures using deep learning. *Aerospace* 2018;5:50.
- [25] Melville J, Alguri KS, Deemer C, Harley JB. Structural damage detection using deep learning of ultrasonic guided waves. *AIP Conf. Proc.*, vol. 1949, AIP Publishing LLC; 2018, p. 230004.
- [26] De Marchi L. Sparse signal processing and deep learning for guided waves NDT and SHM. *Proc. Meet. Acoust. ICU*, vol. 38, Acoustical Society of America; 2019, p. 55017.
- [27] Ewald V, Groves RM, Benedictus R. DeepSHM: a deep learning approach for structural health monitoring based on guided Lamb wave technique. *Sensors Smart Struct. Technol. Civil, Mech. Aerosp. Syst.* 2019, vol. 10970, International Society for Optics and Photonics; 2019, p. 109700H.

- [28] Song H, Yang Y. Noncontact super-resolution guided wave array imaging of subwavelength defects using a multiscale deep learning approach. *Struct Heal Monit* 2020;1475921720942958.
- [29] Li Y, Xu K, Li Y, Xu F, Ta D, Wang W. Deep Learning Analysis of Ultrasonic Guided Waves for Cortical Bone Characterization. *IEEE Trans Ultrason Ferroelectr Freq Control* 2020.
- [30] Chua LO, Roska T. The CNN paradigm. *IEEE Trans Circuits Syst I Fundam Theory Appl* 1993;40:147–56.
- [31] Salamon J, Bello JP. Deep convolutional neural networks and data augmentation for environmental sound classification. *IEEE Signal Process Lett* 2017;24:279–83.
- [32] Kiranyaz S, Ince T, Gabbouj M. Real-time patient-specific ECG classification by 1-D convolutional neural networks. *IEEE Trans Biomed Eng* 2015;63:664–75.
- [33] Abdeljaber O, Avci O, Kiranyaz S, Gabbouj M, Inman DJ. Real-time vibration-based structural damage detection using one-dimensional convolutional neural networks. *J Sound Vib* 2017;388:154–70. <https://doi.org/10.1016/j.jsv.2016.10.043>.
- [34] Zhang W, Li C, Peng G, Chen Y, Zhang Z. A deep convolutional neural network with new training methods for bearing fault diagnosis under noisy environment and different working load. *Mech Syst Signal Process* 2018;100:439–53. <https://doi.org/10.1016/j.ymsp.2017.06.022>.
- [35] Aranguren G, Monje PM, Cokonaj V, Barrera E, Ruiz M. Ultrasonic wave-based structural health monitoring embedded instrument. *Rev Sci Instrum* 2013;84:125106.
- [36] Ioffe S, Szegedy C. Batch normalization: Accelerating deep network training by reducing internal covariate shift. *32nd Int Conf Mach Learn ICML 2015* 2015;1:448–56.
- [37] Nwankpa C, Ijomah W, Gachagan A, Marshall S. Activation functions: Comparison of trends in practice and research for deep learning. *ArXiv Prepr ArXiv181103378* 2018.
- [38] Li M, Zhang T, Chen Y, Smola AJ. Efficient mini-batch training for stochastic optimization. *Proc. 20th ACM SIGKDD Int. Conf. Knowl. Discov. data Min., 2014*, p. 661–70.
- [39] Kingma DP, Ba JL. Adam: A method for stochastic optimization. *3rd Int Conf Learn Represent ICLR 2015 - Conf Track Proc 2015*:1–15.
- [40] Duchi J, Hazan E, Singer Y. Adaptive subgradient methods for online learning and stochastic optimization. *J Mach Learn Res* 2011;12.
- [41] Tieleman T, Hinton G. Lecture 6.5-rmsprop, coursera: Neural networks for machine learning. Univ Toronto, Tech Rep 2012.
- [42] Graves A, Mohamed A, Hinton G. Speech recognition with deep recurrent neural networks.

2013 IEEE Int. Conf. Acoust. speech signal Process., Ieee; 2013, p. 6645–9.

- [43] Kingma DP, Welling M. Auto-encoding variational bayes. ArXiv Prepr ArXiv13126114 2013.
- [44] Moulines E, Bach F. Non-asymptotic analysis of stochastic approximation algorithms for machine learning. Adv Neural Inf Process Syst 2011;24:451–9.

Chapter 5. Non-destructive inspection of skin-stringer composite flat panel by data driven method and ultrasonic guided-wave transfer function method

5.1. Introduction

Modern aircraft manufacture (e.g., Boeing 787 and Airbus A380) commonly uses multilayer-reinforced composite materials that introduce both complexities of material and geometry, leading to significant challenges of inspection. Ultrasonic guided waves, by their nature, sensitive to divergence happened in the structure, are widely used in numerous applications [1-4].

Ultrasonic guided waves can be launched in two ways using contact transducers [5] or non-contact transducers (e.g., air-coupled transducers) [6]. Contact transducers are suitable for generating high energy waves penetrating deeper than shallow surface waves, which helps investigate compounded like skin-stringer composites. However, contact transducers, like PZTs, are permanently mounted on the structure, less flexible to move around. The inconvenience will be more noticeable when a considerable quantity is needed for large-scale monitoring [7,8]. As a rescue, non-contact transducers (air-coupled transducers) gain great attention in detecting anomalous behavior of the structure [9,10]. The energy processed by non-contact transducers is usually less than that of contact transducers due to air medium, which leads to a less inquiring depth of the structures. However, the flexibility in motion and the single-sided accessibility drive

non-contact transducers to various applications of the large-field inspection and challenging conditions (only single side available).

In this chapter, both contact and non-contact transducers were investigated to inspect the skin-stringer composite panel. The data-driven method was utilized to simulated damage location by analyzing the data acquired from the PTZs encircled the cross-section with challenging geometry. The transfer function method was also employed to deal with dual-output scenarios by performing two air-coupled transducers. Moreover, the shear-tie region was also investigated and discussed using air-coupled transducers.

5.2. The cross-sectional damage characterization of the composite panel with skin-stringer geometry

5.2.1. Data-driven matched field processing (DDMFP)

Matched field processing is a well-known framework that exploits the model characteristics to locate targets with high resolution and accuracy [11]. However, this method also suffers due to a lack of understanding of the environment, when the wave propagating field is complex, such as intricate geometry, layered material distribution. Instead of investigating the details of the environment to construct a dedicated model, we constructed a model directly from data itself, then integrate this model with matched field processing to locate the target efficiently. Under this idea, we build the matched field like the following way [13]:

$$P = W_{pristine}^+ * (d_{damage} - d_{pristine}) \quad (5.1)$$

Where $W_{pristine}$ is the replica vector, the model, built by the pristine data, using interested transmit-receive pair at certain frequency. d_{damage} is the data acquired from the damaged panel at a

certain frequency. d_{pristine} is the data from pristine panel at a certain frequency. P is the final result of this matched field process, indicating the energy distribution of the defect. The physical meaning of this whole equation is to backpropagate the difference between the damage data and the pristine data. The result of the sensor location is most substantial when the sensor is located closest to the defect. The experimental set up is shown in Figure 5.1, including top view, bottom view, and sensor placement. The material properties and lay-up of this composite panel are the same as the last section. The system has full-matrix data acquisition capability with 12 channels; all of them can be either transmitter or receiver. The transmitting signal with central frequency 300kHz modulated with a hanning window, sampled by 12.5 MHz. The narrowband contacted sensors have been used in this experiment [14].

5.2.2. Results: defect localization on the skin-stringer cross-section

Two defect locations are examined in this section, and one is on the stringer, the other is positioned on the skin. The defect is simulated by a small piece of clay, which is easy to change the defect position. Figure 5.2 (b) shows the defect on the skin between the sensor 2 and sensor 3 with arrow indicator. Figure 5.2 (a) shows the results from DDMFP, y-axis is the power in dB scale, x-axis is the sensor index corresponding to the real positions of sensors. The two largest peaks are in the positions 2 and 3, which means defect is around sensor 2 and sensor 3, that is same as the experimental setup.

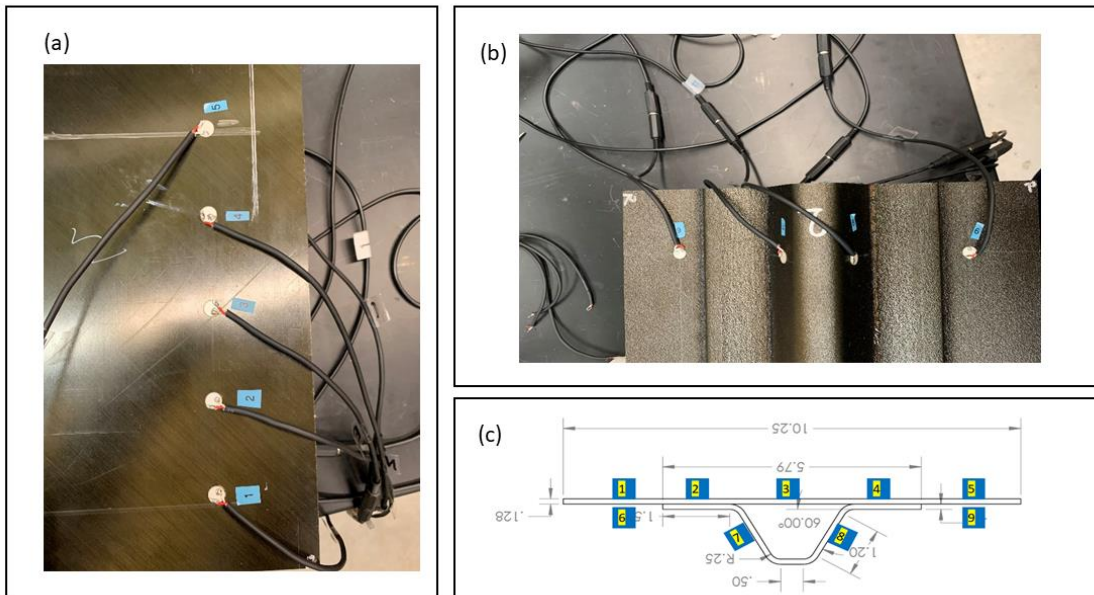


Figure 5.1. Experimental setup, (a). Top view of the composite panel; (b). bottom view of the composite panel; (c). sensor placement.

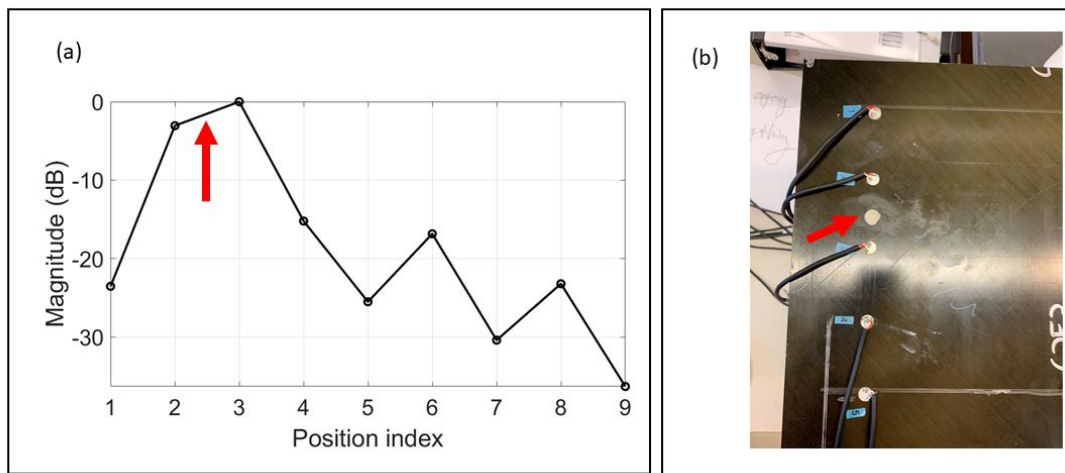


Figure 5.2. Damage on the skin. (a) the damage location identified by algorithm; (b) real damage location.

The other defect is placed on stringer between sensor 7 and sensor 8 shown in Figure 5.3(b) and (c) indicated with an arrow from the bottom view and a red dot from the cross-section view. The results are shown in Figure 5.3 (a), only sensor 8 is successfully resolved due to the complexity of the geometry in this region as well as intricate wave propagation paths.

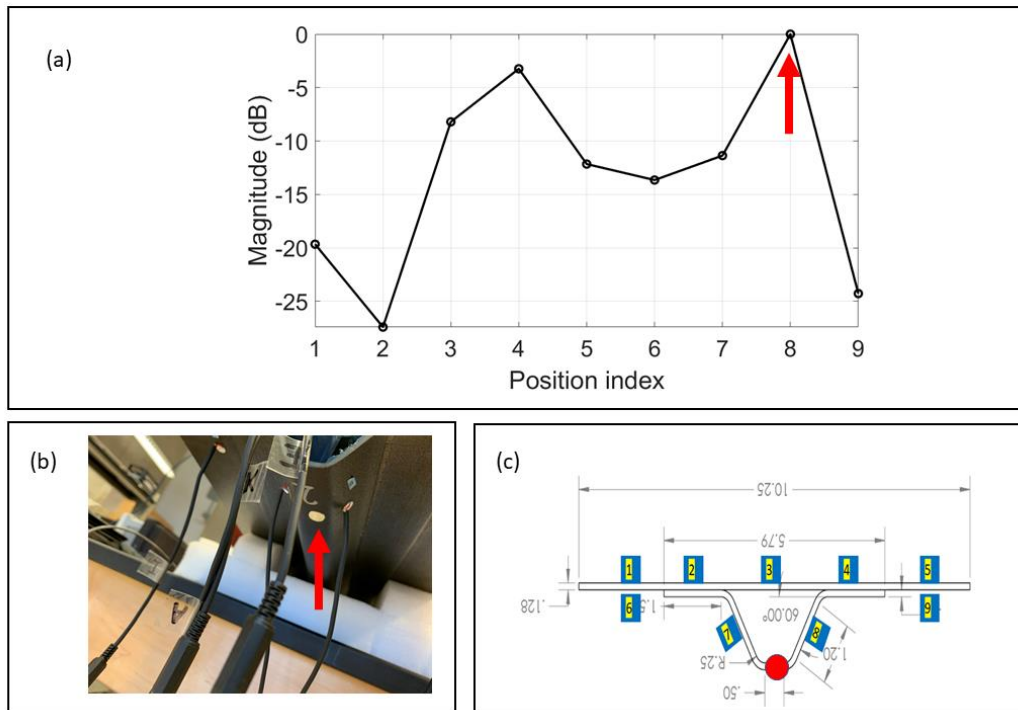


Figure 5.3. Damage on the stringer. (a) the damage location identified by the algorithm. (b) bottom view of real damage. (c) front view of real damage.

5.3. The Excitation localization by Convolutional Neural Network (CNN)

5.3.1. Simulated data preparation from ABAQUS

The excitation localization of the plate was investigated in this subsection. The data were simulated using Abaqus CAE. The aluminum plate was modeled with dimension $1\text{m}\times 1\text{m}$, thickness 1mm , Young's modulus 67Gpa , Poisson's ratio of 0.33 , and density 2700kg/m^3 . 12-receiver locations were assigned around the studying area with a rectangular shape shown in Figure 5.4. The first boundary condition (BC1) was z-directional displacement and rotation equal to zero. The second boundary condition (BC2) was x-directional displacement and rotation equal to zero, y-directional displacement and rotation equal to zero. This study would not use any of the material properties of this plate. The analysis was pure data-driven, which intended to use on the composite structures [15]. Aluminum plate easy to simulate would always be the best candidate to choose.

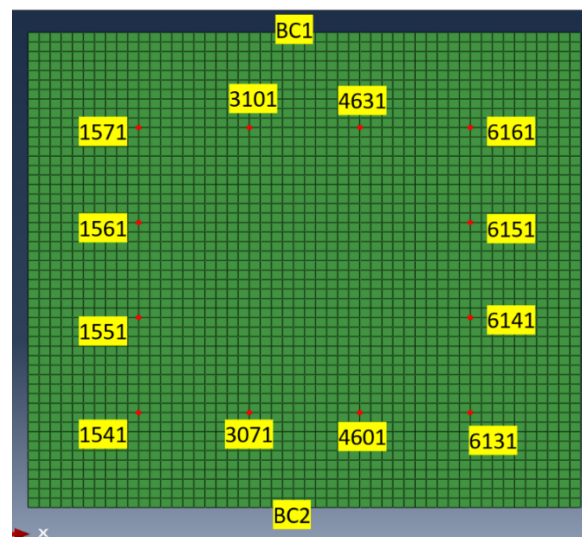


Figure 5.4. Sensor locations in Abaqus simulation.

A single pulse was used as the excitation shown in Figure 5.4, with 1kHz central frequency with an amplitude equal to 1. The various data were collected by looping over different amplitude values from 1 to 128 within all 81 actuated positions.

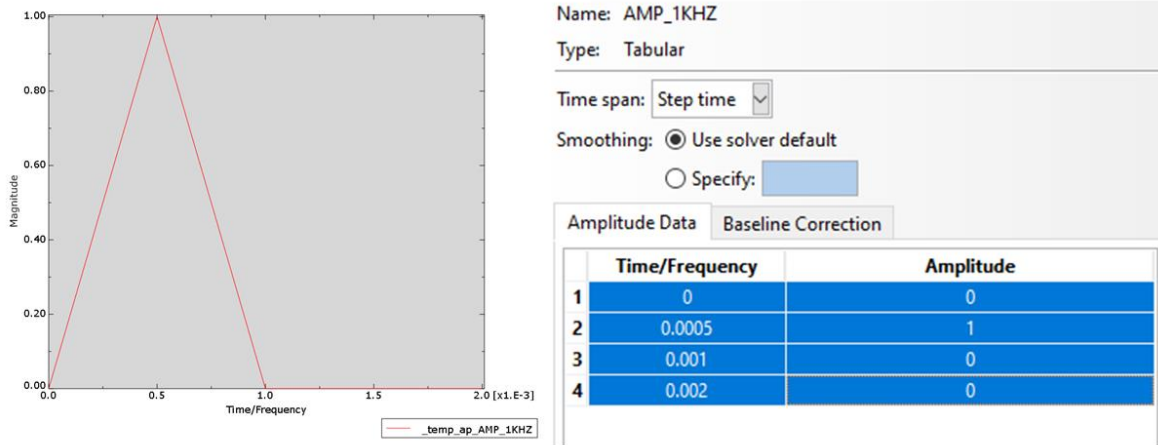


Figure 5.5. The pulse excitation applied in the simulation.

5.3.2. Training scheme by using MATLAB Deep Learning Toolbox

The training schematic of excitation localization was shown in Figure 5.7. 1D-CNN [16] was applied by training the assembled set of the data shown in Figure 5.6. One curve in Figure 5.6 meant data from 12 receivers aligned to a single row or column vector under one type of excitation. The size of a single data vector corresponds to the input layer's size in the training scheme.

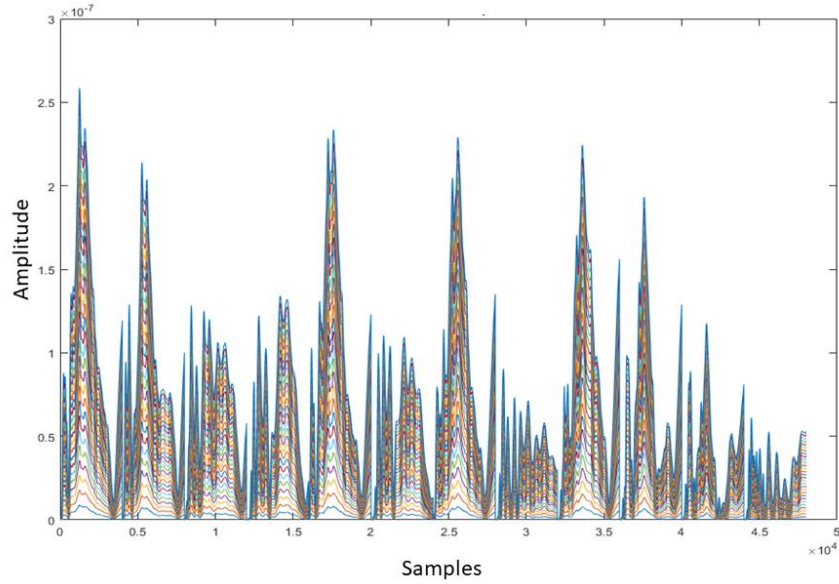


Figure 5.6. The assembled receiving signal with 20 excitations.

MATLAB deep learning toolbox was employed in this study to gain the benefit of the well-established deep learning techniques [17]. The training scheme in detail was shown in Figure 5.7. The 2D convolutional layer was used to approach 1-D CNN training with one dimension equal to one. Since the raw data themselves were varied with different triggering amplitudes, the batch-normalization layer was used to diminish the covariate shift issue. The covariate shift issue was initially found when researchers solved the classical question, “Dog & Cat” characterization. The model found itself challenging to distinguish between monochrome dogs and cats when trained under colored photos. False alarms happened even if the ground truth maintained the same. Batch normalization [18] allowed the network to learn the knowledge within a specific layer not or less affected by the former layers, which reduces the covariate shift issue. ‘Relu’ activation layer was used to introduce nonlinearity during the training so that the model would not only learn some

linear properties [19]. Max pooling layer helped reduce the less effective features to make the whole process faster.

```
%% Training Algorithm
%%Hyperparameter
conv_size = 50;
conv_filter =64;
pooling_size = 10;

Layers = [
    imageInputLayer([width,height,channel])
    convolution2dLayer([1,conv_size],conv_filter );
    batchNormalizationLayer
    reluLayer
    maxPooling2dLayer([1,pooling_size],'Stride',[1,2]);

    convolution2dLayer([1,conv_size],conv_filter );
    batchNormalizationLayer
    reluLayer
    maxPooling2dLayer([1,pooling_size],'Stride',[1,2]);

    fullyConnectedLayer(81)
    softmaxLayer
    classificationLayer
    ];

training_Y_set = categorical(Y_training);
test_Y_set = categorical(Y_test);

options = trainingOptions('adam',...
    'LearnRateSchedule','piecewise',...
    'LearnRateDropFactor',0.2,...
    'LearnRateDropPeriod',5,...
    'MaxEpochs',44, ...
    'ValidationData',{X_test,test_Y_set}, ...
    'ValidationFrequency',30, ...
    'GradientDecayFactor',0.9,...
    'SquaredGradientDecayFactor',0.99,...
    'Epsilon',10^-8,...
    'MiniBatchSize',64,...
    'Plots','training-progress',...
    'ExecutionEnvironment','multi-gpu');
```

Figure 5.7. CNN training schedule.

The ‘adam’ was used as an optimization means to accelerate the training, which combined the advantages of the SGD with momentum and RMS prop [20]. The mini-batch gradient descent was used to accelerate the training process further.

5.3.3. Results of impact location prediction

The locations of all excitations were shown in Figure 5.8(b), with a total of 81. All the red dots were the locations with all 128 kinds of excitation and learned by the model. The final trained model was examined by a test point off-set the training positions shown in Figure 5.8(a). As expected, even if the test points were not in the training set, the closest training would hold the high possibility to indicate the test point location, the closer to the test points: the lighter color, the higher values.

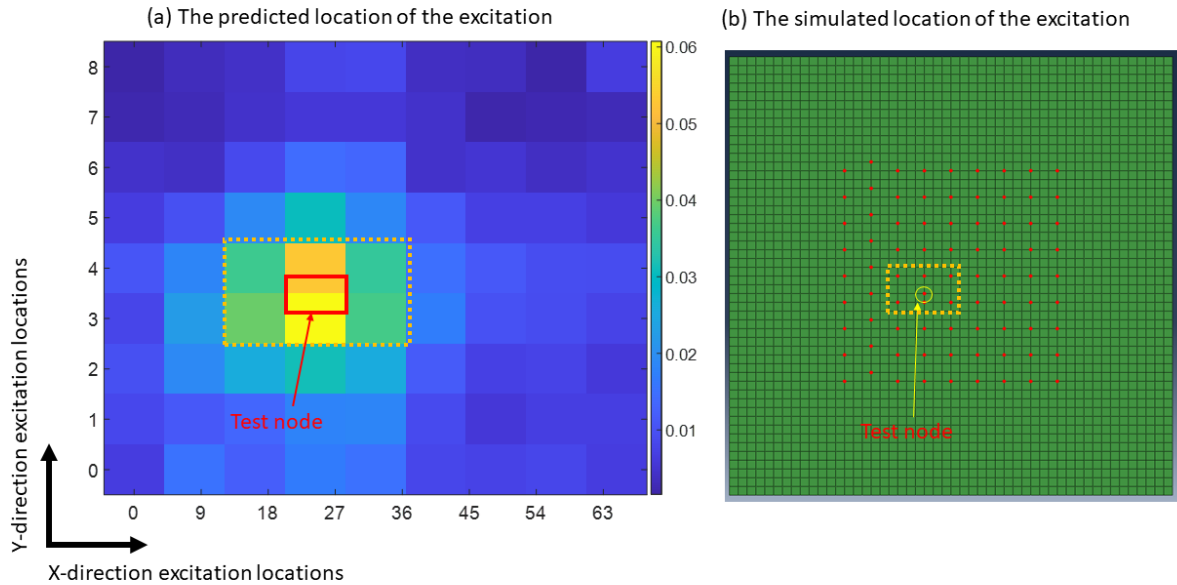


Figure 5.8. The result compared with simulated ground truth: (a) The predicted location of the excitation; (b) The simulated location of the excitation.

5.4. Ultrasonic guided-wave transfer function extraction on inspecting composite aerospace structures

The transfer function is one of the stable and sensitive signatures of the structure, which will not change unless an unexpected anomaly (defects) occurred. Therefore, the comparison of the transfer functions of different states becomes appealing for researchers to identify the defects. “single-input single-output” (SISO) is the typical candidate to extract the transfer function yet requiring a deconvolution of the excitation from the reception, which demands to know the precise excitation spectrum. However, the coupling of the excitation signal, the transmitter frequency response, and the transducer-to-medium response make it challenging to determine the effective excitation spectrum [21]. A more robust transfer function extraction than SISO is a “dual-output” approach where two receiving sensors yield the transfer functions [22-24]. “Dual-output” allows to passively inspect the structure without knowing the knowledge of the real excitation spectrum [25-30].

The dual-output passive inspection scheme is shown in Figure 5.9. The goal is to achieve and track the structural transfer function H_{AB} to identify the damage between A and B. The source in this section keeps unknown. The formulation of the first measured signal from receiver 1 is like the following:

$$RM_1(f) = S(f) \cdot H_{SA}(f) \cdot ST_1(f) \cdot RR_1(f) \quad (5.2)$$

Where, $S(f)$ is the input signal, $H_{SA}(f)$ is the structure transfer function between unknown source on plate S and point A . $ST_1(f)$ is the structure-to-air-to-transducer I coupling response, and $RR_1(f)$ is the receiver 1 frequency response.

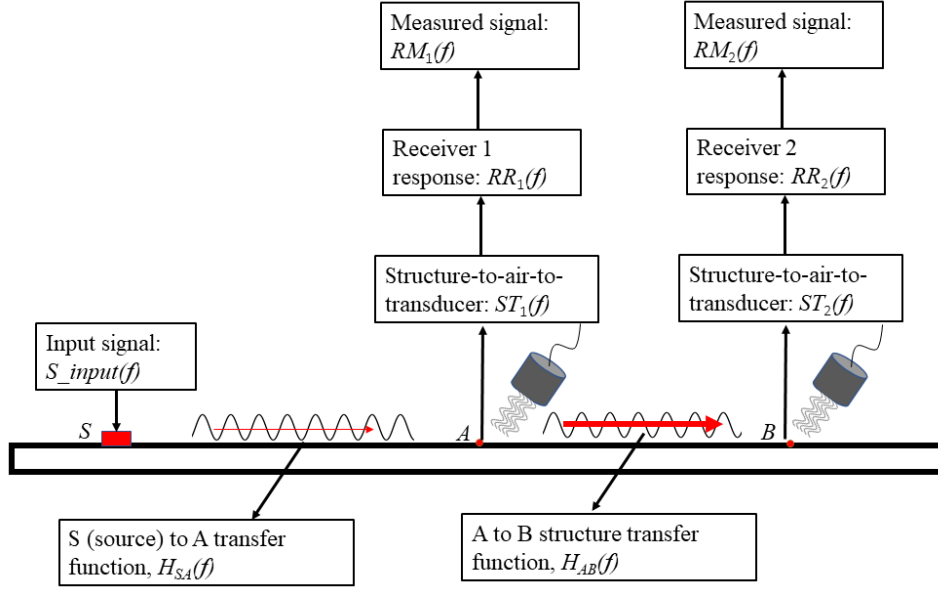


Figure 5.9. The structural transfer function extraction by a dual-output scheme.

Similarly, the second measured signal from receiver 2 is as follows:

$$RM_2(f) = S(f) \cdot H_{SA}(f) \cdot H_{AB}(f) \cdot ST_2(f) \cdot RR_2(f) \quad (5.3)$$

Where, $H_{AB}(f)$ is the structure transfer function between point A and point B. $ST_2(f)$ is the structure-to-air-to-transducer 2 coupling response, and $RR_2(f)$ is the receiver 2 frequency response.

The assumption was made as follows: (1) the air is uniform in the room; (2) two same receivers with no manufactural difference. Therefore: $ST_1(f) = ST_2(f)$ and $RR_1(f) = RR_2(f)$. The deconvolution was yielded like:

$$Deconv = \frac{RM_2(f)}{RM_1(f)} = H_{AB}(f) \cdot \frac{SR_2(f)}{SR_1(f)} \cdot \frac{RR_2(f)}{RR_1(f)} = H_{AB}(f) \quad (5.4)$$

The time-domain transfer function can be calculated by inverse Fourier transformation:

$$H_{AB}(t) = \int_{-\infty}^{\infty} H_{AB}(f) \cdot e^{i2\pi ft} df \quad (5.5)$$

Hence, the structural transfer function between two receivers had been isolated and translated in the time domain to prepare for the feature extraction to feed in damage index (DI) estimation.

$$DI = \sqrt{(\mathbf{y} - \mathbf{x}) \times \mathbf{S}^{-1} \times (\mathbf{y} - \mathbf{x})^T} \quad (5.6)$$

Where, \mathbf{y} is the feature vector, \mathbf{x} is the average baseline vector, \mathbf{S} is the baseline covariance matrix. The value of DI represents the deviation from the normal statistics of the baseline signals. The defect gave the large value of DI.

5.4.1. Experimental setup

The experiments performed on one curved panel shown in Figure 5.10. The panel was extraordinarily complicated, including the skin, the stringer, five shear-ties, and one C-frame. The first simplification was to divide the panel into two zones: the simple zone (13cm to 23cm and 30cm to 41cm) and the complex zone (23.5cm to 29.5cm).

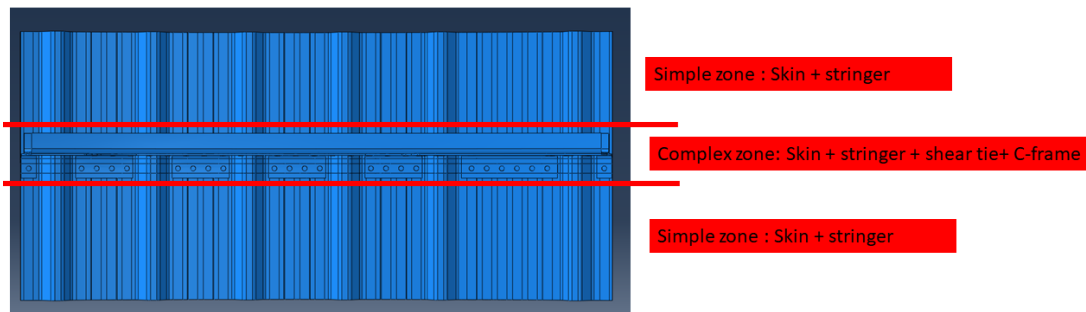


Figure 5.10. The zone definition of curved composite panel 4_1.

The mini-impactor as a means to generate input signal with the pivoting length 5.08cm made by the composite was shown in Figure 5.11(a). The mini-impactor easy to change operating position provided strong signal strength yet hard to calibrate the excitation waveform. Two mini-bat air-coupled transducers (Figure 5.11(b)) were as two receivers whose signals were first amplified by a preamplifier (Figure 5.11(c)). All signals captured by receivers were recorded by PicoScope (Figure 5.11(d)) and processed in the computer.

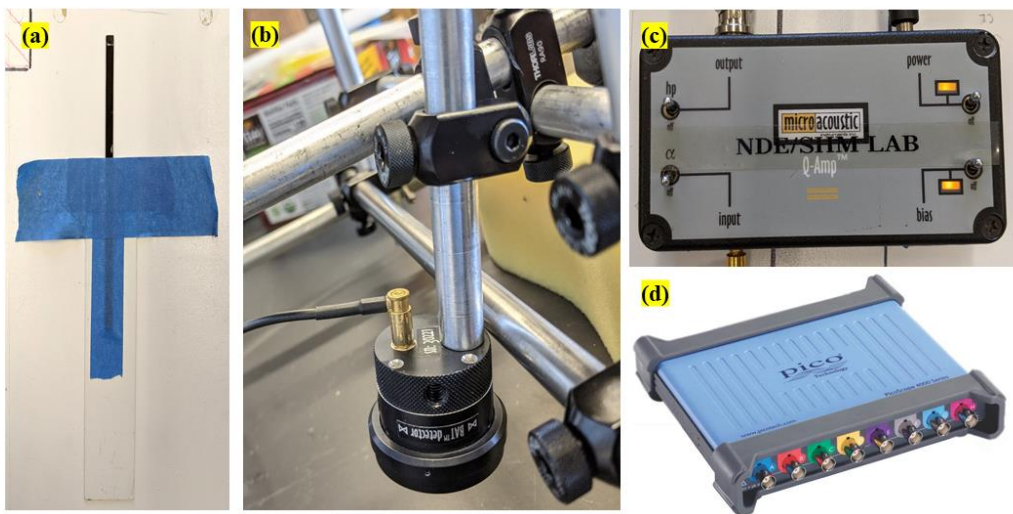


Figure 5.11. The devices used in the experiment.

5.4.2. Damage detection of the simple zone of curved composite (skin-stringer structure)

In the test on stringer 2, two receivers were 18.415 cm away from each other over the stringer; the mini-impactor is 3.81cm away from the first sensor with foam in the middle to avoid the direct transmission from the mini-impactor to the first receiver through the air. Both receivers have a 3.81cm lift-up with 13° with respect to the vertical direction. In the simple region, data

points frequency is every 1 cm. The data point started from 13 cm till 41 cm without 23.5 cm to 29.5 cm (lying in the complex zone).

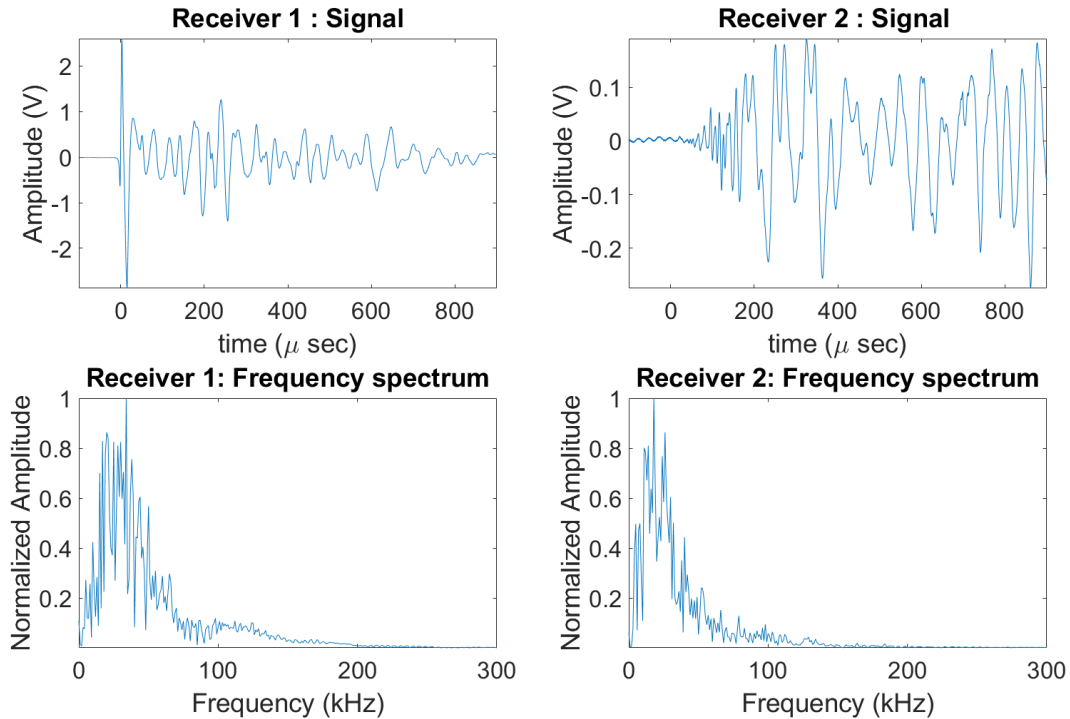


Figure 5.12. Stringer 2: Signal and frequency spectra of receiver 1 and receiver 2.

The signals of stringer 2 were captured by receiver 1 and receiver 2 shown in Figure 5.12. The signal strength of receiver 1 was 10-times higher than that of receiver 2 due to the large damping ratio of the composite panel. The mini-impactor played a vital role in generating high strength signals and maintain movability. However, the signals from two receivers stayed in the same frequency band, between 20kHz ~80kHz, low enough (below 100kHz) to keep traveling with small attenuation, as well as high enough (20kHz) to avoid ambient noise.

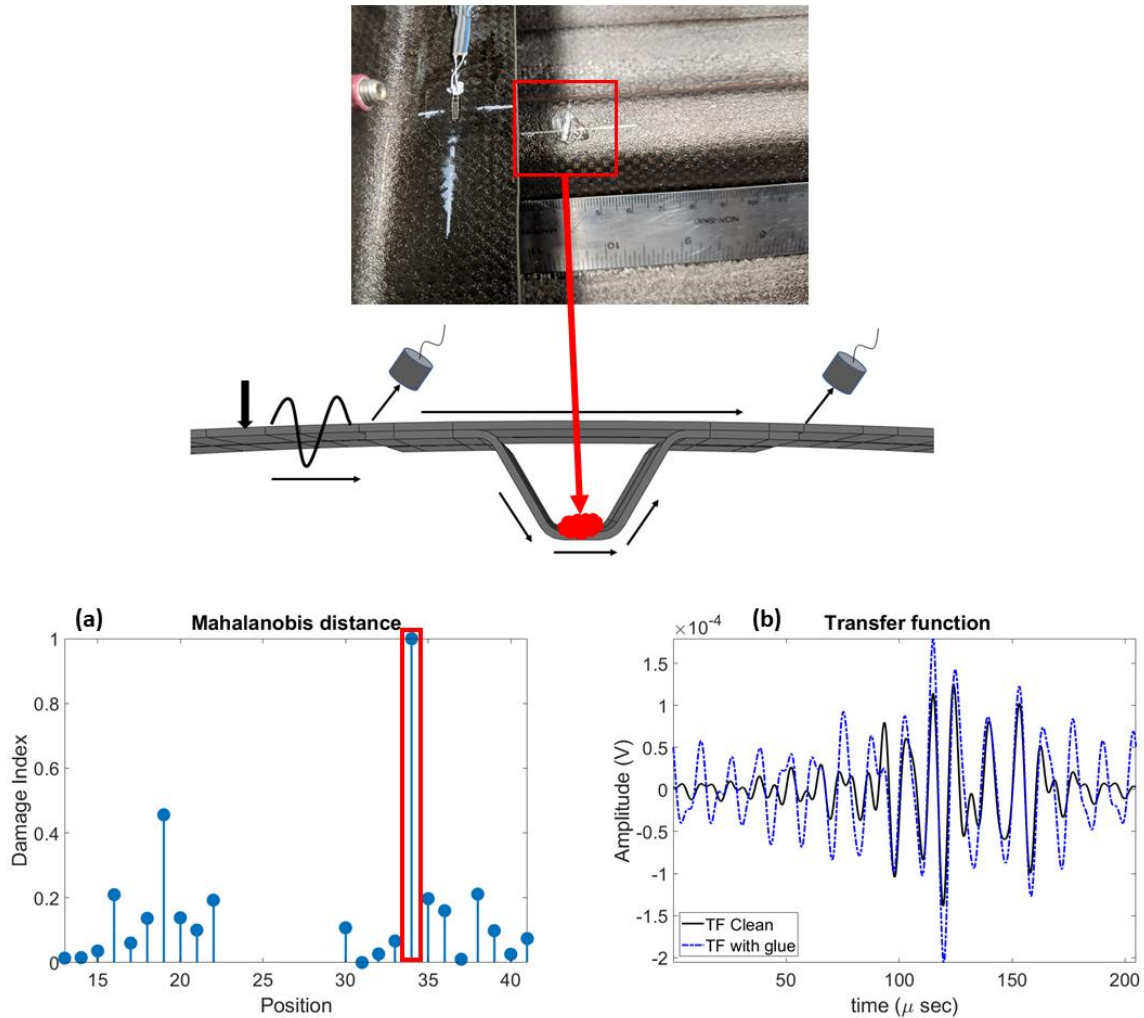


Figure 5.13. Damage localization on stringer 2: (a) Mahalanobis distance; (b) transfer function comparison on clean stringer and stringer with hot glue.

The hot glue was on the top of the cap top of stringer 2, shown in Figure 5.13. The extraction of the structural transfer function from these measurements, shown in Figure 5.13(b), has an improved signal-to-noise ratio with distinctive waveform features regarding magnitudes and time arrivals. By its nature, the transfer function is less dependent on the transduction responses and highlights the coherence between two receivers, which was the property of the

transduced medium. The transfer function was achieved between 1kHz to 115kHz. The clean panel without hot glue showed amplitude changes compared to the one with the hot glue. Two features were computed from the transfer function, root-mean-square (RMS) and skewness. The RMS was good at monitoring the changes of the signal strength [31]. And the skewness, on the other hand, was tracking the shape changes of the signal. Two features were fed in the Mahalanobis distance to estimate the distance between the clean panel and “damage” panel shown in Figure 5.13(a). The hot glue was located at 34 cm, aligned with the ground truth in the picture. (Notice that the rule shows between 4cm and 5cm, which needs to be added 30cm because the total rule length was 30cm.).

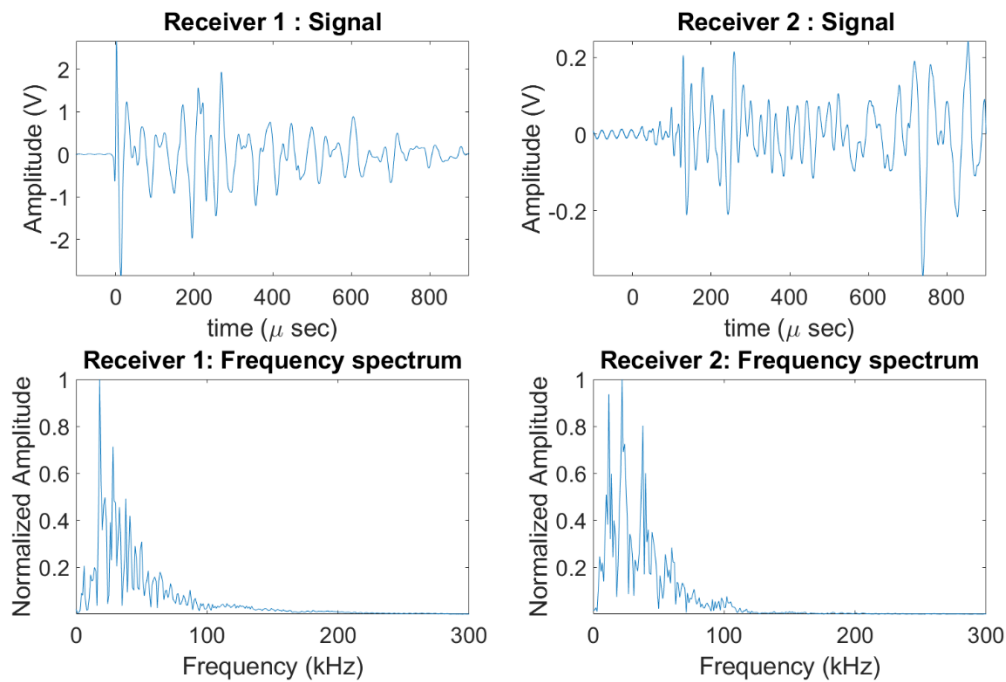


Figure 5.14. Stringer 3: Signal and frequency spectra of receiver 1 and receiver 2.

The second test was conducted on stringer 3 with hot glue on the stringer flange. The typical waveforms measured by two receivers of an air-coupled system were shown in Figure 5.14. The large attenuation also affected the signal at receiver 2 due to the significant wave leakage and scattering while it was traveling across the skin-to-stringer assembly.

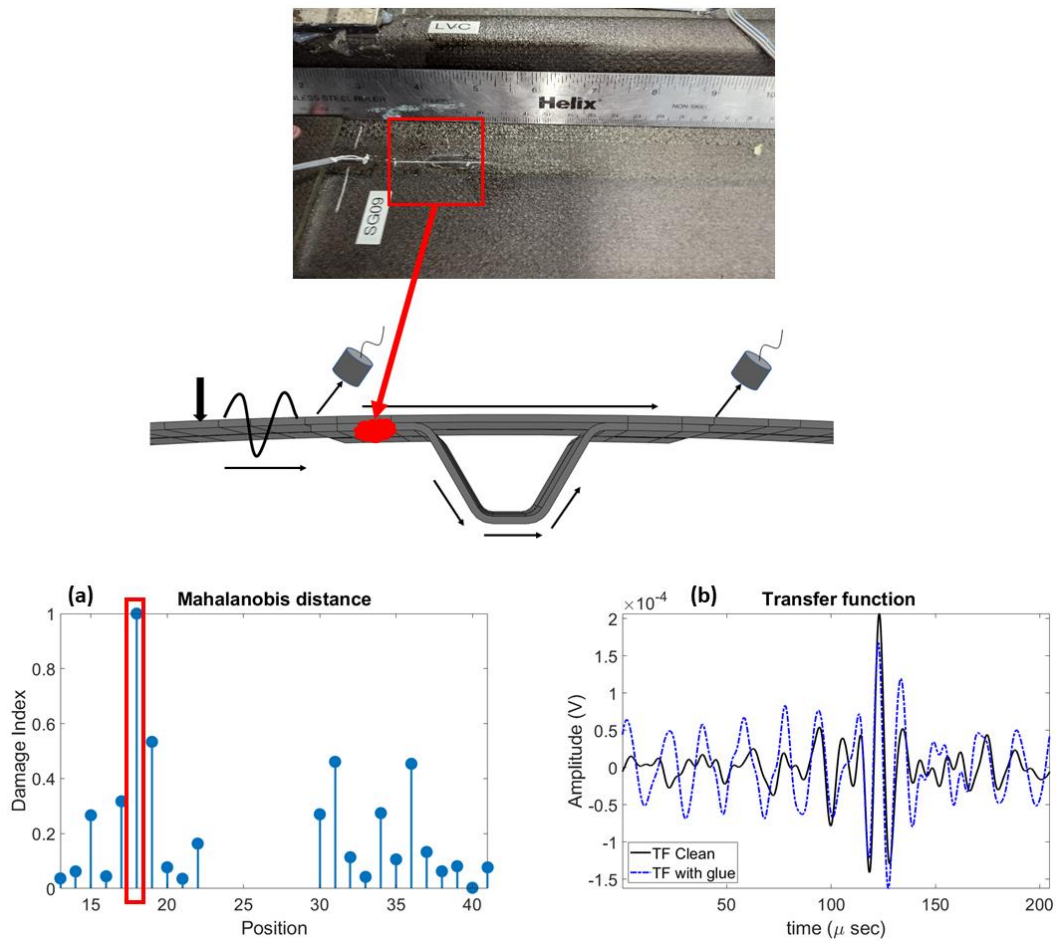


Figure 5.15. Damage localization on stringer 3: (a) Mahalanobis distance; (b) transfer function comparison on clean stringer and stringer with hot glue.

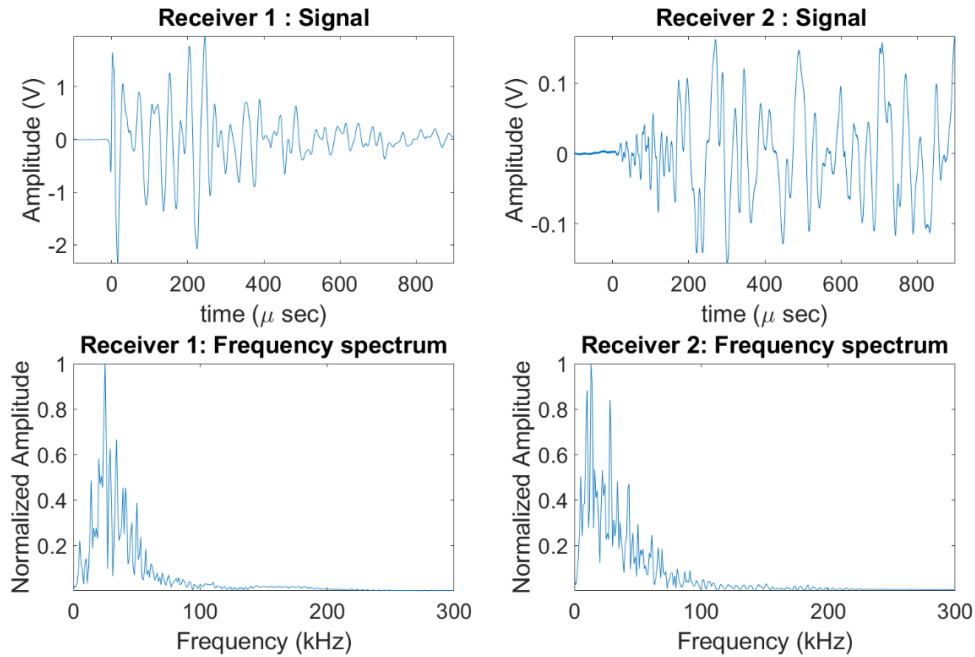


Figure 5.16. Stringer 4: Signal and frequency spectra of receiver 1 and receiver 2.

The damage location and ground truth photo were illustrated in Figure 5.15. The transfer function between two receivers was extracted with an enhanced signal-to-noise ratio with outstanding waveform features. The transfer function was obtained after filtering out higher frequency band, staying in 1kHz to 115kHz. The magnitudes of the transfer function with hot glue were larger than the one without at both tests in Figure 5.14 and Figure 5.15. This observation can be explained by the fact that the leakage in the skin-to-stringer region was reduced due to the damage or hot glue that happened on the stringer flange and stringer cap region. This reduction of leakage resulted in increasing transmission energy. Two features, RMS and skewness, were fed in the Mahalanobis distance estimator to measure the deviation between the clean one and the one with hot glue. The final decision was made, shown in Figure 5.15(a) identifying the real location (18cm) consistent with the ground truth picture.

The third test was on stringer 4 with the hot glue in the heel region. The signal waveforms recorded by air-coupled transducers were shown in Figure 5.16. The signals both in the time-domain and frequency-domain were similar as measured before in stringer 2 and stringer 3. The operating frequency band stayed at 0~ 100kHz, with the second signal's strength suffering significant attenuation from the medium.

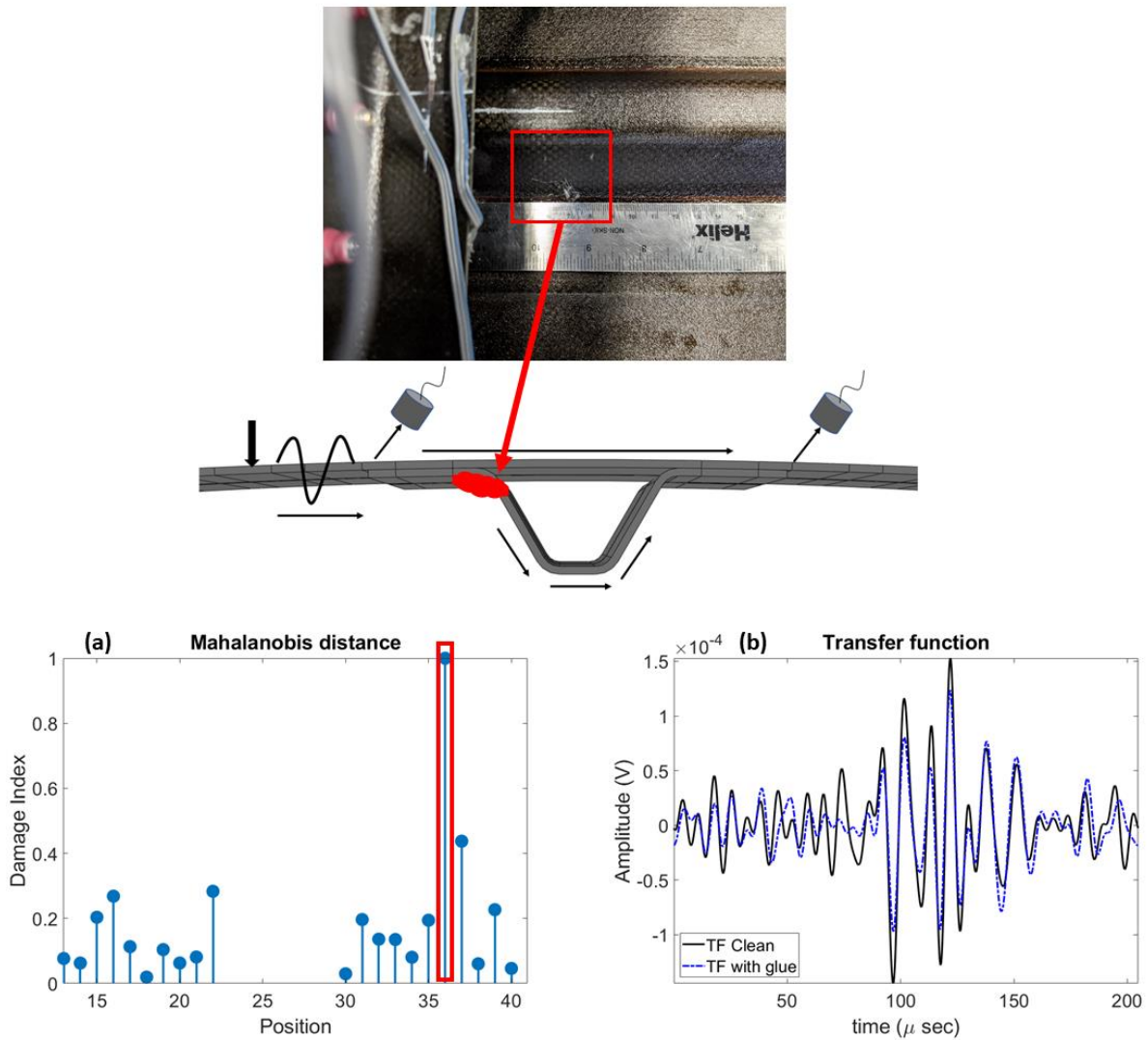


Figure 5.17. Damage localization on stringer 4: (a) Mahalanobis distance; (b) transfer function comparison on clean stringer and stringer with the hot glue.

The transfer function extraction of stringer 4, the ground truth photo, and Mahalanobis distance decision was shown in Figure 5.17. The transfer functions in both clean and hot-glued cases were stable in phase but considerable variation in amplitude, shown in Figure 5.17(b). The shape of the transfer function has slight changes, proving the efficacy of transfer function features, RMS and skewness. The Mahalanobis distance estimated the hot-glued appeared in position 36cm, which was consistent with the ground truth shown in both the illustration and the photo.

5.4.3. Damage detection of curved composite skin-stringer-shear_tie structure

The complex zone defined in this chapter, shown in Figure 5.10, consisted of the skin, the stringer, the shear-tie, and C-frame. However, the C-frame, a deep-inner part, was away from the skin, which was an inaccessible area using ultrasonic guided waves due to significant attenuation. Therefore, the boundary-touch approach was trying to investigate the second deep-inner part, the shear-tie. The shear-tie was an essential connection of stingers perpendicular to the stringers to make the whole panel stiff and resist effectively twisting and bending moment. The efficient way to trace the wave propagating through the shear-tie region was to set the contact pico-sensors along the possible wave propagating path, shown in Figure 5.18. The mini-impactor was the means of the excitation to maintain both high energy and movability. The first pico-sensor was placed on the shear-tie around 3 cm down from the skin serving channel B (on the left-hand side of the stringer). The second pico-sensor was placed in the middle bottom area of the shear-tie serving channel C. The third pico-sensor was placed on the shear-tie around 3 cm down from the skin serving channel D (on the right-hand side of the stringer). The fourth pico-sensor was placed on the skin outside the panel, the same as the position of the second mini-bat receiver discussed in the last subsection.

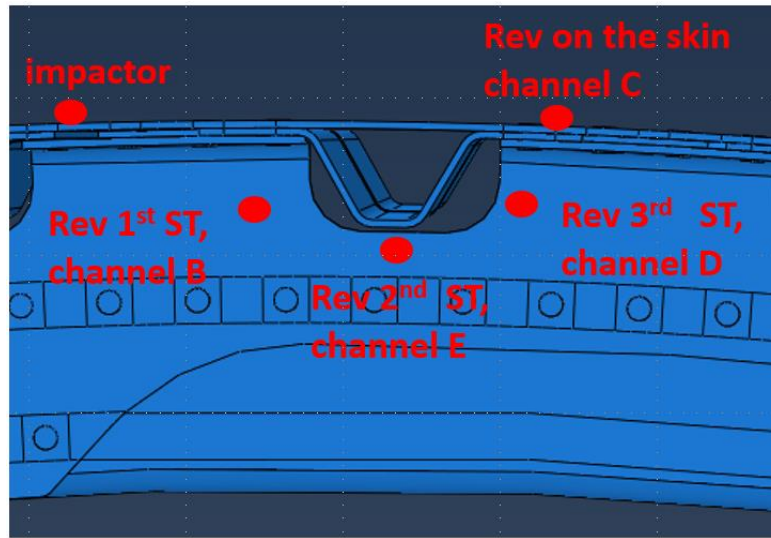


Figure 5.18. Investigation of the ultrasonic waves propagating through the shear-tie.

The signals from all four pico-sensors were shown in Figure 5.19. From the time arrival point of view, sensor B was the first to achieve the signal because it was the closest one to the source, even if it was on the shear-tie region. The sensor C was the second to acquire the signal because the time arrival was mostly contributed by the wave propagating through the skin region. Surprisingly, sensor D got the signal earlier than Sensor E. It was possible that the wave reached the sensor C, and some of them leaked to the shear-tie received by the sensor D. The sensor E located on the middle bottom of the shear tie was capturing the signal only traveling through the shear-tie.

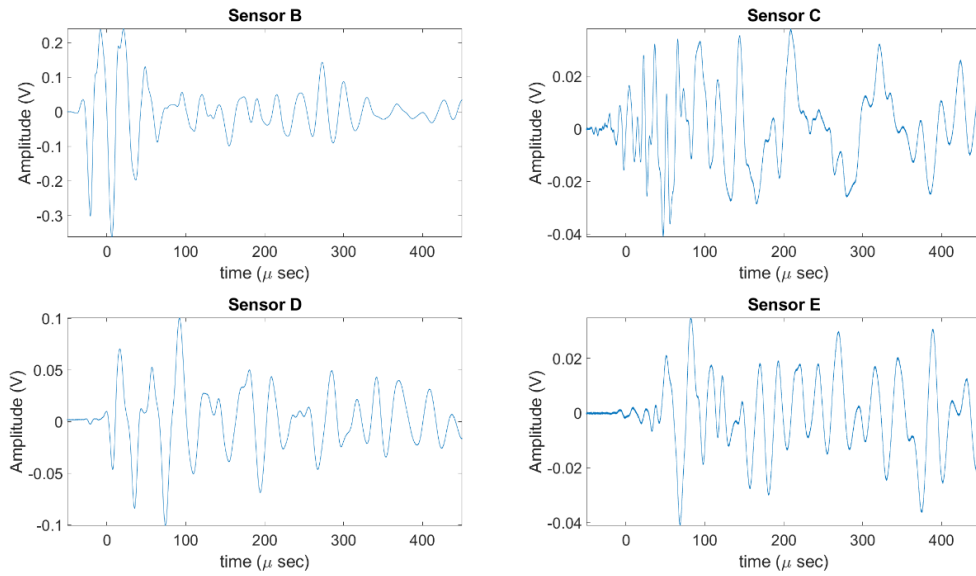


Figure 5.19. Signal for tracing waves in shear-tie triggered by impactor.

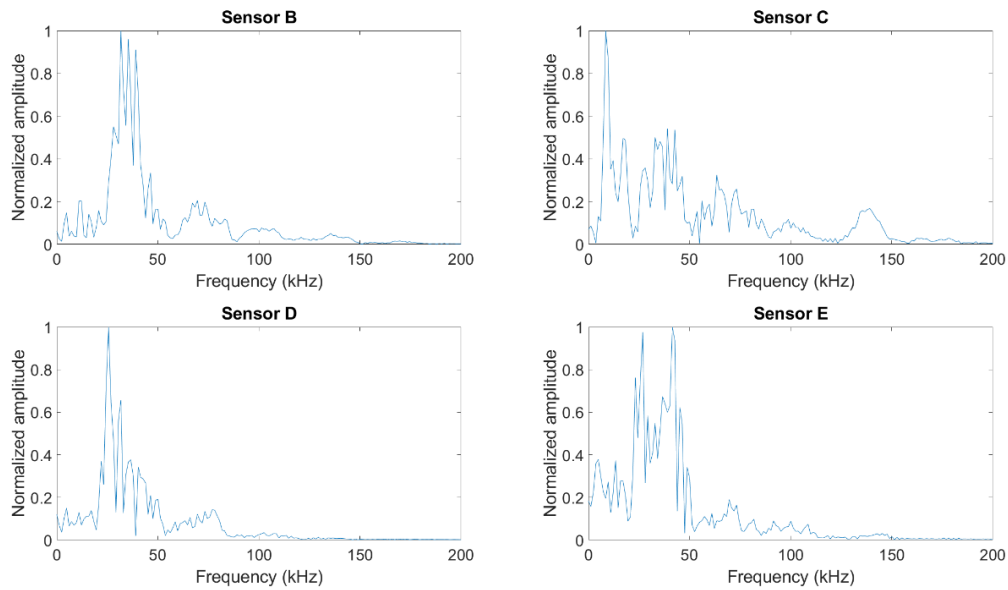


Figure 5.20. Frequency spectra for pico-sensors on the shear-tie region triggered by the impactor.

All signals in Figure 5.19 were analyzed in frequency-domain shown in Figure 5.20. The sensor B was the first testing point on the shear-tie achieving a 20kHz to 50kHz frequency band, which indicated the wave traveling through the shear-tie staying in the low-frequency range. The sensor E located on the middle bottom of the shear-tie region was the second testing point on the shear-tie. The signal from sensor E mostly lay on 20kHz to 50kHz, similar to the frequency band shown by sensor B, which also demonstrated that the signal between 20kHz to 50kHz maintains the endurance in the shear-tie region. The sensor D was the third testing point on the shear-tie, whose signal was also staying between 20kHz to 50kHz. The sensor C on the outside skin region included the wave from the skin, the stringer, and the shear-tie, which also had a significant portion of the signal between 20kHz to 50kHz. After tracing the signal from the impactor through the shear-tie eventually captured by sensor C, it was reasonable to draw a conclusion that the waves between 20kHz to 50kHz were the most promising part to penetrate to shear tie and reached the receiver on the outside skin region.

The first test for monitoring the shear tie region was conducted using a mechanic actuator as the transmitter and three pico-sensors as receivers shown in Figure 5.21. Figure 5.21(a) showed all sensor locations: the mechanic actuator was on the outer skin same position as the mini-impactor placed before. The first pico-sensor was located on the outside skin same position as the air-coupled transducer's, named Receiver 1. The second pico-sensor was situated in the same place as the second air-coupled transducer named Receiver 2. The third pico-sensor was located on the middle bottom of the shear tie inside the panel, named the Middle bottom receiver.

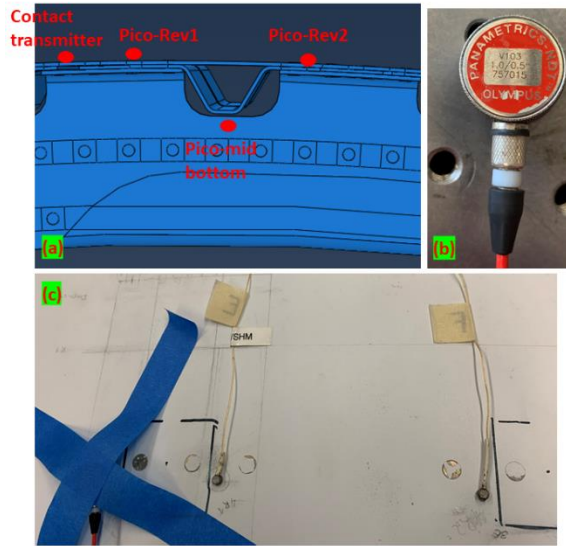


Figure 5.21. The shear-tie region investigation with contact transmitter and three pico-sensors: (a) the illustration of the experiment; (b) the transmitter; (c) real experiment on the surface of the panel.

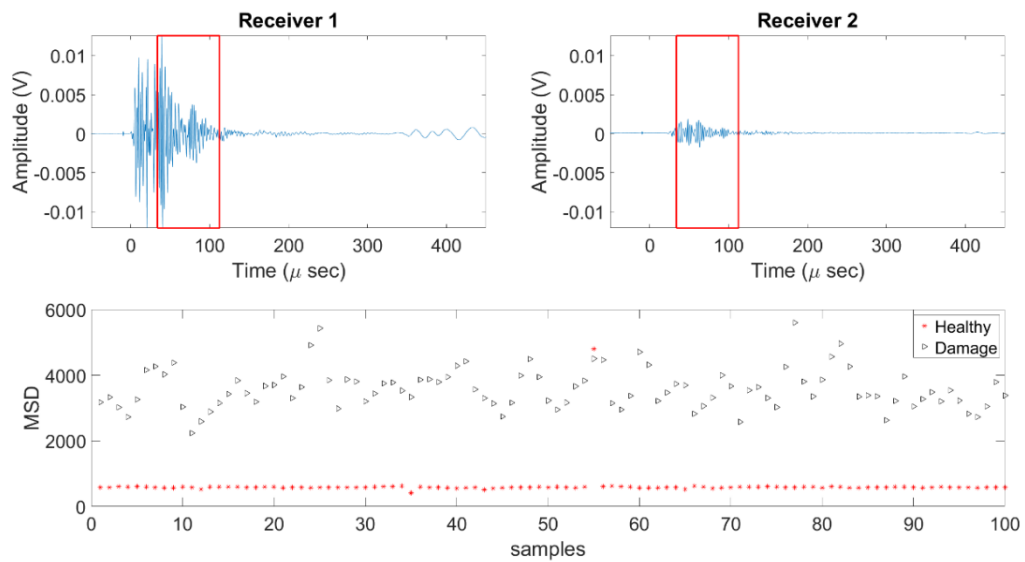


Figure 5.22. Investigation of transfer function between receiver 1 and receiver 2 on the surface.

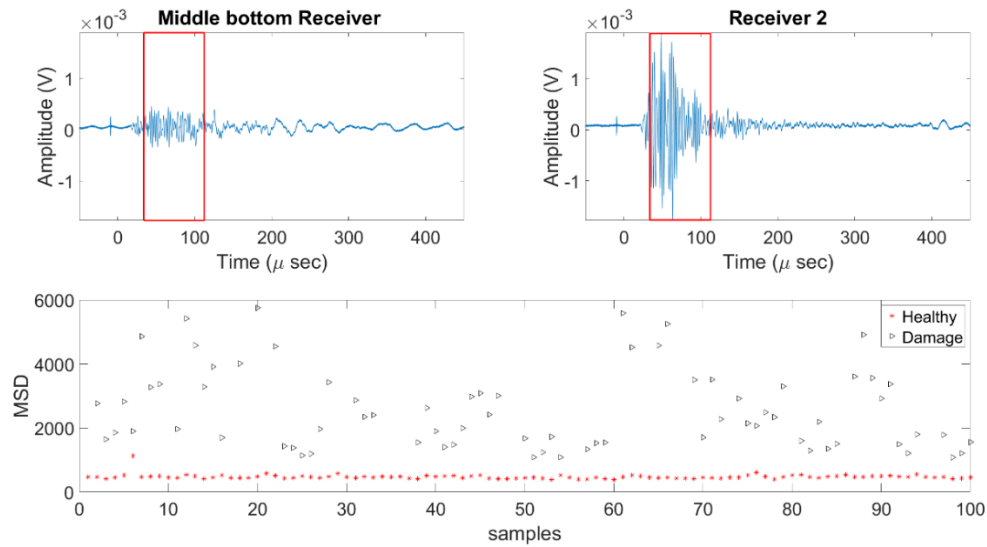


Figure 5.23. Investigation of transfer function between middle bottom pico-receiver and pico-receiver 2 through shear-tie.

The actuator excited 300 times mechanically, and three receivers collected a total of 300 signals. The tests were done in three locations: Loc3_1 stringer 4_ST3_4 served as the healthy case; Loc3_1 stringer 3_ST2_3 with a through fracture served as the damage case; Loc4_1_stringer4_ST3_4 served as the baseline case. The statistical was employed to analyze the randomness in the signal, mostly from ambient noise. The reconstructed signal was achieved by randomly selecting 20 out of 300-time series and averaging them. The amount of the reconstruction signal was 100-time series. The signal in the red box was analyzed, shown in Figure 5.22. The rule of selection was to avoid the first wave package (skin propagation) and focus on the possible shear-tie signals. The transfer function was extracted between 0kHz to 50kHz, which was discussed as the primary frequency band containing the signal traveling through the shear-tie. The features from

the transfer function were RMS and skewness to feed in the Mahalanobis distance calculator. The MSD versus the samples provided a clear boundary between healthy cases and damaged cases.

To further verify the difference in Figure 5.22 with the contribution of the shear-tie region, the transfer functions of the middle bottom receiver to the second receiver were also extracted, shown in Figure 5.23. The same way was used to reconstruct the sample vectors and feature vectors. The boundary between healthy cases and damaged cases was still held, which indicated the differentiation shown in Figure 5.22 with the contribution of the shear-tie region.

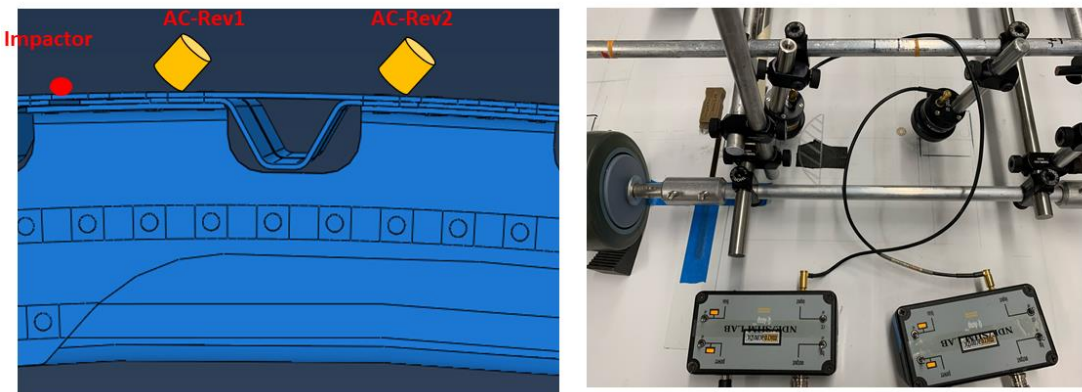


Figure 5.24. Shear tie region inspection using the impactor and air-couple receivers.

The second test for investigating the health condition of the shear-tie region was to use air-coupled transducers and the mini-impactor. The reason for choosing air-coupled transducers over pico-sensors was the flexibility and repeatability of the in-situ maintenance. Because all contact transducers required the couplant between medium and themselves to keep wave efficiently penetrate to the solid and to capture the reflection back to the receivers. It would be too inconvenient to search a large field of an object. Besides, the contact actuator required a huge amplifier to provide enough energy for the transmitting waves, the mini-impactor, however,

transmitted waves in a contact manner without the couplant requirement. Therefore, mini-impactor and air-coupled transducers were the best candidate couple for in-situ maintenance in practice.

The positions of the mini-impactor and two air-coupled receivers were shown in Figure 5.24. The mini-impactor was in the same location as the actuator above. And two air-coupled receivers (mini-BAT) were also at the same locations as those of two pico-sensors. Same as before, two amplifiers amplified the signals acquired by the air-coupled transducers.

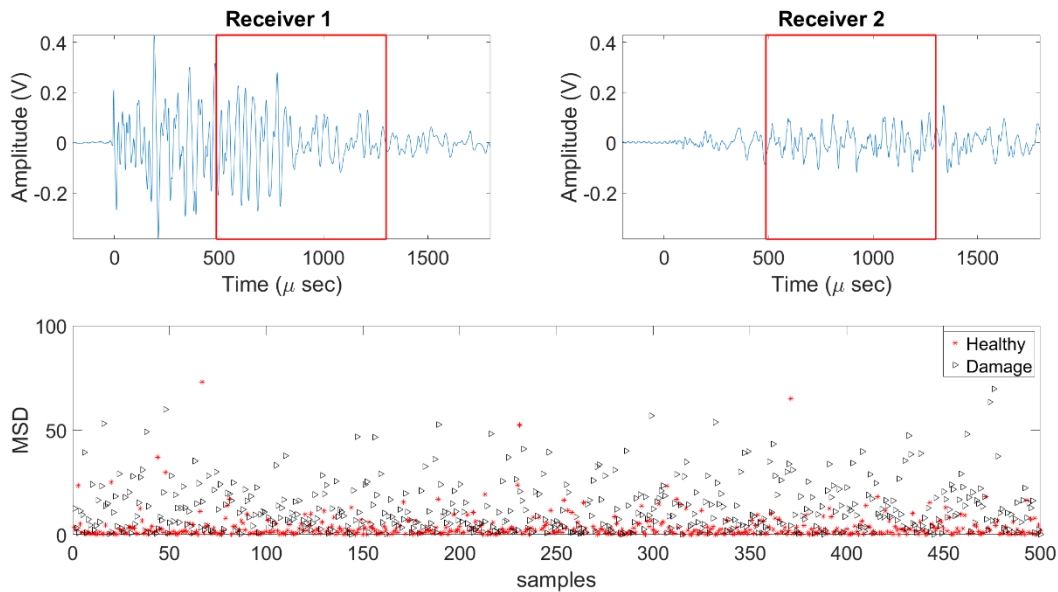


Figure 5.25. Investigation of transfer function between AC-receiver 1 and AC-receiver 2 with 500 test samples on the surface.

Three shear-tie areas were scanned: Loc 3_1 stringer4_ST3_4 served as the healthy case; Loc 3_1 stringer3_ST2_3 served as the damage case; Loc 4_1 stringer_ST3_4 served as the baseline case. These three locations were chosen due to their similar geometry. Only shear-tie 2 in the Loc3_1 panel was totally fractured. 50 impacts were made for each case. The signal from the

impactor was much more random than the mechanical actuator because of the manual operation. Therefore, it was necessary to apply statistical analysis to the acquired signals. The reconstructed signal was yielded by averaging 10 impacts randomly picked up from a total of 50 impacts. 500 reconstructed sample study was shown in Figure 5.25. The signals in the red box were studied. It should be noted that red boxes were selected same both receiver 1 and receiver 2.

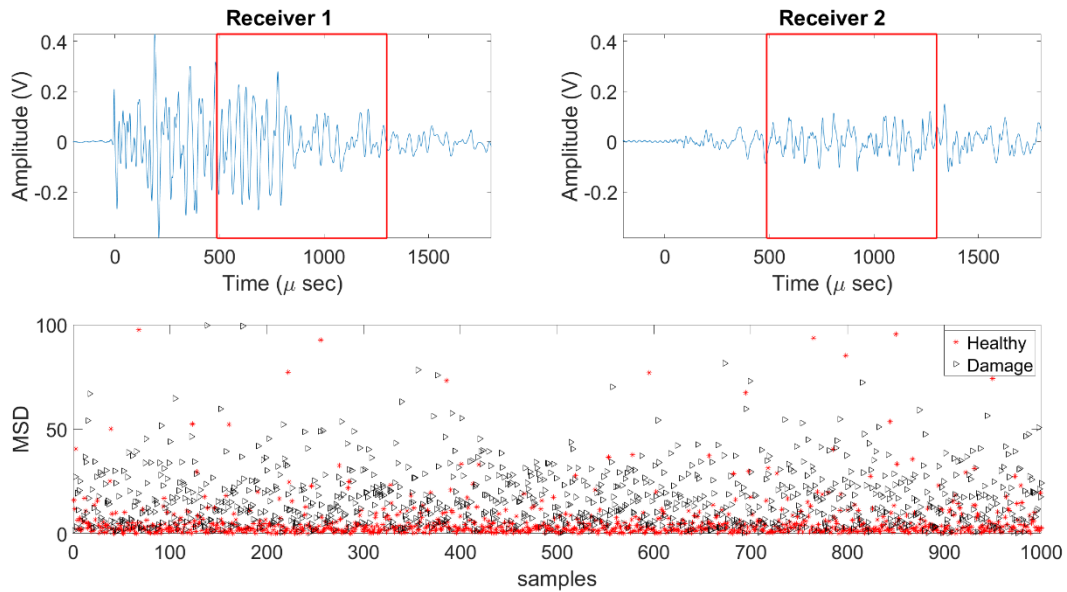


Figure 5.26. Investigation of transfer function between AC-receiver 1 and AC-receiver 2 with 1000 test samples on the surface.

RMS and skewness were extracted from the transfer function of receiver 1 to receiver 2. The samples versus MSD were shown in the bottom figure of Figure 5.25. The boundary was blurred than that of Figure 5.22 and Figure 5.23 because the signal from the impactor was less stable than that from the mechanical actuator. Moreover, the air-coupled transducer had the less signal strength than the contact pico-sensors.

Figure 5.26 showed the results by reconstructing 1000 samples, which took around 1 hour to get the results. The boundary became a little clearer than the one with 500 samples. Receiver operating characteristic (ROC) curves [32] were generated to compare two cases shown in Figure 5.27. The threshold was selected from 0 to 100 with 10000 intervals. The accumulative probabilities of both detection and false alarm were shown in the first row of Figure 5.27. The ROC curves of cases with both 1000 samples and 500 samples were shown in the bottom plot of Figure 5.27. 1000-sample-reconstruction curve trended to the left upper corner a little more than that of the one with 500 samples.

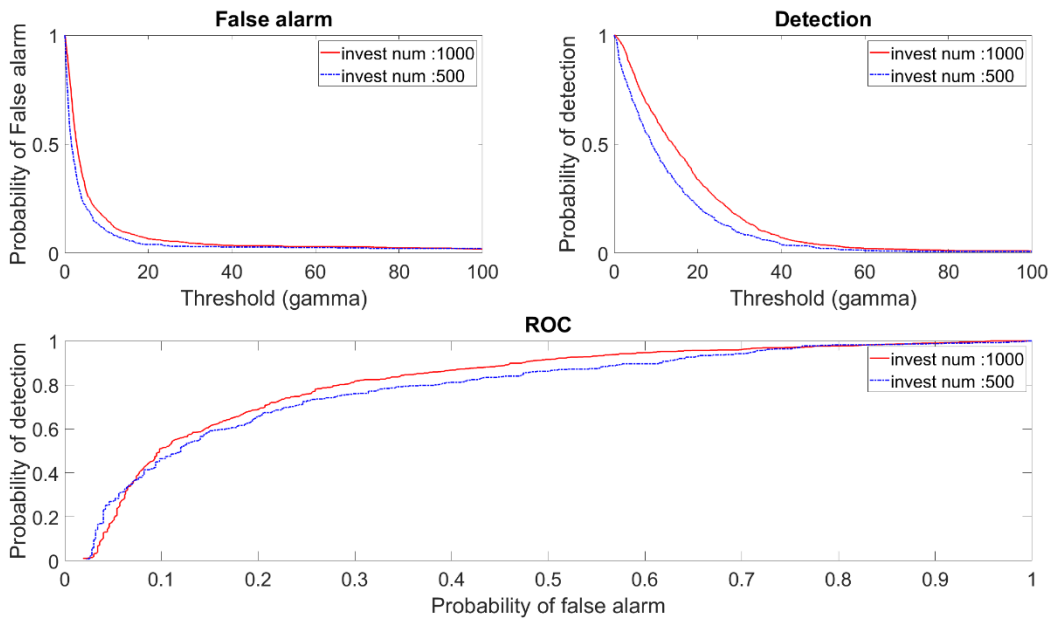


Figure 5.27. Receiver operating characteristic of detectability of air-couple receivers in shear-tie region.

5.5. Conclusions

This chapter has investigated the skin-stringer complex composite panel by various methods: the data-driven matched field processing for cross-sectional defect identification; the convolutional neural network for locating impact source; the transfer function approach for damage detection both skin-stringer structure and skin-stringer-shear_tie structure. The composite skin_stringer_shear-tie panel, including both complexities of geometry and material properties, challenges researchers to explore new methods inclining to data-driven yet on the basis of the physics understanding. In the data-driven matched field processing, the replica (or model) was built from the pristine data instead of estimating wave structure on this complex panel, which increased the reliability. The idea of backpropagation originated from wave physics, time reverse and backpropagation to the source. Therefore, the excellent combination of physics and the data-driven method can overcome the difficulty in such a complex object. Later, the pure data-driven process was discussed by exploiting the simulation data achieved from ABAQUS, which showed a promising source identification without even knowing any physics knowledge of the object. This pure data-driven method will push the boundary for understanding the new material.

Moreover, the transfer function approach for damage detection was also investigated by scanning the large-scale panel. The method was modified from the traditional “Single-in and Single-out” (SISO) to “Dual-output,” releasing the condition that the accurate excitation signal can be ignored. Also, “dual-output” modification minimized the impacts of the transducers’ response and the transducers-to-structure coupling effects compared to SISO. The structural coherence (the structural transfer function) between two receivers was brought out using a deconvolution operation and reducing the incoherent disturbance. Both simple zone and complex zone were discussed under the transfer function approach. The simulated damage on the stringer

flange, stringer heel, and stringer cap were identified by tracing the transfer function variations. The complex zone, including shear-tie, was also investigated by involving statistical analysis for damage detection confidences.

5.6. Acknowledgements

This work was funded by the Federal Aviation Administration Joint Center of Excellence for Advanced Materials (FAA Cooperative Agreement 12-C-AM-UCSD)

This work was in collaboration with Prof. Hyonny Kim and Chaiane Wiggers De Souza, who were acknowledged for designing and fabricating the test panels, manufacturing the mini-impactor, and shims. Chaiane also participated greatly with most experiments in this chapter.

Chapter 5 is, in part, has been published in Ranting Cui, Guillermo Azuara, and Francesco Lanza di Scalea. "Composite elastic property identification through guided wave inversion and damage detection by data-driven process." *In Health Monitoring of Structural and Biological Systems XIV*, vol. 11381, p. 113810I. International Society for Optics and Photonics, 2020. The dissertation author was the primary investigator and author of this paper.

5.7. References

- [1] Giurgiutiu V. Structural health monitoring (SHM) of aerospace composites. *Polym. Compos. Aerosp. Ind.*, Elsevier; 2015, p. 449–507.
- [2] Datta SK, Shah AH, Bratton RL, Chakraborty T. Wave propagation in laminated composite plates. *J Acoust Soc Am* 1988;83:2020–6.
- [3] Datta SK, Ju TH, Shah AH. Scattering of an impact wave by a crack in a composite plate 1992.
- [4] Guo N, Cawley P. The interaction of Lamb waves with delaminations in composite laminates. *J Acoust Soc Am* 1993;94:2240–6.
- [5] Michaels JE, Lee SJ, Croxford AJ, Wilcox PD. Chirp excitation of ultrasonic guided waves.

Ultrasonics 2013;53:265–70.

- [6] Castaings M, Hosten B. Ultrasonic guided waves for health monitoring of high-pressure composite tanks. *Ndt E Int* 2008;41:648–55.
- [7] Tzou HS, Tseng CI. Distributed piezoelectric sensor/actuator design for dynamic measurement/control of distributed parameter systems: a piezoelectric finite element approach. *J Sound Vib* 1990;138:17–34.
- [8] Ng TH, Liao WH. Sensitivity analysis and energy harvesting for a self-powered piezoelectric sensor. *J Intell Mater Syst Struct* 2005;16:785–97.
- [9] Castaings M, Cawley P. The generation, propagation, and detection of Lamb waves in plates using air-coupled ultrasonic transducers. *J Acoust Soc Am* 1996;100:3070–7.
- [10] Castaings M, Cawley P, Farlow R, Hayward G. Single sided inspection of composite materials using air coupled ultrasound. *J Nondestruct Eval* 1998;17:37–45.
- [11] Baggeroer AB, Kuperman WA, Schmidt H. Matched field processing: Source localization in correlated noise as an optimum parameter estimation problem. *J Acoust Soc Am* 1988;83:571–87.
- [12] Tabian I, Fu H, Khodaei ZS. A convolutional neural network for impact detection and characterization of complex composite structures. *Sensors (Switzerland)* 2019;19:1–25. <https://doi.org/10.3390/s19224933>.
- [13] Lubeigt E, Rakotonarivo S, Mensah S, Chaix J-F, Baqué F, Kuperman WA. Passive structural monitoring based on data-driven matched field processing. *J Acoust Soc Am* 2019;145:EL317–22.
- [14] Yan J, Downey A, Cancelli A, Laflamme S, Chen A, Li J, Ubertini F. Concrete crack detection and monitoring using a capacitive dense sensor array. *Sensors* 2019;19:1843.
- [15] Gulgec NS, Takáč M, Pakzad SN. Convolutional neural network approach for robust structural damage detection and localization. *J Comput Civ Eng* 2019;33:4019005.
- [16] Kiranyaz S, Ince T, Gabbouj M. Real-time patient-specific ECG classification by 1-D convolutional neural networks. *IEEE Trans Biomed Eng* 2015;63:664–75.
- [17] Kim P. Matlab deep learning. *With Mach Learn Neural Networks Artif Intell* 2017;130:21.
- [18] Santurkar S, Tsipras D, Ilyas A, Madry A. How does batch normalization help optimization? *ArXiv Prepr ArXiv180511604* 2018.
- [19] Yarotsky D. Error bounds for approximations with deep ReLU networks. *Neural Networks* 2017;94:103–14.
- [20] Kingma DP, Ba JL. Adam: A method for stochastic optimization. *3rd Int Conf Learn*

Represent ICLR 2015 - Conf Track Proc 2015:1–15.

- [21] Roth PR. Effective measurements using digital signal analysis. *IEEE Spectr* 1971;8:62–70.
- [22] Capriotti M, Lanza di Scalea F. Robust non-destructive inspection of composite aerospace structures by extraction of ultrasonic guided-wave transfer function in single-input dual-output scanning systems. *J Intell Mater Syst Struct* 2020;31:651–64. <https://doi.org/10.1177/1045389X19898266>.
- [23] Capriotti M, Cui R, di Scalea FL. Guided wave techniques for damage detection and property characterization in composite aerospace structures. *Heal. Monit. Struct. Biol. Syst. XIII*, vol. 10972, International Society for Optics and Photonics; 2019, p. 1097204.
- [24] Capriotti M, Kim HE, Scalea FL di, Kim H. Non-Destructive inspection of impact damage in composite aircraft panels by ultrasonic guided waves and statistical processing. *Materials (Basel)* 2017;10:616.
- [25] Tippmann JD, Lanza Di Scalea F. Passive-only damage detection by reciprocity of Green's functions reconstructed from diffuse acoustic fields with application to wind turbine blades. *J Intell Mater Syst Struct* 2015;26:1251–8. <https://doi.org/10.1177/1045389X14538539>.
- [26] Mariani S, Nguyen T, Phillips RR, Kijanka P, Lanza di Scalea F, Staszewski WJ, Fateh M and Carr G. Noncontact ultrasonic guided wave inspection of rails. *Struct Heal Monit* 2013;12:539–48. <https://doi.org/10.1177/1475921713498533>.
- [27] Liang AY, Sternini S, Capriotti M, di Scalea FL. Help-High Speed Ultrasonic Rail Inspection by Passive Noncontact Technique. *Mater Eval* 2019;77.
- [28] di Scalea FL, Zhu X, Capriotti M, Liang A, Mariani S, Sternini S, Wilson R. High-speed non-contact ultrasound system for rail track integrity evaluation. *Heal. Monit. Struct. Biol. Syst. XII*, vol. 10600, International Society for Optics and Photonics; 2018, p. 106000J.
- [29] Lanza di Scalea F, Sternini S, Liang AY. Robust passive reconstruction of dynamic transfer function in dual-output systems. *J Acoust Soc Am* 2018;143:1019–28.
- [30] Datta D, Cui R, di Scalea FL, Wilson R. High-speed Rail Inspection by a Non-contact Passive Ultrasonic Technique. 2021.
- [31] Rizzo P, Sorri E, di Scalea FL, Viola E. Wavelet-based outlier analysis for guided wave structural monitoring: application to multi-wire strands. *J Sound Vib* 2007;307:52–68.
- [32] Fan J, Upadhye S, Worster A. Understanding receiver operating characteristic (ROC) curves. *Can J Emerg Med* 2006;8:19–20

Chapter 6. Ultrasonic beamforming imaging for damage characterization in solids

6.1. Introduction

In Nondestructive inspections (NDIs), ultrasonic imaging meets the need to detect the defects enclosed in the solids and not easily accessible from the surface. In a specific situation, the defect reflection of the ultrasonic waves may not be in a favorable direction of the sensing array (the broadside of the array). The particular location, orientation, geometry of the defect, or sometimes the defect coupled with the multilayered structure, make it difficult to access the real flaw from the transducer placed on the surface. As an interposed medium, the wedge connected to the transducer array allows directing the actuating energy to maximize the defect reflections [1]. One of a typical application of wedge-ultrasonic imaging for NDI is the detection of “transverse defects” (TDs) which usually grows with an angle close to the vertical direction [2].

Optimum array processing has been used for decades in NDI [3-8]. The total-focus-method (TFM) is one of the common imaging techniques using the delay-and-sum (DAS) algorithm by intersecting elliptical focus lines from various transmitter-receiver pairs [9]. An enhancement of DAS is the delay-multiply-and-sum (DMAS) algorithm [11], which increases the resolution by intersecting the multiplication before summation, in other words, adding more potential wave propagation paths.

In this section, the time domain beamformer and frequency-domain beamformer were investigated to reconstruct defect images in solids (the aluminum block and railheads). The real-

time imaging prototype regarding hardware and software was discussed to achieve both higher accuracy and speed. Finally, the comparisons between traditional A-scan and time-domain beamformer were performed.

6.2. Time delay estimation with the wedge

The estimation of the wave traveling time is a crucial factor to properly backpropagate the received signals to expected locations further identify the potential defect. The classical Delay-and-Sum (DAS) requires the knowledge of the locations of all array element transmitter-receiver pair and that of the focus point $P(x,y)$ in the solid. The wave starts from transmitter i , to virtual transmitter interface point i , reflected by focus point $P(x,y)$, back to virtual receiver interface point j , eventually back to receiver j . All paths are shown in Figure 6.1(a) according to Ref.[11]. The refraction happens at the wedge-solid interface in both transmitted and reflected waves. In this section, only longitudinal (L-) waves are considered in the wedge material, although in fact both shear (S-) and longitudinal (L-) waves exist. This simplification was used due to the fact that the conventional ultrasonic transducer arrays are always employed with the gel coupling layer, which are preferably detecting mostly L-waves. Generally, the time estimation of transmitter-receiver i,j pair can be demonstrated as

$$\tau_{ij,xy} = \frac{d_{i,xy}^1}{c_{LW}} + \frac{d_{i,xy}^2}{c_{L,S}} + \frac{d_{j,xy}^3}{c_{L,S}} + \frac{d_{j,xy}^4}{c_{LW}} \quad (6.1)$$

Where, c_{LW} is the L-wave speed in the wedge material, $c_{L,S}$ is the L-wave speed or S-wave speed in the solids. $d_{i,xy}^{(1)}$ is the distance from transmitter i to virtual point i on the interface calculated by Eq. (6.2). $d_{i,xy}^{(2)}$ is the distance from virtual point i on the interface to focus point P

(x,y) calculated by Eq. (6.3). $d_{j,xy}^{(3)}$ is the distance from the focus point $P(x,y)$ reflected back virtual point j on the interface calculated by Eq. (6.4). Finally, $d_{j,xy}^{(4)}$ is the distance from virtual point j , on the interface to receiver j , on the array calculated by Eq. (6.5).

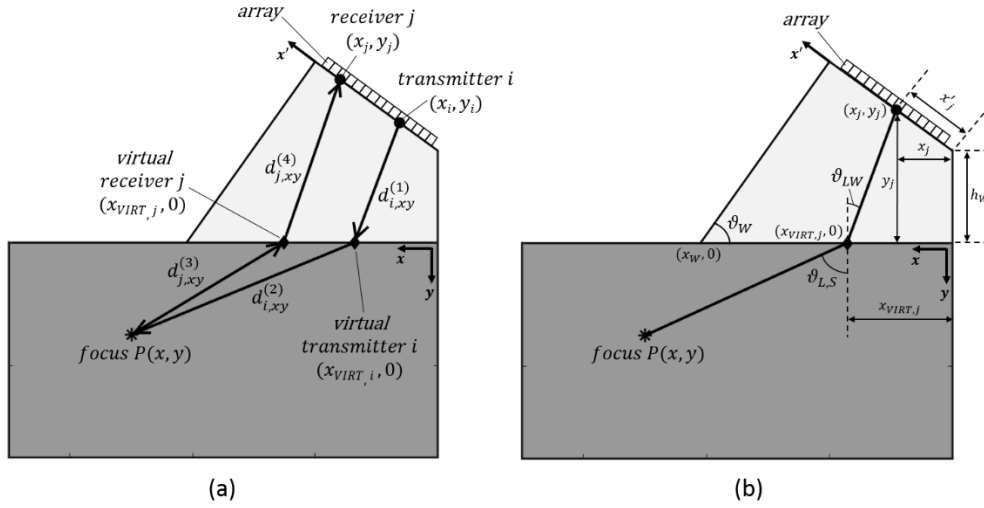


Figure 6.1. Time delay calculation with wedge [11].

$$d_{i,xy}^1 = \sqrt{(x_i - x_{VIRT,i})^2 + (y_i - y_{VIRT,i})^2} \quad (6.2)$$

$$d_{i,xy}^2 = \sqrt{(x_{VIRT,i} - P_x)^2 + (y_{VIRT,i} - P_y)^2} \quad (6.3)$$

$$d_{j,xy}^3 = \sqrt{(x_{VIRT,j} - P_x)^2 + (y_{VIRT,j} - P_y)^2} \quad (6.4)$$

$$d_{j,xy}^4 = \sqrt{(x_j - x_{VIRT,j})^2 + (y_j - y_{VIRT,j})^2} \quad (6.5)$$

$$\frac{\sin(\theta_{LW})}{\sin(\theta_{LS})} = \frac{c_{LW}}{c_{LS}} \quad (6.6)$$

Moreover, the wave propagating in the special interface area is shown in Figure 6.1(b) governed by Snell's law, shown in Eq. (6.6).

6.3. Experimental setup

The experimental test was implemented to test two kinds of algorithms shown in detail in next section. Figure 6.2 shows the experimental setup as an example on the rail. The transducer wedge connected to the probe was a Rexolite wedge (Olympus NDT SA12-N55S), shown in Figure 6.2 (a), 73mm in length, 15mm in height, and 54° wedge angle.

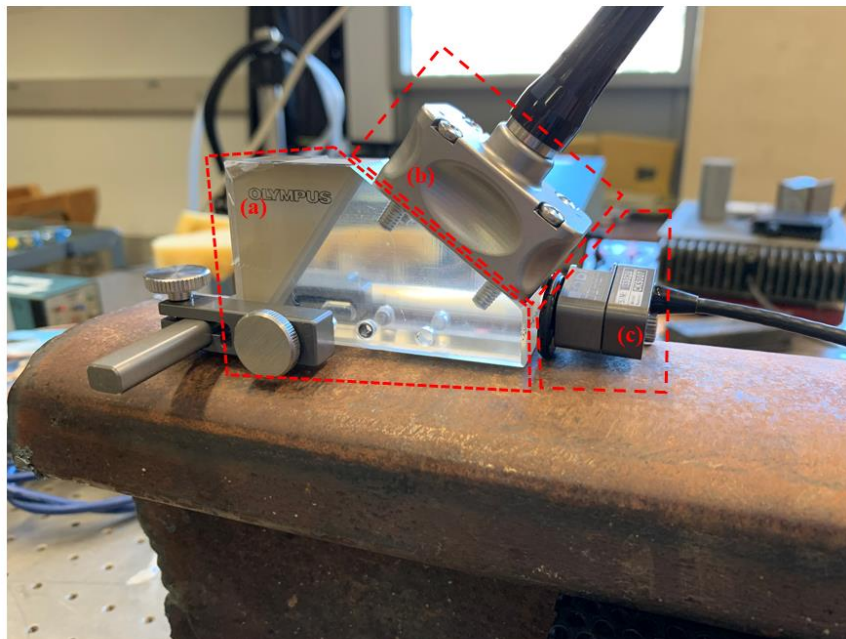


Figure 6.2. Experimental Setup: (a) Wedge; (b) Probe; (c) Encoder.

The probe, shown in Figure 6.2(b), was a 64-element linear array (Olympus NDT Array, 5L64-38.4X10-A12-P-2.5-OM), with central frequency at 5 MHz, 38.4mm ×10mm total active area, and 0.6mm element pitch.

The encoder, shown in Figure 6.2(c), was a spring-loaded encoder with 2.5m encoder cable, a universal clamp system. It is designed to provide encoded linear position of probes in manual scanning operations. The encoder resolution is 16.00counts/mm.



Figure 6.3.A full-matrix capture (FMC) controller.

The array probe, encoder and computer were all connected to a full-matrix capture (FMC) controller (Advanced OEM Solutions, Cincinnati, OH, USA) shown in Figure 6.3. The FMC controller can generate adjustable pulse excitations and allow to access raw radio frequency (RF) waveforms in reception. Two screws helped connect the probe and the transducer wedge to ensure

the decent connection. The gaps of the wedge/solid interface and the probe/wedge interface were filled with conventional ultrasonic gel couplant to guarantee proper transmission/reception of the ultrasonic waves. Each transducer in the array firing sequentially, and all transducers receiving at each firing.

6.4. Frequency domain beamforming (FDB) algorithm and results

6.4.1. FDB Algorithm

In this subsection, experiments were conducted using a 64×64 FMC scheme, with total 4096 waveforms. Figure 6.4 shows Frequency domain beamforming algorithm in detail. The raw signal matrix was formed with the dimension 1501×4096 , where each signal contained 1501 points due to the memory limitation of the FMC controller.

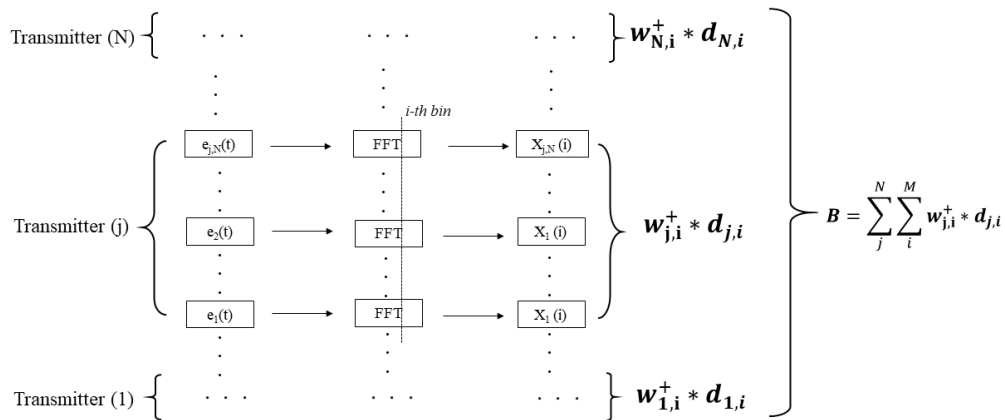


Figure 6.4. Frequency domain beamforming algorithm workflow [12].

FDB algorithm applied the backpropagation of ultrasonic waves in the frequency domain. First, the Fast Fourier Transformation (FFT) was applied to each column (each time series, the hamming window function was used to avoid leakages [13]). Later, due to the knowledge of negative time in time was equivalent to the complex conjugate phase in frequency domain, the backpropagation was performed by multiplying exponential term ($e^{-1j*2 \pi*\tau}$) with the snapshot of the signal, including all signal in one frequency bin. Eventually, the final image was achieved by coherently summing beamformers of enough frequency bins on account of the image resolution requirement. The more beamformers were summed, the higher resolution the image approached. FDB algorithm was quite popular in the underwater acoustic application because of quick and precise location identification of the source without knowing the geometry of the source [14]. Only a few frequency bins were needed to investigate the source location, which was fast and accurate. However, in the ultrasonic imaging scenarios the geometry of the defect (reflector or source) became much more crucial, which led to the more summation of the beamformers of different frequency bins to achieve desired resolution resulting in expansive computation. Whereas the best resolution was still held by FDB algorithm, which drives researcher to take a more in-depth study.

6.4.2. Results: the aluminum block with two drilling hole defects

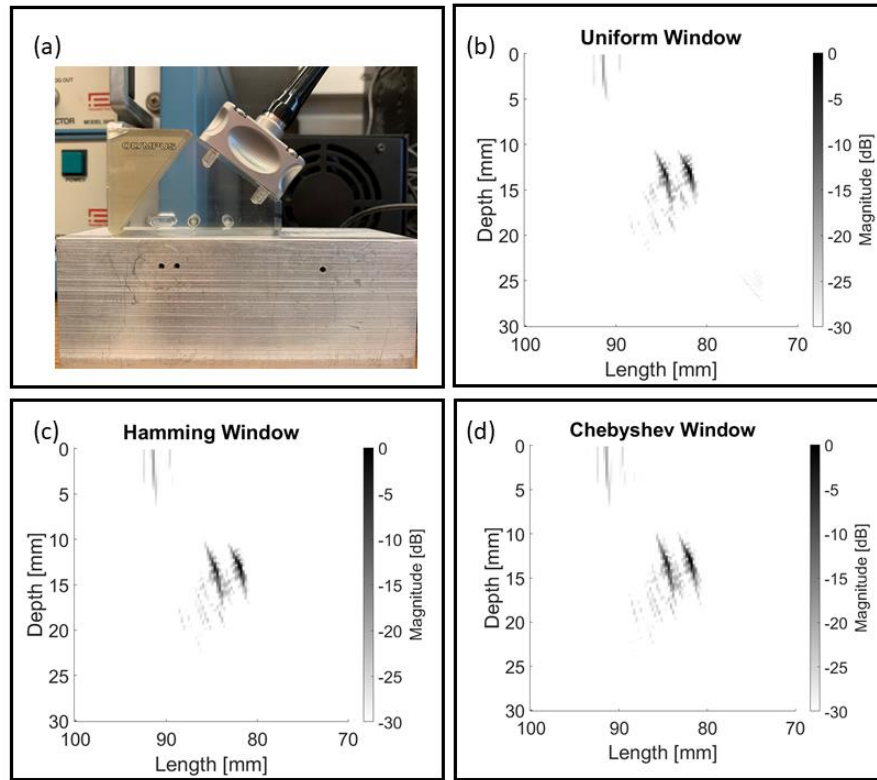


Figure 6.5. Two holes imaging in aluminum block: (a) the real experiment; (b) the result with uniform window; (c) the result with hamming window; (d) the result with Chebyshev window.

The test piece used was an aluminum block with two 2.5 mm-diameter holes drilled at about 13mm from the top surface. The distance between the two holes was 6mm, shown in Figure 6.5. The wavelength of the ultrasonic waves in aluminum were 1.3mm for the L-wave. All experimental results with depth and length in mm, and amplitude scale in dB. Figure 6.5(a) was the experimental setup for this test. Figure 6.5 (b) showed no spatial window functions were applied to sensor array. Second, the Hamming window function was examined to improve the resolution of the final image, shown in Figure 6.5 (c). Then, the Chebyshev window was also examined to achieve a good improvement, shown in Figure 6.5 (d). The reason for studying

Chebyshev window function was due to its equal side lobe nature [12]. In contrast of other window function suppressing the side lobe and maintaining the main lobe, Chebyshev window treated the side lobe equally to avoid the situation that the actual signal coming from the direction besides broadside, which is commonly used in radar systems.

6.4.3. Results: the railhead with one drilling hole defect

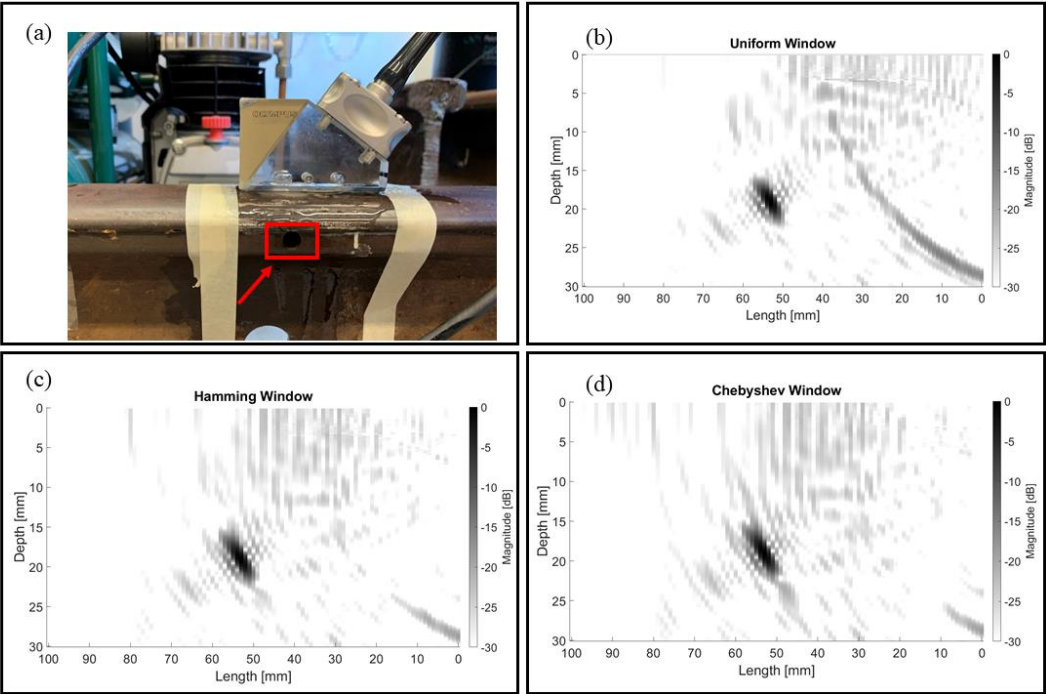


Figure 6.6. Drilling hole imaging in railhead: (a) real experiments; (b) results with uniform window; (c) results with hamming window; (d) results with Chebyshev window.

The second test piece used was a 136RE rail track with 20mm-diameter hole drilled at about 18mm from the top surface. The experimental setup with the hole on the rail head was shown in Figure 6.6(a). The wavelength of ultrasonic wave in steel was 1.13mm for the L-wave. All

experimental results with depth and length in mm, and amplitude scale in dB. Figure 6.6(b) showed no spatial window function applied on the sensor array. Figure 6.6(c) showed the results after applying the hamming window function and Figure 6.6(d) also investigated the Chebyshev window function in this case. It showed the hamming window as a static window gave the best resolution in term of less side lobes and the sharp main lobe in both cases according to Figure 6.5 and Figure 6.6.

6.5. Time domain beamforming (TDB) algorithm and results

6.5.1. TDB Algorithm

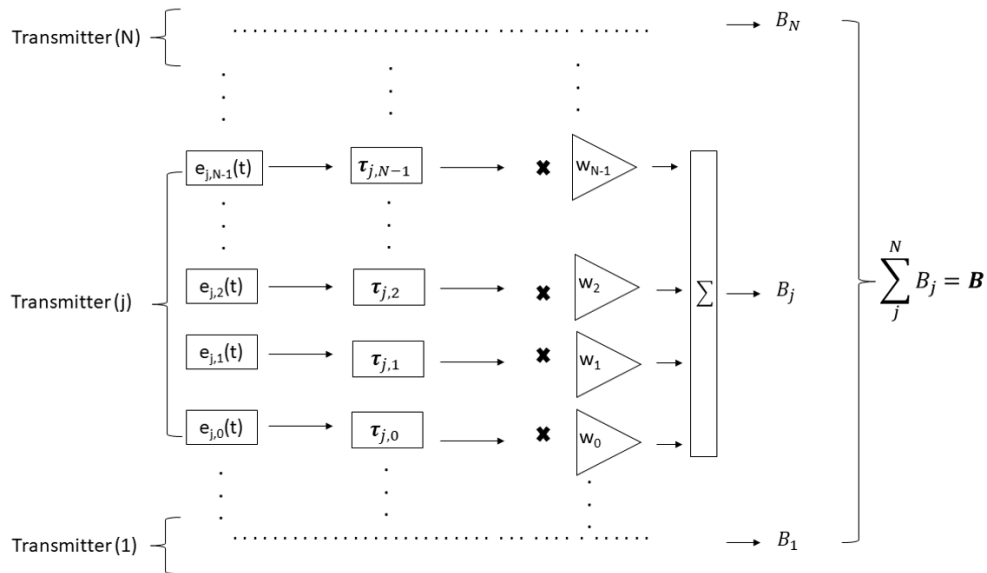


Figure 6.7. Time domain beamforming algorithm workflow [12].

The TDB algorithm, in contrast with the FDB algorithm, applied the backpropagation of the ultrasonic waves in time. The huge advantage of this approach is computation efficiency, with no need for FFT and the beamformer summation of multiple frequency bins. It also needs a high sampling rate to acquire enough data points to precisely applied the wave backpropagation in the time domain. The sampling frequency should be around five times Nyquist law by convention, 12.5 MHz satisfying this requirement. The small amount of data (the small searching area in contrast with underwater acoustic application) allows this algorithm more suitable in real-time without compromising geometry resolution. The algorithm runs by first calculating the time delay sample indices. Then Hilbert transform is applied to each time series to allow the wave package smoother instead of jumping up and down. The compounding amplitudes of sample indices were formed to the image of the searching area. On the decibel scale, the higher the dB is, the worse the defect is.

6.5.2. Averaging and the prob-wedge coupling impact

```

%% Acquisition parameters
daqvalues.start=20; %value in microseconds
startsamples=round(daqvalues.start/10e6*Fs);
samples=1501;%2^11;%1024;
daqvalues.range=(samples-1)/Fs*1e6; %value in microseconds

daqvalues.TimeSlot=20000; %value in microseconds
% daqvalues.TimeSlot=ceil(daqvalues.range*Narray/1000)*10000;

daqvalues.wedgedelay=0; %value in microseconds

%% Generation parameters
daqvalues.widthpulsar=0.2; % 0.1 is for 5MHz; 0.2 for 2.5MHz ; 0.22 for 2.25MHz

```

Figure 6.8. Auto configuration file adjustment.

This subsection tried to find the best way to increase the resolution in terms of the defect geometry. One improvement of the experimental setup was the configuration file adjustment shown in the Figure 6.8. “daqvalues” was a structure type of variable in MALLAB, including “start” (the time in microsecond start to save the time series), “samples” (total samples need to acquire), “TimeSlot” (buffer size for storing data), “widthpulser” (the frequency of the pulse generated from the controller). With all these adjustable options inbuilt in MATLAB scripts, the experiments would be performed more effectively and efficiently.

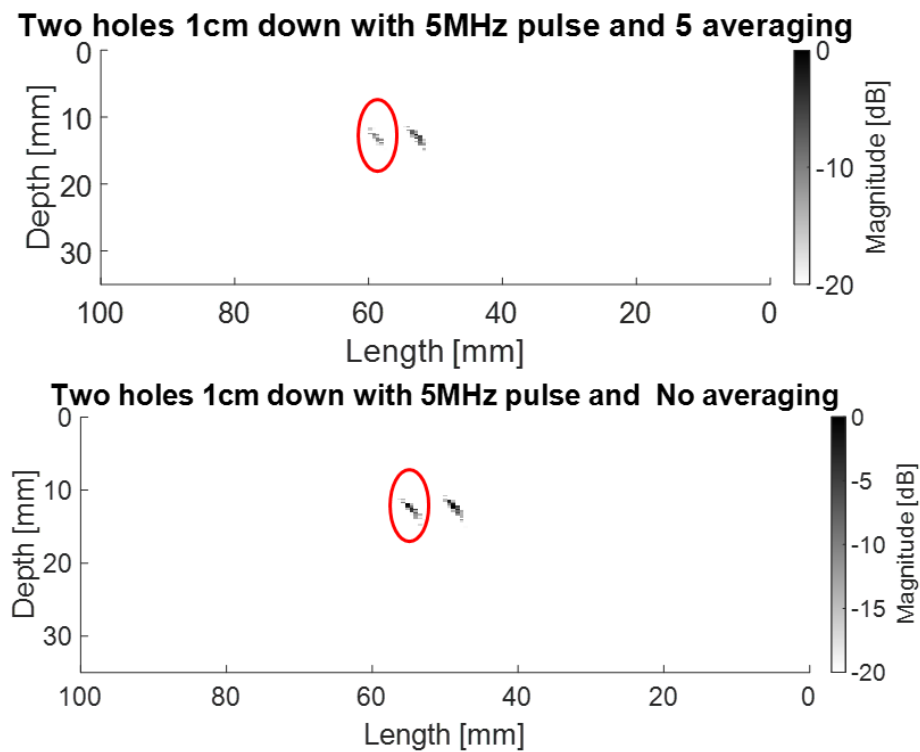


Figure 6.9. The comparison of the imaging on averaging and no-averaging.

As a continuation of improving resolution, averaging several tests to achieve a higher resolution of the defect was a possible way. Figure 6.9 showed the comparison of the averaging and no averaging of two-hole imaging of the aluminum block. It turned out the different averaging tests on the same location were doing the opposite way to improve the resolution due to the high precision of this application. Because if and only if the tests were applied on the exact same location, the averaging will achieve resolution improvement. Otherwise, the tiny shakes of the device will cause image resolution degradation. Moreover, those tiny shakes were not avoidable for a human-controlled experiment because of the gel couplant benefiting the wave traveling through, in the meantime providing the difficulty to hold the device in the exact same location for different tests.

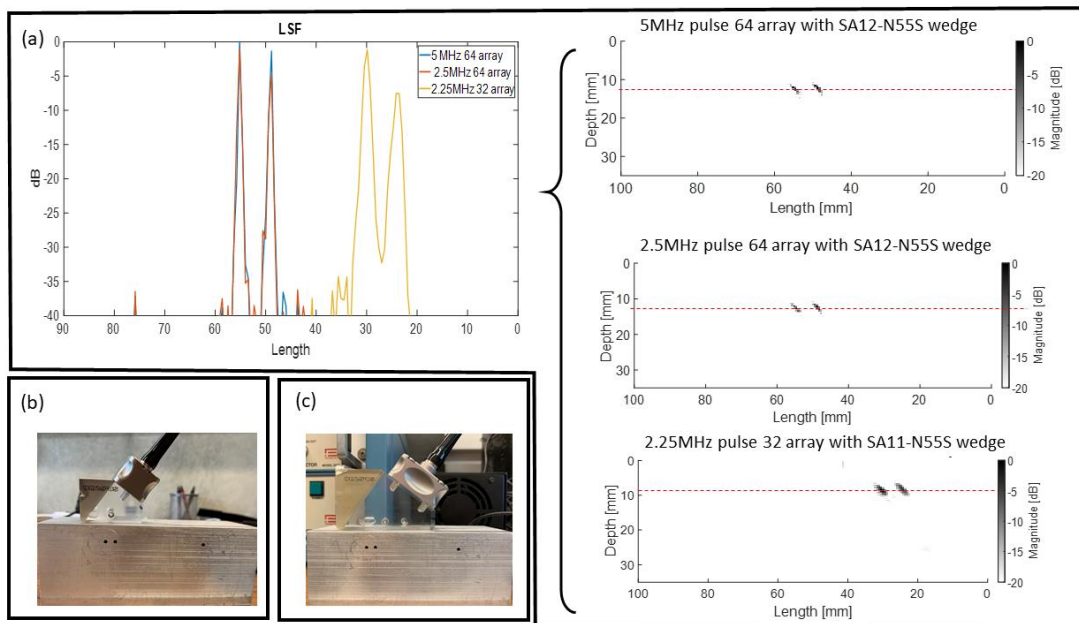


Figure 6.10. The coupling impact between probe and wedge: (a) comparisons among three different scenarios; (b) 32 array with SA11-N55S wedge; (c) 64 array with SA12 - N55S wedge.

Moreover, the matching degree between probe and wedge was another factor in improving or degrading the defect imaging quality. Under the current experimental circumstance, three different tests were performed to look for the best combination of the probe, wedge, and the frequency of transmitting pulse. The Rexolite wedges, either SA11-N55S or SA12-N55S, were like filters, only allowing the waves under 2.5MHz to pass through. The two probes had the central frequencies, 2.25MHz and 5MHz respectively. The first combination used a 64-element probe with the 5MHz-central-frequency pulse and SA12-N55S wedge; the second combination was using 64-element probe with the 2.5MHz-central frequency pulse and SA12-N55S wedge; the third combination was using a 32-element probe with the 2.25MHz-central frequency pulse and SA11-N55S wedge. The first and second combinations used the setup shown in Figure 6.10(c), and the third combination used the setup shown in Figure 6.10(b). Figure 6.10(a) showed the results of each case in terms of 2D defect image reconstruction and linear spread function on the aluminum block mentioned above. The first two combinations showed similar and better results among the three with thinner main lobe and lower side lobe. In contrast the third combination gave fat main lobe, which increases the ambiguity of the defect location. The first combination was chosen due to the probe working better with the designed 5MHz central frequency.

6.5.3. 3D defect reconstruction in real-time with encoder

To make a more straightforward application in the field, the real-time 3D defect reconstruction with encoder control was required. Figure 6.11 showed an interface screenshot of the real-time experiment on the 136RE railhead with a drilled hole. From left to right, the first figure showed the real-time 2D image reconstruction; the second figure showed the real-time 3D image reconstruction stitching the 2D images together in real-time; the third figure monitored the

experiment real-time; the fourth figure showed the test piece applied in this subsection. The MATLAB command window traced the encoder control by counting the loop number, which represented the encoder working status.

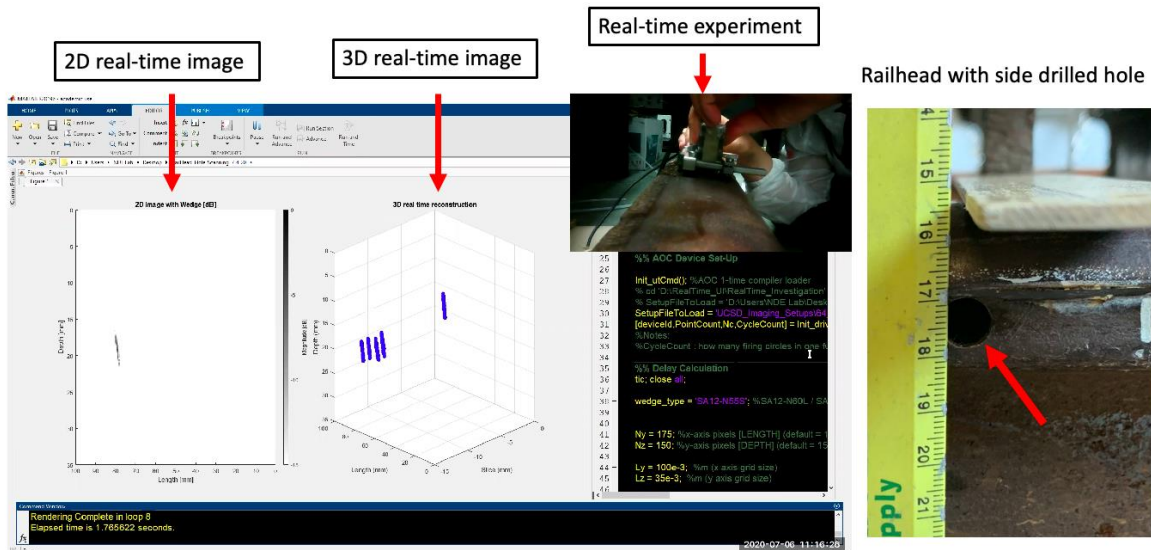


Figure 6.11. The real-time 3D image reconstruction with encoder control.

6.5.4. Results: Experimentation in Transportation Technology Center, Inc (TTCI) defect library.

The experiments presented in this section were done in the TTCI rail defect library, Colorado, USA. There were four pieces of railhead tested in this section with various types of natural transverse defects (TD) as follows: Section #1(B6) 115RE Head center 21% TD; Section #2(B8) 136RE Head center 5.9% TD; Section #3(N3) 136RE Head corner 14% TD and Section #4(“TDinWeld”) 136RE TD in the weld with 7.3% area. The prototype was scanning along the transverse direction shown in Figure 6.12(1). The system would yield a 2D defect image under the current location, shown in Figure 6.12(2) and (3). The primary defect would be stored and stitched

on the 3D defect reconstruction plot, shown in Figure 6.12(4). Then the loop would continue to the next location, eventually constructing an entire 3D defect image.

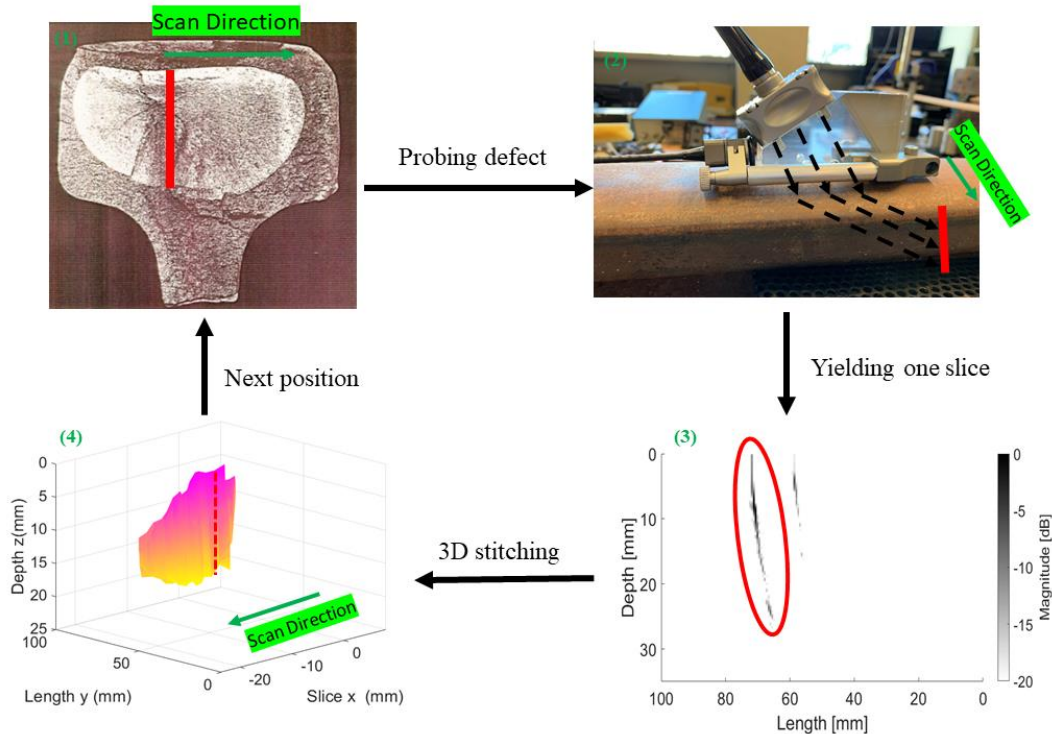


Figure 6.12. The scheme of 3D defect reconstruction of railhead.

The first test was applied on the sample #1 (B6) 115RE railhead center with 21% TD. The two algorithm TDB and FDB were compared in this section. The left subfigure in Figure 6.13 was the on-site experiment of sample #1. The first row of Figure 6.13 was results from TDB algorithm in 2D defect image and 3D defect image. The second row of Figure 6.13 was results from FDB algorithm in both 2D defect image and 3D defect image. The results from two rows provided similar resolution yet FDB was more time consuming due to multiple-frequency-bin summation was required to achieve higher resolution. The running time of FDB algorithm was 40 times longer than TDB algorithm. Therefore, the following discussion was based on TDB algorithm.

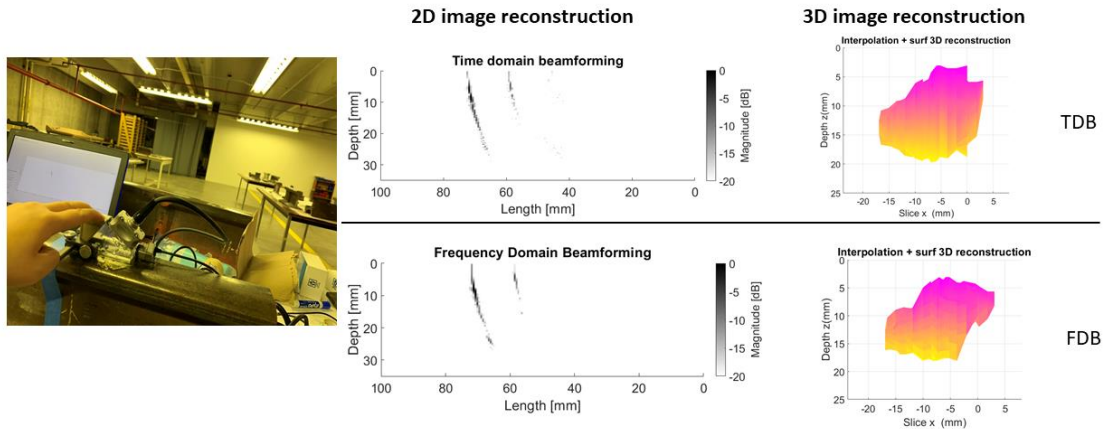


Figure 6.13. The comparison between TDB and FDB on the sample B6 115RE.

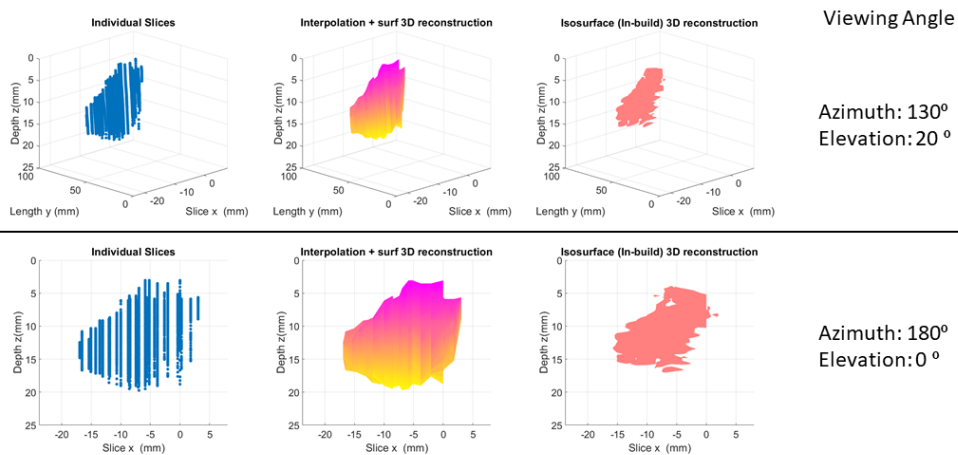


Figure 6.14. Comparison of 3D imaging reconstructions.

Another 3D image generation issue was properly choosing the stitching method to reconstruct the image, shown in Figure 6.14. The first column showed the raw point slice from the individual test. The first method was implemented by interpolating within each slice as well as between slices to make the smoother connection then using the ‘surf’ function in MATLAB to

reconstruct the 3D image. The other one was directly applied ‘isosurface’ function in MATLAB to do reconstruction. ‘isosurface’ in MATLAB involved in-built interpolation would cause reduction of the raw data, which led to an underestimation of the defect size.

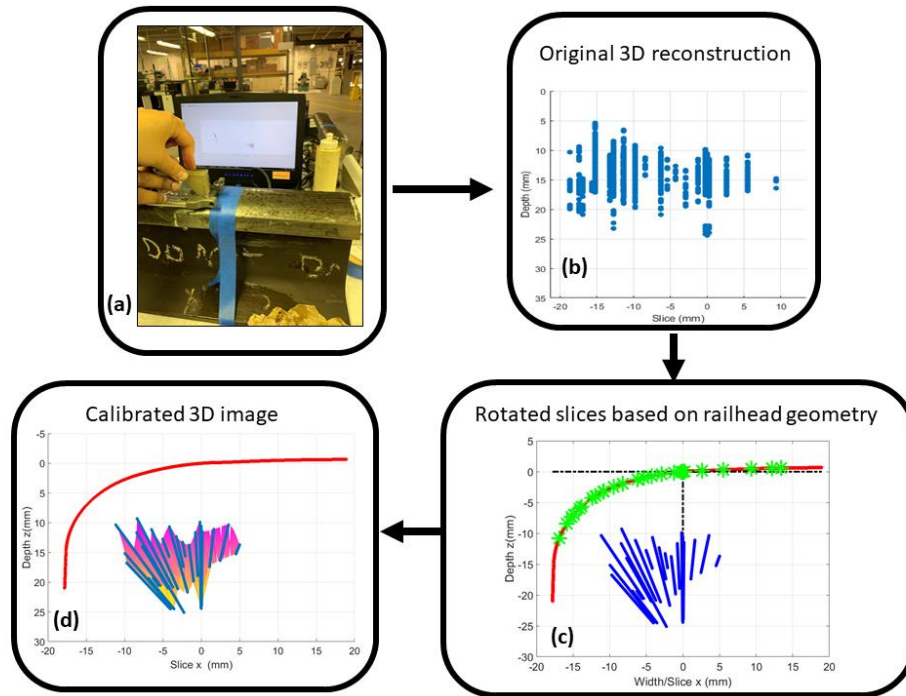


Figure 6.15. The geometry calibration and reconstruction on the sample N3 136RE.

The second test was applied on the sample#2 (N3) 136RE railhead. The geometry calibration was considered in this sample since the scanning was most on the railhead corner area where the railhead curvature was significant. The on-site experiment was shown in Figure 6.15(a). Figure 6.15(b) showed the original point cloud from the stitched from 2D imaging. The anchor points on the railhead section were defined according to the experiment. All slices were then rotated based on the anchor points on the railhead corner surface, shown in Figure 6.15(c). Finally, the calibrated 3D image was reconstructed and presented in Figure 6.15(d). The geometry

calibration aided the curvature impact from the railhead corner to make the final image closer to the actual defect.

The third test was applied on the sample #3 (B8) 136RE railhead. Most scanning on this sample happened on the railhead top area flatter than the corner area. So the geometry calibration would not be applied in this sample. The on-site experiment was shown in Figure 6.16 (a) top, and the bottom is the real-time 2D image of that position. Figure 6.16 (b) showed the 3D defect reconstruction using the “interpolation + surf” method discussed above. The first column was the raw slices, and the second column was the reconstructed image. The first row was in the viewing angle azimuth 130° and elevation 20° , which provided the potential to investigate the orientation of the defect in 3D. The second row was in the viewing angle azimuth 180° and elevation 0° , which was the best angle to size the defect.

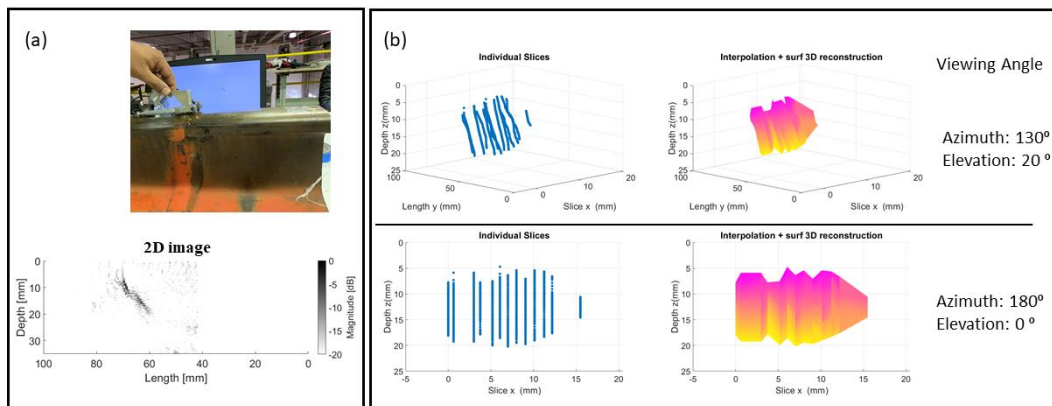


Figure 6.16. The defect reconstruction of sample B8 (136RE): (a). Real experimental setup and 2D real-time defect imaging; (b) 3D-point clouds and surface reconstruction.

The final test was applied on the sample #4 (TD-in-the-weld) 136 RE railhead. The most scanning position was on the flat area on the top of the railhead, same as sample #3, so the geometry calibration was not applied in this sample. The on-site experiment was shown in Figure 6.17(a) top and the bottom is the real-time 2D image of one position. Figure 6.17 (b) showed the 3D defect reconstruction using the “interpolation + surf” method, same as sample#3. The first column was raw slices and the second column was the reconstructed image. The first row was in the viewing angle azimuth 130° and elevation 20° , which provided the potential to investigate the orientation of the defect in 3D. The second row was in the viewing angle azimuth 180° and elevation 0° , which was the best angle to measure the defect size.

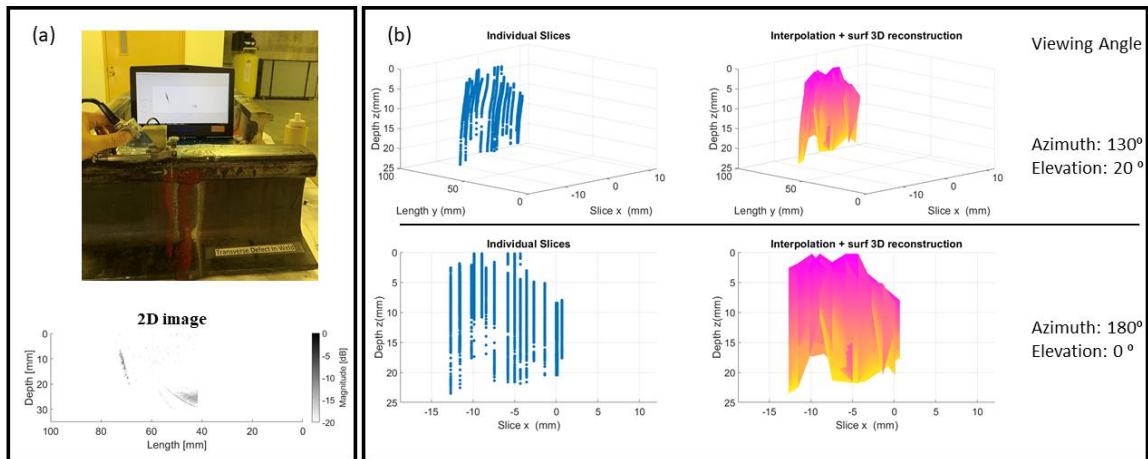
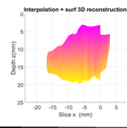
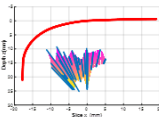
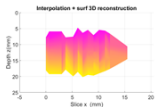
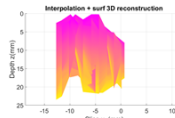


Figure 6.17. The defect reconstruction of sample TD-in-the-weld (136RE): (a). Real experimental setup and 2D real-time defect imaging; (b) 3D-point clouds and surface reconstruction.

6.6. Conclusions

Ultrasonic imaging potentially proves its ability to accurately estimate the damage, leading to reduced maintenance costs by informed decision-making. This study demonstrates the improvements in algorithms (TDB and FDB) and real application calibration to the traditional 3D image reconstruction to make this detection realistic to transverse defects on the railhead. The results of four testing samples were compared with those of the traditional A-scan shown in Table 6.1. The comparison has been done in terms of the primary defect of the individual railhead sample. Tests on Samples #1 and #2 were underestimated the size of the TD, whereas those on sample #3 and sample #4 were overestimated the size of the TD compared to A-scan. However, the overall results were relatively consistent with A-scan results with little deviation, which could be caused by operation area or analysis interpolation error.

Table 6.1 Comparison between A-scan and Ultrasonic imaging.

| Test sample | TTCI A-scan | UCSD imaging | Main defect |
|----------------|--|--|---|
| # 1 (B6) | Head area 3.98 inch ² = 2.568e3mm ² Defect width: 1.3" = 33.02mm Defect depth:0.8" = 20.32mm Defect percentage = 21%TD | Head area 3.98 inch ² = 2.568e3mm ² Defect width: 20.03mm Defect depth: 19.73mm Defect percentage = 12.07% TD |  |
| # 2 (N3) | Head area 4.82 inch ² = 3.11e3mm ² Defect width: 1" = 25.4mm Defect depth:0.85" = 21.59mm Defect percentage = 14%TD | Head area 4.82 inch ² = 3.11e3mm ² Defect width: 16.17mm Defect depth: 21.71mm Defect percentage = 8.87% TD |  |
| # 3 (B8) | Head area 4.82 inch ² = 3.11e3mm ² Defect width: 0.8" = 20.83mm Defect depth:0.45" = 11.43mm Defect percentage = 5.9%TD | Head area 4.82 inch ² = 3.11e3mm ² Defect width: 15.5mm Defect depth: 20.2mm Defect percentage = 7.91% TD |  |
| # 4 (TDinweld) | Head area 4.82 inch ² = 3.11e3mm ² Defect width: 0.9" =22.86mm Defect depth:0.5" =12.7mm Defect percentage = 7.3%TD | Head area 4.82 inch ² = 3.11e3mm ² Defect width: 13.38mm Defect depth: 23.49mm Defect percentage = 7.87% TD |  |

This study shows that the portable ultrasonic imaging system will be a potential replacement of current hand verification techniques for rail flaws by an inspection vehicle. The 3-D defect reconstruction images significantly improve the representation of the internal flaws in terms of size and orientation to provide practical suggestions for maintenances.

6.7. Fatigue history prediction of the railway track (future work /preliminary study)

Prognostics have been widely used for predicting the failure time of the component, which provides maintenance suggestions of replacement or running under strict monitoring. One of the leading prognostics applications is remaining useful life (RUL) estimation [15, 16]. Data-driven-based methods and physics-based methods are two major groups in prognostic. Data-driven-based methods allow us to learn the former history of the problem in order to predict based on the known knowledge, which proves accuracy and efficiency in the real application [17, 18].

The incredible attention has recently focused on impressive results achieved from deep learning (DL)[19,20] in fault diagnosis and the RUL estimation. A long short-term memory (LSTM) [21] model was proposed for RUL estimation to exploit the information of sequential sensors. However, LSTM requires a large amount of training data and significantly memory consuming during the training.

In this preliminary study, we propose a three-layer DL network for RUL prediction. The large amplitude noise added on the approximated theoretical crack growth curves yields realistic scenarios for the indication of the real experiment. By adjusting the learning rate, the model was trained efficiently with little compromising the accuracy.

6.7.1. Data preparation and training schedule

The data in this section generated based on the approximated theoretical curve of linear elastic fracture mechanics (LEFM)[22], the crack growth state was demonstrated by Paris law shown in Eq.6.7.

$$\frac{da}{dN} = A\Delta K^m \quad (6.7)$$

Where, $\Delta K = K_{max} - K_{min}$, $\frac{da}{dN}$ was the fatigue crack growth rate per cycle. da is the increment of the crack, dN is the increment cycle of the test. The exponent m was often near 3 for steel, which might be rationalized as the damage accumulation related to the plastic zone volume. A was close to 10^{-11} for steel alloy [23].

The approximated theoretical curve was generated, shown in Figure 6.18(a), the initial states with ΔK between [5, 20], using the function: *crack growth rate* = $\log\left(\frac{4}{\Delta K^1}\right)$. The Paris' law state followed Eq.6.7. The noise with standard Gaussian distribution and 0.3 amplitude was added to the approximately theoretical curve yielding the final studied curve. The approximately theoretical curve involved the nonlinear property, which helped the following study general enough to project the real experiment scenario. The final time series was realistic by adding noise. Because the real measurement of the crack growth would be jumping up and down, which resulted in difficulty in tracking the primary trend. The extreme case was studied here by adding exaggerate the level of noise to touch the worse-case scenario, on the contrary, leading this method more robust to the real experiments.

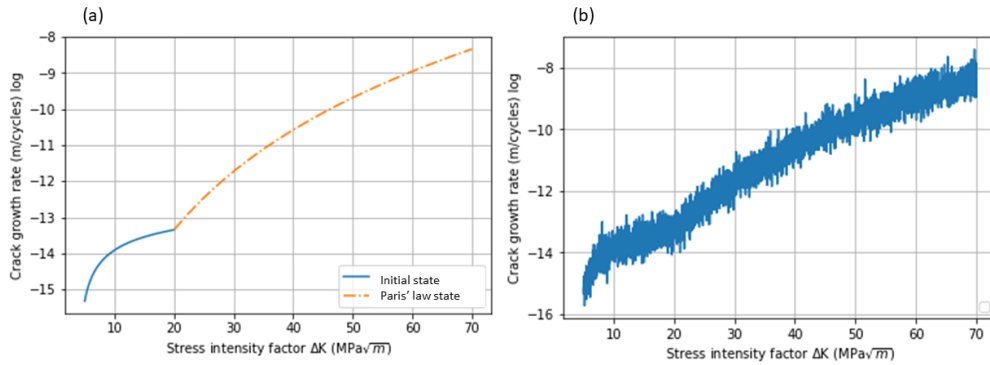


Figure 6.18. Data preparation: (a) The theoretical curve; (b) The theoretical curve with gaussian noise.

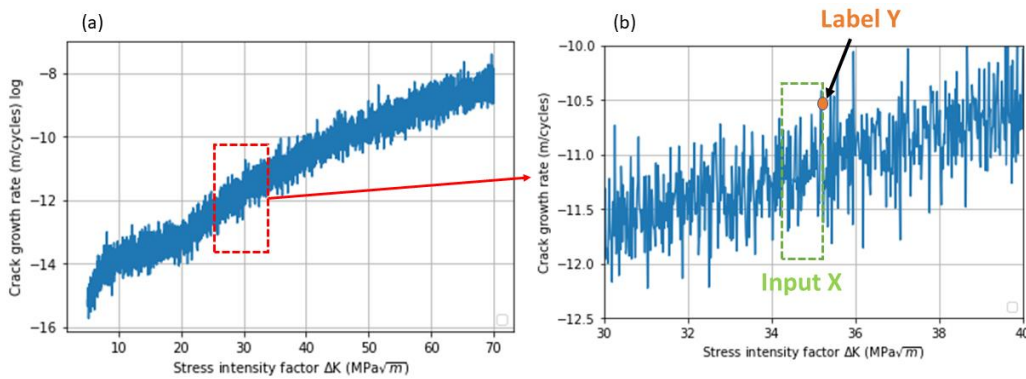


Figure 6.19. Data preparation: (a) The theoretical curve with gaussian noise; (b) Zoom-in window.

The DNN was performed on the training set to predict the curves on the validation set. The specific procedure of data preparation was shown in Figure 6.19. Figure 6.19(b) was the zoom-in of the red box in Figure 6.19(a). In the green box in Figure 6.19(b), the final value in the green box was used as a label and the rest of the data values were inputs of this area.

The whole process needed two parts of data: the training set and the validation set, shown in Figure 6.20. The goal of this study aimed to predict the remaining useful life corresponding to the second part of the whole series. Therefore, the whole series was divided into two with the first part as the training set and the second half as the validation set. The prediction was made based on

the training set data verified and compared with the validation set to prove the effectiveness of the prediction.

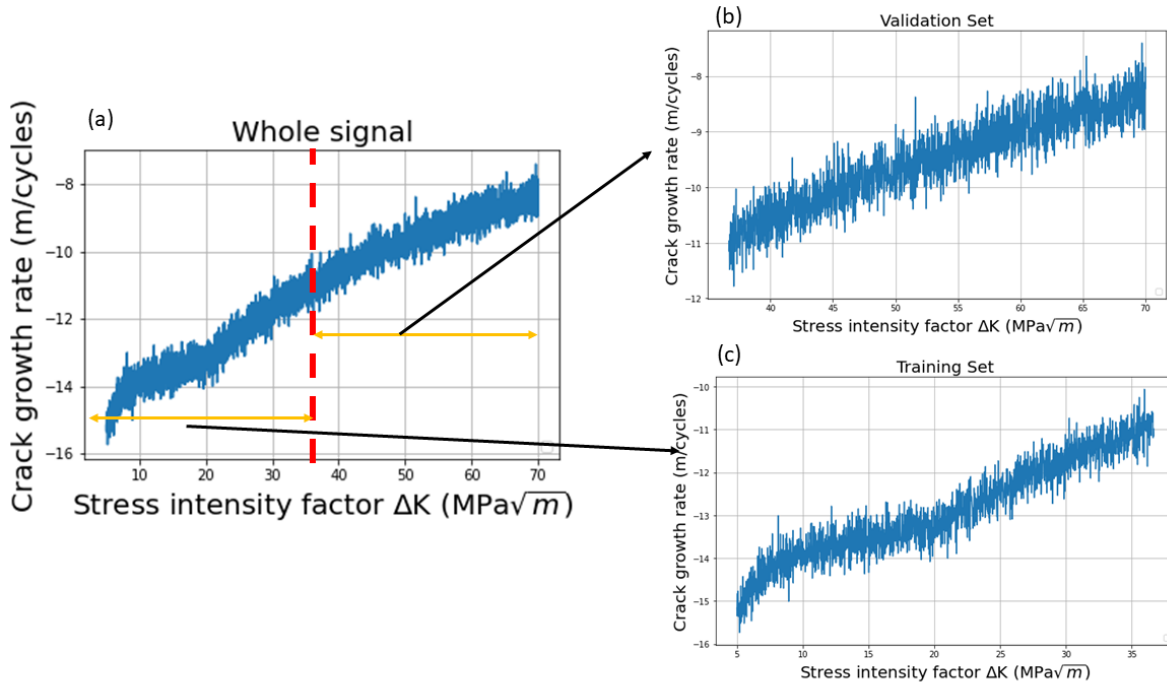


Figure 6.20. Data preparation: (a) whole signal; (b) validation set; (c) training set.

The training was implemented using open-source software: Tensor Flow, Keras. The loss was estimated by mean square error (mse). The “ Colab ”, one of the online servers, was used to training the model. There were three neuron layers: The first layer with ten neurons followed by “Relu”(rectified linear unit) activation function; the second layer also with ten neurons followed by “Relu” activation function; the third layer was a one-neuron layer yielding the prediction. Stochastic gradient descent (SGD) with momentum [24] was chosen as the optimization method. SGD was a powerful tool to accelerate the training speed. On the contrary to the traditional batch gradient descent traveling through the whole training per iteration, SGD learned one example per each epoch and yielded the learning process, reporting to researchers if the training was on the

right track. However, the side effect was also quite severe due to the significant oscillation, which might lead to the overshoot when the model was close to the optimum. The cure of this problem was adding momentum to keep the training progress traveling in the same direction and prevent oscillations. The momentum was set to 0.9 which indicated averaging 10 iterations during the training.

6.7.2. Results

The prediction was compared with the validation set shown in Figure 6.21. This prediction was made by using $3e-7$ for learning rate, also called step size. The results showed the high degree match between two sets, which indicated the learning rate may be too small to over train the model resulting in less computational efficiency. However, on the other hand, the oscillation was small regarding epochs shown in Figure 6.22. The loss gradually going down also indicated the convergence of this training process.

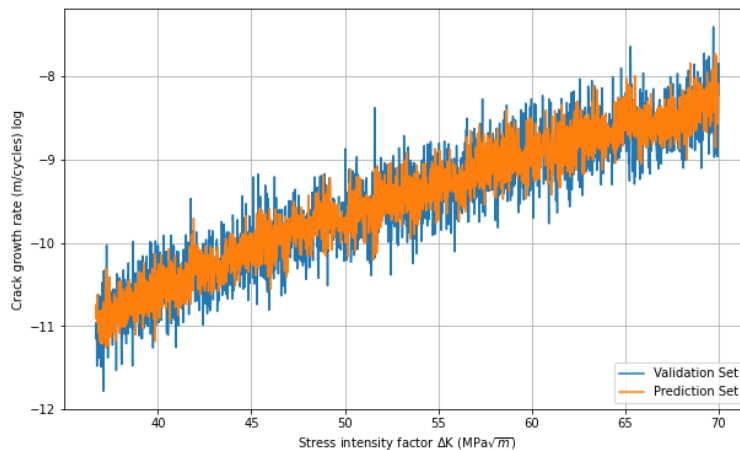


Figure 6.21. The comparison of the validation set and the prediction set.

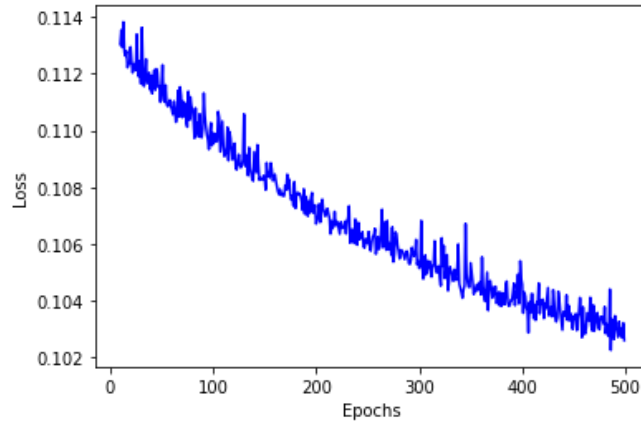


Figure 6.22. The training convergence analysis.

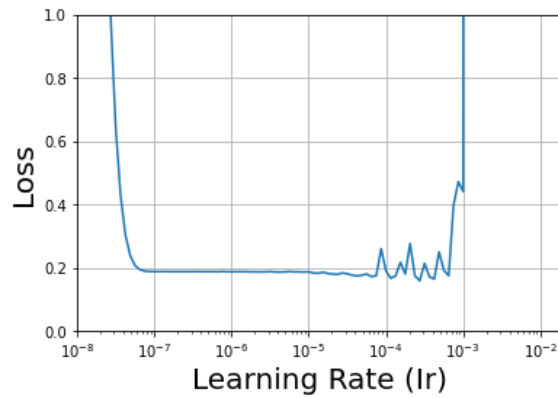


Figure 6.23. The training efficiency analysis of the loss and the learning rate.

The analysis of loss and learning rate was necessary to find the best learning rate fast and effective, shown in Figure 6.23. Learning rate between $5e-4$ to $3e-7$, the loss was almost plateau, which demonstrated the fact that learning rate in this region yielded similar accuracy yet cost distinct consuming time. The larger the learning rate was, the less the time consumption would be.

The best learning rate chosen to test was $3e-4$, the corresponding results were shown in Figure 6.24. The learning rate was larger than last result, the Figure 6.24(b) showed the larger oscillation accordingly yet the final convergence was still held under this size of the learning rate.

Figure 6.24(c) showed the result comparison between the prediction and validation, which was less matching than that shown in Figure 6.21. However, the running speed was significantly improved in terms of larger step size.

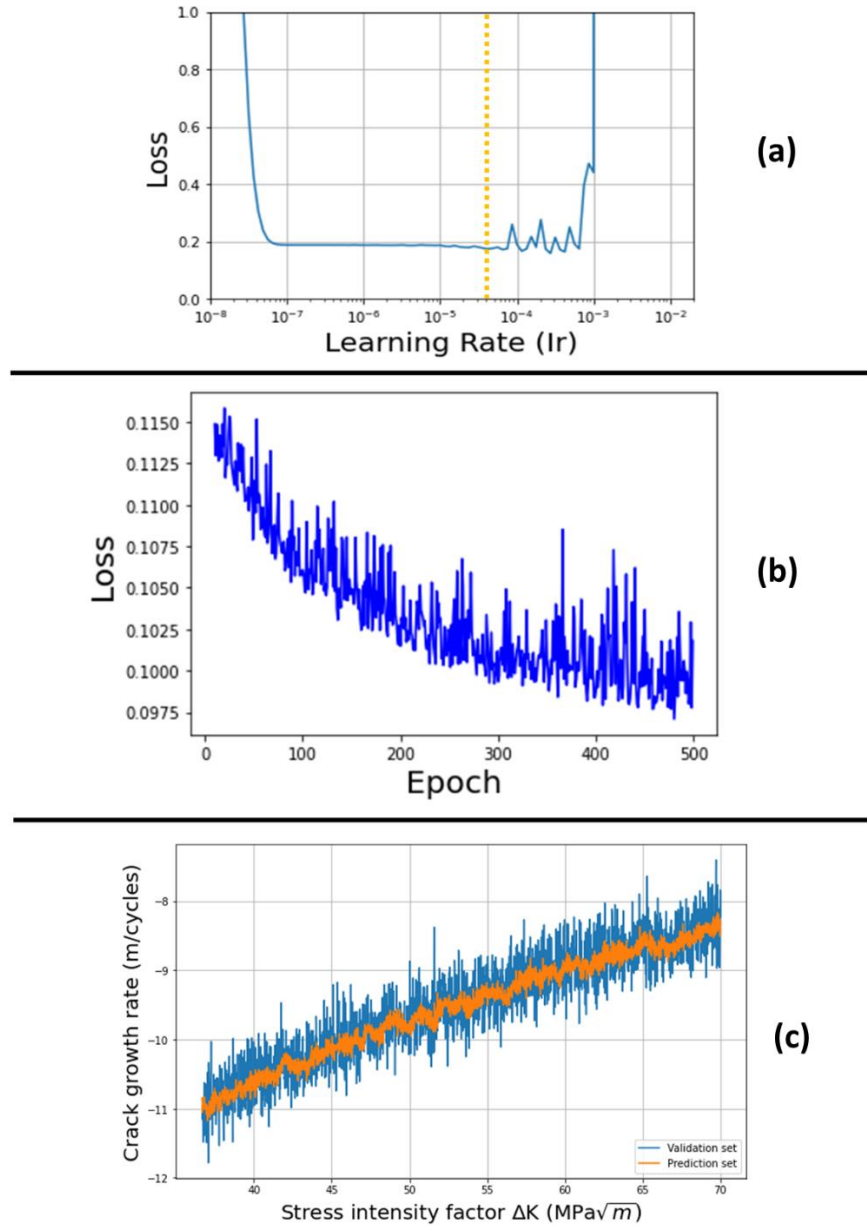


Figure 6.24. The efficient learning rate discussion with the largest learning step

The preliminary study of remaining useful life estimation was implemented using the approximately theoretical curves with considerable amplitude noise. The DNN was used for making the prediction given the initial state of the crack growth with nonlinear properties. The efficiency of the training schedule was discussed by comparing the loss and learning rate to yield a suitable learning rate with acceptable as well as high speed. The prediction of the second pairs' law state was quite matched with the validation set of the given signal, which theoretically proved that this methodology was capable of predicting the real data from the experiment.

6.8. Acknowledgments

This work was funded by the US Federal Railroad Administration (contract # 693JJ619C000008). And field experiments were collaborated with Transportation Technology Center, Inc (TTCI) rail defect library.

Team members at UCSD Dr. Albert Liang, Dr. Simone Sternini, Dr. Margherita Capriotti, Diptojit Datta, Izabela Batista. The author would like to thank FRA Program Manager Dr. Robert Wilson and FRA Office of Research, Development and Technology Division Chief Gary Carr for technical advice and project oversight.

Chapter 6 in part, has been published in Chengyang Huang, Ranting Cui, and Francesco Lanza di Scalea "Deliverable 1.1: Chapter on Task 1 - SAFT Imaging Algorithm Finalization and 3D Image Generation based on Laboratory Tests at TTCI and UCSD", U.S Department of Transportation, Federal Railroad Administration, February, 2021. The dissertation author was the primary investigator and author of this technical report.

6.9. References

- [1] Drinkwater BW, Wilcox PD. Ultrasonic arrays for non-destructive evaluation: A review. *NDT E Int* 2006;39:525–41. <https://doi.org/10.1016/j.ndteint.2006.03.006>.
- [2] Lanza di Scalea F, Moore PO. Ultrasonic testing applications in the railroad industry. *Non-Destructive Test Handbook*, 3rd Ed, PO Moore, Ed, Am Soc Nondestruct Testing, Columbus, OH 2007:535–52.
- [3] Holmes C, Drinkwater BW, Wilcox PD. Advanced post-processing for scanned ultrasonic arrays: Application to defect detection and classification in non-destructive evaluation. *Ultrasonics* 2008;48:636–42. <https://doi.org/10.1016/j.ultras.2008.07.019>.
- [4] Holmes C, Drinkwater BW, Wilcox PD. Post-processing of the full matrix of ultrasonic transmit-receive array data for non-destructive evaluation. *NDT E Int* 2005;38:701–11. <https://doi.org/10.1016/j.ndteint.2005.04.002>.
- [5] Engholm M, Stepinski T. Adaptive beamforming for array imaging of plate structures using Lamb waves. *IEEE Trans Ultrason Ferroelectr Freq Control* 2010;57:2712–24.
- [6] Hall JS, Michaels JE. Minimum variance ultrasonic imaging applied to an in situ sparse guided wave array. *IEEE Trans Ultrason Ferroelectr Freq Control* 2010;57:2311–23. <https://doi.org/10.1109/TUFFC.2010.1692>.
- [7] Matrone G, Savoia AS, Caliano G, Magenes G. The delay multiply and sum beamforming algorithm in ultrasound B-mode medical imaging. *IEEE Trans Med Imaging* 2015;34:940–9. <https://doi.org/10.1109/TMI.2014.2371235>.
- [8] Matrone G, Savoia AS, Caliano G, Magenes G. Depth-of-field enhancement in Filtered-Delay Multiply and Sum beamformed images using Synthetic Aperture Focusing. *Ultrasonics* 2017;75:216–25. <https://doi.org/10.1016/j.ultras.2016.11.022>.
- [9] Holmes C, Drinkwater B, Wilcox P. The post-processing of ultrasonic array data using the total focusing method. *Insight-Non-Destructive Test Cond Monit* 2004;46:677–80.
- [10] Huang L, Labyed Y, Simonetti F, Williamson M, Rosenberg R, Heintz P, Sandoval D. High-resolution imaging with a real-time synthetic aperture ultrasound system: a phantom study. *Med Imaging 2011 Ultrason Imaging, Tomogr Ther* 2011;7968:79681I. <https://doi.org/10.1117/12.878767>.
- [11] Sternini S, Liang AY, Lanza di Scalea F. Ultrasonic synthetic aperture imaging with interposed transducer–medium coupling path. *Struct Heal Monit* 2019;18:1543–56.
- [12] Van Trees HL. *Optimum array processing: Part IV of detection, estimation, and modulation theory*. John Wiley & Sons; 2004.
- [13] Harris FJ. On the use of windows for harmonic analysis with the discrete Fourier transform.

Proc IEEE 1978;66:51–83.

- [14] Kuperman WA, Hodgkiss WS, Song HC, Akal T, Ferla C, Jackson DR. Phase conjugation in the ocean: Experimental demonstration of an acoustic time-reversal mirror. *J Acoust Soc Am* 1998;103:25–40.
- [15] Ahmadzadeh F, Lundberg J. Remaining useful life estimation. *Int J Syst Assur Eng Manag* 2014;5:461–74.
- [16] Jardine AKS, Lin D, Banjevic D. A review on machinery diagnostics and prognostics implementing condition-based maintenance. *Mech Syst Signal Process* 2006;20:1483–510.
- [17] Eker ÖF, Camci F, Jennions IK. Major challenges in prognostics: study on benchmarking prognostic datasets 2012.
- [18] Gebraeel N, Elwany A, Pan J. Residual life predictions in the absence of prior degradation knowledge. *IEEE Trans Reliab* 2009;58:106–17.
- [19] Tabian I, Fu H, Khodaei ZS. A convolutional neural network for impact detection and characterization of complex composite structures. *Sensors (Switzerland)* 2019;19:1–25. <https://doi.org/10.3390/s19224933>.
- [20] LeCun Y, Bengio Y, Hinton G. Deep learning. *Nature* 2015;521:436–44.
- [21] Graves A, Fernández S, Schmidhuber J. Bidirectional LSTM networks for improved phoneme classification and recognition. *Int. Conf. Artif. neural networks*, Springer; 2005, p. 799–804.
- [22] Knott JF. *Fundamentals of fracture mechanics*. Gruppo Italiano Frattura; 1973.
- [23] González-Velázquez JL. Fatigue. *Struct Integr* 2020;12:187–223. https://doi.org/10.1007/978-3-030-29241-6_7.
- [24] Bottou L. Stochastic gradient descent tricks. *Neural networks: Tricks of the trade*, Springer; 2012, p. 421–36.

Chapter 7. Conclusions

Solving inverse problems, recognizing damage patterns, and exploiting the computational intelligence to identify the possible defect locations are primary means of the NDE and SHM community to understand damages on the laminated composite components. Chapter 2 explored the potential for ultrasonic guided waves in high frequency (~100s of kHz) region to identify elastic properties of composite laminates by its nature of advantages regarding large ranges and high sensitivity to both lamina-by-lamina properties and laminate engineering properties due to the coupling of longitudinal and traversal, normal and shear stresses/strains cross-sectional distributions. Moreover, ultrasonic guided waves relaxed the restriction of boundary conditions of the test part, such as boundary reflections, making themselves capable of installing on the structure in service. Three fundamental guided modes of axial (S_0), flexural (A_0), and shear-horizontal (SH_0) were considered, which were typically used in general.

Chapter 3, as a continuation, provided experimental validation of the proposed framework examined in simulation in chapter 2 by using guided wave dispersion curves to identify the elastic properties of composite laminates. The measuring phase velocity dispersion curves of the plate were achieved by the 2D-FFT method, then matching these curves to SAFE-predicted curves through a Simulated Annealing optimization algorithm. It is meaningful to examine experimentally the effectiveness of a single guided wave propagation direction to identify global “engineering” constants of the laminate, both in the wave launching direction and traversal direction. It was proved that the coupling of normal and shear stresses/strains improved the elastic property identification with the increasing numbers of the off-axis laminae (e.g., $\pm 45^\circ$ and 90° laminae for a 0° wave propagation direction). However, this study had been limited to the elastic

properties of the composite. It is theoretically possible to extend the framework to the visco-elastic property identification by including the appropriate complex stiffness coefficients in the SAFE formulation.

Chapter 4 extended the studied object from a composite plate to a complex skin-to-stringer composite panel for defect detection and localization. A Convolutional Neural Network (CNN) was designed for this application, including the enhancements of Batch Normalization, Minibatch-ADAM optimization, and L2-Norm Regularization. This study was tested on various damages scenarios based on the well-trained model of simulated damages, such as simulated damages that co-located with the trained locations, simulated damages that were offset from the trained locations, eventually, the real damage (a slit cut on the stringer cap). To ensure the accuracy, at the meantime, be limited by the computational power, the algorithm utilizes three different classification models. One was for distinguishing the general locations, on stringer cap or not. The second was specifically for the damage classified not on the stringer cap to predict the accurate location. The third was targeted for the damage classified on the stringer cap to predict the precise location. The results indicated that the damage imaging performance depended on the type of signal excitations, the higher-energy excitations improving the damage imaging performance, therefore, the summation version producing the comprehensive prediction.

Chapter 5 introduced three techniques for damage detection and localization regarding composite materials. The first method showed a data-driven matched field processing to identify the simulated damages (clay added mass) on the stringer-to-skin cross-section. The second method, another designed CNN for the excitation localization, was investigated using data from ABAQUS, preliminarily proving the benefit to operate the model with the real experimental data. The third method aimed to improve mobility and flexibility by using air-coupled transducers through

structural transfer function extraction, reducing the influence of the random excitation source. Using features gathered from the transfer functions, a statistical anomaly analysis produced damage indices to trace the peaks, therefore, identifying the damage location along the scanning direction. Later, a discussion concerning the skin-to-stringer-to-shear_tie structure was conducted by air-coupled transducers and mini-impactor through the transfer function extraction. A Receiver Operating Characteristic (ROC) curve was employed to find a stable status for the damage detection.

Chapter 6 investigated the 2D and 3D defect reconstructions on an aluminum block with simulated damages (two drilling holes) and railhead with transverse defects (TDs) by ultrasonic-bulk-wave beamforming algorithm. Two algorithms (frequency-domain-beamforming and time-domain-beamforming) were discussed and compared. A real-time 2D and 3D defect imaging script with encoder control was operated on the railhead with natural transverse defects. This study helped rail maintenance engineers to knowledgeable decisions based on given defect sizes. Moreover, a preliminary study of the remaining-useful-life of the rail track follows given the size of the defect on the railhead by imaging. A deep-neuron network was designed to predict the remaining life based on the current status with a considerable noise level. The trade-off between accuracy and computational efficiency in terms of learning rate was discussed to find the best strategy to perform the training. This study provided some insights into dealing with future experimental data, especially with a low signal-to-noise ratio.